

Florida Institute of Technology

Scholarship Repository @ Florida Tech

Theses and Dissertations

7-2022

Infrared Search for N-Butane and Trans-2-Butene in Titan's Atmosphere

Brendan Steffens

Follow this and additional works at: <https://repository.fit.edu/etd>



Part of the [Astrophysics and Astronomy Commons](#)

Infrared Search for *N*-Butane and *Trans*-2-Butene in Titan's Atmosphere

by

Brendan Steffens

Bachelor of Science - Physics
Department of Physics
Northern Illinois University
2017

A dissertation
submitted to the College of Engineering and Science
at Florida Institute of Technology
in partial fulfillment of the requirements
for the degree of

Doctor of Philosophy
in
Space Sciences

Melbourne, Florida
July, 2022

We the undersigned committee
hereby approve the attached dissertation
Infrared Search for *N*-Butane and *Trans*-2-Butene in Titan's Atmosphere by
Brendan Steffens

Manasvi Lingam, Ph.D.
Assistant Professor
Aerospace, Physics and Space Sciences
Major Advisor

Conor Nixon, Ph.D.
Associate Chief
Planetary Systems Laboratory
NASA Goddard Space Flight Center

Daniel Batchelder, Ph.D.
Subject Matter Expert in Physics
Southeastern Universities Research Association

Hamid Rassoul, Ph.D.
Professor
Aerospace, Physics and Space Sciences

Yi Liao, Ph.D.
Professor
Biomedical, Chemical Engineering and Sciences

Csaba Palotai, Ph.D.
Associate Professor
Aerospace, Physics and Space Sciences

David Fleming, Ph.D.
Associate Professor and Department Head
Aerospace, Physics, and Space Sciences

ABSTRACT

Title:

Infrared Search for *N*-Butane and *Trans*-2-Butene in Titan's Atmosphere

Author:

Brendan Steffens

Major Advisor:

Manasvi Lingam, Ph.D.

This dissertation constitutes a study of the possible presence of trace hydrocarbons, namely *n*-butane ($n\text{-C}_4\text{H}_{10}$) and *trans*-2-butene ($\text{trans-2-C}_4\text{H}_8$) in Titan's atmosphere. These molecules, both of which bear specific connections of interest to Titan's astrobiological potential, are predicted by photochemical models to occur at detectable abundances within Titan's atmosphere. In spite of this, neither has been detected to date, by any means. For this work, both of these molecules were characterized in the laboratory by obtaining a comprehensive set of high-resolution, infrared cross section measurements at cold temperatures appropriate for Titan. In the case of *n*-butane, a pseudoline list (i.e. an empirical model of a spectral line list) which can be directly integrated into existing radiative transfer codes, was also derived. Using the NEMESIS planetary retrieval code, these results were implemented in the modeling of observations of Titan coming from Cassini CIRS and NASA IRTF in search of emissions of these molecules. The NASA IRTF observations were designed and calibrated to be optimized toward investigating Titan's *n*-butane and *trans*-2-butene abundances. Ultimately, this study claims no explicit detection of either molecule. Instead, a comprehensive set of upper limits on the abundances of *n*-butane in Titan's atmosphere is attained, and rough upper limits are derived for the first time for *trans*-2-butene. The up-

per limits for these molecules will be crucial in further constraining photochemical models, as a major effort is currently underway to fully add Titan's C₄ chemistry to these models. Results from this work may also provide insight into the formation of Titan's ubiquitous hazes, clouds, and may even shed light on the composition of Titan's unique lakes and seas.

Table of Contents

Abstract	iii
List of Figures	xiv
Abbreviations	xxxii
0.1 Acronyms	xxxii
0.2 Symbols	xxxiii
0.3 Nomenclature	xxxiii
0.4 Abbreviations	xxxvii
Acknowledgments	xxxviii
Dedication	xlii
Preface	xliii
1 Titan - Background	1
1.1 Discovery and Exploration	4
1.1.1 Initial Discovery and Detection of Atmosphere	4
1.1.2 The Voyager Missions	5
1.1.3 Infrared Space Observatory (ISO)	7
1.1.4 Hubble Space Telescope (HST)	8

1.1.5	Cassini	9
1.1.6	Huygens Probe Landing	10
1.1.7	Ground-based observations	11
1.1.8	Upcoming Dragonfly mission	14
1.2	Titan’s Orbital Parameters	14
1.3	Atmosphere	16
1.3.1	Atmospheric Composition	17
1.3.2	Atmospheric Chemistry	21
1.3.3	Hydrocarbons: Moving from C ₃ to C ₄	22
2	Methodology	26
2.1	Phase 1: Laboratory Spectroscopy of Targeted Molecule	27
2.1.1	Brief Primer Concerning Radiative Transfer Theory	28
2.2	Phase 2: Observations of Targeted Body	29
2.3	Phase 3: Radiative Transfer Modeling of Observations	30
2.4	Connecting the Dots	32
2.5	Chapter 2 Conclusion	33
3	Laboratory spectroscopy	35
3.1	Introduction	35
3.2	The “Ratioing” Process	39
3.3	Absorption Cross-sections and Band Intensities	40
3.3.1	The Linearity Test: When Is σ_ν Equivalent to S?	43
3.3.2	Cross Sections and Band Intensities - Conclusion	44
3.4	N-butane (n-C ₄ H ₁₀)	45
3.4.1	The Molecule	45

3.4.2	Experimental Conditions	55
3.4.3	Cross-Section Measurements	58
3.4.4	Pseudoline List Generation	61
3.4.5	Results and Discussion	73
3.4.6	N-Butane: Conclusion	76
3.5	Trans-2-Butene (Trans-2-C ₄ H ₈)	77
3.5.1	The Molecule	77
3.5.2	Experimental Conditions	81
3.5.3	Cross-Section Measurements	85
3.5.4	Linearity Test	88
3.5.5	Results and Discussion	92
3.5.6	Butenes, Carbenes, and 1,2-Dimethylcyclopropane: A Chiral Connection	99
3.6	Limitations in Use of These Results	104
4	Atmospheric modeling	107
4.1	NEMESIS in detail	108
4.2	Cassini spacecraft	112
4.2.1	The Composite Infrared Spectrometer Instrument	113
4.2.2	The CIRS Observations	117
4.2.3	Modeling	121
4.2.4	CIRS Modeling - N-Butane Upper Limit Results	132
4.2.5	CIRS Modeling - N-Butane Discussion	148
4.2.6	N-Butane Modeling - Conclusion	151
4.3	NASA Infrared Telescope Facility	152

4.3.1	The Texas Echelon Cross Echelle Spectrograph (TEXES) Instrument	156
4.3.2	The data	159
5	Conclusion	171
5.1	Brief Summary	171
5.2	Conclusions and Future Steps	173
5.2.1	Laboratory Work: <i>n</i> -C ₄ H ₁₀	173
5.2.2	<i>Trans</i> -2-C ₄ H ₈	175
5.2.3	Cassini CIRS Modeling	177
5.2.4	2021 IRTF/TEXES Modeling	180
5.2.5	Summary	181
5.3	Leveraging Experience, and Moving Forward	182
5.3.1	A Final Word	185
A	TEXES User Guide	208
A.1	Introduction	208
A.1.1	Contact	209
A.1.2	Acknowledgements	209
A.2	Acquiring/Installing IDL:	209
A.3	Getting Started	210
A.4	Using <code>rdpipe.pro</code> and <code>lacetoms_ver2.pro</code>	212
A.5	Corrections to your data	216
A.5.1	Blackbody correction	217
A.5.2	Doppler correction	217
A.5.3	Jansky conversion	218

A.6 Closing remarks	219
-------------------------------	-----

List of Tables

1.1	Characteristics of Titan and its orbit about Saturn [31; 32; 33; 34].	16
1.2	Characteristics of Titan and its orbit about Saturn [31; 32; 33; 34].	16
1.3	Tabulated summary of molecules detected by remote sensing in Titan’s atmosphere, as well as their abundances, as measured by different spacecraft/observatories. Omitted entries in the table correspond to species that have not been measured with that respective spacecraft/observatory. See Table 1.4 for further details and citations.	18
1.4	Titan’s atmospheric constituents and how they were first detected. Abbreviations: IRIS (Infrared Interferometer Spectrometer [36]), SWS (Short Wavelength Spectrometer [37]), G-B (former Ground-Based observatory), INMS (Ion and Neutral Mass Spectrometer [38]), IRTF TEXES (NASA’s Infrared Telescope Facility, Texas Echelon Cross Echelle Spectrograph [39]), ALMA (Atacama Large Millimeter/Submillimeter Array). Table adapted from Table 6.1 in Coustenis and Taylor (2008)[23].	20

1.5	Production and loss of the ten most abundant trace molecules of Titan’s atmosphere. It can be seen that the primary loss mechanism for many of these molecules is in fact condensation in the lower atmosphere, where these species can precipitate and end up on Titan’s solid surface or in its lakes and seas [62].	22
3.1	Configuration of Bruker instrument during n -C ₄ H ₁₀ data acquisition.	57
3.2	Spectral regions defined for our study of n -butane. The bands of either n -butane conformer in each of the four regions are also identified.	60
3.3	Integrated intensity in 10^{-19} cm ⁻¹ / (molecule·cm ⁻²) of n -butane, normalized to a 100% purity sample, for each of the four regions, as a function of temperature. In the case of our room temperature results, we are able to compare to results from PNNL (shown in the bottom two rows), with which we find good agreement [115]. A graphical comparison between our room temperature results and those of PNNL is presented in Figure 3.12.	73
3.4	Experimental conditions of pure and N ₂ -broadened <i>trans</i> -2-butene spectra. Each spectrum used a path length of $L = 20.38$ cm. The column labeled Res(B), shows the associated Bruker resolution parameter for the spectrum. The actual spectral resolution is then calculated as $\frac{5}{9} \cdot \text{Res(B)}$	83
3.5	Spectral regions defined for our study of <i>trans</i> -2-butene.	86

3.6	Experimental conditions of the N ₂ -broadened <i>trans</i> -2-butene spectra used in our linearity test. Each of these was gathered at spectral resolution R=0.062 cm ⁻¹ . The volume mixing ratio (VMR) of <i>trans</i> -2-butene (i.e. sample pressure divided by total pressure including N ₂) is also shown.	91
3.7	Estimated partial pressure fractions of CO ₂ contamination originating from within the <i>trans</i> -2-butene sample. These were found by simulating the CO ₂ ν ₂ band and comparing to the observed spectra. These partial pressures are then used to ensure that the calculations of cross-sections, which rely on the measurements of the <i>trans</i> -2-butene sample pressure and the total pressure within the gas cell, are not skewed by the presence of this CO ₂	93
3.8	Tabulated results for the study of <i>trans</i> -2-butene, in the form of average integrated cross-sections [10 ⁻¹⁸ cm molecule ⁻¹] and their standard deviation at each of the temperatures used, for each of the three regions defined in Table 3.5. The average percent error for our results across the full spectral region studied here is calculated to be 4.02 %. For purposes of comparison, the same are also shown for NIST (National Institute of Standards and Technology), derived from measurements of <i>trans</i> -2-butene acquired at room temperature (no uncertainties provided), at a spectral resolution of 2 cm ⁻¹ [70]. .	95

4.1	Cassini CIRS Observations: The final column shows the average projected detector footprint for the observation set. Note that Titan’s atmospheric scale height is approximately 50 km in the stratosphere. The EQ observations are described more thoroughly in Nixon et al. (2013) [60], whereas details for the T3, T10 and other Cassini-Titan flybys can be found in Nixon et al. (2019) [128]. . . .	118
4.2	Altitude ranges and number of co-added spectra.	119
4.3	Upper Limits for EQ Data, derived from $\Delta\chi^2$ curves, using the constant profile, and the photochemically predicted profiles of Loison et al. (2019) [65] and Krasnopolsky et al. (2014) [146]. These are reported at the peak altitudes of the <i>n</i> -butane contribution functions shown in Figure 4.10. Strengths of the resulting minima in the curves (also measured in σ) are shown as well, in addition to the gas abundance (in ppb) corresponding to that minimum.	134
4.4	Upper Limits for T3 Data. Note that the ellipses marking empty entries in the table correspond to instances where a minimum in the $\Delta\chi^2$ curve was not observed at all.	135
4.5	Upper Limits for T35 Data	136
4.6	Rough upper limits (in ppb) for <i>trans</i> -2-butene in the new IRTF/-TEXES data, estimated by first calculating <i>n</i> -butane’s upper limits using its pseudoline list, and then scaling those results by the ratio of band intensities in the region.	170

List of Figures

1	The ν_4 band of CO ₂ , demonstrating the typical structure of a molecular rovibrational band. The individual transitions (lines) that form the band are organized into three regions which we label the P, Q, and R branches. These correspond to specific changes in rotational quantum number J	xxxiv
2	Energy diagram for the conformational states of the n -butane molecule. Two stable conformers are observed, separated by 3.8 kJ per mole. Note that that the two rotational states at 60° on either side of 0° are effectively identical and both called <i>gauche</i> . Image adopted from ‘Basic Terminology of Stereochemistry’ by Moss. (1996).	xxxvii
1.1	Saturn and Titan, as viewed by the Cassini spacecraft. Image credit: NASA/JPL-Caltech/Space Science Institute.	2
1.2	Artist’s impression of Titan’s largest hydrocarbon lake, Kraken Mare, with view of Saturn in the background. Image credit: NASA / John Glenn Research Center.	2

1.3	Temperature profiles retrieved for equatorial and northern latitudes using Voyager 1 observations. Curves A, D, E, and F correspond to latitudes of 0°, 30°, 50°, and 70°, respectively. The temperature retrieval model’s contribution functions are also shown (using the top horizontal axis) for the Q-branch and P-branches of methane’s ν_4 band, demonstrating the different altitude sensitivities for different portions of this molecular vibrational band which has been so crucial for Titan science. The P-branch, which is slightly lower in energy than the Q-branch (i.e. slightly longer in wavelength or lower in wavenumber) is seen to penetrate deeper into the atmosphere, yielding maximum sensitivity at a slightly lower altitude than that of the Q-branch. Figure adapted from Figure 5 of Coustenis and Bezdard, Icarus, 1995 [15].	6
1.4	The surface of Titan, as seen by the Huygens lander probe. The rocky looking globules, which are 10-15 cm in size, are actually likely to be mostly water ice. Image was taken with the Descent Imager/Spectral Radiometer instrument [24].	12
1.5	SOFIA observatory and infrared telescope. May she rest forever in peace.	13
1.6	The Dragonfly rotorcraft, shown in stages, parachuting down through the Titan atmosphere before activating its propellers for a soft landing. Dragonfly will then fly to dozens of different nearby sites to study Titan’s surface and lower atmosphere.	15
1.7	Visual representation of the species shown in Table 1.3. This figure has been adapted from Figure 5 of MacKenzie et al. (2021) [35]. . .	19

2.1	The three areas that contribute to characterizing a planetary atmosphere, demonstrating the concept that efficient intercommunication between each of these three areas is a necessary component of the procedure.	33
3.2	Schematic for a general Fourier Transform Spectrometer (FTS)[85].	36
3.1	A Bruker IFS 125 HR. Projecting out of the page is the long ‘scan’ arm of the interferometer, on which a moving mirror is able to travel along the observed track. Perpendicular to the scan arm is a second arm that houses the infrared light source, the filled gas cell, and the detector. This image and more information about other Bruker instruments can be found on their main website: www.Bruker.com .	37
3.3	The two isomers of butane. (a) <i>n</i> -butane, the focus of this section, and (b) isobutane, which still needs to be characterized more thoroughly in the future!	46
3.4	The two conformers of <i>n</i> -butane. The <i>trans</i> conformer is more stable (by 0.9 kcal mol ⁻¹), as the two methyl groups are crowded in the <i>gauche</i> structure. Image generated by Brendan Steffens.	51

3.5	<p>Band centers (cm^{-1}) of the $n\text{-C}_4\text{H}_{10}$ fundamentals grouped by their vibrational symmetries. The bands in bold in the $660\text{--}1560\text{ cm}^{-1}$ region are the ones we adopted for the vibrational partition function calculations in this work, toward the calculation of the n-butane pseudo-line list, which will be described later on in this Chapter. The band centers in parenthesis are model predictions by Shimanouchi (1972) [110] with uncertainty codes being A($0\text{--}1\text{ cm}^{-1}$), B($1\text{--}3\text{ cm}^{-1}$), C($3\text{--}6\text{ cm}^{-1}$), D($6\text{--}15\text{ cm}^{-1}$), E($15\text{--}30\text{ cm}^{-1}$). [§]Infrared inactive. ^{&}Torsional bands. [@]Experimental values reported by Murphy et al. (1991) [111]. The values in square brackets are the newly suggested band centers based on the observed spectra from our study. This table was adapted from Table 3 of our paper on this work, Sung et al. (2020) [112].</p>	53
3.6	<p>Samples of pure (green curve) and N_2-mixture spectra (in magenta) of $n\text{-C}_4\text{H}_{10}$ obtained at 278 K. A few representative band centers from both the <i>trans</i> and <i>gauche</i> conformers have been identified with the help of model predictions (though the values labeled here are our <i>updated</i> values, as listed in Figure 3.5. For example, ν_{17} (labeled n731) reads as ν_{17} band of <i>trans</i> butane conformer, and it is centered at 731 cm^{-1}. Note that the features near 667 cm^{-1} are contamination from the CO_2 (ν_2), as marked in the figure. This CO_2 contamination is described more thoroughly later in this Chapter. This figure has been adapted from Figure 2 of our publication on this work, Sung et al. (2020)[112].</p>	54

3.7	Experimental conditions for each of the 28 spectra collected for our study for <i>n</i> -butane. The ‘B0174’ spectral labeling is a convention of the JPL Molecular Spectroscopy Laboratory. P_s and P_t refer to the sample pressure (<i>n</i> -butane) and total pressure (<i>n</i> -butane+N ₂).	59
3.8	Samples of absorption cross-sections for <i>n</i> -butane.	60
3.9	The Voigt profile, a valid lineshape for modeling both the temperature <i>and</i> pressure broadening aspects of spectral lines. This is the form that is adopted for each spectral line in a pseudoline list. Figure adapted from Scipy main website [117].	62
3.10	Demonstration of the pseudoline list’s ability to model <i>n</i> -butane at a variety of temperatures and pressures. Each panel (a)-(d), corresponding to Regions I-IV, as defined in Table 3.2, shows the fitting residuals from the <i>n</i> -butane pseudoline list. The bottom portion of each panel shows the synthetic spectra generated from the pseudoline list, and the upper portions show the fitting residuals for various subsets of the 28 spectra we collected, as a function of temperature. Agreement to within better than 2% is seen in the first three regions, i.e. panels (a), (b), and (c), and to within 4% in the final region, in panel (d).	67

3.11	Panels (a) through (d) show the retrieved volume scale factors (VSFs) for the individual pure (solid circles) and mixture (open circles) laboratory spectra that we collected. The mean VSFs were found to be 0.991, 1.000, 1.000, and 0.997 for Regions I-IV, respectively, with standard deviations of less than 4.7, 3.7, 3.4, and 3.9 %; these can be interpreted as measurement uncertainties associated with the pseudolines.	70
3.12	Graphical comparison of our room temperature integrated <i>n</i> -butane intensity measurements (red curves) compared to those of PNNL (blue points) [115]. The top panel shows results for Regions I, II, and III, and Region IV's results are contained in the bottom panel. It can be seen that in general, good agreement between our results and those of PNNL is observed. Additionally, minimal temperature dependence is seen to the integrated cross-section measurements, as expected [120; 121; 122].	71
3.13	Exerpt from the HITRAN-formatted pseudoline list for <i>n</i> -butane produced by this work.	72

3.14 The four possible isomers of the butene molecule. The structure of *trans*-2-butene can be seen in the top left, along with 1-butene (bottom left), with the only significant difference between the two molecules being the placement of the double bond. Also shown is *cis*-2-butene (top right), the stereoisomer of *trans*-2-butene, which differs in having both of its methyl groups on the same side of the double bond. Lastly, *iso*-butene (bottom right), is the final isomer, with the fourth methyl group attached to the number 2 carbon, rather than attached to the end and forming a four-carbon-long chain. In spite of all of these rather simple differences, all four molecules are entirely distinct from one another, spectroscopically speaking, and thus they each require separate laboratory work in order to disentangle their possible contributions to remote sensing observations of planetary atmospheres. 77

3.15 Vapor pressure curve of *trans*-2-butene, used to inform the lower bound of the temperature range that we can study this molecule in the Bruker spectrometer. Approaching temperatures low enough such that the target molecule's vapor pressure may accidentally be exceeded (which starts to occur around 0.1 Torr) must be avoided, as this leads to condensation within the gas cell and a major delay in data collection; obviously, the condensed *trans*-2-butene ice in the gas cell changes the transmission spectra being recorded, invalidating the collection of *gaseous* spectra. Moreover, the only way to remove the condensation and resume data collection at cold temperature is to heat up the Bruker, and then cool it down again, and then pull vacuum on it, which, depending on the required temperature change, may take a full day or two. In this figure, the only available vapor pressure data for *trans*-2-butene are shown: the red points are data points from the CRC Handbook of Chemistry and Physics [129; 110], and the green curve comes from the Antoine coefficients reported by the National Institute of Standards and Technology [115]. 85

3.16	Sample of pure and N ₂ -mixture spectra of <i>trans</i> -2-C ₄ H ₈ obtained at 210 K. The pure spectrum (blue curve) was obtained with sample pressure P _s = 1.40 Torr at resolution R = 0.0039 cm ⁻¹ , whereas the N ₂ -broadened spectrum (green curve) was obtained with sample pressure P _s = 1.81 Torr, total pressure P _{tot} = 759.8 Torr, at resolution R = 0.062 cm ⁻¹ . Several representative band centers for <i>trans</i> -2-C ₄ H ₈ are identified, using the notation of McKean et al. (1985) [124] (i.e. s=strong, vw=very weak, etc. and A, B, C refer to band contour type). Note that the features around 667 cm ⁻¹ are contamination from CO ₂ . The partial pressure contributions from CO ₂ to the spectra are shown (in the same color scheme), estimated by simulating CO ₂ 's ν ₂ band. See text for further details.	87
3.17	Sample of cross-sections for N ₂ -broadened <i>trans</i> -2-C ₄ H ₈ derived at multiple different temperatures and pressures, with cooler colors denoting colder temperatures; these temperatures and the other relevant experimental conditions are listed in the legends. Panel (a) roughly corresponds to Region I, and panel (b) roughly corresponds to Region II.	89

3.18	<p>Linearity test for <i>trans</i>-2-C₄H₈ for (a) entire spectral region studied and (b) in 960-970 cm⁻¹ region, which contains the strongest <i>trans</i>-2-butene features observed. Even for an interval marked by the strongest features, a linear relationship is seen between the integrated absorbance, $A \equiv \int_{\nu} -\log(\tau)d\nu$, and the optical burden (i.e. <i>trans</i>-2-butene number density times path length), even in the 960-970 cm⁻¹ region. The slope, representing the intensity, has dimensions of length·energy⁻¹. See Varanasi et al. (1977) [130], Varanasi et al. (1987) [131], and Sharpe et al. (2004) [115] for additional examples of this methodology.</p>	92
3.19	<p>Integrated cross-section results for each of the three spectral regions, arranged by decreasing temperature. The red horizontal dashed line and accompanying pink envelope in each panel is the mean and standard deviation, respectively, for the seven linear regime spectra ('8a','8b',..., '8g') described in Section 3.5.4. Error bars on the individual data points are a combined estimate of the various sources of uncertainty discussed in Section 3.5.5. It can be seen that uncertainties grow larger at colder temperatures, presumably due to outgassing and degassing inside the cell and inlet tubes, which becomes more relevant at the lower pressures required to be used at these lower temperatures. The data point at $T = 160K$ is mainly for qualitative comparison and locating of band centers, as stated in the text.</p>	97

3.20	1,2-dimethylcyclopropane (C_5H_{10}), a possible constituent of Titan's atmosphere which would likely be present in both its enantiomeric forms.	100
3.21	Production of either enantiomer of 1,2-dimethylcyclopropane is possible when singlet carbene reacts with <i>trans</i> -2-butene.	101
3.22	Triplet carbene reacting with <i>trans</i> -2-butene can produce both the enantiomers of the <i>trans</i> -1,2-dimethylcyclopropane molecule, but also, via a separate mechanism (bond rotation followed by ring closure) can also produce the non-chiral <i>cis</i> -1,2-dimethylcyclopropane.	101
3.23	Singlet carbene, when reacted with <i>cis</i> -2-butene, produces <i>only cis</i> -1,2-dimethylcyclopropane.	102
3.24	Triplet carbene reacts with <i>cis</i> -2-butene. This can produce either the achiral <i>cis</i> -1,2-dimethylcyclopropane molecule, or one of the two enantiomers of the chiral <i>trans</i> -1,2-dimethylcyclopropane molecule.	103
4.1	Example of spectral data gathered in the methane (CH_4) ν_4 region, from Saturn's atmosphere. It is seen that, as expected, the spectrum is a quickly and sharply varying function of wavenumber ν due to the presence of multiple strong methane lines in this region. This figure has been adapted from Irwin et al. (2008)[79].	109
4.2	The smoothly-varying, rearranged absorption of methane from Figure 4.1, which can be integrated much more efficiently than the actual spectrum.	111

4.3	3D rendering of the Cassini spacecraft. The Composite Infrared Spectrometer instrument is highlighted in blue near the bottom. Image is credited to the Cassini CIRS team; more info can be found at http://cirs.gsfc.nasa.gov/	113
4.4	Placement of the three focal planes of CIRS and their respective fields of view. FP1 (10-600 cm^{-1}) was a single circular pixel, optimized for nadir viewing geometries, where as FP3 and FP4 (600-1100 and 1100-1490 cm^{-1} , respectively) were linear arrays of ten square pixels which could be rotated with respect to the target, allowing latitudinal maps across the disk of a targeted body to be constructed, in addition to limb-viewing geometries, with the linear arrays angled perpendicular to the disk-tangent, permitting altitude-dependent investigations of spectral properties. This figure has been adapted from Figure 1 of Flasar et al. (2004) [21].	115
4.5	Adapted from Figure 7 of Nixon et al. (2019) [128], the disk of Titan is shown along with the footprint of CIRS in the “FIRLMBINT” (i.e. Far-Infrared Limb-Integration) mode, one of multiple viewing modes employed to gather a wide variety of observations of Titan, as well as Cassini’s other Kronian targets. The linear arrays of FP3 and FP4 can be seen on the left at the top of the disk, whereas the circular pixel of FP1 is on the right.	116

4.6	Display of the retrieved temperature profiles for all three data sets (solid curves), in addition to the <i>a priori</i> profiles (dashed curves) used for each of the three cases [140; 145]. For each of the colored curves, the 1σ uncertainty in the retrieved profile is identified by the corresponding, similarly-colored shading.	123
4.7	One example of the model’s fit to the Cassini CIRS observations. Top panel: the model excluding any <i>n</i> -butane (red curve) and also including approximately 76 ppb <i>n</i> -butane (purple curve), with 1σ noise envelope shown in gray. Bottom panel: residuals (i.e. the data minus the model), which follow the same color scheme, and an additional green curve showing <i>n</i> -butane’s laboratory transmission spectrum at $T = 200K$ [112], which has been convolved to the 0.5 cm^{-1} CIRS resolution. Note the strong Q-branch of <i>n</i> -butane’s ν_{14} band around 1466 cm^{-1} as we saw in Section 3.4.3, and the fact that even this particularly <i>strong</i> vibrational feature has become substantially broadened at CIRS resolution in the green curve for the laboratory <i>n</i> -butane spectrum.	124

4.8	Normalized temperature contribution contour plot for the EQ data in the 136-216 km altitude range, showing high sensitivity corresponding to that particular altitude range, as expected. The regions of strong sensitivity to temperature in terms of the wavenumber axis correspond to the individual transitions in methane’s ν_4 band, since it is the methane abundance that we hold constant as the temperature profile is varied during the NEMESIS calculation in order to fit the observations. Hence, this aspect explains why the ‘ghost’ of a methane spectrum can be seen in a figure like this. Spooky... . . .	126
4.9	The dependence of the <i>n</i> -butane upper limit calculations on three different altitude profiles is explored here. The black horizontal dashed lines approximate the range of altitudes in which my models and observations are most sensitive. See Figures 4.8 and 4.10 regarding this sensitivity. Note that ultimately, the placement of the red curve (constant profile) is rather arbitrary in a figure such as this, since my analysis will involve scaling it to achieve a set of differing abundances.	129
4.10	The <i>n</i> -butane contribution curves at 1465 cm^{-1} (very close to the Q-branch of the strong ν_{14} band of <i>n</i> -butane) for each of the nine cases that were explored (i.e. three different data sets, three different profiles). All of the <i>n</i> -butane results which follow will be reported at the altitudes corresponding to the peaks shown for these curves. Please note that the legends appearing in the central panels also apply to the other two panels in that row, which belong to the very same data set.	130

4.11	Sample $\Delta\chi^2$ curve, this one belonging to the EQ data, 136-216 km altitude range, and using the constant n -butane profile. The fit improvement is seen to be maximized for an n -butane abundance of roughly 80 ppb, although the significance of that improvement, statistically speaking, is fairly small at 1.25σ . All of the $\Delta\chi^2$ curves display 1, 2, and 3σ upper limits, as denoted in the legend. These are marked by colored dashed vertical lines at their corresponding abundances. Additionally, the minimum of the $\Delta\chi^2$ curve (if present) is marked by a blue dashed horizontal line, and quantified in the legend.	132
4.12	1, 2, and 3σ upper limits for the abundance of n -butane, marked by left-pointing arrows, for the EQ data set. The upper limit point colors correspond to the similarly colored profile curves. The blue, vertical dashed line marks the upper limit of 513 ppb which was derived by Hewett et al. (2020) [92], to be discussed further in Section 4.2.4.	137
4.13	1, 2, and 3σ upper limits for the abundance of n -butane, marked by left-pointing arrows, for the T3 data set. The upper limit point colors correspond to the similarly colored profile curves.	137
4.14	1, 2, and 3σ upper limits for the abundance of n -butane, marked by left-pointing arrows, for the T35 data set. The upper limit point colors correspond to the similarly colored profile curves.	138
4.15	$\Delta\chi^2$ curve for EQ data, using the constant n -butane profile.	139
4.16	$\Delta\chi^2$ curve for EQ data, using the Loison n -butane profile.	140
4.17	$\Delta\chi^2$ curve for EQ data, using the Krasnopolsky n -butane profile.	141

4.18	$\Delta\chi^2$ curve for T3 data, using the constant n -butane profile.	142
4.19	$\Delta\chi^2$ curve for T3 data, using the Loison n -butane profile.	143
4.20	$\Delta\chi^2$ curve for T3 data, using the Krasnopolsky n -butane profile.	144
4.21	$\Delta\chi^2$ curve for T35 data, using the constant n -butane profile.	145
4.22	$\Delta\chi^2$ curve for T35 data, using the Loison n -butane profile.	146
4.23	$\Delta\chi^2$ curve for T35 data, using the Krasnopolsky n -butane profile.	147
4.24	Estimated integration times for targeted C ₄ hydrocarbons based on profiles from Loison et al. 2019 [65] and scaled to explore a range of possible stratospheric abundances for each molecule. Required integration times for 3, 4, and 5 σ detections are shown for a variety of possible abundances. Photochemically predicted abundances for several models are marked by vertical dashed lines.	155
4.25	Schematic look at the TEXES instrument; the dotted-dashed line shows the path of light through the instrument when operating in high-resolution mode. Figure adapted from Figure 1 of Lacy et al. (2002) [39]	157
4.26	A small subset of the observatories at the summit of Mauna Kea, on Hawaii. From left to right: Subaru Telescope, Keck I and Keck II, and NASA IRTF. Maui, the next closest island to Hawaii, can just be seen on the horizon between Keck II and IRTF.	159
4.27	A charming and talented young space scientist enjoys the view from 14,000 feet before commencing his observing run at NASA IRTF.	160

4.28	Reduced data in the 956 cm ⁻¹ region (in green), with the HITRAN linelist for ethylene (C ₂ H ₄) overlaid in black, and scaled to be of similar brightness, for the purpose of comparison. It can be seen that the vast majority of large spectral lines in the data are coming from ethylene. This is true of the 965 cm ⁻¹ region as well.	161
4.29	Weighted averaging of zonal temperature measurements from CIRS [152]. The disk of Titan is shown, with white concentric circles representing areas of “constant weighting” in the averaging scheme we used to derive the temperature profile. Obviously, stronger weights are given to areas that are closer to the sub-Earth observer point, which is represented by a white dot at the center of all of the circles, as those areas will contribute more flux to the observations. Various latitude bands are shown in black. Credit to Nick Lombardo for helping to generate this figure.	163
4.30	Model fit of the full 965 cm ⁻¹ region. A χ^2 value of 1.016 is achieved in this case.	165
4.31	A closer look at a spectral line-dense region of the 965 cm ⁻¹ model fit. A good example of the model lineshape still needing some improvement is observed around 965.20-965.25 cm ⁻¹ . Improving features such as this in the model’s fit of these observations before actually <i>publishing</i> these results in a fourth “Titan’s C ₄ hydrocarbons”-paper is an obvious next step, though it is extremely unlikely that such minor changes will significantly impact the resulting upper limits determined for <i>n</i> -butane and <i>trans</i> -2-butene and reported here. .	166

4.32	Model fit of the full 956 cm^{-1} region. A χ^2 value of 1.016 is achieved in this case as well.	167
4.33	A closer look at a spectral line-rich region of the 956 cm^{-1} model fit.	167
4.34	Upper limits retrieved for <i>n</i> -butane for the 2021 IRTF/TEXES observations centered on 956 cm^{-1}	168
4.35	Upper limits retrieved for <i>n</i> -butane for the 2021 IRTF/TEXES observations centered on 965 cm^{-1}	169
5.1	Schematic depiction of idealized communication channels between the three main components of characterization of planetary atmospheres.	184

List of Acronyms, Symbols, Nomenclature or Abbreviations

0.1 Acronyms

- NASA: National Aeronautics and Space Association
- JPL: Jet Propulsion Laboratory
- PNNL: Pacific Northwest National Laboratory, a U.S. Department of Energy laboratory that specializes in chemistry, data analytics, and Earth science.
- CIRS: Composite Infrared Spectrometer, an instrument which flew on the NASA Cassini mission
- NEMESIS: Non-linear Optimal Estimator for Multivariate Spectral analysis, a radiative transfer and planetary atmosphere retrieval tool
- IRTF: Infrared Telescope Facility, a NASA observatory on Mauna Kea, Hawaii
- TEXES: Texas Echelon Cross Echelle Spectrograph, a high resolution spectrograph which has been implemented at NASA's Infrared Telescope Facility as well as other observatories

0.2 Symbols

- cm^{-1} : inverse centimeters, or ‘wavenumbers’ - the most common unit used in infrared spectroscopy to describe spectral ranges. These can be thought of as a *spatial* frequency, i.e. the number of wavelengths per unit space, rather than a temporal frequency, which measures the number of wavelengths crossing a point in space per unit *time*. In infrared spectroscopy, we discuss the energy of light in terms of the number of wavelengths that fit into a single centimeter, since, at infrared energies, this gives us a reasonable number range (hundreds, thousands, etc., rather than extremely large or extremely small numbers) with which to discuss the locations of spectral features.

0.3 Nomenclature

Most of the nomenclature in this dissertation that may not be familiar to the reader generally involves laboratory spectroscopy and the characterization of rovibrational spectral features. Several of the more important jargon terms are defined here. You are free to read through this section now or to skip over it and come back on a term by term basis as these terms arise. Note that when reading this dissertation electronically, you can jump to this section easily by searching for the word ‘Nomenclature’. You can then jump back to the section you were reading before with Command/Alt + Left Arrow (in Adobe Acrobat Reader), or Command+left bracket (in Mac Preview).

An important convention regarding the terminology of rovibrational transitions is explained in Figure 1. Molecular vibrational bands, corresponding to a specific

way that a molecule (or a portion of it) can rotate or vibrate, frequently have the *rovibrational* structure seen in this Figure. Individual *rovibrational* transitions (which correspond to the same vibrational transition, but different *rotational* transitions) are observed to be organized into three “branches”, which we call the **P branch**, the **Q branch**, and the **R branch**. These correspond to different changes in the rotational quantum number J . The P branch correspond to transitions with $\Delta J = 1$, the R branch correspond to transitions with $\Delta J = -1$, and the Q branch is built of transitions with $\Delta J = 0$.

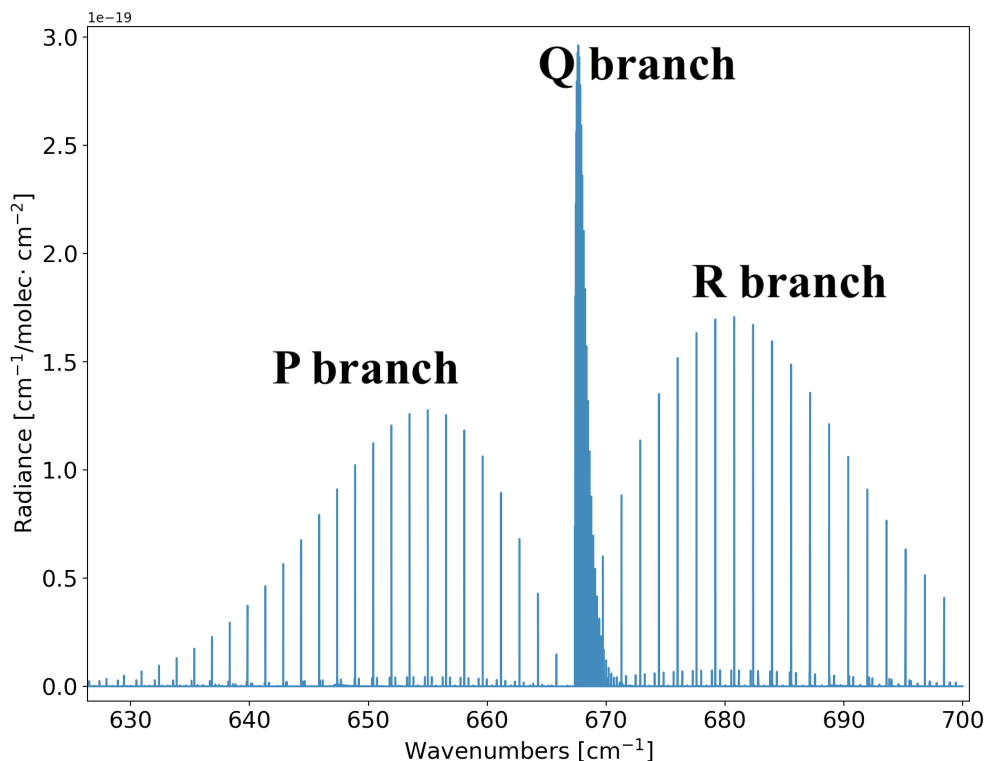


Figure 1: The ν_4 band of CO_2 , demonstrating the typical structure of a molecular rovibrational band. The individual transitions (lines) that form the band are organized into three regions which we label the P, Q, and R branches. These correspond to specific changes in rotational quantum number J .

These concepts are introduced here mmainly because they will occasionally be

used to point to various spectral features in the laboratory results for *n*-butane and *trans*-2-butene, and locate those features in terms of Q, P, and R branches. Also important is the fact that observations of each branch of a vibrational band, which spans a slightly different energy range than the other two, will be sensitive to a different altitude range of a given planetary atmosphere.

Two additional important jargon terms in rovibrational spectroscopy are **hot bands** and **combination bands**:

- Hot bands are composed of transitions between two excited states of the molecule. Thus, the ground state is not involved in these transitions. As an example, a transition from the first excited energy state to the second excited state would contribute to a hot band. These are named hot bands because their intensities will be strongly temperature-dependent, as the higher the temperature of the sample, the more of the molecular population will be in an excited state to begin with, and thus, more molecules are *ready* to engage in hot band transitions.
- Combination bands are composed of transitions for which two or more modes are excited by a single photon. If we consider rovibrational mode A with energy E_A , and an additional rovibrational mode B with energy E_B , a photon with energy $E_A + E_B$ may excite both modes simultaneously. This is particularly important for molecules that have low-lying (i.e. low energy) torsional modes, such as the two molecules that were studied in this dissertation, as these modes yield a large number of transitions contributing to a combination band. For example, for a torsional mode with a small energy E_T , and

considering a vibrational mode with much larger energy E_ν , excitations can occur via photons with energy of $E_\nu + E_T$, and $E_\nu + 2E_T$, ..., etc.

Additional information on these (and other rovibrational spectroscopy jargon) can be found on the [Chemistry Living Library website](#), part of the Libre Texts project [1].

Another term that should be clarified here is **broadening gas**, which will be used frequently in the discussion of laboratory work. In the lab, we speak of gas mixture that is mostly N₂, for example, with a small percentage being the gas of interest (perhaps a hydrocarbon that is being studied) as being *broadened* by N₂. This is done to achieve higher total pressures, as well as to better simulate the planetary atmosphere of focus; for instance, as we will see, Titan's atmosphere is 98% N₂ by volume, and thus, N₂ was an excellent choice of broadening gas for our study of Titan's potential trace hydrocarbons.

The term **conformer** should also be introduced here. Many of the larger molecules exhibit several conformers, meaning that there are multiple *stable* configurations in which the various components (atoms, or sub-molecular components, like methyl groups) can be rotated with respect to one another. A typical example, and the one that will be relevant to the study of *n*-butane, concerns normal (zigzag) hydrocarbon structures, and the two methyl groups by which the chain is book-ended. These methyl groups can be aligned with one another, or rotated with respect to each other by some angle. At certain angles, stable configurations exist, meaning that for a molecule in those states, it would require *additional* energy to cause the methyl groups to change their alignment and change the conformation of the

molecule.

This is demonstrated in Figure 2, which depicts the various conformational states of the *n*-butane molecule and their relative energies. It is observed that two stable conformations, or conformers, are possible: the *trans* or *anti* conformer, with the methyl groups rotated by 180° with respect to one another, and the *gauche* conformer, in which they are rotated only 60° from each other.

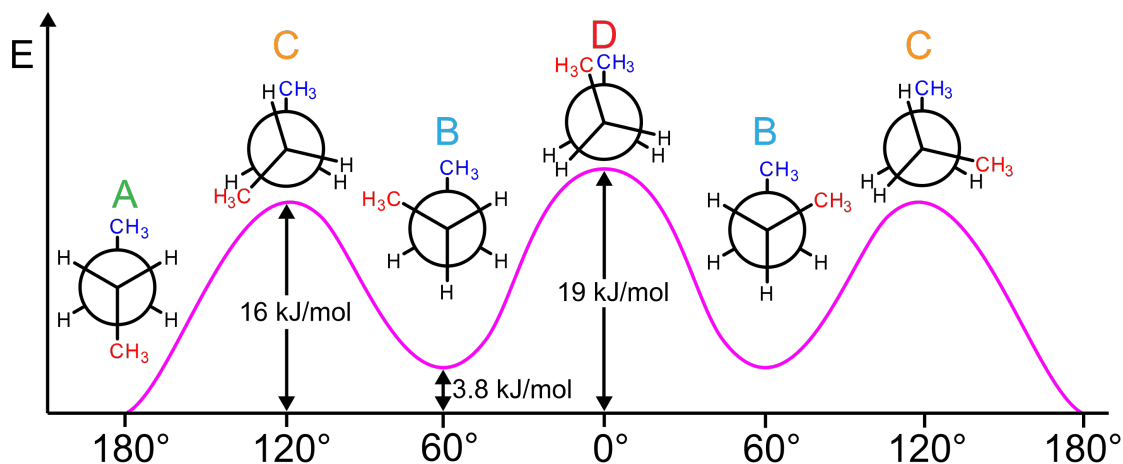


Figure 2: Energy diagram for the conformational states of the *n*-butane molecule. Two stable conformers are observed, separated by 3.8 kJ per mole. Note that the two rotational states at 60° on either side of 0° are effectively identical and both called *gauche*. Image adopted from 'Basic Terminology of Stereochemistry' by Moss. (1996).

0.4 Abbreviations

- ppb: parts per billion, a typical volume mixing ratio unit used when discussing atmospheric trace gases.

Acknowledgements

Firstly, I would like to acknowledge the immense help and guidance received from my mentor, Dr. Conor Nixon. This work would not have been possible without his input and his support. I really cannot put to words how valuable and enjoyable my relationship with Conor has been. I fondly recall a key moment that happened a year and a half ago: recovering from physical illness, and struggling with mental illness, I was utterly overwhelmed with my workload. I remember asking Conor if I could take a few days off of our main research project, to recover my health, and to catch up on other looming tasks. Instead of permitting me to take a few days, Conor urged me to simply take “as much time as I needed”. So I did. I took about two weeks, in fact. And then I came back, fully refreshed, and wrote an observing proposal for NASA IRTF, which was promptly accepted, marking a hugely important milestone in my graduate career. Thank you so much for sticking with me, Conor, until the very end, and possibly beyond!

I also wish to acknowledge help received from my academic advisor, Dr. Manasvi Lingam, who has been instrumental in helping me navigate the turbulent waters of doctoral study. Manasvi has been nothing but supportive from the first moment of our relationship, and I have been able to rely on his counsel countless times. Manasvi, I believe I am about to have a bit more freetime, and I am thrilled

at the prospect of finally being able to sit down and read your book!

I also wish to acknowledge Dr. Rassoul, whose excellent, inspirational teaching in my Planetary Atmosphere's class at Florida Tech might very well be credited with inspiring the beginning of my interest in atmospheric science. I fondly recall a moment where Dr. Rassoul lectured on Titan, its atmosphere, and how difficult it is to model. I thought to myself, "Boy, I'm happy I won't ever get stuck in *that* field!" Less than three years later, here I am, buried in Titan's hydrocarbons, and the happiest I have ever been.

My thanks also go out to Keeyoon Sung at JPL, who offered me my first NASA internship, a truly wonderful experience, and who put me on the path toward the butane search at Titan. That first internship with Keeyoon was such an immensely wonderful experience; it is no surprise at all that it ended up defining the remainder of my research at Florida Tech. My thanks also, to Keeyoon, for having me back for a *second* internship in the fall of 2021 to solidify my dissertation research with some additional laboratory work. I look forward to future collaboration with you and your colleagues, Keeyoon.

Special thanks go out to Daniel Batchelder, who helped provide my first research project at Florida Tech, and stuck with me until the very end, even volunteering to remain on my committee after leaving Florida Tech to work directly on space exploration with NASA at Kennedy Space Center.

Nick Lombardo played an instrumental role in my analysis of the TEXES data, and even in getting started with the CIRS data too. My thanks go out to him for his patience and time spent in getting me started with that difficult analysis. I also would like to acknowledge the help from the TEXES team, namely Tommy Greathouse and Jon Lacy, who spent a lot of their valuable time making sure that

my analysis was going smoothly, in addition to making major contributions to the 2021 IRTF proposal.

Additionally, my thanks go out to each of my remaining committee members, each of whom has played a key role in my success at Florida Tech in electing to be part of the final step of my journey here.

My parents have been absolutely instrumental to my success as a student, a scientist, and a human being in general. I could not have made it this far without their unwavering support and encouragement. Thank you for never giving up on me through this long journey. Thank you for providing a wonderful, beautiful home in which to summer and recover from each of the long years of study. Thank you for coming out to visit and spend time with me, and being so excited about my studies.

Important help and support came at a really crucial time, from two wonderful friends of mine, Matt and Shannon Boyd, who saw an opportunity to make a huge difference in my life. I am eternally grateful for their help and the initiative they took in lending me a hand. My promise is to pay it forward in as many ways as I can find to do so.

In a lot of ways, no one has been more central to my success as a PhD student, particularly throughout the years represented by this dissertation, as my colleague and best friend, Mehdi Rahmani. Thank you for all of your help, your support, your energy, your humor, your criticism, and your talent for convincing me to take better care of myself along the way. I couldn't have done this without you, and it's been an honor writing dissertations side-by-side with you.

Lastly, but not least...ly, my thanks go out to all of my other friends at Florida Tech; you know who you are. Thank you for spending time with me, keeping me

focused on my work but also encouraging me to have fun along the way. It has been a great couple of years with you weirdos. I hope you'll be willing to do one more Shell Time, with Dr. Steffens, before I head on to the next adventure.....

Dedication

I dedicate this work to my family: my parents, Keith and Cheryl Steffens, for their unwavering support of my interest in science, as well as my brother Eric, his wife Michi, and their two wonderful children (my nephew and niece) Niklas and Nora. If the only outcome of this Ph.D. is that my nephew and niece are just slightly inspired and interested in science and space because that's what cool Uncle B does, I will call it a good Ph.D...

More seriously, thank you, each of you, for being there for me throughout this long adventure. I couldn't have done it without you.

With gratitude and much love,

Brendan

Preface

How does one detect a new molecule in the atmosphere of a world over a billion kilometers away from the Earth? And why do such detections matter to us as planetary scientists and astrobiologists? This sort of work turns out to be a long, complicated process which draws on experience in a variety of fields, from hands-on experimentalism in the laboratory to atmospheric simulation on a computer, with the results of such studies contributing to our understanding of the habitability and the astrobiological potential of other planetary bodies, and simultaneously contributing to our understanding of our home here on Earth.

The planetary body of focus here is Titan, Saturn's largest moon. At this point in time, dozens of molecular species have been detected in Titan's rich atmosphere. Typically, detections have been made by first studying a species spectroscopically in the lab, followed by actual measurement in astronomical observations, via remote sensing techniques from spacecraft and/or ground-based observatories, or via the in situ measurements gathered by the Huygens lander. With each new laboratory study, we unlock a new piece of the wonderful puzzle that is Titan's atmosphere. With each detection of a new species, we see just how that puzzle piece fits into the bigger picture.

For many of us, certainly for the public as a whole, the most exciting part

of Titan's 'bigger picture', so to speak is its potential for life. Both scientists and non-scientists alike wrestle with the tantalizing question of '*Are we alone in the universe?*' As a scientist heavily invested in doing my part to answer that age-old question, and moreover, as a communicator heavily invested in conveying the excitement of our tremendous progress toward answering this question to the public, it is difficult for me to describe Titan as anything short of an extremely exciting candidate for extraterrestrial life in our solar system. In this sense, I consider myself fortunate to have done the work described in this dissertation, toward understanding exactly which organic molecules might be present in Titan's atmosphere, and what potential significance they may hold for Titan's ability to host life.

What follows is my best attempt to communicate my efforts in this endeavor, which have taken place across recent years. Through the course of this work, Titan has quickly transitioned in my mind from a curious Solar System oddity to the absolute center of my most focused attention. My hope is that you, the reader, will experience some portion of that relationship and its excitement as you read further, and that you may derive much enjoyment along the way!

Chapter 1

Titan - Background

This dissertation is a description of a campaign to characterize, search for, quantify, and constrain the abundances of two relatively large, as of yet undetected C₄ hydrocarbons in Titan's atmosphere, the motivation for which has been briefly documented in the Preface. In order to understand that pursuit and its merit, let us first take a moment to appreciate some of the relevant background concerning this truly amazing world: ***Titan**, largest of Saturn's moons.*

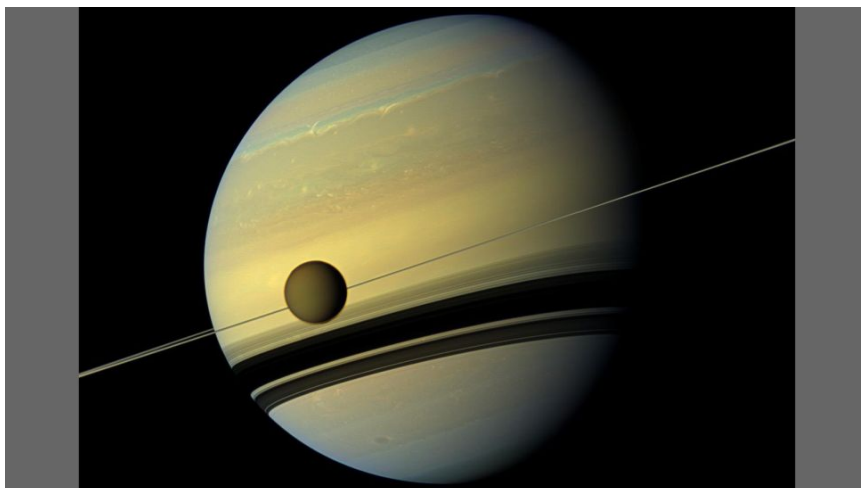


Figure 1.1: Saturn and Titan, as viewed by the Cassini spacecraft. Image credit: NASA/JPL-Caltech/Space Science Institute.



Figure 1.2: Artist's impression of Titan's largest hydrocarbon lake, Kraken Mare, with view of Saturn in the background. Image credit: NASA / John Glenn Research Center.

The second largest moon in the entire solar system, and even larger than *the* Moon itself (and the planet Mercury), Titan is a highly unique planetary body in

our solar system for a variety of reasons, many of these being far more interesting than its sheer size. Perhaps most notably, Titan possesses a massive nitrogen-based atmosphere and is the only planetary body other than Earth known to possess stable liquid features on the surface, these being a network of hydrocarbon lakes and seas, collectively spanning about as much surface area as America's Great Lakes [2]. Titan maintains a methane-based hydrological cycle analogous to the water-based hydrological cycle on Earth. Titan's lower atmosphere is replete with clouds and organic hazes [3]. The highly reducing atmosphere of present day Titan, a repository of prebiotic organic molecules, is understood to serve as a potential analog for the atmosphere of the prebiotic Earth, and therefore provides one of the best laboratories for investigations of the origin of life [4; 5; 6; 7].

Titan is also understood to be one of the many 'ocean worlds' of the outer solar system, possessing a subsurface liquid water ocean layer which is tens to hundreds of kilometers in depth [8]. Though that ocean is buried under approximately 100 km of various layers of ices, recent simulation results from Crósta et al. (2021) have shown that some of Titan's larger impact events in the past may have broken through this ice, causing mixing between organic molecules in the atmosphere, the surface organics, and the liquid water ocean [9]. This has tentatively provided a convenient solution to the once seemingly intractable problem of devising a method by which organic material could ever reach Titan's subsurface ocean in the first place, perhaps allowing life to take hold. Another possibility for mixing Titan's surface organics with liquid water, involving less energetic impact events, is possible as well; such impact events, though perhaps not violent enough to penetrate all the way to the subsurface ocean, could still form a non-permanent but long-lasting melt sheet of liquid water underneath the surface, likely mixing the surface's organic

molecules into that melt sheet. As the melt sheet slowly refreezes over time, the interactions between Titan's surface organic molecules and the liquid water may be preserved, perhaps recording information on the transition from organic molecules to prebiotic chemistry to the origin of life itself. Further details on this exciting possibility can be found in Hedgepeth et al. (2022) [10] and sources cited within. Along with others, these remarkable features of Titan serve as very strong motivation for very close study of this ocean world with its rich potential for astrobiology.

In this introductory chapter, we will familiarize ourselves with the history and progression of our understanding of this fascinating moon. We will also briefly examine each of the major distinguishing features of Titan, as described above. Emphasis will be placed on understanding Titan's atmosphere, as that aspect of Titan is of course most central to the research presented in this dissertation.

1.1 Discovery and Exploration

1.1.1 Initial Discovery and Detection of Atmosphere

Titan was discovered in 1655 by Christian Huygens, who, inspired by Galileo's observations of the four major moons of Jupiter, pointed a telescope of his own making at the Kronian system. At the time, his discovery of Titan recorded just the sixth known natural satellite of the solar system.

Three centuries later, in 1944, Gerard Kuiper (University of Chicago) observed Titan at infrared wavelengths longer than $0.6 \mu\text{m}$ [11]. He was able to identify two absorption bands caused by methane (CH_4) at 619 nm and 725 nm, by comparing his Titan observations to laboratory methane spectra obtained at low pressure.

When he searched Saturn's other moons for the same two methane features and was unable to find them, he concluded that Titan must be unique and must have an atmosphere which contained the methane. A few decades later in 1975, limb darkening was observed unambiguously at Titan, solidifying the evidence for Titan's optically thick atmosphere, though the exact composition of that atmosphere remained unconstrained [12]. Later that year, detections of ethane (C_2H_6 , at $12.2 \mu\text{m}$), monodeuterated methane (CH_3D , at $9.39 \mu\text{m}$), ethylene (C_2H_4 , at $10.5 \mu\text{m}$) and acetylene (C_2H_2 , at $13.7 \mu\text{m}$) were achieved [13], beginning to reveal the complexities of Titan's atmospheric chemistry.

1.1.2 The Voyager Missions

Since that era, astronomers have continued to observe Titan extensively using a multitude of observatories and spacecraft. The first major spacecraft missions that were able to provide useful observations of Titan were the Voyager missions, launched in 1977. Most of the useful Titan data from this pair of missions came from Voyager 1, which was able to execute a flyby of Titan with a closest approach of just 4,394 km in 1980. From the resulting observations, the first model of Titan's atmospheric composition that resembles modern-day understanding emerged: 95% N_2 and 3-4% CH_4 by volume. Once again, many trace hydrocarbons were detected, as well as several nitriles. Additionally, the vertical profiles of many of these trace hydrocarbons were finally constrained using Voyager 1's observations [14]. This was all possible due to Voyager's IRIS (Infrared Interferometer Spectrometer) instrument, which observed at the relatively low resolution of 4.3 cm^{-1} across the wide spectral range of $180 - 2500 \text{ cm}^{-1}$ ($4\text{-}56 \mu\text{m}$). In addition to constraining Titan's atmospheric composition, the Voyager 1 IRIS observations were able to

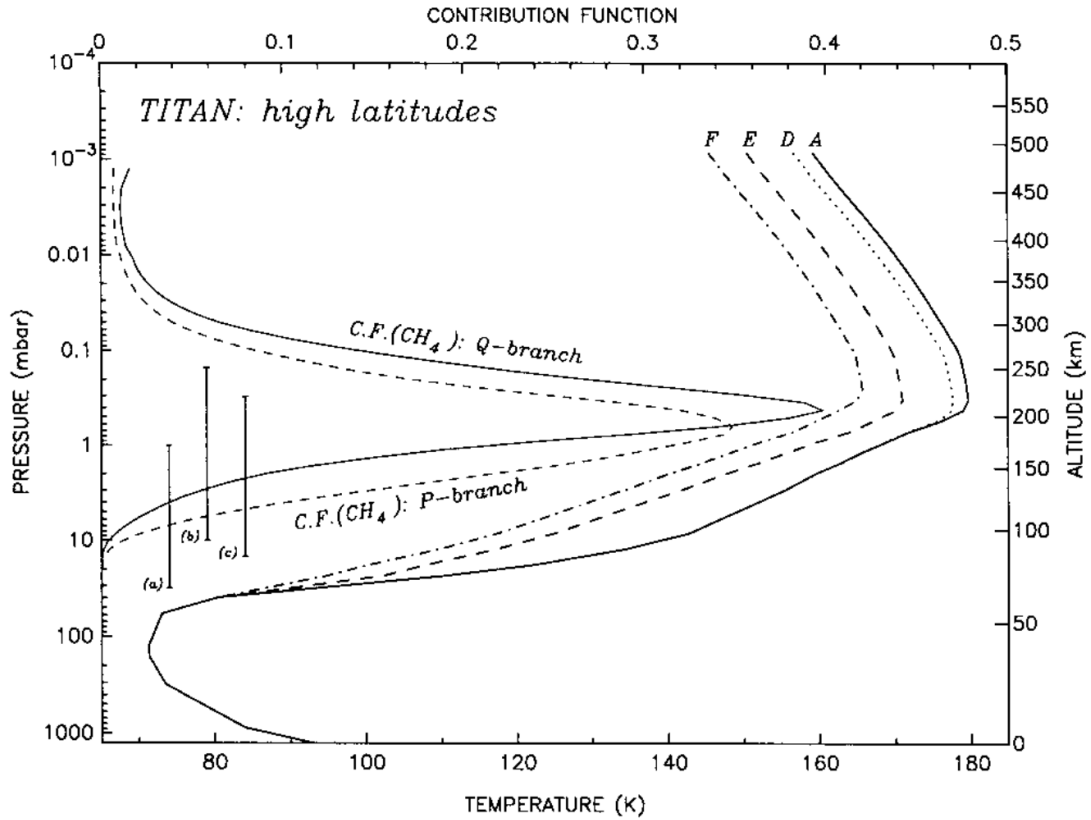


Figure 1.3: Temperature profiles retrieved for equatorial and northern latitudes using Voyager 1 observations. Curves A, D, E, and F correspond to latitudes of 0° , 30° , 50° , and 70° , respectively. The temperature retrieval model's contribution functions are also shown (using the top horizontal axis) for the Q-branch and P-branches of methane's ν_4 band, demonstrating the different altitude sensitivities for different portions of this molecular vibrational band which has been so crucial for Titan science. The P-branch, which is slightly lower in energy than the Q-branch (i.e. slightly longer in wavelength or lower in wavenumber) is seen to penetrate deeper into the atmosphere, yielding maximum sensitivity at a slightly lower altitude than that of the Q-branch. Figure adapted from Figure 5 of Coustenis and Bezar, *Icarus*, 1995 [15].

significantly constrain the surface temperature (94 ± 1.5 K) and surface pressure (1.5 bar), as well as obtain a much more precise measurement of Titan's radius (2575 ± 2 km). Temperature profiles were modeled from the Voyager 1 data as well, as seen in Figure 1.3.

While the Voyager missions provided incredibly useful and insightful observations of Titan, answering many of the important questions held by planetary scientists at the time, these observations also raised many more questions. Some of these were soon to be addressed by ground-based observations and Earth-orbiting observatories, like the Infrared Space Telescope (ISO) and the Hubble Space Telescope (HST).

1.1.3 Infrared Space Observatory (ISO)

Titan was observed in 1997 by the Infrared Space Observatory, a 60 cm Earth-orbiting telescope chilled by a 2300 liter supply of superfluid helium [16]. Historically, these observations were extremely important in the developing understanding of the composition of Titan's atmosphere, primarily due to the ISO's Short Wave Spectrometer (SWS), which offered an order of magnitude higher spectral resolution (0.4 cm^{-1}) than Voyager 1's IRIS (4.3 cm^{-1}). The higher spectral resolution observations afforded by ISO/SWS allowed Coustenis et al. (2003) [17] to detect and separate the contributions of most of Titan's major and trace gases. For the first time, the cyclic hydrocarbon benzene (C_6H_6) was detected. Additionally, the altitude profile of acetylene (C_2H_2) was constrained. Lastly, the D/H ratio was measured by ISO to be $8.7_{-1.9}^{+3.2} \times 10^{-5}$ [17]. Though it is difficult to interpret this measurement of Titan's D/H enhancement (relative to the solar value), it has been argued, for example, that assuming a geometrically thin protonebular disk at the Saturn system, this D/H enrichment could not have occurred within the subnebula itself, and is therefore an indication of evolution since Titan's formation [18].

1.1.4 Hubble Space Telescope (HST)

Apart from the Infrared Space Observatory, the other Earth-orbiting platform that has been critical to Titan science is the Hubble Space Telescope. The relatively large (2.4 m) aperture of Hubble allowed for impressive spatial resolution (about 0.1") which was not attainable with ISO and not (until very recently) attainable from ground-based observatories. Several of Hubble's instruments are sensitive in the near-infrared. This has been useful as methane gas is optically thin in several windows in the near-infrared, allowing near-infrared observations to penetrate deep into the lower atmosphere of Titan and even all the way to the surface in some cases.

For instance, Hubble's NICMOS (Near Infrared Camera and Multi-Object Spectrometer) observed Titan in 1999 in the near-infrared windows near 1.1, 1.6, and 2.0 μm , and enabled Titan's surface to be studied. For the first time, distinct topographical features on the surface on the dark trailing side of Titan were unambiguously observed, which ruled out the possibility of a single large ethane ocean on the side of Titan which faces away from Saturn. Albedo maps of the surface were constructed in detail for the first time in this work, though interpretation of these maps was speculative in many cases. Though many extremely brightly reflecting areas were seen on Titan's surface, similarities in brightness of these features between 0.94-1.1 μm and around 2.04 μm suggest that water ice is not the source of this reflectivity, as water ice is much darker at 2.04 μm than in the 0.94-1.1 μm window [19]. Instead, a mixture of some water ice with dark carbonaceous material was invoked to explain the observations. The exact composition of that organic carbonaceous material was left unconstrained, however.

1.1.5 Cassini

A true paradigm shift in understanding of Titan's complexities came with the Cassini-Huygens Mission [20]. Cassini was a flagship class mission to orbit Saturn, observe the giant planet and its ring systems, and perform dozens of flybys of its many moons. Cassini launched in 1997 and entered Saturn orbit in 2004. It was originally intended to observe the Saturnian system for just four years, but ultimately, the mission was extended on two separate instances. Cassini ultimately lasted until 2017. It finished its enormously successful mission when it was directed into a suborbital trajectory through Saturn's atmosphere to be destroyed and prevent it from possibly contaminating one of Saturn's astrobiologically significant moons, such as Titan or Enceladus.

Powered by nuclear RTGs (radioisotope thermoelectric generators), the two metric ton Cassini spacecraft carried a dozen different instruments that allowed Cassini to observe in the radio, infrared, the visual, and the UV, and also permitted investigation of the local plasma and magnetic field environments. A mass spectrometer was also carried for *in situ* sampling of particles near Saturn and in Titan's atmosphere. Most critical to the work described in this dissertation is the Cassini Composite Infrared Spectrometer (CIRS) instrument, which observed the Saturnian system in the 10-1400 cm^{-1} (7.1-1000 μm) range [21]. The CIRS instrument and its observations will be described much more thoroughly in Section 4.2.1.

Importantly, Cassini also carried a landing probe called *Huygens*, which was designed to descend to Titan's surface, taking critically important measurements of the atmosphere during its descent.

1.1.6 Huygens Probe Landing

On December 17th of 2004, the Cassini spacecraft, about to engage in a flyby of Titan, performed a small orbital correction that fixed it onto an actual collision course with Titan. A few days later, the spacecraft released the Huygens probe. Huygens had no thrusting/maneuvering capabilities of its own, so at this point, it was confined to the suborbital trajectory which would intersect with Titan, forcing it to land there. The remaining Cassini spacecraft then executed another burn to raise its periapsis, causing it to flyby Titan, rather than collide with the atmosphere [22].

Huygens had targeted a southern-latitude, day-side landing site on Titan. Protected by a heat shield during its long descent through the atmosphere, it eventually deployed a series of parachutes, causing it to decelerate to about 5 m/s as it landed on the surface. Officially, the mission was planned to end with Huygens's impact on the surface, as it was uncertain what the surface conditions there would be, and whether or not the probe and its science instruments would survive the impact in a capacity able to make further measurements and communicate them to Cassini [23].

Ultimately, Huygens *did* survive the impact, and its battery supply lasted much longer than originally anticipated, allowing it to collect surface data and communicate with the Cassini spacecraft for a little over one hour; those data were then relayed back to Earth for analysis. Interestingly enough, the Huygens signal was also picked up by ground-based observatories on Earth, which received Huygens's signal for a total of 5 hours and 42 minutes (including the atmospheric descent, and the 3 hours 14 minutes spent operating on the surface, during some of which it was not in range for communicating with the Cassini spacecraft) [23].

During its descent, Huygens measured wind speeds in Titan’s atmosphere, finding wind speeds that are weak near the surface and increasing in strength with increasing altitude; a maximum wind speed of 120 m/s was recorded at about 120 km above the surface. Huygens also measured its deceleration through the atmosphere using an accelerometer. As this deceleration is proportional to the density of the atmosphere encountered, this allowed an atmospheric density profile to be obtained. From this, temperature, pressure, and conductivity profiles were able to be derived. An acoustic sounder was also able to measure the speed of sound as Huygens descended; this quantity depends on both the temperature and the mean molecular mass of the local atmosphere [23].

Huygens also carried a gas chromatograph mass spectrometer (GCMS) instrument, which measured the abundances of hydrocarbons and nitriles in the atmosphere from an altitude of 146 km downward toward the surface. One result of these measurements was an accurate altitude profile for both N_2 and CH_4 , the two main constituents of Titan’s atmosphere. The GCMS was also able to detect several noble gases at the level of tens to hundreds of parts per billion. Additionally, it measured the abundance of prominent isotopic species for carbon, nitrogen, hydrogen, oxygen, and argon, allowing for important ratios (e.g. D/H ratio) to be measured more precisely than before. As Huygens impacted the surface, measurements of its impact deceleration and penetration depth allowed mechanical properties of the surface’s material to be investigated [23].

1.1.7 Ground-based observations

More and more so in recent years, ground-based observations have found an important role in Titan science. Notable observatories for studying Titan from the



Figure 1.4: The surface of Titan, as seen by the Huygens lander probe. The rocky looking globules, which are 10-15 cm in size, are actually likely to be mostly water ice. Image was taken with the Descent Imager/Spectral Radiometer instrument [24].



Figure 1.5: SOFIA observatory and infrared telescope. May she rest forever in peace.

surface of Earth include, but are certainly not limited to:

- NASA Infrared Telescope Facility (IRTF), a 3 m telescope on the Mauna Kea summit, Hawaii.
- Atacama Large Millimeter/Submillimeter Array (ALMA), Chile.
- The W.M. Keck observatory, twin 10 m telescopes on the Mauna Kea summit, Hawaii, which are able to utilize adaptive optics.
- Stratospheric Observatory for Infrared Astronomy (SOFIA), technically not *ground*-based, but close enough! A stratospheric jet which carries a 2.5 m infrared telescope, shown in Figure 1.5.

While some work studying Titan's surface has been conducted with ground-based observations (e.g. Gibbard et al. (1997) [25] and [26]), most of these ob-

servations are focused on atmospheric characterization. In recent years, three new molecules were detected with ground-based observations: in 2019, Lombardo et al. (2019) [27] detected propadiene (C_3H_4) using observations from NASA IRTF, using the TEXES instrument (which will be discussed thoroughly later in this dissertation). More recently, Nixon et al. (2020) [28] detected cyclopropenylidene ($c-C_3H_2$) using observations from ALMA, and also using ALMA, Thelen et al. (2020) [29] detected methylcyanoacetylene (CH_3C_3N).

1.1.8 Upcoming Dragonfly mission

The next major mission to the Kronian system will in fact be a Titan-focused lander called Dragonfly [30]. Indeed, ‘hopper’ may be a better term than lander, as Dragonfly will be an 8-propeller rotorcraft capable of short flights through the thick near-surface Titanian atmosphere, allowing it to make measurements in a variety of locations. Set to launch in 2027, Dragonfly will not land on Titan until around 2035. Its science goals are focused on studying the prebiotic chemical processes that are common to both Titan and Earth. In this way, Dragonfly intends to make major progress toward improving our understanding of the parallels between the Hadean Earth and this frozen ocean world.

1.2 Titan’s Orbital Parameters

Titan orbits Saturn at a distance of approximately 20 Saturn radii. The eccentricity of this orbit is fairly large, at $\epsilon = 0.0288$. Titan is tidally locked to Saturn, so its rotational period is equivalent to its orbital period about Saturn (15.945 days), causing the same face of its surface and atmosphere to be pointed toward Saturn



Figure 1.6: The Dragonfly rotorcraft, shown in stages, parachuting down through the Titan atmosphere before activating its propellers for a soft landing. Dragonfly will then fly to dozens of different nearby sites to study Titan’s surface and lower atmosphere.

at all times. Its mass is about 0.0225 times that of Earth ($0.0225 M_{\oplus}$), and, as mentioned earlier, its radius has been measured to be about 2574 km, or about 1.5 times the radius of Earth’s moon. This yields a mean density of 1.8798 g/cm^3 . The resulting surface gravity of Titan is low, at 0.138 g, as is the escape velocity, at 0.236 times that of Earth (2.639 km/s).

Titan’s apparent magnitude varies from 8.2 to 9.0, depending on its location in its orbit as well as Saturn’s location in *its* orbit, since Saturn’s orbit is also eccentric ($\epsilon = 0.0565$). As stated earlier, Titan has a substantial atmosphere, one that is in fact 1.2 times *more* massive than that of Earth. The resulting surface pressure is about 1.45 times that of Earth’s, and the temperature at the surface is around 93.7 K. All of these data are tabulated in Table 1.2.

Table 1.1: Characteristics of Titan and its orbit about Saturn [31; 32; 33; 34].

Periapsis	1,186,680 km
Apoapsis	1,257,060 km
Eccentricity	0.0288
Orbital Period	15.945 days
Inclination	0.34854 degrees, with respect to Saturn equator
Radius	2,574.73 km (1.48 lunar radii)
Mass	1.3452×10^{23} kg (0.0225 M_{Earth})
Density	1.8798 g/cm ³
Surface Gravity	0.138 g
Escape Velocity	2.639 km/s
Albedo	0.22
Apparent Magnitude	8.2-9.0
Surface Temperature	93.7 K
Surface Pressure	1.45 atm

Table 1.2: Characteristics of Titan and its orbit about Saturn [31; 32; 33; 34].

1.3 Atmosphere

One of the most distinguishing aspects of Titan, and the most relevant to the work presented in this dissertation, is the presence of its substantial atmosphere, about 1.2 times the mass of Earth’s atmosphere. Excluding the gas and ice giants, our solar system is known to contain only four bodies with atmospheres of this kind:

Venus, Earth, Mars, and Titan. Located at approximately 10 AU from the Sun, Titan is something of an anomaly with respect to these other rocky bodies, all three of which are located in the inner solar system, within a distance of about 1.5 AU from the Sun. Titan is also the only natural satellite in the solar system with a substantial atmosphere.

Naturally, this atmosphere plays a central role in Titan's astrobiological potential. For, without the surface pressure it exerts, Titan's methanological cycle, including the presence of its perennial lakes and seas, would not be possible. Moreover, the atmosphere itself, as we will now move to discuss, acts as a sort of prebiotic chemical factory: a place in which more and more complex organic molecules are inevitably generated and can be found and detected, as we probe deeper and deeper into the atmosphere, toward the surface. This serves as an incredibly convenient laboratory in which to study prebiotic chemistry and furnishes many analogous environments to those we expect to have been present on the Hadean Earth [4; 5; 6; 7].

1.3.1 Atmospheric Composition

Titan's atmosphere is dominated by molecular nitrogen (N_2 , $\sim 95\%$), the exact abundance of which varies by a couple of percent with altitude. The next most abundant gas is methane (CH_4), whose abundance ranges between 1 and 5% with altitude [24]. The remainder of the atmosphere's composition consists of molecular hydrogen (H_2), argon, and a smattering of trace hydrocarbons and nitriles. As we will soon see, it is that very *smattering* which has provided the molecular targets for this dissertation work.

The rich diversity of trace hydrocarbons and nitriles is initiated by dissociation

Table 1.3: Tabulated summary of molecules detected by remote sensing in Titan’s atmosphere, as well as their abundances, as measured by different spacecraft/observatories. Omitted entries in the table correspond to species that have not been measured with that respective spacecraft/observatory. See Table 1.4 for further details and citations.

Molecule	Formula	Voyager (1980)	ISO (1997)	Cassini (Equator)	Cassini (North Pole)
Ethane	C ₂ H ₆	13 ppm	13 ppm	N/A	N/A
Acetylene	C ₂ H ₂	3 ppm	2ppm	N/A	N/A
Propane	C ₃ H ₈	500 ppb	500 ppb	350 ppb	600 ppb
Ethylene	C ₂ H ₄	150 ppb	80 ppb	150 ppb	500 ppb
Propyne	C ₃ H ₄	5 ppb	8 ppb	5.2 ppb	20 ppb
Diacetylene	C ₄ H ₂	1.4 ppb	1.5 ppb	1.1 ppb	20 ppb
Allene	C ₃ H ₄	N/A	≤5 ppb	N/A	N/A
Benzene	C ₆ H ₆	N/A	0.5 ppb	0.2 ppb	3.8 ppb
Hydrogen cyanide	HCN	170 ppb	150 ppb	77 ppb	780 ppb
Cyanoacetylene	HC ₃ N	≤1 ppb	N/A	0.3 ppb	44 ppb
Cyanogen	C ₂ N ₂	≤1.5 ppb	N/A	0.5 ppb	0.9 ppb
Carbon dioxide	CO ₂	14 ppb	15 ppb	11 ppb	N/A
Water	H ₂ O	N/A	8 ppb	ppb	N/A
Monodeut. methane	CH ₃ D	15 ppm	8 ppm	8 ppm	N/A

of nitrogen and methane in the upper atmosphere, the dissociation being triggered either by solar UV radiation or energetic charged particles in Saturn’s magnetosphere. What follows is a series of various chain reactions during the downward flow of the intermediate products.

Our understanding of the abundances of these hydrocarbons and nitriles, as well as those abundances’ dependence on latitude and season, has improved substantially over the course of our investigation of Titan. This is evident in Table 1.3. Detections of additional trace hydrocarbons and nitriles not displayed in this table (e.g. propadiene C₃H₄ [27], and cyclopropenylidene c-C₃H₂ [28]) have also been made quite recently. Regardless, it can be seen that in spite of much progress having been made, there is still work to be done; in particular, it can be seen that a great number of C₃ molecules have been detected, whereas only two C₄ molecules have been detected! We will return to this specific point momentarily.

Molecules Detected in Titan's Atmosphere by Remote Sensing

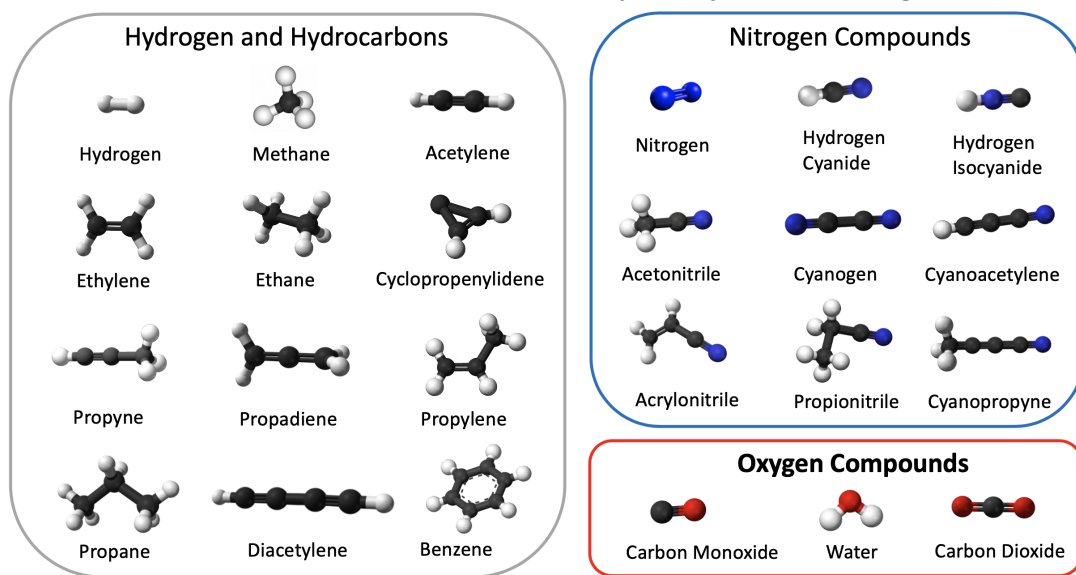


Figure 1.7: Visual representation of the species shown in Table 1.3. This figure has been adapted from Figure 5 of MacKenzie et al. (2021) [35].

Table 1.4: Titan’s atmospheric constituents and how they were first detected. Abbreviations: IRIS (Infrared Interferometer Spectrometer [36]), SWS (Short Wavelength Spectrometer [37]), G-B (former Ground-Based observatory), INMS (Ion and Neutral Mass Spectrometer [38]), IRTF TEXES (NASA’s Infrared Telescope Facility, Texas Echelon Cross Echelle Spectrograph [39]), ALMA (Atacama Large Millimeter/Submillimeter Array). Table adapted from Table 6.1 in Coustenis and Taylor (2008)[23].

Constituent	First detection	Reference(s)
MAJOR:		
N ₂	Voyager radio occultation; UV	[40; 41]
N	Voyager, 113.4 nm multiplet	[41]
CH ₄	G-B in UV, IR: 619 and 725 nm, 1.1 and 7.7 μm	[11; 42; 43]
CH ₃ D	G-B at 1.65 and 8.6 μm	[13; 44]
H	Voyager 1, 121.6 nm	[41]
H ₂	G-B, 3-0 S(1)	[42]
Ar ³⁶ , Ar ⁴⁰	Cassini-Huygens GCMS	[22]
MINOR:		
C ₂ H ₆	G-B, 822 cm^{-1}	[45; 46]
C ₂ H ₂	G-B, 729 cm^{-1} , and Cassini INMS	[47]
C ₂ HD	Cassini/CIRS, 678 cm^{-1}	[48]
C ₃ H ₈	Voyager 1 IRIS, 748 cm^{-1}	[43; 49]
C ₂ H ₄	G-B, 950 cm^{-1}	[45]
CH ₃ C ₂ H	Voyager 1 IRIS, 328 and 633 cm^{-1}	[43; 49]
C ₄ H ₂	Voyager 1 IRIS, 220 and 628 cm^{-1}	[50]
C ₆ H ₆	ISO and Cassini CIRS, 674 cm^{-1}	[22; 48; 17]
HCN	Voyager 1 IRIS, 712 cm^{-1}	[43]
HNC	Herschel, 543.897 GHz	[51]
HC ₃ N	Voyager 1 IRIS, 500 and 663 cm^{-1}	[50]
C ₂ N ₂	Voyager 1 IRIS, 233 cm^{-1}	[50]
solid C ₄ N ₂	Voyager 1 IRIS, 474 cm^{-1}	[52]
CH ₃ CN	220.7 GHz multiplet	[53]
CO	G-B, mm, sub-mm, microwave, and IR	[54]
CO ₂	Voyager 1, 667 cm^{-1}	[55]
H ₂ O	ISO SWS, at 237 and 243 cm^{-1}	[56]
NH ₃ , C ₂ H ₅ CN, C ₂ H ₃ CN, CH ₂ NH	Cassini INMS ionospheric data or ALMA	[57; 58; 59]
C ₃ H ₆	Cassini CIRS	[60]
CH ₂ CCH ₂	IRTF TEXES	[27]
CH ₃ C ₃ N	ALMA	[29]
c-C ₃ H ₂	ALMA	[28]

1.3.2 Atmospheric Chemistry

As stated earlier, the chemistry which takes place in Titan’s atmosphere has its origin in photodissociation and photoionization of N_2 and CH_4 in the upper atmosphere by ultraviolet solar photons and energetic solar wind particles which have been corralled by Saturn’s magnetic field, with the solar UV photons being the dominant driver of Titan’s atmospheric chemistry [61]. N_2 is an effective absorber of photons with wavelengths less than 100 nm, whereas the CH_4 is an effective absorber of Lyman alpha photons (wavelengths between 100 and 145 nm). Longer wavelength photons can penetrate further into the atmosphere and are ultimately absorbed by species that are products from this chemistry.

Of particular importance are acetylene (i.e. ethyne, C_2H_2), and diacetylene (C_4H_2). These two species in particular absorb lower energy solar photons and dissociate to form C_2H and C_4H , which then go on to react with methane, producing methyl radicals (CH_3) and reproducing acetylene and diacetylene. For this reason, acetylene and diacetylene are understood to be catalysts toward destruction of methane, as they absorb the lower energy photons which methane does not absorb, and then subsequently attack methane, as shown in the following example reaction scheme [62; 63]:



Ultimately, these and similar processes serve as the starting point in the development of Titan’s rich suite of hydrocarbons and nitriles, which are depicted in Figure 1.7. In Table 1.5, the main chemical production and loss mechanisms for

ten of the most abundant trace molecules in Titan’s atmosphere are displayed, in order of decreasing abundance.

Table 1.5: Production and loss of the ten most abundant trace molecules of Titan’s atmosphere. It can be seen that the primary loss mechanism for many of these molecules is in fact condensation in the lower atmosphere, where these species can precipitate and end up on Titan’s solid surface or in its lakes and seas [62].

Species	Production	Loss
H ₂	photolysis of CH ₄	Escape at top of atmosphere
CO	O+CH ₃	CO+OH → CO ₂ +H
C ₂ H ₆	CH ₃ +CH ₃ +M→C ₂ H ₆ +M	Condensation
C ₂ H ₂	C ₂ H+CH ₄ → C ₂ H ₂ + H ₂	C ₂ H ₂ +hν → C ₂ H+H, and condensation
C ₃ H ₈	CH ₃ +C ₂ H ₅ +M→C ₃ H ₈ + M	Condensation
C ₂ H ₄	CH+CH ₄ →C ₂ H ₄ +H CH ₂ +CH ₃ →C ₂ H ₄ +H	C ₂ H ₄ + hν →C ₂ H ₂ +2H
HCN	N+CH ₃ →H ₂ CN+H H ₂ CN+H→HCN+H ₂	Condensation
CO ₂	CO+OH→CO ₂ +H	Condensation
CH ₃ CCH	CH+C ₂ H ₄ → C ₃ H ₄ +H	C ₃ H ₄ +hν → C ₃ H ₃ +H H+ CH ₃ CCH→C ₃ H ₅
C ₄ H ₂	C ₂ H+C ₂ H ₂ →C ₄ H ₂ +H	C ₄ H ₂ +hν →C ₄ H+H

1.3.3 Hydrocarbons: Moving from C₃ to C₄

It is easily seen in the previous section that the vast majority of C₃ hydrocarbons which can be ‘built’ out of the molecules available at Titan have already been detected at this point (e.g. C₃H₈, C₃H₆, C₃H₄, etc. See specific citations in Table 1.4.) Over the years, tighter and tighter constraints on the abundances of these

molecules have been placed, at a variety of latitudes, and their roles in the organic chemistry of Titan’s atmosphere are now fairly well understood.

Naturally, our photochemical models for Titan do not make the prediction that Titan simply tends to stop making bigger molecules as soon as three carbon atoms are joined together in some way! The logical next step is therefore to begin to explore the presence of the C₄ hydrocarbons in Titan’s atmosphere, such as butanes, butenes, butynes, etc. Returning briefly to Figure 1.7, it can be seen that only one such hydrocarbon (diacetylene, C₄H₂) has been detected, with one C₄ nitrile also having been detected (cyanopropyne, C₄H₃N). It is apparent that we have only begun to scratch the surface of what Titan’s atmosphere is likely generating, in terms of C₄ molecules.

As we will now move on to see, the entirety of this dissertation work has been an investigation into the possible presence of two of these large C₄ hydrocarbons in Titan’s atmosphere, which are as of yet undetected: these are *n*-butane (*n*-C₄H₁₀) and *trans*-2-butene (*trans*-2-C₄H₈). Along with many other C₄ hydrocarbons, both of these molecules appear in all of the photochemical models that we have for Titan, in a variety of abundances [63; 64; 65; 66; 67]. Additionally, both of these molecules have been shown to be likely products of Titan-processes simulated in the laboratory. For instance, in the laboratory, when Tran et al. (2005) irradiated gas mixtures designed to simulate Titan’s atmosphere under cold Titan temperatures, *n*-C₄H₁₀ was shown to be a very likely product, and highly favored in its production (by two orders of magnitude!) over its isomer, isobutane (*i*-C₄H₁₀) [68].

While *trans*-2-C₄H₈ and several other butene molecules were also observed as a product of the experiments of Tran et al. (2005), they were produced at much lower rates than *n*-butane. Later, however, a different experiment by Kim et al.

(2010) showed that butene molecules were a likely product of cold-temperature irradiation of ethane ices [69]. Additionally, *n*-butane was also produced from this experiment. Considering these results, and the photochemical modeling predictions, *n*-C₄H₁₀ does indeed seem to be a logical first candidate C₄ molecule to search for, with perhaps *trans*-2-C₄H₈ (or some other butene isomer) being a logical follow-up candidate.

An additional pressing motivation to search for these molecules at Titan is their connections with Titan’s astrobiology. Several C₄ hydrocarbons, *trans*-2-C₄H₈ included, are actually naturally in a liquid state on Titan’s solid surface [70]. Additionally, the collective butane and butene groups are estimated to contribute up to a combined 2% of the volume of Titan’s lakes and seas [71]. As biological life (at least as we understand it) requires some sort of liquid medium, with hydrocarbon media being one possibility that has been explored [4], there is an additional incentive behind the search for Titan’s atmospheric C₄ hydrocarbons, as a starting point for understanding this source of these larger organic molecules in Titan’s lakes and seas.

Another interesting connection to Titan’s astrobiology, specific to *n*-butane, is important to mention as well. In recent years, a terrestrial metabolic pathway involving *n*-butane has been discovered [72; 73; 74]. Via such a pathway, terrestrial microbial life near hydrothermal vents can sustain themselves on *n*-butane, ultimately producing CO₂ as a byproduct. While the prospect of exotic microbial life existing in Titan’s atmosphere and subsisting on *n*-C₄H₁₀ should be regarded as speculative, at best, the possibility should certainly not be outright discounted. Additionally, it is likely important to point out that the feasibility of this metabolic pathway *at* Titan, in Titan-like conditions, whether atmospheric or within Titan’s

lakes and seas, seems not to have been rigorously investigated as of yet.

With all of that being said, the motivations behind the search for Titan's C₄ hydrocarbons are quite clear. As stated earlier, contributions to this endeavor which are contained in this dissertation are specific to just two of the many possible C₄ hydrocarbons likely waiting to be found. In the end, this dissertation has involved hands-on laboratory data collection and analysis for those two molecules, in addition to astronomical observations and atmospheric modeling, leading to two publications, with a third nearly ready for submission for publication and a fourth currently in preparation. In addition to the more recent parts of this project which presently remain a work in progress, results obtained here also point quite clearly to additional work (in the laboratory, at the telescopes, and in atmospheric modeling) which can be undertaken in the near future to make additional progress on understanding the role of Titan's atmospheric C₄ hydrocarbons. Those future efforts will be described in the final chapter (Chapter 5) of this dissertation.

In the next chapter, meanwhile, let us begin with a brief roadmap outlining the methodology taken toward detecting/constraining *n*-butane and *trans*-2-butene in Titan's atmosphere, before diving into a more detailed explanation of the individual components of that methodology.

Chapter 2

Methodology

The general methodology behind searching for new molecular signatures in a planetary atmosphere is a procedure that can essentially be broken down into three different phases:

1. Laboratory spectroscopic study of the targeted molecules.
2. Observations of the targeted planetary atmospheres.
3. Radiative transfer modeling of the observations.

This brief chapter means to serve as an introduction to each of these three phases of detecting new molecules. This organization has been adopted to acquaint the reader with the lay of the land, so to speak, before providing a full exposition of the various parts of the methodology and the work that was completed for each.

2.1 Phase 1: Laboratory Spectroscopy of Targeted Molecule

The first phase of work is arguably the most important and often the most overlooked step in the whole procedure. Though quantum mechanical calculations of spectral line parameters are presently possible for small, simple molecules (e.g. Lukashetskaya et al. 2020 [75]), this is not the case for larger hydrocarbons, such as those which have been the target of the search at hand. In this sense, quality laboratory spectroscopic work is truly irreplaceable.

As astronomers, our only real way of learning about a distant planetary body is catching and recording the photons which arrive here (or at a spacecraft) from the targeted portion of the sky. Encoded within that distribution of photons are the quantum mechanical signatures of numerous atomic and molecular species, in a variety of physical contexts; we disentangle those signals by first observing those species in contexts that *we* can specify and carefully control in the laboratory.

This means obtaining the spectrum of the targeted molecule, ideally in a variety of experimental conditions (temperature, pressure) that are designed to be representative of the targeted planetary atmosphere. From the resulting spectra, absorption cross-sections can be measured, and in some cases, a pseudoline list [76] can be derived. (For those unfamiliar with the concept of a pseudoline list, this will be discussed in depth later on in Section 3.4.4.) These products (cross-sections, line lists) will be used later on, in characterizing signals in astronomical observations both qualitatively (via the absorption cross-sections) and quantitatively (via line lists).

In this dissertation, laboratory investigations of the two targeted Titan C_4

hydrocarbons, *n*-butane ($n\text{-C}_4\text{H}_{10}$) and *trans*-2-butene ($\text{trans-2-C}_4\text{H}_8$) were conducted. The molecule *cis*-2-butene, one of the isomers of *trans*-2-butene, was also briefly investigated, but ultimately, that investigation was cut short and that small project will therefore not be discussed at length in this dissertation. The intent is to return to that molecule (and ideally, other similar C_4 hydrocarbons which are likely to be found in Titan’s atmosphere) in the near future and finish the investigation more completely.

2.1.1 Brief Primer Concerning Radiative Transfer Theory

The physics necessary for understanding laboratory spectroscopy from an experimental perspective are largely contained within *optics*, specifically within *radiative transfer*. Naturally, these physics are relevant to the actual modeling of atmospheric observations as well, but it is still sensible to briefly introduce the main concept here.

Though radiative transfer theory certainly contains enormous complexity, fortunately, the relevant portion to the work described here is neatly contained, for the most part, within the Beer-Lambert law, which for our purposes can be written

$$\tau_{obs}(\nu) = \exp(-\sigma_\nu n \xi L). \quad (2.1)$$

The above relates an observed transmission spectrum τ_{obs} and the wavelength-dependent cross-section σ_ν of the absorbing species, the number density $N = n\xi$ of that species (where ξ is the mixing ratio of the absorbing gas, n being the number density of the entire admixture), and the path length L traversed by the beam. The significance of the various parameters in this equation (particularly the cross-

section σ_ν) will be greatly elaborated upon in subsequent sections. For now, it is sufficient to simply point out that transmission of light through a medium falls off exponentially with the (1)distance it must traverse, (2)the density of the gas in its path, and (3)the ‘size’ (absorption cross-sections) of the species present in that gas.

2.2 Phase 2: Observations of Targeted Body

Obviously, remote observations of the planetary body of interest are required in order to investigate which molecules may be present there. This is, of course, assuming in-situ measurements are not available. Though we are fortunate enough to have a few in-situ measurements at Titan, via the Cassini mission and in particular the Huygens Lander Probe [22], the work conducted here has largely been focused on interpreting remote observations specifically, both from ground-based observatories, and from the Cassini instruments themselves, gathered during various flybys of Titan.

The idea here is that if we can use a mathematical model of the physics of radiative transfer to generate synthetic spectra of a *physical* model of an atmosphere (e.g. temperature/pressure profiles, gas profiles, etc.), and if these derived synthetic spectra accurately match the remotely observed spectra of the target body, then we have strong evidence to believe that there is some truth to the accuracy of the *physical* model. Standard statistical analyses can quantify the level of uncertainty behind this accuracy. This, of course, implicitly relies on some level of trust in the mathematical model itself.

2.3 Phase 3: Radiative Transfer Modeling of Observations

There are many radiative transfer modeling codes available nowadays [77; 78; 79]. Each has specific applications for which it is most suitable. For instance, most have been designed specifically for Earth-atmosphere remote sensing applications, and therefore require substantial modification before they can be applied to other planetary atmospheres.

All of the work in radiative transfer modeling described here has utilized the Non-linear Optimal Estimator for Multivariate Spectral Analysis (NEMESIS) radiative transfer tool [79], which was developed to be an extremely flexible modeling suite, capable of modeling observations of any planetary atmosphere, even those of exoplanets! NEMESIS has been utilized extensively in the field of Titan science in particular, though it has been applied to other planetary atmospheres as well, such as those of the outer gas giants and ice giants, e.g. [80; 81; 82].

NEMESIS consists of two primary parts. A forward model, and a retrieval (or inversion) model. Each of these components is described below in turn:

1. Forward model: This is a model of the actual physics of radiative transfer. It calculates a synthetic spectrum, taking as input an assumed atmospheric structure (gas abundance profiles as a function of altitude, temperature profile, haze/aerosol cross-sections, etc.)
2. Retrieval model: This part of NEMESIS takes the forward model's output and compares it to the observations that the user is attempting to model. It then adjusts the parameters which the user has selected in advance as being

‘variable’, and attempts to vary them in an effort to minimize the discrepancy between the synthetic spectrum and the observations.

During the iterations of the retrieval and inversion modeling process, a fitting algorithm is used which is based on an optimal estimation technique, described in detail in Rodgers et al. (2000) [83]. The technique tries to minimize a cost function which is very similar to a χ^2 “goodness-of-fit” metric. Through any given iteration of the fitting, the solution that NEMESIS lands upon is penalized for deviating from both the *a priori* state but also from the model which was generated in the previous iteration. Marquart-Levenberg minimization (i.e. the common “damped least squares”, or DLS method) is utilized by NEMESIS, which descends a downhill trajectory with respect to the aforementioned cost function, until convergence (a criterion whose tightness is set in advance by the user) is achieved.

Ultimately, the result of a NEMESIS calculation is the retrieval of the user-selected variables after they have been adjusted through several iterations, and the spectral model that results from those changes to the *a priori* profiles. It should be noted that one possible limitation is inherent within the χ^2 minimization process, namely that a local, rather than a global χ^2 minimum can be unintentionally reached within χ^2 space. It can be demonstrated that this is *not* occurring by repeating the retrievals multiple times, with each beginning with a different set of *a priori* profiles. Typically, the *a prioris* used are generated from a Gaussian distribution about the “nominal” *a priori*. Since, as stated previously, NEMESIS penalizes each iteration’s calculated solution for deviating from the *a priori*, demonstrating that the retrieved results are not overly-sensitive to the initial set of *a prioris* in this way indicates that a global minimum, rather than a local minimum, is being converged upon within χ^2 space.

Though such steps are necessary in some cases, they can generally be omitted, provided that they have been conducted in the past with sufficiently similar data sets. As NEMESIS has been used extensively with similar Cassini CIRS data sets to those which were used in this work [84; 60], which will be described more thoroughly in Chapter 4, this process was deemed unnecessary for this particular study. Future work that does go through these steps explicitly will be able to assess the veracity of this procedure and test its impact on the results.

2.4 Connecting the Dots

We have now seen that three distinct ‘phases’ are inherent to the procedure of detecting new molecules in a planetary atmosphere. Naturally, these three parts of the procedure, while distinct, are not independent of one another. In Figure 2.1, a simplistically depicted representation of the interconnected nature of the three phases is presented. Later, to conclude this dissertation in Chapter 5, we shall return to this figure, filling in some of the ‘blanks’. It will then be argued that better, more frequent communication is needed between those involved in each of these three phases of this whole process, in order to facilitate more efficient progress in the future.

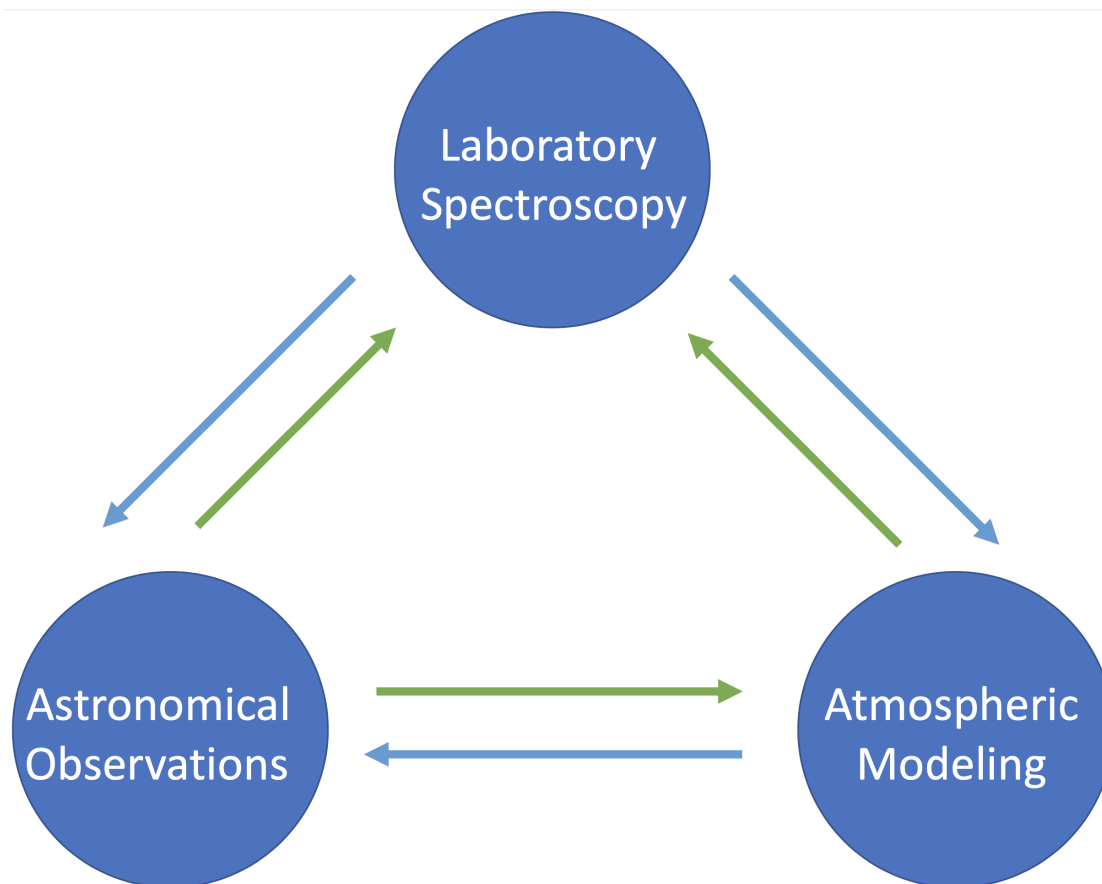


Figure 2.1: The three areas that contribute to characterizing a planetary atmosphere, demonstrating the concept that efficient intercommunication between each of these three areas is a necessary component of the procedure.

2.5 Chapter 2 Conclusion

This concludes a brief introduction to the general methodology which goes into the search for new molecules in a planetary atmosphere, beginning with laboratory spectroscopy, followed by observations of the targeted body, and concluding with radiative transfer modeling of those observations. The next two chapters will describe the implementation of each of these phases of the methodology with specific regards to the work conducted in the search for Titan's *n*-butane and

trans-2-butene.

Chapter 3

Laboratory spectroscopy

3.1 Introduction

Essential to the successful understanding of any planetary atmosphere, laboratory molecular spectroscopy has been a major portion of this dissertation work, laying the groundwork for future searches for new trace gas species in the atmosphere of Titan. These laboratory experiences took place across two separate (but related) internships at NASA Jet Propulsion Laboratory (JPL) in Altadena, California. In JPL's molecular spectroscopy lab, we are able to use a variety of gas cells, filled to some sample pressure with a molecule of interest for a given planetary atmosphere, in order to study the spectra of potentially detectable molecules in the very conditions that they may be found for the atmosphere of interest.

We simulate those atmospheric conditions in the gas cell by manipulating its temperature (via a liquid helium cooling cycle), and by controlling the total pressure (by adding or removing an appropriate broadening gas). Further, we are able to control the spectral resolution at which we study these molecules, which

is helpful in some cases, for instance, when astronomical observations of a specific spectral resolution must be modeled. The mechanism for controlling spectral resolution during the data acquisition will be discussed shortly.

The instrument at JPL which allows us to spectroscopically characterize Titan gases at cold Titan temperatures is a Bruker IFS (Interferometer Spectrometer) 125 HR (High Resolution). A photo of this instrument in the same configuration as that of the instrument at JPL is shown in Figure 3.1; no photography of the actual instrument nor anything else within the lab was permissible. The Bruker is a Fourier Transform Spectrometer (FTS), consisting of a classic Michelson interferometer with a moving mirror.

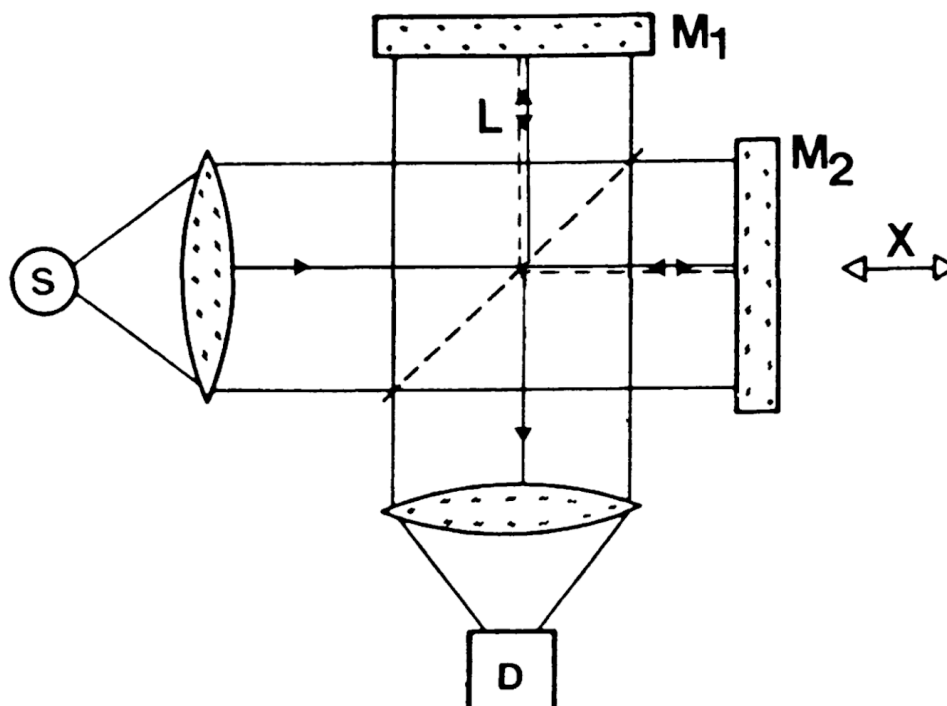


Figure 3.2: Schematic for a general Fourier Transform Spectrometer (FTS)[85].

The workings of a FTS instrument are shown schematically in Figure 3.2. A source (S) emits continuous light across a certain spectral bandpass. This light is



Figure 3.1: A Bruker IFS 125 HR. Projecting out of the page is the long ‘scan’ arm of the interferometer, on which a moving mirror is able to travel along the observed track. Perpendicular to the scan arm is a second arm that houses the infrared light source, the filled gas cell, and the detector. This image and more information about other Bruker instruments can be found on their main website: www.Bruker.com.

directed through a beam splitter (diagonal dashed line in the figure), which sends half of the incoming flux upward a distance L towards a flat, fixed mirror M_1 , and transmits the other half of flux through a distance $L + x$ toward a moving mirror M_2 whose position is continuously adjusted (i.e. x varies, in steps of size Δx). The light from both arms of the spectrometer then travel their respective distances a second time before being recombined at the beam splitter again. This recombined beam, which at this point contains a signal that amounts to a very precise measure of *distance* (i.e. the position of the moving mirror M_2), is then directed through the gas cell containing the sample to be studied, and ultimately impinges on the detector D , which measures the intensity of the light. The resulting data set is called an interferogram, $I(\Delta x)$, where Δx is some small increment of distance for the moving mirror fM_2 .

The interferogram, which can be thought of as a continuous waveform which has been finitely sampled at a number of points N , equidistant by spacing Δx , must then be transformed into the frequency domain, via a Discrete Fourier Transform, in order to extract spectral data for the sample. Mathematically, the Discrete Fourier Transform [85] is written

$$\tau(k\Delta\nu) = \sum_{n=0}^{N-1} I(n\Delta x) e^{\frac{2\pi i \cdot nk}{N}}. \quad (3.1)$$

Note that the index n here is unrelated to the number density n that we saw in the similar looking Beer-Lambert law (Equation 2.1 of Chapter 2); instead, the index n runs over the number of different positions (N in total) of the moving mirror M_2 for which the detector recorded an interferogram.

Via this equation, the interferogram $I(x)$, i.e. the intensity of the detected

light with the moving mirror M_2 at a position $x = n\Delta x$ for some n , is converted into a sampled transmission spectrum $\tau(\nu)$, i.e. the *transmitted* intensity (through the sample gas) at a given wavenumber $\nu = k\Delta\nu$. And with that conversion, the original signal, which was a precise measurement of the moving mirror's *distance*, is transformed into a precise measure of *frequency*. The fact that the molecules in the gas sample transmit light *preferentially* as a function of frequency means that the stored spectrum contains information about the molecules themselves which are present within the gas cell, and the fact that the transformed spectrum is measured precisely in the frequency domain means that high (spectral) resolution is achieved.

3.2 The “Ratioing” Process

An important part of the measurement of transmission spectra is the collection of *empty cell spectra*. What this means is that for every spectrum gathered at a given set of experimental conditions (temperature, sample pressure, total pressure, and resolution), we must also collect a spectrum of the *empty* gas cell. This can be done either before the cell is loaded with sample gas and the data collected, or after the data is collected and the gas cell has been evacuated to vacuum.

The empty cell spectrum records any absorptions that are occurring from within the instrumentation and the gas cell themselves. These absorptions occur due to the various windows (e.g. the ZnSe and KBr windows that the beam must pass through, to be discussed later), and also due to any residual gas (usually water vapor) that remains in the gas cell due to the fact that the pump cannot pull a *perfect* vacuum before sample gas insertion.

The procedure is to divide the recorded data spectrum by the associated empty cell spectrum, which yields a ‘normalized’ (for lack of a better word) transmission spectrum, free of signals from material due to the instrument itself and from residual gases within the instrument. For the remainder of this chapter, this procedure will be referred to as the ‘ratioing process’.

3.3 Absorption Cross-sections and Band Intensities

Typically, in the literature, we report absorption cross-sections for a given molecule, rather than reporting the raw transmission spectra data described by Equation 3.1. Many examples of such reporting are available in the literature [86; 87; 88; 89; 90; 91; 92; 93; 94]. Demonstrating how the cross-sections are calculated from the transmission spectra gathered in the laboratory is rather simple, in fact. In doing so, however, emphasis will be placed on a crucial and rather tricky subtlety in understanding the connection between absorption cross-sections and a similarly defined quantity, the band intensity (S). Only by firmly solidifying this connection right now will we be able to later demonstrate the full scope of contexts to which the measured cross-sections can be applied in actual atmospheric modeling work.

Beginning by considering a measured transmission spectrum $\tau(\nu)$, from Beer’s Law, we have

$$\tau(\nu) = \exp(-\sigma_\nu n \xi L), \quad (3.2)$$

where σ_ν is the absorption cross-section [cm^2] at wavenumber ν , $N = n \xi$ is the number density of sample gas [cm^{-3}] (n being the number density of the full

admixture including broadening gas and ξ being the volume mixing ratio of sample gas), and L is the path length [cm] of the gas cell. Then, by the all-important **Law of Conservation of Things that Obviously Must Add to Unity**, the corresponding expression in the absorption domain (i.e. the absorbance) is

$$\alpha(\nu) = 1 - \tau(\nu) = 1 - \exp(-\sigma_\nu n \xi L), \quad (3.3)$$

as what was *not* absorbed must inevitably have been transmitted.

We can integrate this absorbance over an isolated vibrational band defined by $\nu_1 < \nu < \nu_2$ to obtain the integrated absorbance A of that interval,

$$A_{\nu_1 \rightarrow \nu_2} = \int [1 - \exp(-\sigma_\nu NL)] d\nu. \quad (3.4)$$

If the argument of the exponential within the integrand is small (i.e. the sample is optically thin), then

$$\tau(\nu) = \sigma_\nu NL \ll 1, \quad (3.5)$$

and we can binomial-expand the exponential, obtaining

$$A = \int [1 - (1 - \sigma_\nu NL)] d\nu = \int \sigma_\nu NL d\nu. \quad (3.6)$$

But the number density and path length of the gas in the cell do not depend on wavenumber ν , so we have

$$A = NL \int \sigma_\nu d\nu = NL \cdot S(\nu), \quad S(\nu) \equiv \int \sigma_\nu d\nu, \quad (3.7)$$

where the integrated band strength $S(\nu)$ has been defined. When studying a

molecule, what we would *really* like to know, for all ν , is $S(\nu)$, the band intensity, which is fundamental and intrinsic to the *molecule* itself, coming purely from geometric and quantum mechanical considerations, and therefore not depending at all on the experimental measurement conditions such as temperature and pressure [95].

Looking at the right hand side of Equation 3.7, it is tempting to say “Hang on...if $S(\nu)$ is fundamental to the molecule itself, and $S(\nu)$ is just the integration of the molecule’s absorption cross-sections σ_ν across some wavenumber interval, then the absorption cross-sections σ_ν must also be fundamental to the molecule itself, and therefore must also be independent of the experimental conditions!” However, this is true only in the special case that we used to *arrive* at Equation 3.7, namely Equation 3.5, our assumption of $\sigma_\nu NL \ll 1$, i.e. the assumption of optical thinness. When this condition is satisfied, absorption cross-sections measured under those conditions are *indeed* (to a very good approximation) independent of the experimental conditions under which they were measured. Further, a test that this condition is *satisfied* is contained in the right hand side of Equation 3.7: if it can be systematically shown that the integrated absorbance increases linearly with the quantity $N \cdot L$, which here we shall define as the “optical burden”, then the condition is necessarily satisfied, and the plot of such a relationship, the integrated absorbance as a function of optical burden, has slope equal to $S = \int \sigma_\nu d\nu$. In the next section, the implications of being able to demonstrate this linear relationship from one’s measurements of transmission spectra are shown and discussed.

3.3.1 The Linearity Test: When Is σ_ν Equivalent to S ?

It is worth taking a moment to attempt to understand the results of the previous section at a conceptual level, and to check to see whether or not they are consistent with intuition. Equation 3.7 says that if we have measured a transmission spectrum and then calculated the integrated absorbance A , then upon a second measurement of that integrated absorbance but using a longer gas cell with length $L' > L$, to which we have added enough sample gas so as to hold the original density constant ($N' = N$), we would measure a larger integrated absorbance $A' > A$. This makes intuitive sense; if the beam has to travel through *more* of the absorbing gas before being detected (simply because the column of gas is longer), we would expect less of that beam to arrive at the detector, and thus expect an increased measure of integrated absorbance. Along a similar vein, if we remeasured A using the original cell of length L but simply filled that cell with *more* sample gas, perhaps to a density $N' > N$, we would also measure an increased integrated absorbance. This also makes perfect intuitive sense; once again, albeit for a different *reason*, the beam is forced to encounter more of the absorbing gas along its way to the detector (not because the column is longer, but because the probability of encountering an absorber within the column at any given moment has increased), and the beam is therefore absorbed more strongly.

Because increasing $L \rightarrow L'$ and increasing $N \rightarrow N'$ both have the same qualitative effect on A , it makes sense to merge these two quantities into a single product (the “optical burden”, as mentioned previously), and observe that the integrated absorbance increases linearly with that optical burden, with some slope S . As the only other thing that we could presumably vary in this equation so as to cause an increased integrated absorbance $A' > A$ is to actually increase the molecule’s *fun-*

damental physical ability or likelihood to absorb photons of energy contained within this wavenumber interval, it is therefore precisely **that** property which is recorded in S . We call such a property, the ability or likelihood of a specific molecule to absorb photons within a specific band of energies, the intensity of the band, or the band intensity, and we note that it appears to be specific to *this* particular molecule, and exists entirely independent of what length our gas cell is and how much gas is present within that cell. For, temporarily imagining that we do not hold any understanding of quantum mechanical theory, were we to repeat the whole experiment with a completely *different* molecule, we would have no *a priori* reason to believe that this new molecule will absorb those photons with the same likelihood, i.e. the same intensity S (though it certainly could, at least in principle); thus, the band intensity S must be measured for each molecule individually. It is this **intrinsic** molecular quantity that we are interested in measuring and reporting to a database so as to populate a repository with information concerning which molecules absorb effectively in which particular wavenumber intervals.

3.3.2 Cross Sections and Band Intensities - Conclusion

This has been a rather lengthy explanation of what appeared at a first glance to be a relatively straightforward set of mathematical operations on the measured quantity τ , the observed transmission spectrum. But the purpose of going through these steps in such gory detail is now made clear: *we cannot directly measure the band intensity S , even though that is what we wish to measure*, as it would allow us to extract objective information about a particular molecule itself. We *can*, however, directly calculate the quantity σ_ν , the absorption cross-sections, rather trivially from the transmission spectra, by inversion of Equation 3.2 and simplifying

solving for σ_ν . If we are careful to be doing so only at thin optical depth, we ensure that the measured cross-sections are in fact (approximately) equivalent to the band intensities. Thus, the reported “cross-sections” under such conditions are effectively band intensities, valid for representation of the molecule *at any optical depth*, and suitable for reporting to molecular absorption databases. Other scientists can safely use such “cross-sections” in their work without needing to know any quantitative details concerning the experimental set up for which the initial transmission spectra were gathered.

This whole process, demonstrating that experimentally measured absorption cross-sections were carefully done at sufficiently thin optical depth such that they are (approximately) equal to molecular band intensities, is neatly verifiable in the literature for such work by simply showing that the integrated absorbance A increases linearly with optical burden $N \cdot L$. We will soon see that such a “linearity test” was necessary in the case of the study of *trans*-2-butene, whereas it was not strictly necessary in the case of the study of *n*-butane. The reasons for this important difference will be elaborated upon in Section 3.4, which will describe the *n*-butane work, and in Section 3.5, which will describe the work with *trans*-2-butene.

3.4 N-butane ($n\text{-C}_4\text{H}_{10}$)

3.4.1 The Molecule

The first molecule which was spectroscopically characterized in the infrared in the laboratory for this work was *n*-butane ($n\text{-C}_4\text{H}_{10}$), shown below. All of the results described in this section (Section 3.4.1) were published in 2020 in Journal

of Quantitative Spectroscopy and Radiative Transfer:

- Sung, Keeyoon, **Brendan Steffens**, Geoffrey Toon, Deacon Nemchick, and Mary Ann Smith. “Pseudoline Parameters to Represent *n*-Butane ($n\text{-C}_4\text{H}_{10}$) Cross-Sections Measured in the 7-15 μm Region for the Titan Atmosphere.” *Journal of Quantitative Spectroscopy and Radiative Transfer* 251 (May 2020): 107011. <https://doi.org/10.1016/j.jqsrt.2020.107011>

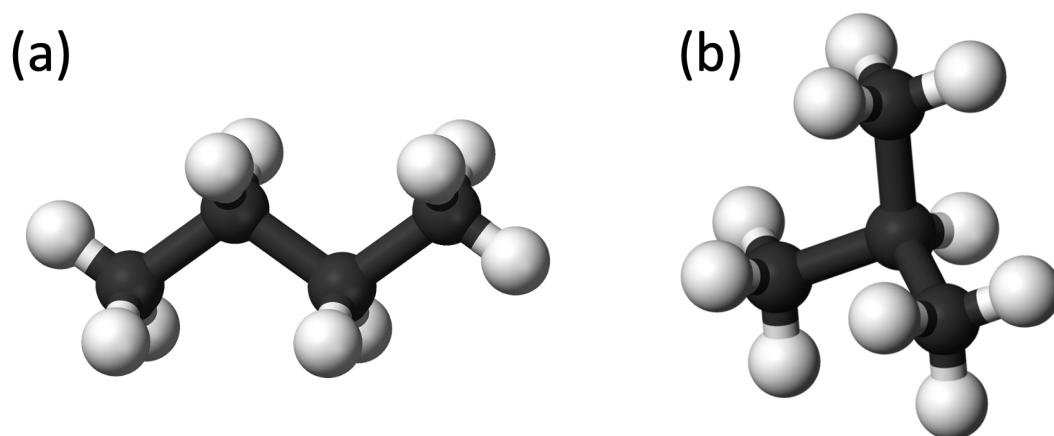


Figure 3.3: The two isomers of butane. (a) *n*-butane, the focus of this section, and (b) isobutane, which still needs to be characterized more thoroughly in the future!

Butane (C_4H_{10}), with four carbon atoms and ten hydrogen atoms, is a fully hydrogenated (or fully saturated) alkane that comes in two different isomers, as seen in Figure 3.3: the ‘normal’, zig-zag chain isomer *n*-butane (a), and the tetrahedrally structured isobutane (b).

As discussed at the end of Chapter 1, the presence of hydrocarbons as large as *n*-butane has been a long-standing prediction of photochemical models for Titan’s atmosphere. For instance, the seminal photochemical modeling paper on Titan’s atmosphere by Yung et al. [63] actually draws specific attention to the large abun-

dance predicted for butane. In their model, butane arises from the same chemistry that produces propane (C_3H_8), which has already been observed multiple times [43; 96; 84]. More recent photochemical models [66; 65; 64; 67] predict that butane molecules are generated at a comparable production rate to that of propane. For reference, the disk-averaged abundance of propane was observed to be 476 ppb by Cassini/CIRS, which is about ~ 100 times higher than the Cassini/CIRS detection sensitivity [97]. The production rate of butane has been estimated to be only a factor of seven times lower than that of the very abundant propane (abundances of order 500 ppb [84]) in Titan’s atmosphere [98], which could yield a disk-averaged *n*-butane abundance of ~ 68 ppb, which is well above the sensitivity of Cassini/CIRS. Thus, the detection of butane is naturally anticipated from Cassini/CIRS, or perhaps from upcoming JWST/MIRI or ground-based NASA IRTF observations [99].

Specific chemical pathways for the production of butane in Titan’s atmosphere have been proposed. For instance, butane might be formed through the addition of methyl and propyl radicals, as in the model of Vuitton et al. (2019) [66]. First,



followed by the three body reaction



where the overset M in these reactions refers to an unspecified third body, most likely N_2 .

Interestingly, butane was observed to form naturally when simulated Titan

atmospheric samples were irradiated by ultraviolet radiation in experimental conditions designed to be similar to those of the Titan atmosphere. In the laboratory experiments conducted by Adamkovics et al. (2003) [100], for instance, in which the net production rates were measured for large gas-phase hydrocarbons formed from the ultraviolet (120-300 nm) irradiation of simple mixtures of Titan's precursor gases, the net rate of production of butane was observed to be $1.3 \times 10^{10} \text{ cm}^3 \text{ s}^{-1}$. This is almost *fifty* times greater than the measured production rate of propyne (C_3H_4), for instance, which has already been detected in abundance by Voyager/IRIS [43].

In a similar but separate experiment, when gas mixtures designed to simulate Titan's atmosphere were ultraviolet irradiated (mostly at wavelengths of 185 and 254 nm, from a mercury lamp source) in the laboratory under cold Titan temperatures, *n*- C_4H_{10} was shown to be a very likely product. Moreover, *n*-butane was highly favored in its production, by approximately two orders of magnitude, over its isomer, isobutane (*iso*- C_4H_{10}) [68]. This last result was the primary reason as to why it was decided that *n*-butane should be characterized in the laboratory and sought at Titan first, before its cousin, *iso*-butane.

Also very interesting, butane is in fact predicted to be the most abundant C_4 -hydrocarbon in the photochemical modeling of Saturn as well [101], which may lend support to the expectation of finding it at Titan, a member of the Kronian system. It has also been shown that butane's high freezing point ($\sim 136 \text{ K}$) can potentially play a role in the nucleation of Titan's hazes and clouds [102], those being phenomena which we understand to be important to terrestrial life as we know it. Along with acetylene (C_2H_2), butane has also been proposed to be a good candidate for species that could contribute to the composition of the evaporite on

Titan’s surface [103], both in its pure form but perhaps also as part of an acetylene-butane co-crystal structure [104; 105].

Finally, butane molecules are expected to form up to 1% of the composition of Titan’s lakes and seas [71]. These stable liquid lakes and seas on Titan’s surface render Titan one of the most unique places in the solar system. As biology as we understand it requires some sort of liquid medium, it has been suggested that these liquid hydrocarbon lakes could be a repository for Titan’s hydrocarbon-based (rather than H₂O-based) life [4]. For this reason, it is crucial to begin to understand the compositions of these stable liquid features, which are likely linked to atmospheric transfer processes and Titan’s entire ‘methanological cycle’ in general [106].

Summarizing, with the large abundances of both propane and butane being predicted by multiple photochemical models, and with propane having been uncontroversially detected in Titan’s atmosphere already, and considering the multiple chemical production channels of butane identified and even simulated and constrained in the laboratory, an actual, explicit detection of butane at Titan has been highly anticipated for quite some time.

This possible detection of butane would most likely come from the Cassini-CIRS observations, or if not from those, from the upcoming JWST/MIRI observations [99], or perhaps from high-resolution ground-based observations from NASA IRTF. Cassini/CIRS in particular has been instrumental toward constraining atmospheric models for Titan in the recent past. For remote observations such as these to be properly interpreted, however, the spectra of *both* butane isomers (*n*-butane and isobutane) must be carefully characterized in the laboratory. The 2500–3280 cm⁻¹ (3.1–4.0 μm) region for isobutane has been characterized recently at temperatures

(200–300 K) and pressures (~ 10 Torr) representative of Titan [91; 107]. Prior to the *n*-butane work at JPL in 2019 described here, not much work had been done, however, in the 7–15 μm region for representing this gas at cold Titan temperatures. It is worth reiterating here that the application of quantum-mechanical modeling techniques via empirical Hamiltonians [108; 109] to produce precision spectroscopy is extremely challenging for larger, polyatomic hydrocarbons such as *n*-butane.

An additional complication is that *n*-butane has two conformers (*trans*, which is also called *anti* in *n*-butane’s case, and *gauche*), seen in Figure 3.4. Each of these conformers independently has three low-lying torsional states (i.e. lower energy than the vibrational fundamentals). In fact, *n*-butane is the simplest hydrocarbon (simplest meaning all single bonds) to exhibit this *trans/gauche* conformerism. The *trans* conformer is the more stable of the two, due to the crowding of the two methyl groups in the *gauche* structure. The energy difference between the two conformers is only $0.9 \text{ kcal mol}^{-1}$, however, and this makes it extremely difficult to enrich one conformer relative to the other in any given sample. Thus, any laboratory study of the spectrum of *n*-butane is bound to record a convolution of the spectra of the *trans* and *gauche* conformers.

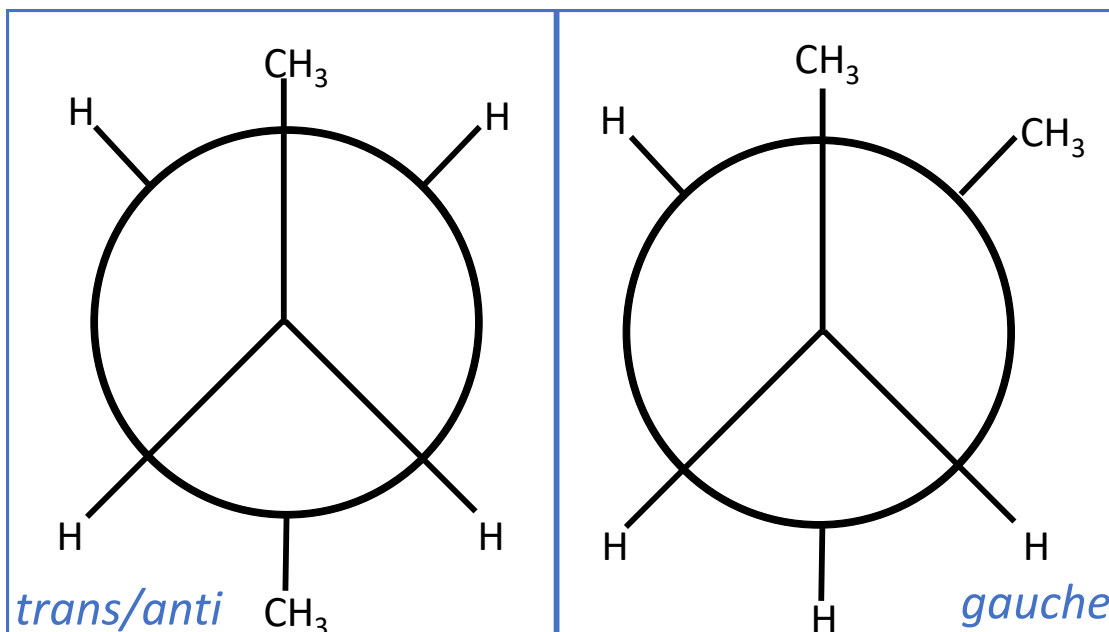


Figure 3.4: The two conformers of *n*-butane. The *trans* conformer is more stable (by $0.9 \text{ kcal mol}^{-1}$), as the two methyl groups are crowded in the *gauche* structure. Image generated by Brendan Steffens.

The low-lying torsional states of either conformer generate numerous combination and hot bands, even in the mid-infrared spectral region, making the calculation of their spectroscopic features from theory highly intractable. For these larger hydrocarbons, however, their contributions coming from the hot-band and combination band features simply cannot be neglected. This is true even at cold temperatures because of the generic low-lying states which involve the torsional states. One technique for capturing all of this information in one go, rather than attempting to calculate it from any theory, is to measure absorption cross-sections, as discussed previously in Section 3.3. A further step is to generate a pseudoline list [76], which can be used for quantitative analysis of possible emissions in remote sensing observations from the targeted gas. A pseudoline list is effectively an empirical model of an *actual* spectral line list, generated by fitting multiple

transmission spectra acquired at a variety of temperatures and pressures. This will be discussed in much more detail in Section 3.4.4.

As seen in Figure 3.5, with $N = 14$ atoms, *n*-butane has $3N-6=36$ fundamental vibrational modes. The band centers of these modes are roughly predicted by Shimanouchi (1972) [110] and they are reported in the NIST Chemistry Webbook. For the *trans* conformer, there are ten infrared active bands which fall into the 7–15 μm region that we were able to study at JPL in 2019. Of those ten, we were able to identify nine of them. For the *gauche* conformer, there are actually thirteen infrared active bands falling into that same spectral region, but we were able to identify only eight of those in our spectra. It is possible that some of the modes that could not be identified in our data were simply too low in intensity to be resolved at the experimental conditions that we explored. Future studies with higher spectral resolution could study *n*-butane samples with larger optical depth (through the use of a longer path length gas cell) and potentially locate those ‘missing’ bands.

All of the identified *n*-butane bands are presented in Figure 3.5, along with newly suggested values of the band centers from our observed spectra.

<i>trans</i> C ₄ H ₁₀			
ag [§]	au	bg [§]	bu
v ₁ (2965,C)	v ₁₂ (2968,C)	v ₂₀ (2965,C)	v ₂₇ (2968,C)
v₂ (2872,C)	v ₁₃ (2930,C)	v ₂₁ (2912,C)	v₂₈ (2870,C)
v₃ (2853,D)	v ₁₄ (1461,C); [1466]	v₂₂ (1460,C)	v₂₉ (2853,E)
v₄ (1460,C)	v ₁₅ (1257,C); [1263]	v₂₃ (1300,C)	v ₃₀ (1461,C); [1471.1, 1466.3, 1462.3] [@] ; [1466]
v₅ (1442,D)	v ₁₆ (948,B); [948]	v₂₄ (1180,D)	v ₃₁ (1461,C); [1457.0][@]
v₆ (1382,C)	v ₁₇ (731,B); [732]	v₂₅ (803,D)	v ₃₂ (1379,B); [1383.3][@]
v₇ (1361,D)	v ₁₈ (194, E) [§] ; [206.2(v₂₅)][@]	v₂₆ (225,E)[§]	v ₃₃ (1290,B); 1294.3 [@] ; [1295]
v₈ (1151,C)	v ₁₉ (102,E) [§] ; [121.3(v₂₆₇)][@]		v₃₄ (1009,C) – not seen
v₉ (1059,C)			v ₃₅ (964,B); [965.8][@]
v₁₀ (837,C)			v ₃₆ (271,E); [262.0][@]
v₁₁ (425,C)			
<i>gauche</i> C ₄ H ₁₀			
a [§]	a	b [§]	b
v ₁ (2968,C)	v ₁₂ (1168,D) [1175]	v ₂₀ (2968,C)	v₂₇ (1450,D)
v ₂ (2968,C)	v ₁₃ (1077,D); [1079][@]	v ₂₁ (2968,C)	v ₂₈ (1380,C) [1384]
v ₃ (2920,D)	v ₁₄ (980,D) [985.9]	v ₂₂ (2920,D)	v₂₉ (1370,D)
v₄ (2870,C)	v₁₅ (827,D) – not seen	v₂₃ (2870,C)	v₃₀ (1233,C)
v₅ (2860,D)	v ₁₆ (788,C); 798.5 [@] [790]	v₂₄ (2860,D)	v ₃₁ (1133,D); [1136.5][@]
v₆ (1460,C)	v₁₇ (320,C)	v₂₅ (1460,C)	v ₃₂ (980,D); 965.8 [@] ; [985.9]
v₇ (1460,C)	v₁₈ (201,E)^{§torsion}	v₂₆ (1460,C)	v ₃₃ (955,C); 956.5 [@] ; [957]
v₈ (1450,D)	v ₁₉ (101,E) ^{§torsion} ; [116][@]		v ₃₄ (747,C); 747.2 [@] ; [747.4]
v₉ (1380,C)			v ₃₅ (469, D); [429.2][@]
v₁₀ (1350,C)			v₃₆ (197, E)^{§torsion}
v₁₁ (1281,C)			

Figure 3.5: Band centers (cm⁻¹) of the *n*-C₄H₁₀ fundamentals grouped by their vibrational symmetries. The bands in bold in the 660–1560 cm⁻¹ region are the ones we adopted for the vibrational partition function calculations in this work, toward the calculation of the *n*-butane pseudoline list, which will be described later on in this Chapter. The band centers in parenthesis are model predictions by Shimanouchi (1972) [110] with uncertainty codes being A(0–1 cm⁻¹), B(1 – 3 cm⁻¹), C(3 – 6 cm⁻¹), D(6 – 15 cm⁻¹), E(15 – 30 cm⁻¹). [§]Infrared inactive. [&]Torsional bands. [@]Experimental values reported by Murphy et al. (1991) [111]. The values in square brackets are the newly suggested band centers based on the observed spectra from our study. This table was adapted from Table 3 of our paper on this work, Sung et al. (2020) [112].

A few examples of transmission spectra that were collected are displayed in Figure 3.6, showing various absorption band features from both conformers. For the purposes of detecting this molecule in remote sensing observations, it is worth observing here that *n*-butane has particularly strong transitions near 1466 cm⁻¹ (6.8 μm), which are ~ 5 cm⁻¹ lower in wavenumber than the originally predicted values; these bands may be covered by the Cassini/CIRS and or upcoming JWST/MIRI observations.

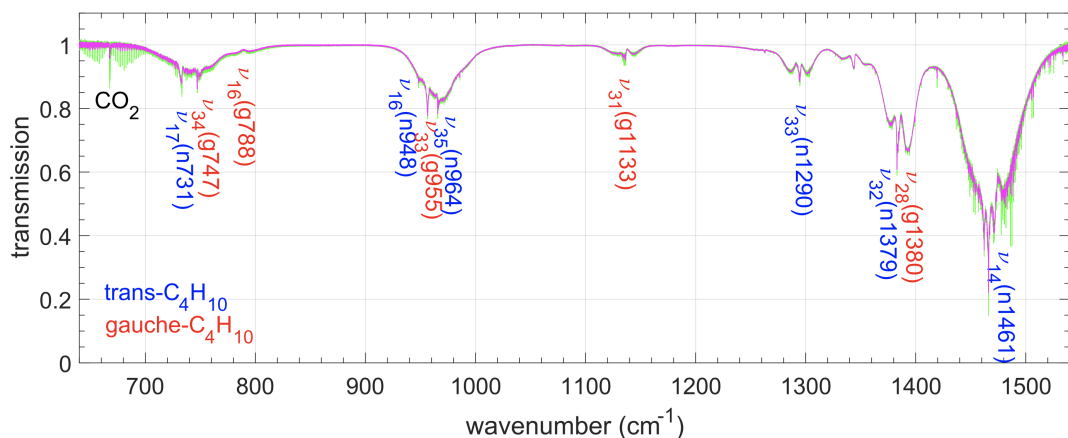


Figure 3.6: Samples of pure (green curve) and N_2 -mixture spectra (in magenta) of n - C_4H_{10} obtained at 278 K. A few representative band centers from both the *trans* and *gauche* conformers have been identified with the help of model predictions (though the values labeled here are our *updated* values, as listed in Figure 3.5. For example, ν_{17} (labeled n731) reads as ν_{17} band of *trans* butane conformer, and it is centered at 731 cm^{-1} . Note that the features near 667 cm^{-1} are contamination from the CO_2 (ν_2), as marked in the figure. This CO_2 contamination is described more thoroughly later in this Chapter. This figure has been adapted from Figure 2 of our publication on this work, Sung et al. (2020)[112].

It is worth noting here that this spectral region is home to the characteristic hydrocarbon band features that are indicative of the CH_3 rocking, deformation, and scissoring modes. For this reason, n -butane is not the only Titan hydrocarbon that is spectroscopically active in this spectral region. Some specific and important interferences with n -butane include C_2H_6 (ν_6) at 1379.2 cm^{-1} near the n -butane ν_{32} band, C_2H_6 (ν_8) at 1468 cm^{-1} and (ν_{11}) at 1469 cm^{-1} near the n -butane ν_{14} , ν_{30} , and ν_{31} bands, and C_3H_8 (ν_5) at 1462 cm^{-1} and (ν_{17}) at 1464 cm^{-1} near the n -butane ν_{14} , ν_{30} , and ν_{31} bands [88; 84]. Finally, CH_3CN , which has also been detected [113], has its strongest absorption bands around 1400 cm^{-1} . Such interferences must be pointed out, for, if not properly attributed, the features of n -butane emissions in Titan observations may be misinterpreted as contributions

coming from other molecules, or the other way around. Therefore, high-resolution spectroscopy of *n*-butane at Titan-relevant temperatures and pressures will facilitate much more accurate interpretations of the CIRS observations, in addition to any future observations of Titan that we are fortunate enough to be able to characterize.

3.4.2 Experimental Conditions

For our spectroscopic characterization of *n*-butane in the mid-infrared, 28 pure and N₂-mixture spectra were collected at JPL. This was done at Titan-appropriate conditions between temperatures of 298 K and 180 K in increments of about 25 K, using the Bruker IFS-125 HR Fourier-transform infrared spectrometer described earlier in this chapter (Figure 3.1). As a reference point, Titan’s *surface* temperature (~ 93 K [23]) is actually much lower than the lowest temperature of the range we explored here. Unfortunately, though the instrument and the gas cell are capable of *reaching* those lower temperatures, it was unwise to do so in this case, as *n*-butane’s saturation vapor pressure would be exceeded at those lower temperatures, causing it to condense within the gas cell. These issues and their implications will be described much more thoroughly in the following section on the largely similar work with *trans*-2-butene, for which the same problem was present. Additionally, this issue is also discussed in Chapter 4 where it is identified as a potential limitation in the atmospheric modeling analysis which utilizes these *n*-C₄H₁₀ results.

Returning for now to a description of the experiment itself, the *n*-butane sample, which was purchased from Sigma Aldrich Incorporated, was stated as high-purity of $\geq 99\%$ *n*-butane. We employed the same cold copper gas cell [114] that

has been used multiple times in the past for previous work on Titan’s other hydrocarbons by the JPL Molecular Spectroscopy laboratory, such as propane (C_3H_8) [88], and propene (C_3H_6) [90]. The cell is bracketed by a pair of wedged ZnSe windows and housed in a separate vacuum shroud with KBr windows, which protects the cell windows from collecting cryodeposits at cold temperatures. The temperature of the gas cell was regulated via a closed-cycle helium-cooled refrigerator and a heater attached to the body of the cell. A pair of silicon-diode temperature sensors were also attached to the cell body: the first of these is close to a heat reservoir connected to the cold finger of the gas cell to provide a temperature control feedback loop, and the other is attached to the cell body farthest away from the heater, to be used as an indicator of gas sample temperature. Excellent temperature regulation was observed during our study; typically, stability was better than 0.1 K over several days during the data acquisition period.

Table 3.1 summarizes the configuration parameters for the interferometer, a Bruker 125HR, which was configured with a Globar infrared source, a KBr beam splitter, and a liquid N_2 -cooled MCT (Mercury Cadmium Telluride) detector. Maximum optical path differences of 128.6, 64.3, and 8.04 cm were used, providing unapodized spectral resolutions of 0.0039, 0.008, 0.062 cm^{-1} . We used an optical filter which encompasses the 650-1550 cm^{-1} region in order to obtain the desired bandpass. The aperture diameter was set to 2.0 mm for all spectra that we collected. The entire path of the optical beam through the Bruker FT-IR chambers was evacuated to pressure of less than 10 mTorr (1.33 Pa) during the data acquisition.

Table 3.1: Configuration of Bruker instrument during $n\text{-C}_4\text{H}_{10}$ data acquisition.

Spectral Region	650-1550 cm^{-1}
No. of spectra	28 (11 pure, 17 N_2 -mixed)
IR source	Globar
Beam splitter	KBr
Resolution	0.0039, 0.008, 0.06 cm^{-1}
Aperture (diameter)	2.0 mm
Cell length	20.38 cm
Windows (wedged)	ZnSe (cell); Kbr (vacuum shroud)
Detectors	HgCdTe (liquid- N_2 -cooled)
Sample and purity	$n\text{-C}_4\text{H}_{10}$ (99%), N_2 (99.99999%)
FTS pressure	<10 mTorr (including residual H_2O)

We monitored sample pressures continually using three sets of MKS Baratron transducers with 0-10, 0-100, and 0-1000 Torr (0-13.33, 0-133.32, 1333.22 HPa) pressure ranges. We selected a variety of total pressures and sample volume mixing ratios in order to obtain sufficient optical depth for the respective experimental conditions, which are summarized in Figure 3.7. Pure sample spectra were collected at a given temperature, and then mixture spectra were obtained after subsequent insertion of N_2 , which was executed by a standard procedure designed to minimize uncertainty in the sample partial pressure: the sample inlet tube was first evacu-

ated up to the shut-off valve of the gas cell after each insertion of pure sample. For preparation of admixtures, before adding N₂ to the cell, we pressurized the sample line with N₂ up to the gas cell shut-off valve, effectively preventing any possible back-flow of the *n*-butane already present in the gas cell. Partial pressure of the *n*-butane sample was obtained from the initial pressure measurement of the pure *n*-butane sample for the ensuing admixture spectra.

The range of temperatures explored in this study (180 - 297 K) was selected to provide a broad range appropriate to remote sensing within the atmospheres of both Titan and Earth. Additionally, this temperature range was used to ensure proper sample pressures producing sufficient optical density, without any significant part of the measured absorption features becoming saturated.

3.4.3 Cross-Section Measurements

After the spectra were collected, we then calculated absorption cross-sections. This is straightforward using Beer’s Law (Equation 3.2), as discussed in Section 3.3. Solving that relation for the cross-section σ_ν , we get

$$\sigma_\nu = -\frac{1}{n\xi L} \log(\tau), \quad (3.10)$$

where τ is the observed transmission spectrum, n is the number density of gas in the cell, ξ is the mixing ratio of the sample gas (*n*-butane in this case) and L is the path length of the cell ($L = 20.38$ cm for the cold copper gas cell used here).

We measured cold cross-sections for the four spectral regions defined in Table 3.2. Those regions were defined this way as they then do well to isolate individual vibrational bands or groups of bands from the neighboring ones. The cross-section

Spectra	650–1550 cm ⁻¹			Resolution (cm ⁻¹)
	T (K)	P _s (Torr)	P _t (Torr)	
Pure sample spectra				
B0174.1a	295.5(3)	13.26(5)		0.0039
B0174.1b	295.2(3)	21.90(2)		0.0039
B0174.6a	298.0(3)	19.75(3)		0.062
B0174.2a	278.0(1)	16.35(3)		0.0039
B0174.2d	278.0(1)	22.35(9)		0.0039
B0174.7a	278.1(1)	19.27(1)		0.0039
B0174.3a	249.8(1)	11.20(5)		0.0039
B0174.4a	225.1(1)	6.50(1)		0.0039
B0117.5a	199.8(1)	1.07(3)		0.0039
B0182.1a	200.0(1)	5.04(1)		0.0039
B0182.2a	180.0(1)	1.00(1)		0.0039
N₂-broadened spectra				
B0174.1c	295.8(5)	21.90(2)	122.4(1)	0.0078
B0174.1d	295.0(5)	21.90(2)	242.5(3)	0.0078
B0174.1e	295.6(5)	5.91(1)	65.4(2)	0.0039
B0174.6b	298.0(5)	19.75(1)	798.0(1)	0.062
B0174.2b	278.0(1)	16.35(3)	184.4(2)	0.0078
B0174.2c	278.0(1)	16.35(3)	758.5(5)	0.062
B0174.2e	278.0(1)	22.35(9)	99.8(1)	0.0078
B0174.7b	278.1(1)	19.27(1)	155.2(1)	0.0039
B0174.7c	278.1(1)	19.27(1)	750.0(1)	0.062
B0174.7d	278.1(1)	19.27(1)	750.0(1)	0.062
B0174.3b	249.8(1)	11.20(5)	93.0(5)	0.0078
B0174.3c	249.8(1)	11.20(5)	262.8(2)	0.0078
B0174.4b	225.1(1)	6.50(1)	134.9(1)	0.0078
B0174.4c	225.1(1)	6.50(1)	319.4(2)	0.062
B0174.5b	199.8(1)	1.07(3)	110.5(2)	0.0078
B0181.1b	200.0(1)	5.04(1)	97.3(1)	0.0056
B0181.1c	200.0(1)	5.04(1)	299.7(1)	0.0056

Figure 3.7: Experimental conditions for each of the 28 spectra collected for our study for *n*-butane. The ‘B0174’ spectral labeling is a convention of the JPL Molecular Spectroscopy Laboratory. P_s and P_t refer to the sample pressure (*n*-butane) and total pressure (*n*-butane+N₂).

measurements which we report do compensate for the 99% purity assay of the *n*-butane sample. However, we made no attempt to actually discriminate between the contributions from *n*-butane’s two conformers, both of which are expected to be present and in abundances which vary as a function of temperature.

Table 3.2: Spectral regions defined for our study of *n*-butane. The bands of either *n*-butane conformer in each of the four regions are also identified.

Region	Coverage (cm^{-1})	Bands from <i>trans</i> conformer	Bands from <i>gauche</i> conformer
I	660 - 680 cm^{-1}	ν_{17}	ν_{34}, ν_{16}
II	860 - 1060 cm^{-1}	ν_{16}, ν_{35}	$\nu_{33}, \nu_{32}, \nu_{14}$
III	1060 - 1200 cm^{-1}	(none)	ν_{31}
IV	1200 - 1538 cm^{-1}	$\nu_{33}, \nu_{32}, \nu_{14}, \nu_{30}, \nu_{31}$	ν_{28}

A small sample of the measured cross-sections for *n*-butane, in two different regions, is shown in Figure 3.8. Pure *n*-butane cross-sections are shown in red, whereas N_2 -broadened cross-sections are shown in cyan. Additionally, for purposes of comparison, we also display the PNNL cross-sections for *n*-butane at room temperature in this region in purple [115].

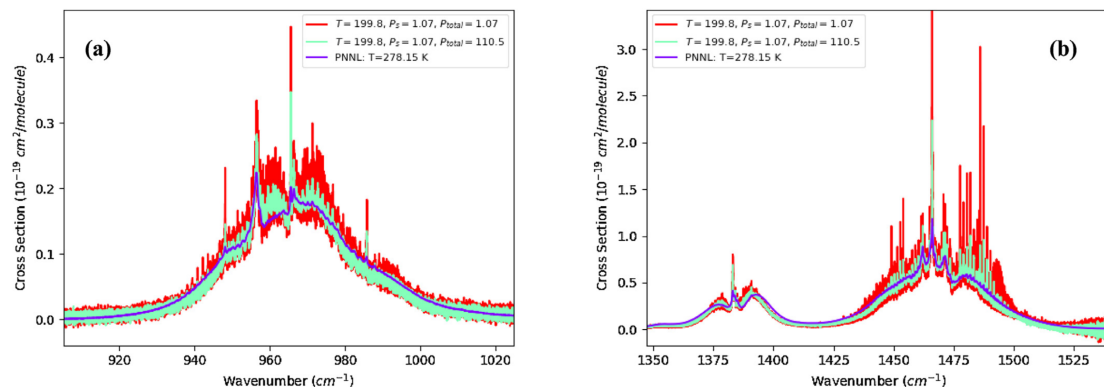


Figure 3.8: Samples of absorption cross-sections for *n*-butane.

3.4.4 Pseudoline List Generation

Going one step beyond the measurement of absorption cross-sections, part of the scope of our $n\text{-C}_4\text{H}_{10}$ work was to actually derive a pseudoline list for this particular molecule. For the reader unfamiliar with *pseudoline* lists, see Toon et al. (1992) [76], where the term/concept originated, or Toon et al. (1999) [116] for a slightly more recent example. For examples of the derivation of pseudoline lists and their use in very similar contexts to what will be described with respect to our n -butane work, see Sung et al. (2013) [88], and or Sung et al. (2018) [90]. A detailed description of the method and the features that make it so useful is provided now.

Pseudoline is effectively a way of generating an empirical model of an *actual* spectral line list. This is accomplished by adopting an evenly spaced wavenumber grid, and assuming that each point on that spectral grid can be modeled by a mean absorption coefficient. Further, it is assumed that this mean absorption coefficient can be modeled by a finite set of ‘effective’ line parameters, such as the line intensity S and lower state energy E'' , which can be derived from laboratory spectra. The intensity of a line (see also Section 3.5.4) quantifies how strongly absorbing the molecule is for photons of that particular energy, whereas the lower state energy quantifies the initial energy state of the molecule before the photon of that energy is absorbed.

In the pseudoline method, a valid molecular lineshape profile is adopted, that being the Voigt profile, which is a convolution of a Gaussian and a Lorentzian (Figure 3.9). The Gaussian component of this lineshape allows Doppler (temperature) broadening of spectral lines to be modeled, whereas the Lorentzian component allows pressure broadening to be incorporated. The larger the range of pressures and temperatures across which the laboratory spectra are collected, the more robust

and flexibly applicable to a variety of planetary atmospheres the pseudoline list will be.

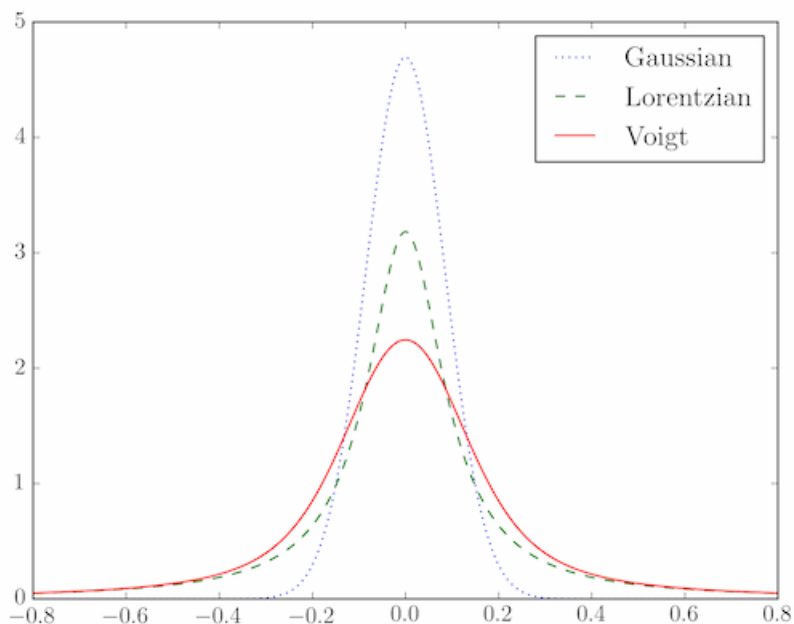


Figure 3.9: The Voigt profile, a valid lineshape for modeling both the temperature *and* pressure broadening aspects of spectral lines. This is the form that is adopted for each spectral line in a pseudoline list. Figure adapted from Scipy main website [117].

A more ‘layperson-friendly’ description of the pseudoline method goes as follows: we assume that the molecule’s spectrum can be represented by a grid of evenly spaced spectral pseudo“lines” which may or may not actually exist in reality. Obviously, the molecule’s spectrum is most certainly *not* a set of evenly spaced spectral lines in the wavenumber domain. No matter what grid we adopt, there are bound to be some wavenumber points on the grid (i.e. specific energies) where no quantum mechanical transitions are permitted, and thus, no spectral lines would be found in the actual spectrum. We control for this by allowing the

Voigt profile for our pseudo“lines” to go to zero, in those instances, as dictated by the pseudoline parameters retrieved for that particular grid point.

The pseudoline approach yields a number of advantages over measurement of absorption cross-sections alone at discrete temperatures and pressures. As a pseudoline list is ultimately derived by fitting numerous spectra and using a physical model of line shape (i.e. the Voigt profile) and instrumental line shape function, the pseudoline parameters which result are thus independent of the instrument which collected them and the spectral resolution at which they were collected. Moreover, the spectral features which are understood to be coming from impurities (such as CO₂ and H₂O, in the case of both molecules that were characterized for this dissertation) may actually be modeled during the fitting of the spectra, allowing the resulting pseudoline list to be free of those impurities.

Another advantage is that the resulting pseudoline list is automatically compiled into a HITRAN-formated linelist [118], which can be readily implemented into existing radiative transfer codes. The final advantage is that since the pseudoline list was derived using spectra over a range of temperatures and pressures, it can be used to calculate cross-sections for the molecule anywhere in that range of temperature and pressures. Note that the reverse is not true: one cannot necessarily go from absorption cross-section measurements to a pseudoline list without additional input. All 28 of the *n*-butane spectra were fit simultaneously in order to derive the pseudoline list, which adopted a wavenumber grid with spacing of 0.005 cm⁻¹, selected in consideration of the resolving of the sharpest *n*-butane features that were seen in the spectra, but also in consideration of computation expense.

A crucial part of this fitting process is the availability of prior measurements of vibrational and torsional band centers, which go into an approximation of the

partition function for the molecule. As canonically defined, the partition function (Z) characterizes the way that energy of a system is distributed across the various states (E_i) that the system can be found in, as a function of temperature T :

$$Z = \sum_i \exp\left(\frac{-E_i}{kT}\right). \quad (3.11)$$

An approximation of the partition function of the molecule is required in order to compute the lower state energy (E'') at any point along the pseudoline grid. The pseudoline intensities are first determined at the reference temperature of $T_0=296$ K, and then these are used in the determination of the lower state energies, via

$$\frac{S(T)}{S(T_0)} = \frac{Q_t(T_0)}{Q_t(T)} \frac{\exp\left(\frac{-c_2 E''}{T}\right) 1 - \exp\left(\frac{-c_2 \nu}{T}\right)}{\exp\left(\frac{-c_2 E''}{T_0}\right) 1 - \exp\left(\frac{-c_2 \nu}{T_0}\right)}, \quad c_2 = 1.4388 \text{ cm K}^{-1}. \quad (3.12)$$

Note that in the above, c_2 is called the “second Boltzmann constant”, and arises often in the general field of spectroscopy [95]. Q_t is the total partition function of n -butane, which is the product of the vibrational and rotation partition functions,

$$Q_t = Q_{vib} \times Q_{rot}. \quad (3.13)$$

To tackle the vibrational contribution, we utilized the harmonic oscillator approximation, expressed by

$$Q_\nu(T) = \prod_n \left[\frac{1}{1 - \exp\left(\frac{-c_2 E_{\nu,n}}{T}\right)} \right]^{dgn}, \quad (3.14)$$

where for n -butane, the index n runs from 1 to 36, covering the 36 vibrational modes discussed in Section 3.4.1 and tabulated in Figure 3.8. The exponent dgn ,

which stands for degeneracy, is unity for each of the 36 vibrational modes for *n*-butane.

Note that we include in our calculation of the vibrational partition function the three torsional modes available to *n*-butane ($\nu_{18}, \nu_{19}, \nu_{36}$). This is important to mention, as, because these torsional modes are much lower in energy than the other vibrational modes, and due to the dependence on that energy in Equation 3.14 above, they form a dominant contribution to the partition function of *n*-butane. Unfortunately, as these torsional modes are outside of the mid-infrared spectral range that was accessible to us (they lie in the approximate range of 100-225 cm^{-1} for both conformers), we were unable to improve the existing constraints on the band centers for those modes. It is worth specifically pointing this out because those band centers presently carry the largest uncertainties, by far, as reported by Shimanouchi et al. (1972) [110], and thus, we were forced to adopt those large uncertainties ($\pm 15\text{-}30 \text{ cm}^{-1}$) in our partition function calculation for the *n*-butane pseudoline list: this represents one of the more prominent sources of uncertainty that we report in our results in Sung et al. (2020) [112].

A further complication for *n*-butane is the simultaneous existence of the two conformers (also discussed in Section 3.4.1), *gauche* and *trans*. The vibrational partition function of each must be computed separately. Once computed, the two of them are then combined [119] via

$$Q_{vib} = \frac{Q_{vib,trans} + K \times Q_{vib,gauche}}{1 + K}, \quad (3.15)$$

$$\text{where } K = \exp\left(\frac{-\Delta G}{RT}\right), \quad \Delta G = 0.9 - TR \log 2, \quad (3.16)$$

where in the final equality, the 0.9 is understood to carry dimensions of energy.

The rotational contribution to the partition function is then approximated via

$$\frac{Q_{rot}(T)}{Q_{rot}(T_0)} = \left(\frac{T}{T_0}\right)^\beta. \quad (3.17)$$

In the above, β takes the value of unity for diatomics, 1.5 for polyatomics which lack torsional modes, and 2.0 for polyatomic molecules which do exhibit torsional modes, such as is the case with *n*-butane: thus, we adopted $\beta = 2.0$ for this calculation [112].

The pseudoline list endeavor for *n*-butane was quite successful. In Figure 3.10, the fitting residuals (i.e. the pseudoline list’s ability to fit just a subset of the full 28 initial spectra from which they were generated, as a function of temperature) are shown for four representative regions, which were defined in Table 3.2. Excellent agreement, to within 2% is observed in the first three regions in panels (a) through (c), whereas agreement to within 4% is seen in the final region in panel (d), which contains *n*-butane’s strong ν_{14} band, among others. It is worth noting here that the ν_2 band of CO₂, seen near 667 cm⁻¹ in panel (a), was fitted out during the derivation of the pseudoline list, leaving essentially no contamination from CO₂.

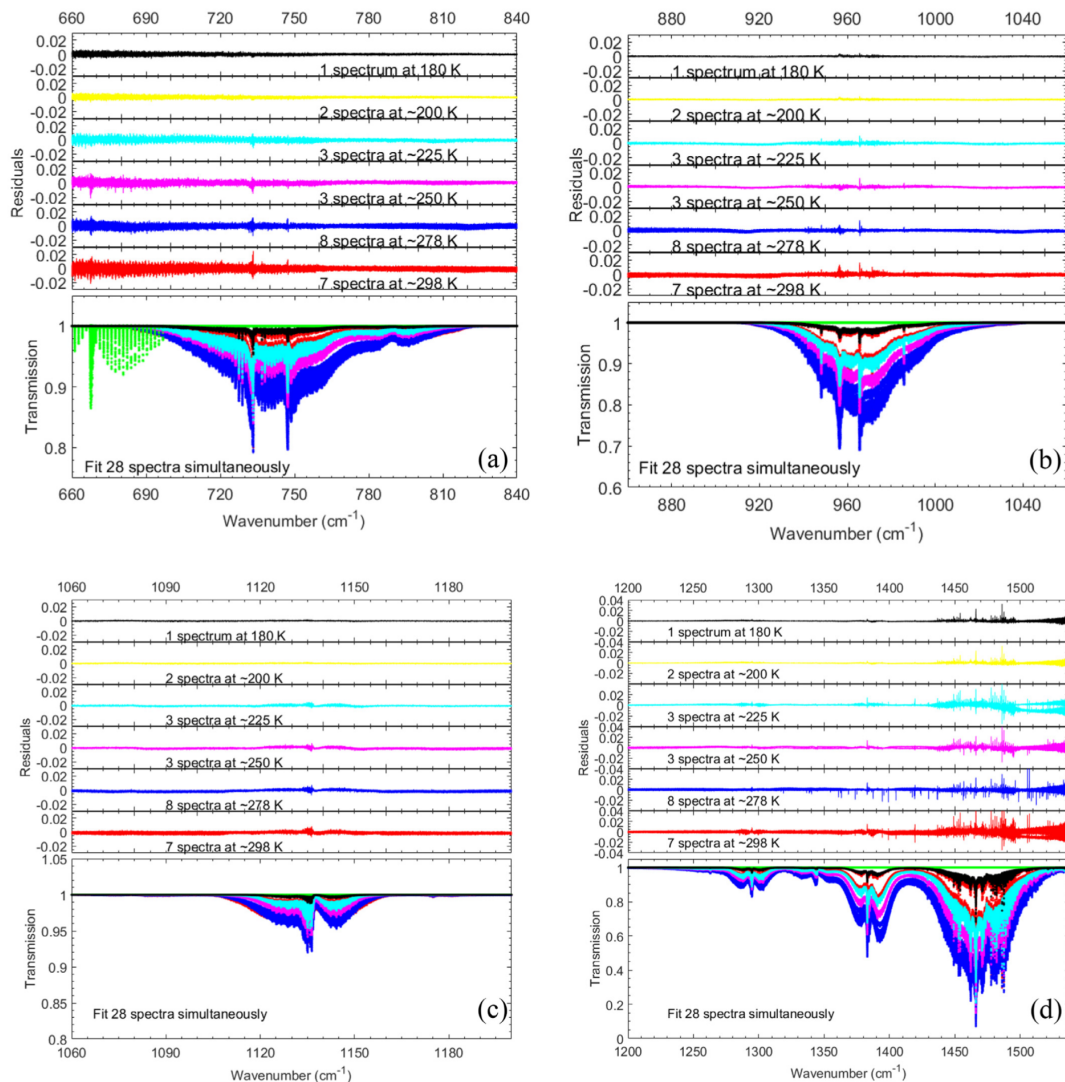
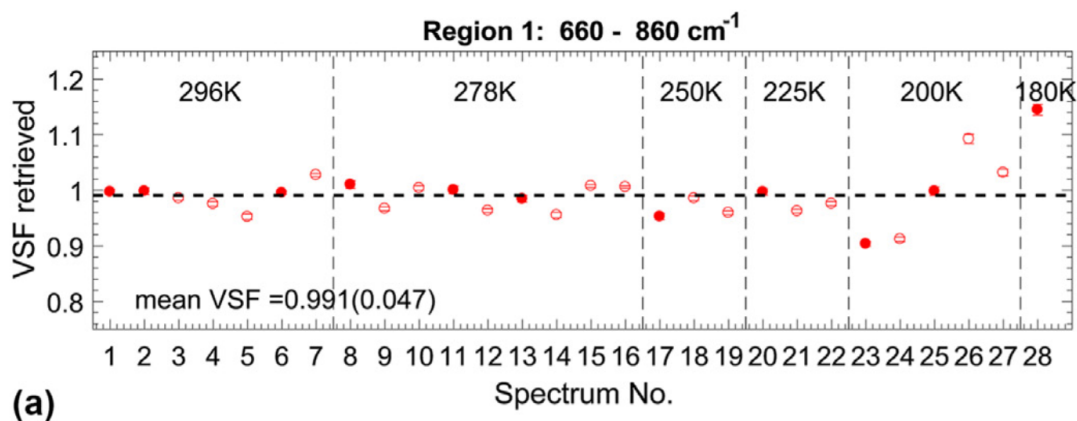


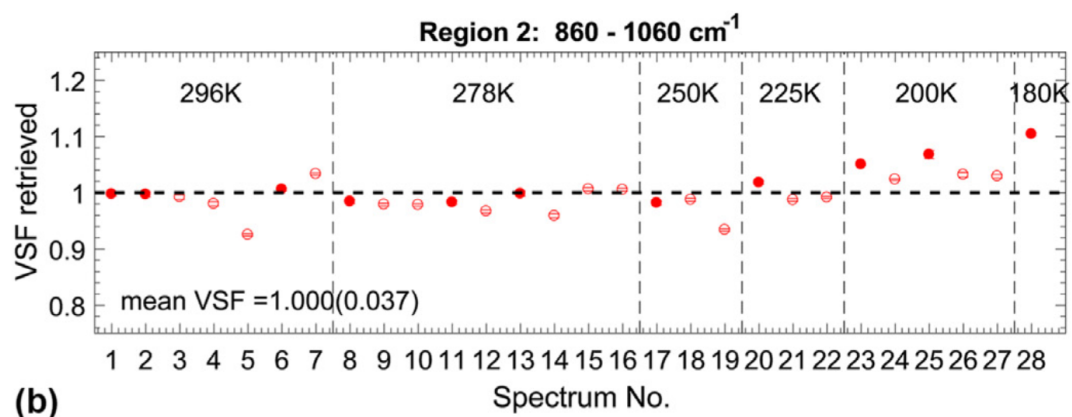
Figure 3.10: Demonstration of the pseudoline list’s ability to model *n*-butane at a variety of temperatures and pressures. Each panel (a)-(d), corresponding to Regions I-IV, as defined in Table 3.2, shows the fitting residuals from the *n*-butane pseudoline list. The bottom portion of each panel shows the synthetic spectra generated from the pseudoline list, and the upper portions show the fitting residuals for various subsets of the 28 spectra we collected, as a function of temperature. Agreement to within better than 2% is seen in the first three regions, i.e. panels (a), (b), and (c), and to within 4% in the final region, in panel (d).

In the case of Region 4, panel (d), where slightly higher fitting residuals of around 4% are observed, the 0.005 cm^{-1} wavenumber grid that we adopted in

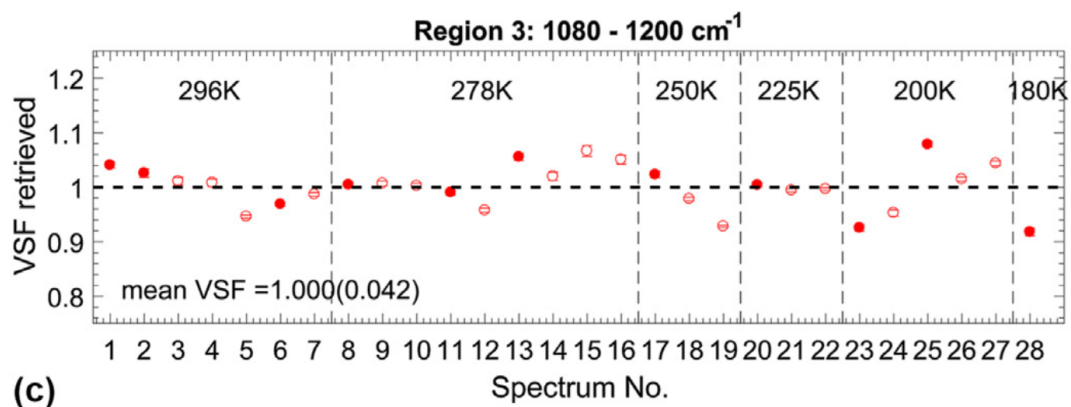
the pseudoline derivation likely did not fully resolve the finer structure of the Q-branch transitions that were observed in that region, particularly in the low-pressure conditions. Additionally, a good portion of the persistent residuals belong to water transitions, rather than unaccounted-for features of *n*-butane. Those water features arise from residual water in the evacuated instrument chamber. The component we see here, which has survived our ratioing process, was later successfully fitted out during the multispectrum fitting.

A final test on the reliability of the pseudoline list involves fitting each of the 28 *n*-butane spectra individually. In doing so, we attempt to ‘retrieve’ the amount of *n*-butane required in order to successfully fit the spectrum, and report the amount needed in terms of a volume-scaling factor (VSF), with respect to the original partial pressure measurement of *n*-butane for that particular spectrum upon its collection (Figure 3.11). Ideally, each of these VSFs would come out to unity. Naturally, however, there is some deviation from unity for all spectra, and these deviations can be interpreted as a measure of the uncertainty of the pseudoline list.





(b)



(c)

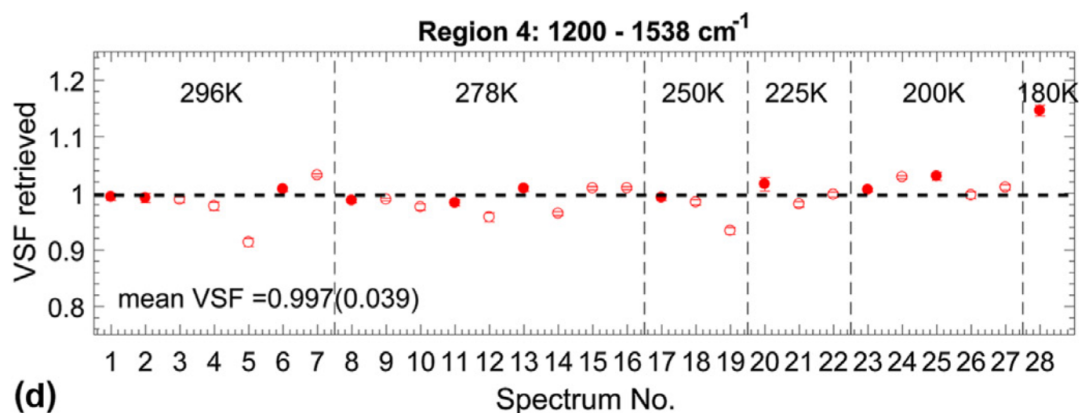


Figure 3.11: Panels (a) through (d) show the retrieved volume scale factors (VSFs) for the individual pure (solid circles) and mixture (open circles) laboratory spectra that we collected. The mean VSFs were found to be 0.991, 1.000, 1.000, and 0.997 for Regions I-IV, respectively, with standard deviations of less than 4.7, 3.7, 3.4, and 3.9 %; these can be interpreted as measurement uncertainties associated with the pseudolines.

We obtained integrated intensity measurements for *n*-butane by simply summing up the pseudoline intensities across each of the four spectral regions defined in Table 3.2. It is expected that these integrated intensities (which, once again, are *fundamental to the molecule, not the experimental conditions*) are independent of temperature, as suggested by Crawford et al. (1958) [120], Breeze et al. (1965) [121], and Sams et al. (2005) [122]. This can be seen both in Table 3.3, and is also clear to within a reasonable tolerance in Figure 3.12.

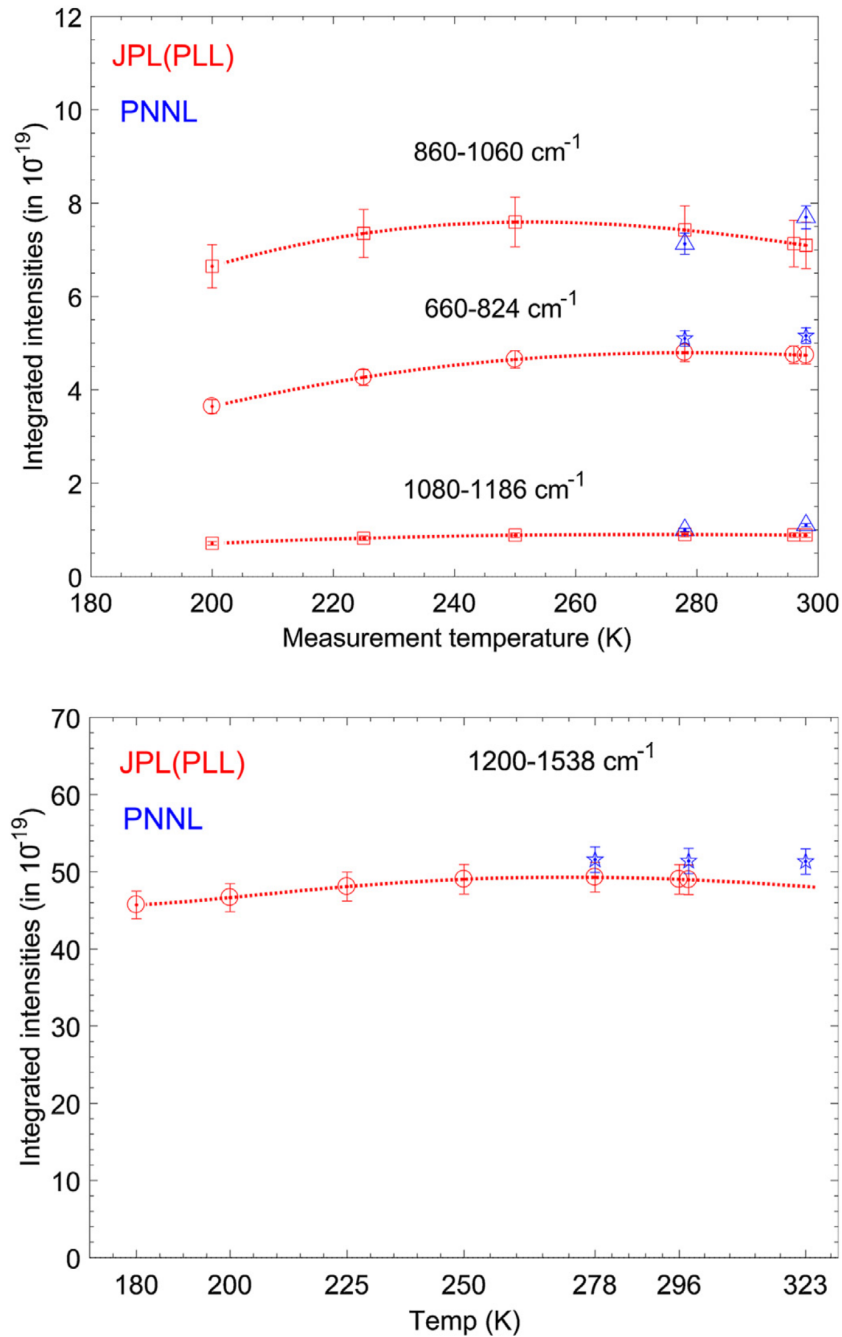


Figure 3.12: Graphical comparison of our room temperature integrated *n*-butane intensity measurements (red curves) compared to those of PNNL (blue points) [115]. The top panel shows results for Regions I, II, and III, and Region IV's results are contained in the bottom panel. It can be seen that in general, good agreement between our results and those of PNNL is observed. Additionally, minimal temperature dependence is seen to the integrated cross-section measurements, as expected [120; 121; 122].

The pseudoline list that we derived from this work has been compiled and stored online, freely accessible to any interested in implementing it in radiative transfer calculations. For the interested reader, the *n*-butane pseudoline list (and other pseudoline results from the JPL Molecular Spectroscopy Laboratory) can be found via the following link: <https://mark4sun.jpl.nasa.gov/pseudo.html>. Additionally, the full cold cross-section measurements have been submitted to the HITRAN database [118] and are also available for public use.

MMI	freq(cm ⁻¹)	S(296 K)	N2 Self--E''	n--shift
770	965.540000	8.582E-23	0.000E+00.1200.2000	690.06600.72--0.003000
770	965.545000	8.713E-23	0.000E+00.1200.2000	588.46200.72--0.003000
770	965.550000	9.356E-23	0.000E+00.1200.2000	668.97150.72--0.003000
770	965.555000	9.024E-23	0.000E+00.1200.2000	659.60710.72--0.003000
770	965.560000	8.389E-23	0.000E+00.1200.2000	575.10120.72--0.003000
770	965.565000	8.919E-23	0.000E+00.1200.2000	715.02740.72--0.003000
770	965.570000	8.795E-23	0.000E+00.1200.2000	653.25630.72--0.003000
770	965.575000	9.191E-23	0.000E+00.1200.2000	685.03610.72--0.003000
770	965.580000	9.234E-23	0.000E+00.1200.2000	680.54050.72--0.003000
770	965.585000	8.959E-23	0.000E+00.1200.2000	594.73470.72--0.003000
770	965.590000	9.386E-23	0.000E+00.1200.2000	616.09900.72--0.003000
770	965.595000	9.239E-23	0.000E+00.1200.2000	539.73610.72--0.003000
770	965.600000	1.129E-22	0.000E+00.1200.2000	807.39280.72--0.003000
770	965.605000	9.697E-23	0.000E+00.1200.2000	467.20030.72--0.003000
770	965.610000	1.119E-22	0.000E+00.1200.2000	571.36150.72--0.003000
770	965.615000	1.072E-22	0.000E+00.1200.2000	538.32240.72--0.003000
770	965.620000	1.040E-22	0.000E+00.1200.2000	546.64760.72--0.003000
770	965.625000	1.044E-22	0.000E+00.1200.2000	534.95400.72--0.003000
770	965.630000	1.111E-22	0.000E+00.1200.2000	626.76720.72--0.003000
770	965.635000	1.154E-22	0.000E+00.1200.2000	633.26460.72--0.003000
770	965.640000	9.636E-23	0.000E+00.1200.2000	388.57240.72--0.003000
770	965.645000	1.067E-22	0.000E+00.1200.2000	554.15800.72--0.003000
770	965.650000	1.122E-22	0.000E+00.1200.2000	623.21940.72--0.003000
770	965.655000	1.077E-22	0.000E+00.1200.2000	577.92590.72--0.003000
770	965.660000	1.022E-22	0.000E+00.1200.2000	570.75240.72--0.003000
770	965.665000	1.055E-22	0.000E+00.1200.2000	632.40400.72--0.003000

Figure 3.13: Exerpt from the HITRAN-formatted pseudoline list for *n*-butane produced by this work.

3.4.5 Results and Discussion

As the lower state energies have been empirically derived for each of the individual pseudolines, the pseudoline intensities can be obtained at any temperature within the range of our initial measurements (180-298 K) via Equation 3.12. We calculated integrated intensities using the pseudolines by integrating them over the four wavenumber regions defined in Table 3.2; these integrated intensities are compared with those of PNNL in Table 3.3 and were displayed graphically in Figure 3.12.

Table 3.3: Integrated intensity in $10^{-19} \text{ cm}^{-1}/ (\text{molecule}\cdot\text{cm}^{-2})$ of *n*-butane, normalized to a 100% purity sample, for each of the four regions, as a function of temperature. In the case of our room temperature results, we are able to compare to results from PNNL (shown in the bottom two rows), with which we find good agreement [115]. A graphical comparison between our room temperature results and those of PNNL is presented in Figure 3.12.

T(K)	Region I	Region II	Region III	Region IV
298	5.06(28)	7.16(26)	0.91(4)	48.96(20)
296	5.06(28)	7.18(27)	0.91(4)	49.01(20)
278	5.08(28)	7.30(27)	0.86(4)	49.28(20)
250	5.06(28)	7.41(27)	0.77(3)	49.02(20)
225	4.99(28)	7.39(27)	0.69(3)	48.07(19)
200	4.94(28)	7.29(27)	0.60(3)	46.65(19)
180	4.97(28)	7.22(27)	0.55(3)	45.71(18)
PNNL 298	5.16	7.70	1.1	51.4
PNNL 278	5.10	7.73	1.0	51.6

In Region I (spanning $660\text{-}860 \text{ cm}^{-1}$), the ν_{17} band (732 cm^{-1}) from the *trans* conformer and the ν_{34} (747.4 cm^{-1}) from the *gauche* conformer are the two main

opacity sources. Our measurements in this region are observed to be in excellent agreement with PNNL in this region, to better than within 2% at both of the temperatures that PNNL measured at (298 and 278 K).

For Region II (spanning 880-1060 cm^{-1}), the ν_{16} and ν_{35} bands from the *trans* conformer and the ν_{33} band from the *gauche* conformer contribute to the opacity. The integrated intensities in this region are observed to be lower than those of PNNL by 5.6% and 7% at 278 K and 298K, respectively. However, considering the combined uncertainty of both results (6.9%, 3.7% from the pseudolines in this region and 3.2% reported by PNNL), the agreement is acceptable.

In Region III (which spans 1060-1200 cm^{-1}), the very weak ν_{31} band from the *gauche* conformer appears to be the only observed feature. Our integrated cross-sections show fairly strong temperature dependence in this region. While this is not obvious from Figure 3.12, it is plain to see in Table 3.3, where the integrated intensities in Region III are observed to increase by almost a factor of two as we span the temperature range from T=180 K to room temperature. The implication here is that substantial portions of the absorption in this Region are due to extremely weak but very numerous hot band features. These will tend to be suppressed as the sample is cooled down, reducing the total absorption in the Region for cooler temperatures.

Our results in this Region are lower than those of PNNL by 14% at 278 K and close to 17% at 298K. This is significantly outside the combined measurement uncertainty of 7.4% for this region. It is worth noting that the rather large drop in intensity is seen in the PNNL data for Region III as well, which decreases by about 10% between 298 K and 278 K. This is greater than the decrease that we observe for our results between those two temperatures, which is closer to 5%. The

accurate characterization of absorption bands in this region may be limited in both data sets simply due to the weakness of the opacity of the ν_{31} band.

In Region IV (spanning 1000-1538 cm^{-1}), several inseparable bands are located, including the most strong band (ν_{14} , from the *trans* isomer). In this Region, our integrated intensities are lower than the PNNL values by 4.5% and 4.7% at 278 K and 298 K, respectively. As with Region II, these discrepancies are slightly larger than the measurement uncertainties of the pseudoline list, but they are still well within the combined uncertainty (7.2%) for both results.

Summarizing, for three of the four Regions, we observe good agreement with the PNNL results for *n*-butane, whereas Region III does show an unexplained discrepancy beyond the combined uncertainty of both sets of results. Future work could potentially characterize this region more effectively by using a gas cell with substantially longer path length; this would allow a more adequate optical depth to be achieved, facilitating measurement of this weaker vibrational feature in the *n*-butane spectrum.

Our measurements are observed to be systematically lower than those of PNNL by a couple percent, though Region I's agreement is quite close. It is presently unknown exactly what has caused this discrepancy, but it is likely that imperfect knowledge of the *n*-butane partition function, as was discussed earlier, has played a major role. Another likely contributor to this discrepancy is the relative abundances of the *trans* and *gauche* conformers. These will gradually vary from 70% *trans*/30% *gauche* at room temperature to around 86% *trans*/14% *gauche* at 180 K [119]. However, it is not possible to properly take this source of uncertainty into account until each of the individual modes are distinguished for both conformers. This discrepancy concerning the two conformers was not discussed or acknowledged

in the PNNL data set, leaving a more thorough comparison with the pseudoline list results rather difficult.

Lastly, some of the rovibrational modes of *n*-butane require substantially higher spectral resolution at the lower pressures and cold temperatures that we explored in this work. Such spectral resolutions are unavailable to conventional Fourier Transform - Infrared spectrometer instruments such as the JPL Bruker. In this sense, this incomplete modeling may contribute to the observed discrepancy in addition to the other sources of uncertainty discussed previously.

3.4.6 N-Butane: Conclusion

This concludes the first half of Chapter 3, which has outlined a comprehensive infrared laboratory spectroscopic characterization of the molecule *n*-butane. This work was largely performed in support of atmospheric remote sensing of Titan from Cassini (CIRS) observations, ground-based observations (e.g. NASA IRTF), and upcoming observations from JWST (MIRI). We measured 28 pure and N₂-broadened spectra at Titan-appropriate temperatures, and from these, we derived cross-sections and a pseudoline list. The cross-sections were reported to the HITRAN database for public use, and the pseudoline list is available for download from the JPL Molecular Spectroscopy Lab's website. The pseudoline list is HITRAN-formatted, meaning it is readily implemented in existing radiative transfer calculations and codes. An additional component of this dissertation is the implementation of the *n*-butane pseudoline list in modeling of both Cassini CIRS observations and NASA IRTF/TEXES observations, which will be discussed in detail in Chapter 4. Before doing so, however, the work done with the second target molecule of this dissertation, *trans*-2-butene, will be discussed.

3.5 Trans-2-Butene (Trans-2-C₄H₈)

3.5.1 The Molecule

The second molecule characterized in this study in the infrared at JPL for the purposes of remote sensing of Titan's atmosphere, is *trans*-2-butene (*trans*-2-C₄H₈), which is depicted along with its isomers in Figure 3.14.

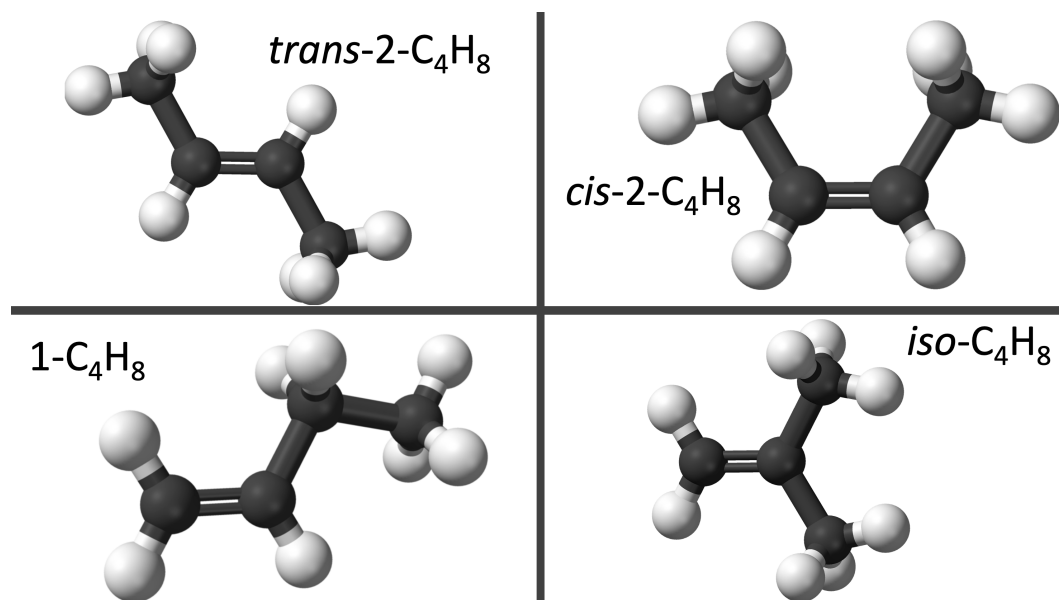


Figure 3.14: The four possible isomers of the butene molecule. The structure of *trans*-2-butene can be seen in the top left, along with 1-butene (bottom left), with the only significant difference between the two molecules being the placement of the double bond. Also shown is *cis*-2-butene (top right), the stereoisomer of *trans*-2-butene, which differs in having both of its methyl groups on the same side of the double bond. Lastly, *iso*-butene (bottom right), is the final isomer, with the fourth methyl group attached to the number 2 carbon, rather than attached to the end and forming a four-carbon-long chain. In spite of all of these rather simple differences, all four molecules are entirely distinct from one another, spectroscopically speaking, and thus they each require separate laboratory work in order to disentangle their possible contributions to remote sensing observations of planetary atmospheres.

Butene, with four carbon atoms and eight hydrogen atoms, is an unsaturated hydrocarbon called an alkene, indicating that it has a double bond in its structure.

Like *n*-butane, butene molecules have been predicted to be present in Titan's atmosphere in photochemical models since the 1980s. In spite of this, it has never been detected by any means.

Butene molecules share with *n*-butane the interesting possible connection between Titan's atmosphere and surface features, in being estimated to contribute up to 1% by volume of Titan's hydrocarbon lakes and seas [71]. As discussed earlier in Chapter 1, these long-standing liquid surface-features render Titan one of the most astrobiologically unique places in the Solar system and a compelling target for further exploration [123]. Also worth reiterating here is the fact that C₄H₈ molecules were demonstrated to be a likely product of irradiation of ethane (C₂H₆) ices in cold, Titan-like conditions [69].

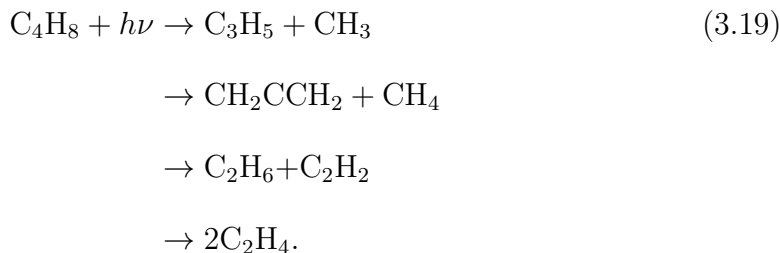
Regarding photochemical model predictions for butene abundances in Titan's atmosphere, the recent Loison et al. (2019) photochemical model [65] predicts butene abundances between 0.1 and 1 ppb in Titan's stratosphere, whereas the much earlier photochemical modeling work of Yung et al. (1984) [63] predicts a slightly larger abundance of 6.3 ppb for this molecule. A brand new study by Willacy et al. (2021) [67] has predicted a butene abundance of about 10 ppb. Butene molecules are also incorporated by the models of Krasnopolsky et al. (2009) [64] and Vuitton et al. (2009) [66], though specific stratospheric abundances predicted by these models do not seem to be reported; the latter does feature detailed chemical pathways for C₄H₈ molecules, though, which are discussed below. Note that like the case of *n*-C₄H₁₀, in spite of these relatively large trace gas abundances, which are above the Cassini CIRS sensitivity, no C₄H₈ molecule has ever been detected in Titan's atmosphere to date.

In the model of Yung et al. (1984) [63], C₄H₈ molecules are formed via the

reaction



and lost via reactions such as



In the model of Vuitton et al. (2019) [66], in addition to the reactions shown above, butene molecules are also formed via the addition of methyl and allyl radicals,



but are also lost via



It is worth stating that none of these photochemical models differentiate between the two stereoisomers (*cis* and *trans*) of 2-butene, nor from the 1-butene or *iso*-butene isomers, though each of these four molecules is spectroscopically distinct from the others and may participate in different chemistries.

A detection of any C_4H_8 molecule in Titan's atmosphere could potentially come from Cassini CIRS observations, though the spectral resolution of those observations is likely to be a hindrance. Future searches for this and other similar molecules could take place with JWST/MIRI data, which are of course not available yet. For

these reasons, the search for *trans*-2-butene in this work has taken place primarily within IRTF/TEXES data, both from legacy data (from 2010) but also in new data, the observations for which were proposed for this very purpose, and were awarded in 2021. Those observations will be discussed in Chapter 4.

With $N=12$ atoms, *trans*-2-C₄H₈ has 30 ($3N-6$) fundamental vibrational modes. Unlike the case of *n*-butane, these vibrational modes of *trans*-2-butene have been comparatively sparsely studied. Some of the locations and relative strengths of these bands were measured several decades ago by McKean et al. (1985) [124]. However, seven of *trans*-2-butene's 30 vibrational modes were not discussed at all in that study (and the authors do not remark as to why), and since then, it seems that little work has been performed to actually remeasure (or improve existing measurements of) these band centers. Those band centers were later *calculated* by Chhiba et al. (1994) [125] using the SPASIBA molecular mechanics potential, which models molecular behavior and interactions using classical mechanics and the Born-Oppenheimer approximation, treating chemical bonds as classical springs, for example [126].

The C₄H₈ isomer 1-butene (CH₂=CH-CH₂-CH₃, Figure 3.14), on the other hand, was further studied in the far infrared by Bell et al. (2000) [127], through which band centers and their associated symmetries and vibrational modes have been fairly well-established for that particular molecule. In fact, this motivated the decision to spectroscopically characterize 2-butene molecules first (beginning with the *trans* isomer), rather than 1-butene, which the JPL Molecular Spectroscopy Laboratory intends to study in the near future. The spectra and absorption cross sections obtained for *trans*-2-butene in this work can serve as a starting point for theorists intending to establish a similar tabulation of its vibrational modes as that

which has already been established for 1-butene.

3.5.2 Experimental Conditions

Unlike with the *n*-butane study, I myself led the collection of our *trans*-2-butene data, in the fall of 2021. This was done using the same instrument as before, a Bruker IFS-125 HR Fourier-transform infrared spectrometer (Figure 3.1). Our temperature range for the *trans*-2-butene study was 298 K to 160 K, in increments of about 30 K. As with the previous sample, the *trans*-2-butene sample came from Sigma Aldrich Incorporated, and arrived with a stated assay value of $\geq 99\%$ purity.

The cold copper gas cell, which has already been described thoroughly previously, was used once again for this work. As before, excellent temperature regulation was observed during the study, with stability being better than 0.1 K over periods of several days during the data acquisition period. The reader is referred back to Table 3.1 for the other relevant instrument configuration parameters, which were essentially identical to those utilized during our study of *n*-C₄H₁₀.

28 high-resolution spectra (Table 3.4) of pure *trans*-2-butene and its mixtures with N₂ were obtained. As with the *n*-butane study, during the acquisition of data, we noticed distinctive features from the ν_2 band of CO₂ near 667 cm⁻¹. Fortunately, the ν_2 band of CO₂ is highly localized and far from the vibrational features of *trans*-2-butene which were investigated. Furthermore, by simulating CO₂ spectra, we were able to estimate the amount of CO₂ contributing to each of the *trans*-2-butene spectra we collected; this process is described in more detail in Section 3.5.5.

Out of the 28 *trans*-2-butene spectra that were collected, 20 were broadened with research-grade (99.999995%) N₂ gas. The spectral resolutions used were se-

lected in consideration of several factors. In particular, Doppler widths and estimates of Lorentz widths at the given pressures and temperatures presented in Table 3.4, and the signal-to-noise ratio to be achieved, were some of the salient factors considered. As a rule of thumb, we used the lowest spectral resolution possible to enhance the spectrum quality (i.e. to increase the signal to noise ratio) which would still resolve the targeted vibrational transitions. For pure sample spectra at low pressures, however, for which the Doppler broadening is very small (and beyond the instrumental resolution of our spectrometer), we had to compromise the spectral resolution in order to achieve a reasonable level of signal-to-noise ratio, e.g. better than 100:1.

We monitored sample pressures continually using three sets of MKS Baratron transducers with 0-10, 0-100, and 0-1000 Torr (0-13.33, 0-133.32, 1333.22 HPa) pressure ranges. Pressures were observed to be very stable during the data collection process, indicative of a well-sealed system. We selected a variety of total pressures and sample volume mixing ratios in order to obtain sufficient optical depth for the respective experimental conditions, which are summarized in Table 3.4. Pure sample spectra were collected at a given temperature, and then obtained again after insertion of N₂, executed by a standard procedure designed to minimize uncertainty in the sample partial pressure: the sample inlet tube was first evacuated up to the shut-off valve of the gas cell after each insertion of pure sample. For the preparation of admixtures, before adding N₂ to the cell, we pressurized the sample line with N₂ up to the gas cell shut-off valve, effectively preventing any possible back-flow of the *trans*-2-butene already present in the gas cell. The partial pressure of the *trans*-2-butene sample was obtained from the initial pressure measurement of the pure *trans*-2-butene sample for the ensuing admixture spectra.

Table 3.4: Experimental conditions of pure and N₂-broadened *trans*-2-butene spectra. Each spectrum used a path length of $L = 20.38$ cm. The column labeled Res(B), shows the associated Bruker resolution parameter for the spectrum. The actual spectral resolution is then calculated as $\frac{5}{9} \cdot \text{Res(B)}$.

Spectrum	T (K)	P _s (Torr)	P _t (Torr)	Res(B) (cm ⁻¹)	Resolution (cm ⁻¹)
B0189.1a	297.0(1)	12.95(1)	12.95(1)	0.018	0.01
B0189.1b	297.6(1)	5.43(1)	5.43(1)	0.007	0.0039
B0189.1c	297.0(2)	5.44(1)	5.44(1)	0.018	0.01
B0189.1d	297.3(1)	5.43(1)	760.9(1)	0.112	0.062
B0189.1e	297.6(1)	5.43(1)	765.3(1)	0.100	0.056
B0189.1f	297.5(3)	7.07(1)	120.0(1)	0.0216	0.012
B0189.1g	297.9(1)	7.07(1)	234.5(2)	0.0216	0.012
B0189.2a	278.2(1)	4.00(1)	4.00(1)	0.007	0.0039
B0189.2b	278.2(1)	5.00(1)	118.5(3)	0.0216	0.012
B0189.2c	278.2(1)	4.00(1)	239.5(3)	0.0216	0.012
B0189.2d	278.2(1)	5.00(1)	763.4(1)	0.112	0.062
B0189.3a	240.1(1)	2.01(1)	2.01(1)	0.007	0.0039
B0189.3b	240.1(1)	3.03(1)	120.2(1)	0.0216	0.012
B0189.3c	240.1(1)	3.03(1)	760.6(2)	0.112	0.062
B0189.4a	210.1(1)	1.40(1)	1.40(1)	0.007	0.0039
B0189.4b	210.1(1)	1.81(1)	109.7(1)	0.0216	0.012
B0189.4c	210.1(1)	1.81(1)	759.8(1)	0.112	0.062
B0189.7a	180.0(1)	0.60(1)	0.60(1)	0.007	0.0039
B0189.7b	180.0(1)	0.59(1)	99.96(1)	0.0216	0.012
B0189.7c	180.0(1)	0.59(1)	299.6(1)	0.112	0.062
B0189.6a	160.0(1)	0.09(1)	0.09(1)	0.007	0.0039

During the addition of both sample and N_2 , the gas was fed first through a copper coil submersed in a dry ice / methanol (CH_3OH) slurry which was continuously kept at a temperature of about 245 K. This forced any water vapor sample impurity to condense out into the copper coil, rather than entering the gas cell. The contribution of water to the cross-sections that we report was negligible due to this process. Note also that the slurry temperature was kept sufficiently *warm* enough such that *trans*-2-butene sample would not also condense out (*trans*-2-butene has vapor pressure of 110 Torr at 245 K). For this, we utilized *trans*-2-butene vapor pressure data from Shimanouchi et al. (1972) [110], as well as from the National Institute of Standards and Technology [115]. The vapor pressure curve of *trans*-2-butene is plotted in Figure 3.15.

The range of temperatures explored in this study (160 - 297 K) was selected to provide a broad range appropriate to remote sensing within the atmospheres of both Titan and Earth [128; 112]. Additionally, this temperature range was used to ensure proper sample pressures producing sufficient optical density, without any significant part of the measured absorption features becoming saturated. Finally, the data provided by Shimanouchi et al. (1972) [110] and Sharpe et al. (2004) [115] also informed our decision to keep experimental temperatures *above* 160 K, even though Titan's lower atmosphere and surface temperature are substantially lower; keeping temperatures ≥ 160 K ensured that no condensation would occur inside the gas cell, eliminating a major source of uncertainty. This is described more thoroughly via Figure 3.15.

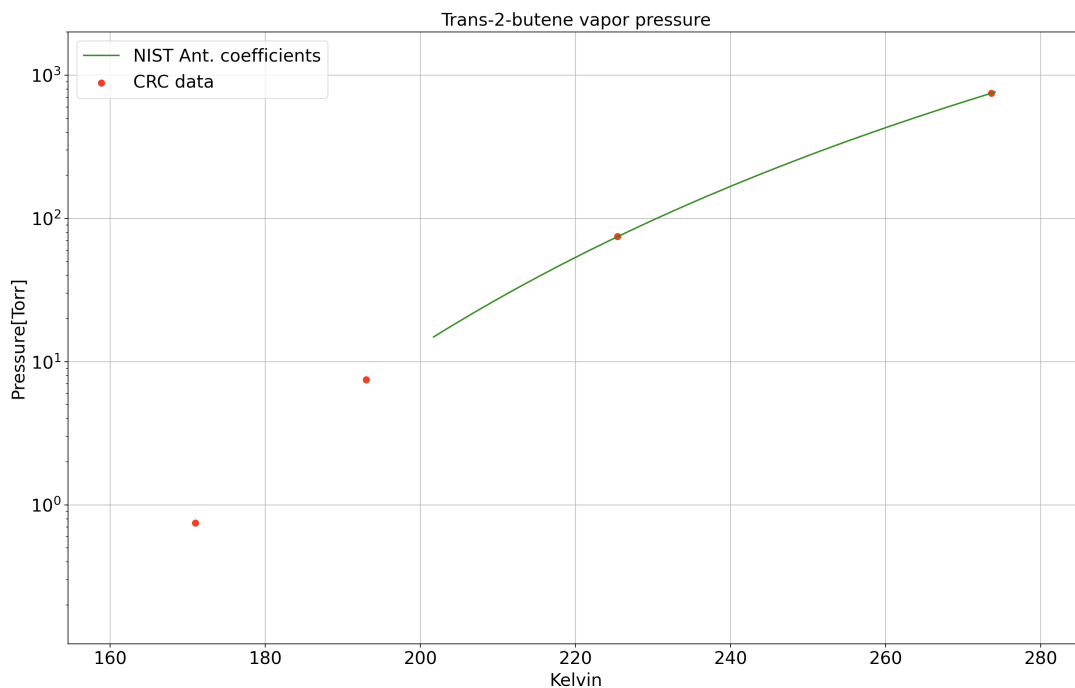


Figure 3.15: Vapor pressure curve of *trans*-2-butene, used to inform the lower bound of the temperature range that we can study this molecule in the Bruker spectrometer. Approaching temperatures low enough such that the target molecule’s vapor pressure may accidentally be exceeded (which starts to occur around 0.1 Torr) must be avoided, as this leads to condensation within the gas cell and a major delay in data collection; obviously, the condensed *trans*-2-butene ice in the gas cell changes the transmission spectra being recorded, invalidating the collection of *gaseous* spectra. Moreover, the only way to remove the condensation and resume data collection at cold temperature is to heat up the Bruker, and then cool it down again, and then pull vacuum on it, which, depending on the required temperature change, may take a full day or two. In this figure, the only available vapor pressure data for *trans*-2-butene are shown: the red points are data points from the CRC Handbook of Chemistry and Physics [129; 110], and the green curve comes from the Antoine coefficients reported by the National Institute of Standards and Technology [115].

3.5.3 Cross-Section Measurements

For our measurements of *trans*-2-butene cross-sections, we defined three spectral regions, shown in Table 3.5. Twelve of the 30 fundamental vibrational modes as

listed in McKean et al. (1985) [124] lie within the full spectral range that we studied here, which, for convenience, we have called Region 3, in Table 3.5. Of those twelve bands, we were able to identify only eight.

An example of the identification of these bands can be seen in Figure 3.16. It can be seen that *trans*-2-butene’s strongest vibrational feature in the studied region is the set of bands near 970 cm^{-1} ($10.3\text{ }\mu\text{m}$). These are by far the most promising targets in the pursuit of identification of this molecule in remote observations of Titan, because this spectral region is relatively free from other hydrocarbon emission, excepting ethylene (C_2H_4) [13].

Table 3.5: Spectral regions defined for our study of *trans*-2-butene.

Region	Coverage
I	$0750 - 1120\text{ cm}^{-1}$
II	$1120 - 1550\text{ cm}^{-1}$
III	$0750 - 1550\text{ cm}^{-1}$

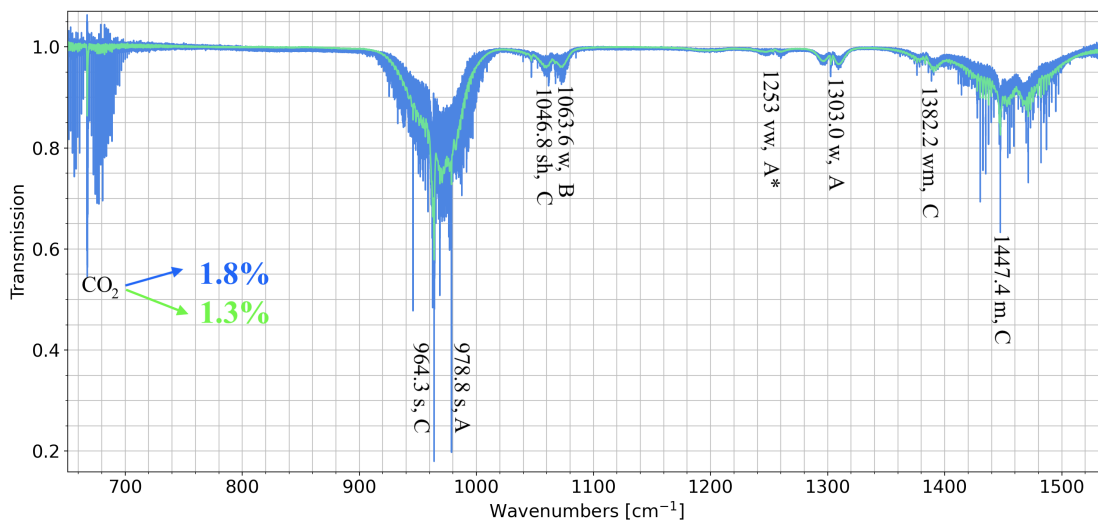


Figure 3.16: Sample of pure and N_2 -mixture spectra of $\text{trans-2-C}_4\text{H}_8$ obtained at 210 K. The pure spectrum (blue curve) was obtained with sample pressure $P_s = 1.40$ Torr at resolution $R = 0.0039 \text{ cm}^{-1}$, whereas the N_2 -broadened spectrum (green curve) was obtained with sample pressure $P_s = 1.81$ Torr, total pressure $P_{tot} = 759.8$ Torr, at resolution $R = 0.062 \text{ cm}^{-1}$. Several representative band centers for $\text{trans-2-C}_4\text{H}_8$ are identified, using the notation of McKean et al. (1985) [124] (i.e. s=strong, vw=very weak, etc. and A, B, C refer to band contour type). Note that the features around 667 cm^{-1} are contamination from CO_2 . The partial pressure contributions from CO_2 to the spectra are shown (in the same color scheme), estimated by simulating CO_2 's ν_2 band. See text for further details.

Samples of the derived cross-sections for Region 1 and Region 2 are shown in Figure 3.17. These regions carry significant contributions from numerous hot and combination bands which remain unidentified at this time. The rovibrational transitions of these bands are smeared out (along with the cold fundamental bands) to produce the observed, continuum-like absorption bands. As cross-sections are direct measurements of the absorption features of the molecule, all contributions from these as yet unidentified bands are captured in the cross-sections. A high-resolution spectrum can show detailed spectroscopic features. As the spectral resolution and other experimental conditions vary from spectrum to spectrum that we gathered, we derived each of the 21 sets of cross-sections independently from one

another, which is intended to provide sufficiently diverse data sets for extrapolation of the cross-sections into intermediate temperatures and pressures not explicitly covered, but contained within the ranges that we explored.

3.5.4 Linearity Test

One important difference between the studies conducted of *trans*-2-butene and *n*-butane involves the availability of prior, reliable measurements of the molecule's vibrational band centers. Particularly important are measurements of the low-lying torsional bands, which form a dominating contribution to the partition function approximation, as we saw in Equation 3.14. These measurements were available and complete for *n*-butane (though, as mentioned before, the uncertainties were quite large for the torsional band centers in particular). They are very incomplete, to the best of our knowledge, for *trans*-2-butene, however [124]. Thus, a pseudoline list could not be derived for that molecule at this time. In Chapter 5, however, the future steps required for doing exactly that are laid out.

Due to this difference, in the case of *n*-butane, the integrated band intensities could simply be calculated by summing up the pseudoline intensities across a given spectral region. For *trans*-2-butene, on the other hand, the cross-sections must be integrated themselves in order to make these measurements. Because of this, a test was warranted to ensure the validity of the spectra used and the experimental conditions employed. Recall that for *n*-butane, on the other hand, a variety of tests were performed to ensure that the *pseudolines* were capable of reproducing the observed spectra to within reasonable tolerances.

A classical way to do this test, as in Varanasi et al. (1977) [130], Varanasi et al. (1987) [131], and Sharpe et al. (2004) [115], and as described previously in Section

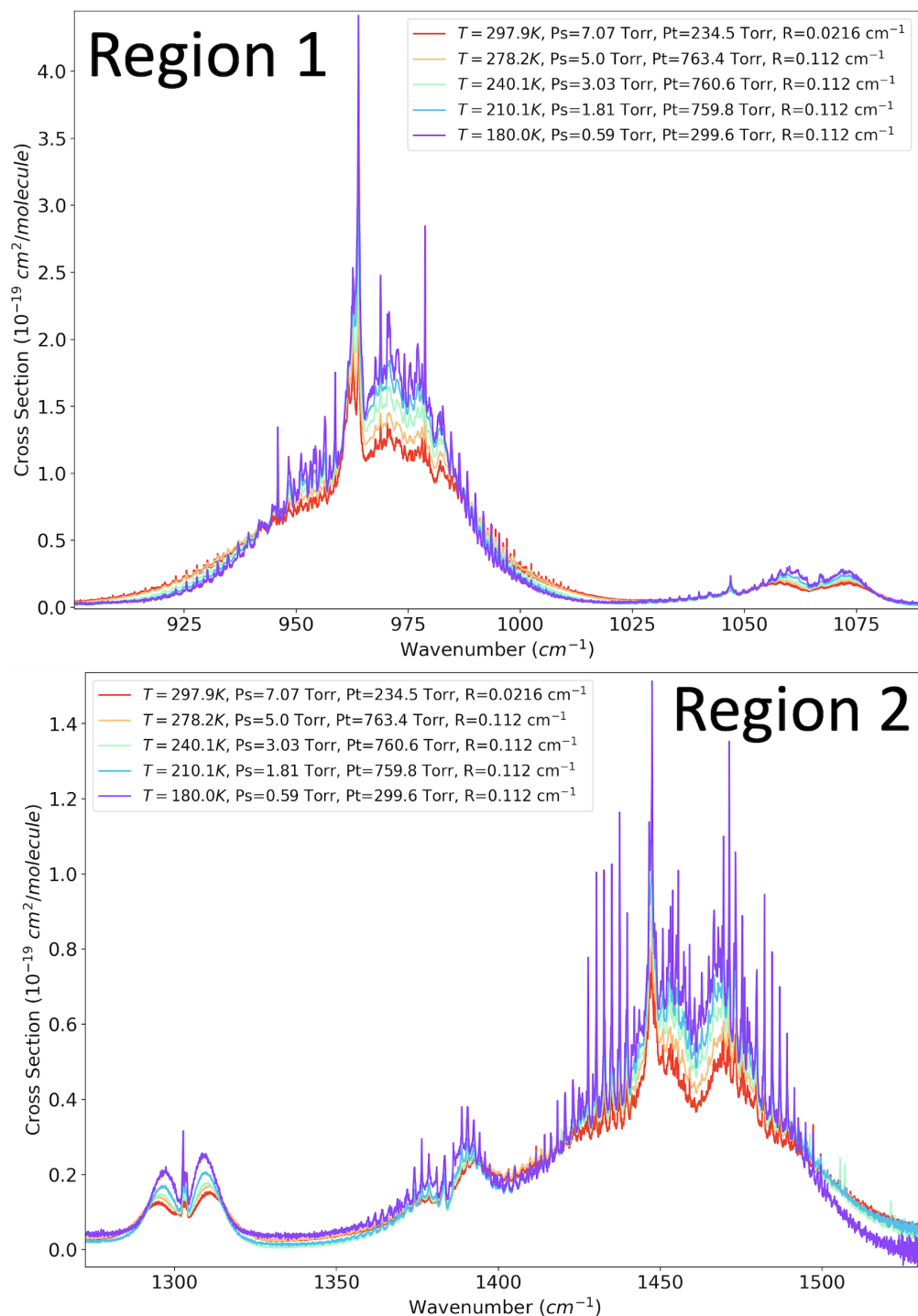


Figure 3.17: Sample of cross-sections for N_2 -broadened *trans*-2- C_4H_8 derived at multiple different temperatures and pressures, with cooler colors denoting colder temperatures; these temperatures and the other relevant experimental conditions are listed in the legends. Panel (a) roughly corresponds to Region I, and panel (b) roughly corresponds to Region II.

3.5.4, is by demonstrating the linearity between the molecule's absorbance and its increasing "*optical-burden*", which was defined as the *trans*-2-butene number density [cm^{-3}] times the gas cell path length [20.38 cm]. This test must be performed in the region of strongest absorbance/intensity in the spectral region studied in order to demonstrate that it is valid even there. Recall Equations 3.4-3.7, in which it was demonstrated that under a specific condition (sufficiently small optical *depth* within the gas cell), there is a directly linear relationship between the absorbance and the optical *burden* itself. If such a linear relationship can be shown, then the slope of this relationship is in fact the integrated intensity (S) of the region, which is intrinsic to the molecule itself, and independent of the experimental conditions under which the molecule was being studied. Because the integrated intensity of the region is what is ultimately the sought after quantity in the literature, this test is conducted to show that at the experimental conditions utilized in the laboratory, the measured cross sections are in fact approximately *equivalent* to those intensities.

The linearity test was conducted at room temperature (~ 297 K) and total (N_2 -broadened) pressure of ~ 760 Torr, collecting seven spectra that covered the range of 0.51 Torr to 18.14 Torr. The individual experimental conditions for each of these seven spectra for this part of our *trans*-2-butene work can be found in Table 3.6.

Table 3.6: Experimental conditions of the N₂-broadened *trans*-2-butene spectra used in our linearity test. Each of these was gathered at spectral resolution R=0.062 cm⁻¹. The volume mixing ratio (VMR) of *trans*-2-butene (i.e. sample pressure divided by total pressure including N₂) is also shown.

Spectrum	T (K)	P _s (Torr)	P _t (Torr)	VMR
B0189.8a	297.0(1)	00.51(1)	760.0(1)	0.00067
B0189.8b	298.0(1)	01.00(1)	760.2(2)	0.00132
B0189.8c	298.3(1)	02.01(1)	759.3(1)	0.00265
B0189.8d	297.2(1)	03.58(1)	760.2(2)	0.00471
B0189.8e	297.3(1)	07.90(1)	760.2(2)	0.01039
B0189.8f	297.7(1)	12.03(1)	760.0(1)	0.01583
B0189.8g	296.9(1)	18.14(1)	761.1(2)	0.02383

The results of this test are shown in Figure 3.18, plotting absorbance as a function of optical burden for the seven spectra. In panel (a), this is shown for the entire spectral region that was studied (750-1550 cm⁻¹), and panel (b) shows this for just the 960-970 cm⁻¹ range, which contains the strongest of *trans*-2-butene vibrational features in the mid-infrared, at 964.3 cm⁻¹ (see Figure 3.16). The linear relationship between absorbance and optical burden in either case is plain to see, validating the integrated cross-section measurements that are reported for *trans*-2-butene.

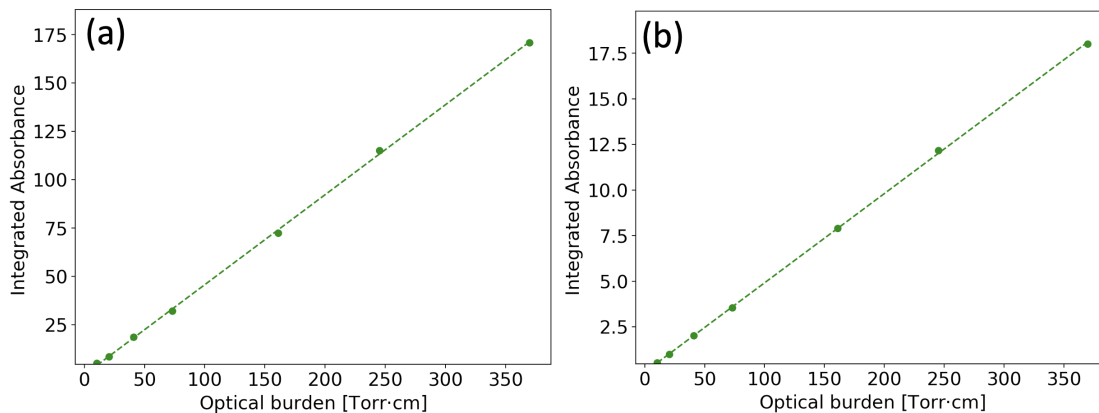


Figure 3.18: Linearity test for *trans*-2-C₄H₈ for (a) entire spectral region studied and (b) in 960-970 cm⁻¹ region, which contains the strongest *trans*-2-butene features observed. Even for an interval marked by the strongest features, a linear relationship is seen between the integrated absorbance, $A \equiv \int_{\nu} -\log(\tau) d\nu$, and the optical burden (i.e. *trans*-2-butene number density times path length), even in the 960-970 cm⁻¹ region. The slope, representing the intensity, has dimensions of length·energy⁻¹. See Varanasi et al. (1977) [130], Varanasi et al. (1987) [131], and Sharpe et al. (2004) [115] for additional examples of this methodology.

3.5.5 Results and Discussion

The primary results from this study are in the form of temperature-dependent cross-sections and their integrated values over wavenumber, for each of the three spectral regions defined in Table 3.5. In order to compensate for the 99% sample purity of the *trans*-2-butene sample that was used in this study, and to investigate the possibility of additional contamination beyond the 1% level in the sample, we simulated the ν_2 band of CO₂ under the experimental conditions of each of the *trans*-2-butene spectra. We then used these simulated spectra to determine the partial pressure of CO₂ contributing to each spectrum. These partial pressures were then used in correction factors when computing the cross-sections for that particular spectrum. We found an average CO₂ contribution of 1.5% across all of our spectra. The individual CO₂ contributions that we found for each of the

spectra are contained in Table 3.7.

Table 3.7: Estimated partial pressure fractions of CO₂ contamination originating from within the *trans*-2-butene sample. These were found by simulating the CO₂ ν_2 band and comparing to the observed spectra. These partial pressures are then used to ensure that the calculations of cross-sections, which rely on the measurements of the *trans*-2-butene sample pressure and the total pressure within the gas cell, are not skewed by the presence of this CO₂.

Spectra	CO ₂ partial pressure fractions
1a, 1b, 1c, 1d, 1e, 1f, 1g	0.02, 0.02, 0.02, 0.02, 0.02, 0.15, 0.015
2a, 2b, 2c, 2d	0.015, 0.015, 0.015, 0.015
3a, 3b, 3c	0.018, 0.019, 0.019
4a, 4b, 4c	0.018, 0.013, 0.013
6a	0.017
7a, 7b, 7c	0.017, 0.017, 0.017
8a, 8b, 8c, 8d, 8e, 9f, 9g	0.017, 0.014, 0.01, 0.01, 0.007, 0.007, 0.007, 0.007

From top to bottom, the spectra in this table are roughly arranged in the chronological order that they were collected in, over the period of about five weeks. It can be seen that the amount of CO₂ contaminating the sample decreases as the study progressed. As we did not use the entirety of the *trans*-2-butene sample, which was housed in a vertically-oriented lecture bottle, and as CO₂ is less massive than *trans*-2-butene, it is suspected that there was an over-density of the CO₂ contaminant near the top of the lecture bottle, and an underdensity near the bottom of the bottle, even though the ‘global’ average of the bottle was likely approximately 1%. (Recall that the *trans*-2-butene sample was rated as pure to $\geq 99\%$.) This point is not crucial to the interpretation of our results (though the correction factors due to CO₂ are!), but merely corroborates the stated assay of

the purchased *trans*-2-butene sample from Sigma Aldrich Incorporated.

Moving on, Ding et al. (2020) [93] conducted a high-temperature spectroscopic study of *cis/trans*-2-butene, in addition to several other molecules, for just the 900-1200 cm^{-1} range. Though their purpose was to measure cross-sections at *high* temperatures, they also obtained one room temperature result as well, at N_2 -broadened total pressure of ≈ 760 Torr, to which we have compared our results. When integrated, the Ding et al. room temperature cross-sections for *trans*-2-butene match the average of our room temperature results in that spectral range to well within 1%.

PNNL reports cross-sections for a *mixture* of *trans*- and *cis*-2-butene [115]. Unfortunately, this is not a valid data set to which to compare our results (as we were able to do with *n*-butane), as either isomer of *butene* is spectroscopically distinct. The National Institute of Standards and Technology (NIST), on the other hand, studied *trans*-2-butene in isolation at room temperature and at spectral resolution of 2 cm^{-1} [70]. We can compare our results to those that were calculated from the NIST data in Table 3.8. A rather large disparity is seen between the NIST results and our results at room temperature. It is worth noting that similar disparities between NIST and the JPL Molecular Spectroscopy Laboratory have been observed in past work for other molecules [112; 90].

Table 3.8: Tabulated results for the study of *trans*-2-butene, in the form of average integrated cross-sections [10^{-18} cm molecule $^{-1}$] and their standard deviation at each of the temperatures used, for each of the three regions defined in Table 3.5. The average percent error for our results across the full spectral region studied here is calculated to be 4.02 %. For purposes of comparison, the same are also shown for NIST (National Institute of Standards and Technology), derived from measurements of *trans*-2-butene acquired at room temperature (no uncertainties provided), at a spectral resolution of 2 cm $^{-1}$ [70].

Source	Temperature	Region 1	Region 2	Region 3
NIST	298 K	9.75	8.09	17.83
JPL	297 K	7.64 (0.16)	5.72 (0.32)	13.35 (0.45)
JPL	278 K	7.85 (0.11)	5.81 (0.13)	13.65 (0.23)
JPL	240 K	7.87 (0.12)	5.67 (0.16)	13.53 (0.27)
JPL	210 K	8.51 (0.53)	6.45 (0.31)	14.96 (0.85)
JPL	180 K	8.50 (0.50)	7.01 (0.65)	15.51 (1.14)

In Figure 3.19, our results are presented in the form of plots showing values for the integrated cross-sections for the spectra, identified by their regions in Table 3.5, and organized by decreasing temperature. In the same figure, these results are also compared to those of the linear regime room temperature spectra discussed in Section 3.5.4, as those are understood to be a reliable measurement of the integrated cross-sections, having already been explicitly shown to lie within the linear regime of absorbance and optical burden. Both mixture spectra and pure *trans*-2-butene spectra (marked by black X's) are shown. The average of the linear regime spectra is marked with a horizontal red dashed line, with a pink envelope indicating the 1σ standard deviation of those measurements. From this, it can be seen that no significant temperature dependence to the integrated cross-sections is present, as proposed by Crawford et al. (1958), Breeze et al. (1965), and Sams et

al. (2005) [120; 121; 122], for example.

The error bars for Figure 3.19 come from the standard deviation of all results collected at a given temperature. These uncertainties are assumed to be a combined representation of multiple sources of uncertainty, such as baseline corrections that we made in the cases of some spectra, as well as a lack of information about the 100% baseline in Region 2 in particular, where the R branches of bands at higher wavenumbers were not fully covered. An additional source of uncertainty comes from potential outgassing and degassing inside the cell and inlet tubes. The relative contribution of this uncertainty source becomes larger at lower pressures, causing an increasing amount of uncertainty in results obtained at lower temperatures (where smaller sample pressures were used to avoid condensation of *trans*-2-butene); this increasing uncertainty with decreasing temperature is evident in these figures as well.

It can be seen that most of our results fall into the band defined by the 1σ uncertainty of the mean integrated cross-section of the linear regime spectra. The most obvious outliers in this respect occur at colder temperatures. For instance, spectrum ‘4a’ (210 K) and spectrum ‘6a’ (160 K) are seen to be outliers in all three spectral regions. However, both of these were pure *trans*-2-butene spectra collected at high resolution ($R=0.0039\text{ cm}^{-1}$) (as indicated by the black X’s). For this reason, they may not be reliable measures of *trans*-2-butene cross-sections, but such high resolution spectra of pure sample are particularly useful for the purposes of identifying vibrational band centers and characterizing the detailed features of those bands.

In addition to the optomechanical stability of our spectrometer and the reliability of our sensors, our measurement uncertainty reported here was also made

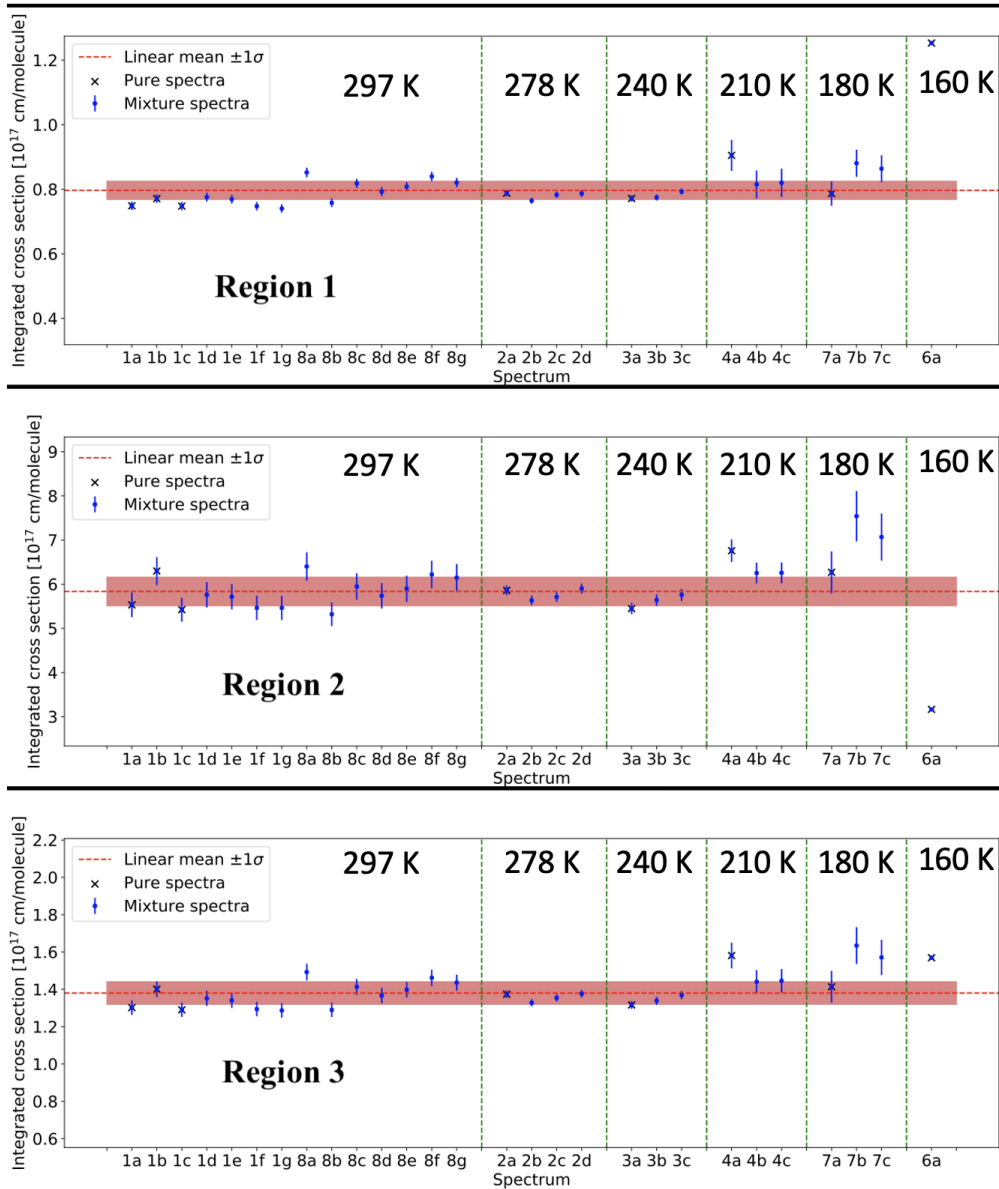


Figure 3.19: Integrated cross-section results for each of the three spectral regions, arranged by decreasing temperature. The red horizontal dashed line and accompanying pink envelope in each panel is the mean and standard deviation, respectively, for the seven linear regime spectra (‘8a’, ‘8b’, ..., ‘8g’) described in Section 3.5.4. Error bars on the individual data points are a combined estimate of the various sources of uncertainty discussed in Section 3.5.5. It can be seen that uncertainties grow larger at colder temperatures, presumably due to outgassing and degassing inside the cell and inlet tubes, which becomes more relevant at the lower pressures required to be used at these lower temperatures. The data point at $T = 160\text{K}$ is mainly for qualitative comparison and locating of band centers, as stated in the text.

possible by the use of a dry ice / methanol slurry. As described in Section 3.5.2, gas sample and broadening N₂ gas were fed through a copper coil submersed in this chilled bath before entering the gas cell, forcing residual water to condense out. Excellent removal of residual water vapor from our data is consistently observed, and this greatly facilitated the process of measuring cross-sections for *trans*-2-butene in the 1300-1550 cm⁻¹ region without having the cross-section measurements being contaminated by the water.

Similar studies to the one presented here still need to be conducted for the three other C₄H₈ isomers shown in Figure 3.14. As each isomer is a possible constituent of Titan's atmosphere and likely plays a unique role in Titan's chemistry and the production / destruction of other molecules, careful laboratory characterization studies of absorption cross-sections or spectral lines are required for each isomer, beginning with a high-purity, specialty gas sample. It is worth noting that once such a characterization is achieved for the *cis*-2-butene isomer specifically, that can be combined with our results here and compared to the earlier results of PNNL [115].

As a means of closing this section, we reiterate that as these various C₄H₈ isomers are thought to be important potential liquids in the lakes and putative subsurface reservoirs of Titan [71; 132], constraining their atmospheric abundances is a reasonable first step toward understanding atmosphere to surface transfer interactions and vice versa [133].

3.5.6 Butenes, Carbenes, and 1,2-Dimethylcyclopropane: A Chiral Connection

Relevant to the discussion of the *trans*-2-butene work, there is an interesting connection to a possible reaction that could take place in Titan's atmosphere which involves chirality. I was fortunate enough to be able to explore this connection with the help of Michael Malaska, a Planetary Scientist at JPL with rich experience in studying Titan's chemistry and astrobiological potential.

Titan's upper atmospheric chemistry directly relates to the molecules and potential prebiotic molecules that are in the *lower* atmosphere and at the surface. For instance, while the production of Titan's haze, the main layer of which is centered around 300 km [62], is not very well understood, large molecules (such as *trans*-2-butene, but also *n*-butane) may play an important role in this process, serving as nucleation sites [102]. Additionally, reactions that involve larger hydrocarbons like *cis*- and *trans*-2-butene specifically may be involved in the production of one of the most simple chiral molecules likely to be found at Titan, such as 1,2-dimethylcyclopropane [134; 135], shown in Figure 3.20.

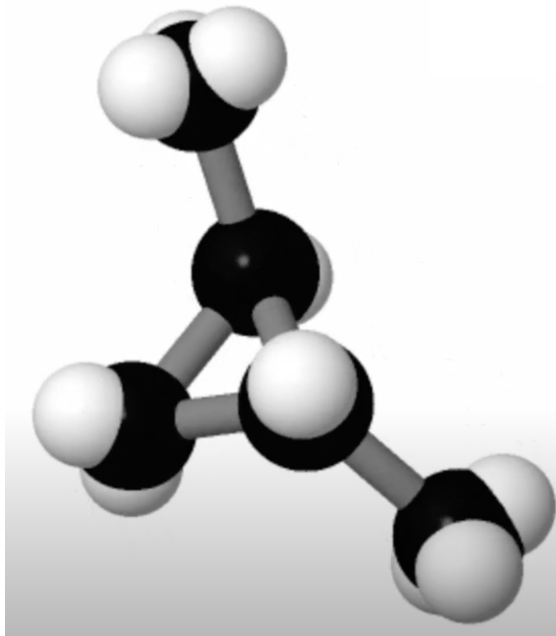


Figure 3.20: 1,2-dimethylcyclopropane (C_5H_{10}), a possible constituent of Titan's atmosphere which would likely be present in both its enantiomeric forms.

Both *trans*- and *cis*-2-butene are involved in a set of reactions with various methylene (CH_2) carbene states which tend to react with double bonds and produce a variety of different forms of 1,2-dimethylcyclopropane molecules, based on the electronic state of the reacting carbene [136]. In some cases, the *cis* version of 1,2-dimethylcyclopropane is produced, but in other cases, the *trans* version is produced (Figure 3.21). The latter molecule is chiral, existing in two enantiomeric versions (S) and (R). Motivated by their connection to the molecule of this study, it is worth taking a moment to develop this reaction scheme in a bit more detail before moving onto the conclusions of the *trans*-2-butene study.

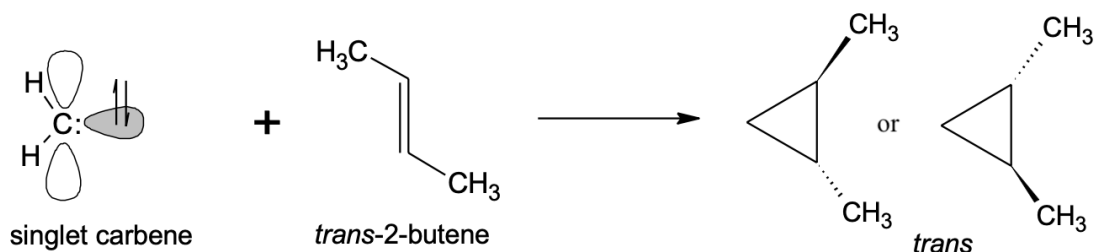


Figure 3.21: Production of either enantiomer of 1,2-dimethylcyclopropane is possible when singlet carbene reacts with *trans*-2-butene.

When singlet methylene carbene reacts in a concerted fashion with *trans*-2-butene, both enantiomers of *trans*-1,2-dimethylcyclopropane can be produced, as seen in Figure 3.21.

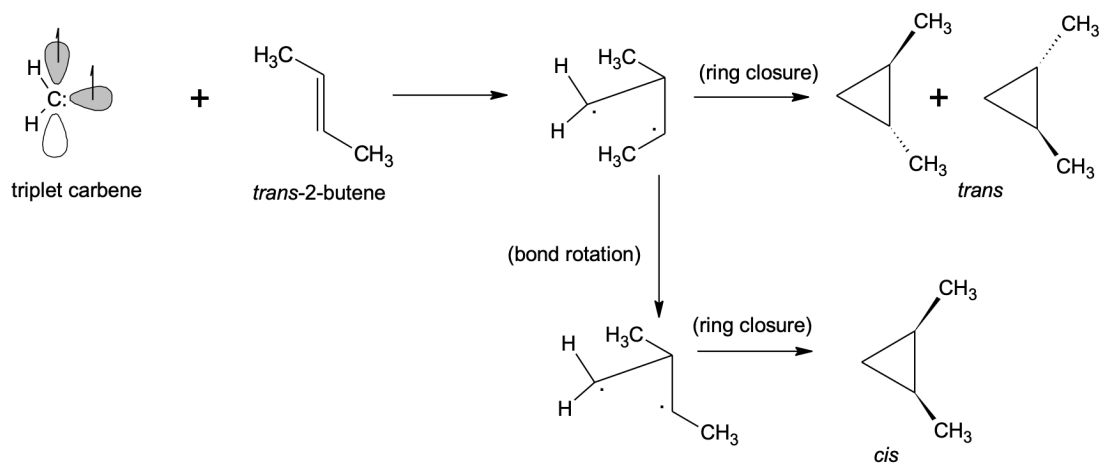


Figure 3.22: Triplet carbene reacting with *trans*-2-butene can produce both the enantiomers of the *trans*-1,2-dimethylcyclopropane molecule, but also, via a separate mechanism (bond rotation followed by ring closure) can also produce the non-chiral *cis*-1,2-dimethylcyclopropane.

On the other hand, when *triplet* methylene carbene reacts stepwise (thus allowing bond rotation) with *trans*-2-butene, both the *trans*-1,2-dimethylcyclopropane (in both enantiomers) and the *cis*-1,2-dimethylcyclopropane (not-chiral) may be

formed, as seen in Figure 3.22.

This pair of reactions (Figures 3.21 and 3.22) are to be compared to the same pair of reactions but using *cis*-2-butene as a reactant, rather than *trans*-2-butene. When singlet methylene carbene reacts with *cis*-2-butene, only the achiral *cis* version of 1,2-dimethylcyclopropane is produced, as seen in Figure 3.23:

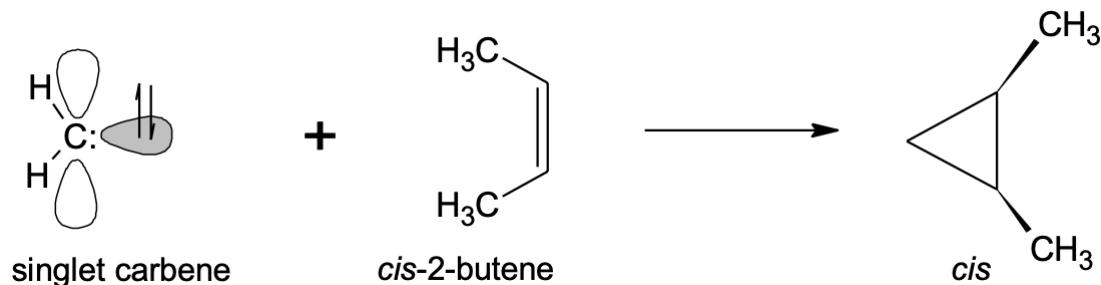


Figure 3.23: Singlet carbene, when reacted with *cis*-2-butene, produces *only cis*-1,2-dimethylcyclopropane.

When triplet methylene carbene reacts with *cis*-2-butene, on the other hand, both the achiral *cis*-1,2-dimethylcyclopropane and the chiral *trans*-1,2-dimethylcyclopropane (in both enantiomers) can be produced, as seen in Figure 3.24:

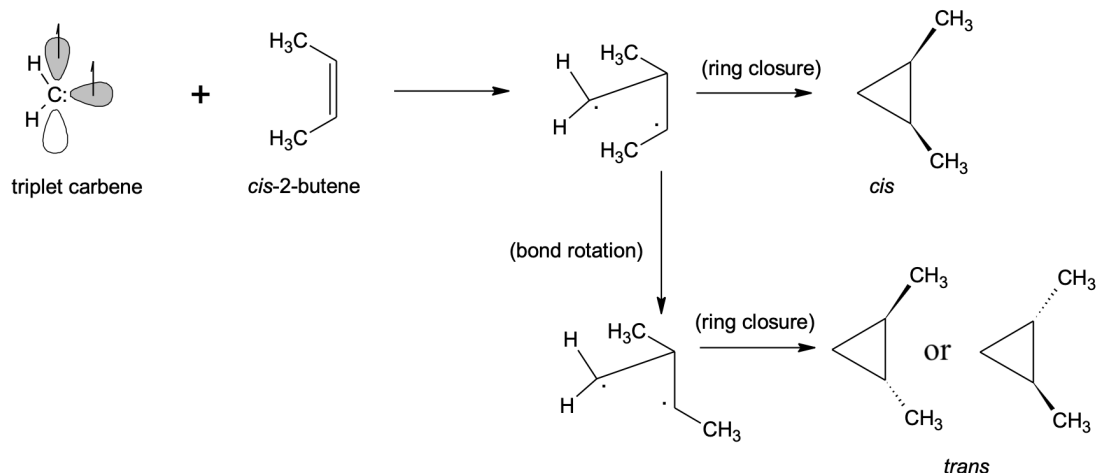


Figure 3.24: Triplet carbene reacts with *cis*-2-butene. This can produce either the achiral *cis*-1,2-dimethylcyclopropane molecule, or one of the two enantiomers of the chiral *trans*-1,2-dimethylcyclopropane molecule.

Summarizing this full reaction scheme, singlet methylene carbene can produce both *cis*- and *trans*-1,2-dimethylcyclopropane, but the resulting mixture will depend on the *initial ratio* of *cis*- and *trans*-2-butene. Triplet methylene, on the other hand, can produce both *cis*- and *trans*-1,2-dimethylcyclopropane, *without* dependence on the initial *cis*- and *trans*-2-butene populations. Thus, the ratio of *cis/trans*-1,2-dimethylcyclopropane abundances is linked with the ratio of *cis/trans*-2-butene abundances, and measuring these ratios (perhaps through existing or future remote sensing observations) can thereby constrain the populations of carbene intermediates in Titan's atmosphere.

To put it differently, by measuring the initial ratio of *cis*- and *trans*-2-butenes in Titan's atmosphere, and then comparing those measurements to measurements of *cis*- and *trans*-1,2-dimethylcyclopropane, it will be possible to determine the ratios of singlet and triplet excited carbene reactive intermediates in Titan's up-

per atmosphere reaction network. Understanding these electronic states will help predict reaction styles and reactant cross-sections, such as whether concerted or stepwise (or other reaction paths such as C-H insertion) reactions will occur. For example, it is known that triplet carbenes have a preferred affinity for *conjugated* double bonds, such as those found in allene or 1,3-butadiene [137].

Infrared laboratory work for 1,2-dimethylcyclopropane would still be required first for that investigation to begin in earnest. Understanding reactions such as these and the abundances of the reactants that go into them is important for future work seeking to measure any possible chirality signals at Titan. As future missions and work, such as the upcoming Dragonfly mission [see Turtle et al. (2018) [30]], begin to pave the way toward teasing out any biologically-relevant chirality signals at Titan (for instance, homochirality, a powerful indication of biological activity [4], could be detected by Dragonfly’s DraMS instrument, [138]), an urgent need exists to characterise any *background* to such signals, arising from abiological processes.

Naturally, the first step toward measuring or constraining the abundances of *any* new molecule at Titan is measurement of absorption cross-sections at cold temperatures, as has been presented here for *trans*-2-butene.

3.6 Limitations in Use of These Results

The results from both of these laboratory studies were obtained with the express intent of their use toward the modeling of planetary atmospheres, specifically that of Titan. As has been said many times, the primary goal behind the characterization of both of these molecules in the infrared was such that their abundances in Titan’s atmosphere could be constrained in existing or upcoming observations,

given that both molecules have unique connections to Titan's astrobiological potential, and are logical next steps for characterization in terms of understanding Titan's atmosphere's full chemistry.

With that said, certain limitations are inherent to the results of both of these studies that need to be acknowledged and understood, particularly on the part of anyone intending to use these results for their intended purpose of constraining the abundances of these gases in Titan's atmosphere. The primary constraint on the use of these results is that they are valid only in modeling within the range of temperatures within which they were initially collected. This is true of both the pseudoline list for *n*-butane, and also the cross-sections for *trans*-2-butene. As the temperature and pressure of Titan's atmosphere naturally varies as a function of altitude, the sensitive altitude regions of models that use these laboratory results need to be checked, such as to ensure that the temperatures there are indeed covered by these laboratory measurements.

We will see in the coming chapter, in which the modeling work using these laboratory results will be discussed, that due to the temperature ranges achieved, this is not a catastrophic issue, as a substantial portion of the stratospheric temperatures are indeed covered within these ranges. However, it is worth expressing all of this candidly anyway, as there is nothing in principle preventing these laboratory results from being valid for modeling emissions in other atmospheres, say, those of Saturn, or the ice giants. In such cases, the temperature profiles within the altitude ranges to which such modeling work is particularly sensitive would need to be very carefully inspected indeed.

In the case of Titan, future laboratory experiments such as those described in this Chapter might be able to improve the lower bound of their temperature

range for other large hydrocarbons with similar saturation vapor pressure curves by expending much more time and care during the sample adding process. This is extremely difficult, and very time-consuming, however. More will be said on this process in [Chapter 5](#).

Chapter 4

Atmospheric modeling

In addition to the laboratory work described in the previous chapter, this dissertation has included extensive work in radiative transfer modeling of various observations of Titan's atmosphere. As discussed in Chapter 2, this is an important part of constraining the abundances of new molecules in a planetary atmosphere: isolating and quantifying the signals of those molecules in actual observations of the atmosphere of interest. This chapter begins with a discussion of some of the more important and technical aspects of NEMESIS, which is the modeling tool that was employed for this, in detail. Next, the search for *n*-butane signals in Cassini CIRS data, starting with a brief introduction to Cassini spacecraft and the CIRS instrument itself, will be discussed. Finally, the much newer observations that were acquired at NASA IRTF in 2021 and the preliminary results that were obtained from those will be briefly described.

4.1 NEMESIS in detail

We begin with a discussion of the inner workings of the NEMESIS planetary atmosphere radiative transfer and retrieval tool, which has been the primary code for modeling spectroscopic observations of Titan’s atmosphere in this dissertation work. For the unfamiliar reader, NEMESIS is described thoroughly in Irwin et al. (2008) [79].

A set of *a priori* profiles for atmospheric pressure, temperature, and the abundances of relevant gases serve as the primary input to a NEMESIS calculation. Though the calculation can be run in several different modes, a particularly useful function of NEMESIS for my purposes has been its ability to be able to operate in ‘correlated-k-approximation mode’. This is an alternative approach to line-by-line calculations, which can be extremely expensive, computationally speaking.

Following for the moment the explanation contained in Irwin et al. (2008), the mean transmission $\bar{\tau}$ of a particular path through an atmosphere, over a wavenumber interval $\nu_0 + \Delta\nu$, is calculated as

$$\bar{\tau}(m) = \frac{1}{\Delta\nu} \int_{\nu_0}^{\nu_0 + \Delta\nu} \exp\left(-m \sum_j k_j(\nu)\right) d\nu, \quad (4.1)$$

where m is the total absorber density (in molecules cm^{-2}) and the sum within the integrand runs over all of the spectral lines of all of the gases that contribute to absorption in this wavenumber range, with the absorption coefficient of the j^{th} line being represented by $k_j(\nu)$, in ($\text{cm}^2 \text{ molecule}^{-1}$). NEMESIS employs a clever transformation of Equation 4.1 in order to *more efficiently* compute the mean transmission $\bar{\tau}$ in a given spectral region. The reason one would even think to do this in the first place, demonstrated in Figure 4.1, is that for Equation 4.1 to yield

a successfully accurate representation of the actual transmission, the resolution $d\nu$ must be sufficiently small such as to resolve each and every line in the region of interest, some of which are likely to be extremely sharp in wavenumber range. And of course, the smaller we set $d\nu$, the more computationally expensive the calculation is bound to be. Figure 4.1 shows the opacity of methane across a small wavenumber interval, and several examples of sharp methane lines that would only be captured by computationally expensive calculations with very small increments of $d\nu$.

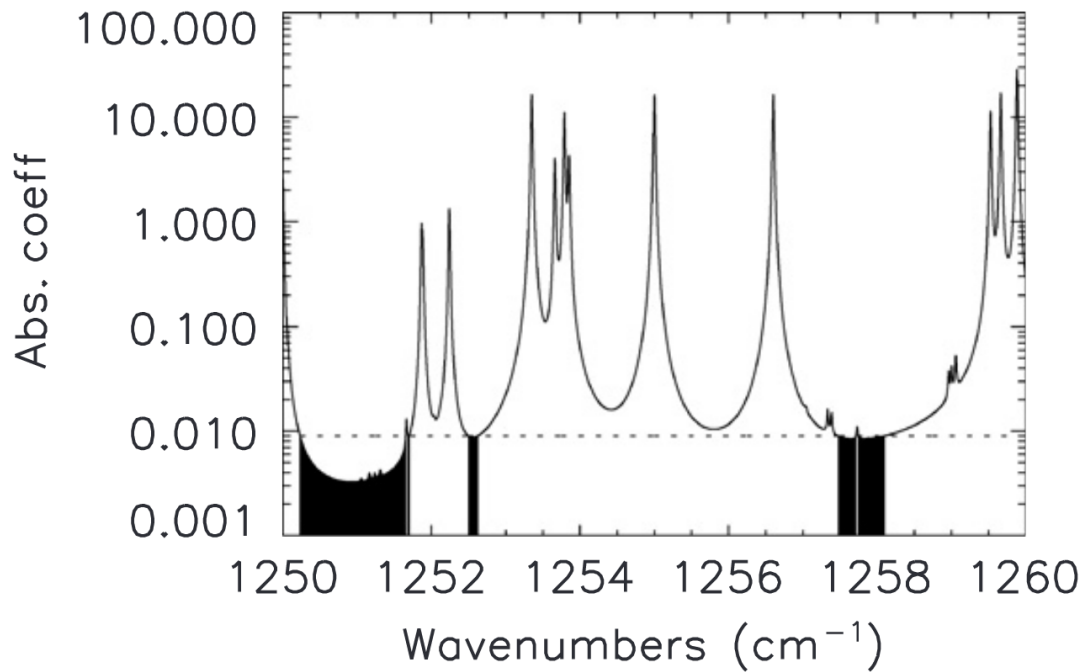


Figure 4.1: Example of spectral data gathered in the methane (CH_4) ν_4 region, from Saturn's atmosphere. It is seen that, as expected, the spectrum is a quickly and sharply varying function of wavenumber ν due to the presence of multiple strong methane lines in this region. This figure has been adapted from Irwin et al. (2008)[79].

However, taking another look at Equation 4.1, it can be observed that in order

to calculate $\bar{\tau}$, within the integration, it is really of no consequence *where* within the wavenumber interval $\nu_0 + \Delta\nu$ a given absorption coefficient k occurs. This is because we are simply summing these absorptions up in the argument of an exponential function, and because summation is a linear operation, and because of course, $e^{a+b+\dots} = e^a \cdot e^b \cdot \dots$. Thus, we are free to rearrange the *order* in which we do this sum to better suit our needs. To accomplish this, we can define $f(k)dk$ as the fraction of the frequency domain occupied by a given absorption coefficient range $k + dk$. Then, we are free to rewrite Equation 4.1 as

$$\bar{\tau}(m) = \int_0^\infty f(k) \exp(-km) dk. \quad (4.2)$$

Next, defining a so-called ‘cumulative function’ $g(k)$,

$$g(k) = \int_0^k f(k) dk, \quad (4.3)$$

and noting that, by the Inverse Function Theorem, the inverse of this function, i.e. $k(g)$, must exist and must be smoothly varying, since $g(k)$ is bound to be a smooth, single-valued, monotonically increasing function, we can then write

$$\bar{\tau} = \int_0^1 \exp[-k(g)m] dg. \quad (4.4)$$

So, we have gone from $k(\nu)$ to $k(g)$ for the exponential argument within the integrand; $k(\nu)$ is a quickly varying function of ν (again, see Figure 4.1) but $k(g)$ is a slowly and smoothly varying function of g , and therefore requires substantially fewer steps in integration, saving on computation time. Figure 4.2 shows this transformation having taken place for the methane spectrum of Figure 4.1, i.e. it

shows $k(g)$ in that case.

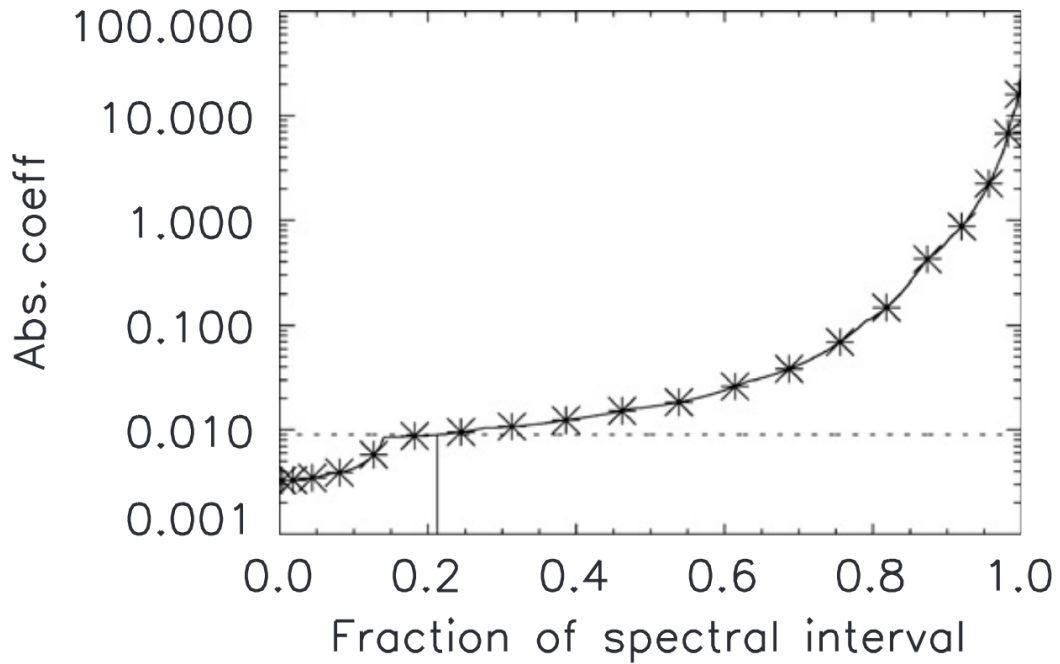


Figure 4.2: The smoothly-varying, rearranged absorption of methane from Figure 4.1, which can be integrated much more efficiently than the actual spectrum.

In practice, one capitalizes on this ‘correlated-k’ trick by computing, in advance of any actual modeling of observations, a set of distribution functions $k(g)$ for each spectrally active gas in the spectral region that will ultimately be modeled. These are computed over an appropriate grid of temperatures and pressures and form a set of so-called ‘k-tables’. Often, these are referred to as ‘opacity tables’, since they effectively record the optical opacity of the molecule as a function of both temperature and pressure, across a given wavenumber interval.

4.2 Cassini spacecraft

Described earlier in Section 1.1.5, the Cassini spacecraft is responsible for the majority of the Titan observations that were modeled for the search for Titan's $n\text{-C}_4\text{H}_{10}$. The entirety of that modeling work is published as of March, 2022:

- **Steffens, Brendan L.**, Conor A. Nixon, Keeyoon Sung, Patrick G. J. Irwin, Nicholas A. Lombardo, and Eric Pereira. “New Constraints on Titan’s Stratospheric n -Butane Abundance.” *The Planetary Science Journal* 3, no. 3 (March 1, 2022): 59. <https://doi.org/10.3847/PSJ/ac53ad>.

What follows is a description of the instrument on Cassini that collected these Titan observations which were modeled with NEMESIS, followed by a description of the actual modeling methodology and the results that were obtained.

4.2.1 The Composite Infrared Spectrometer Instrument

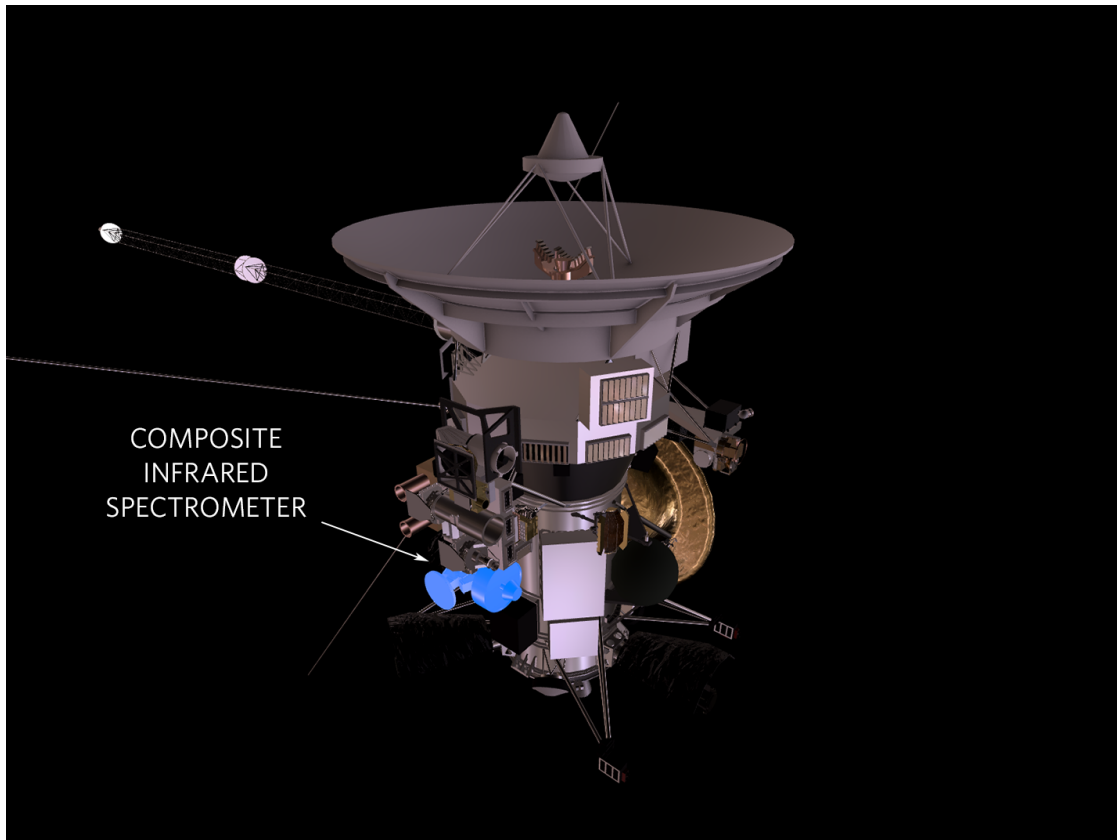


Figure 4.3: 3D rendering of the Cassini spacecraft. The Composite Infrared Spectrometer instrument is highlighted in blue near the bottom. Image is credited to the Cassini CIRS team; more info can be found at <http://cirs.gsfc.nasa.gov/>

One of the many important instruments included on the Cassini spacecraft was the Composite Infrared Spectrometer (CIRS) [21; 139], a Fourier Transform Spectrometer (FTS) which measures thermal emission over two orders of magnitude in wavenumber ($10\text{-}1400\text{ cm}^{-1}$, or in terms of wavelength, 1 mm to $7\text{ }\mu\text{m}$), with a variable spectral resolution which could be set between 0.5 to 15.5 cm^{-1} . CIRS captures data across this wide spectral range via three different focal planes, known as FP1, FP3, and FP4 (FP2 was decommissioned and removed from the instrument be-

fore launch). FP1 ($10\text{-}600\text{ cm}^{-1}$) uses a polarizing interferometer and thermopile detectors with a circular, 4 milliradian field of view. FP3 and FP4 ($600\text{-}1100\text{ cm}^{-1}$ and $1100\text{-}1490\text{ cm}^{-1}$, respectively) are twin 1×10 arrays of square mercury cadmium telluride (MgCdTe) detectors, each with a 0.3×0.3 milliradian field of view, and measured using a traditional Michelson interferometer. CIRS was designed to be able to provide three-dimensional temperature maps of Titan's (and Saturn's) atmosphere, as well as maps of gas composition and aerosol/condensate concentrations, all with good horizontal and vertical resolution. Key to producing altitude-dependent profiles of these quantities are the FP3 and FP4 detectors, which allow CIRS to be run in a "limb-viewing" mode (Figure 4.5), effectively measuring differences in spectra as a function of altitude away from the surface of the targeted body [21].

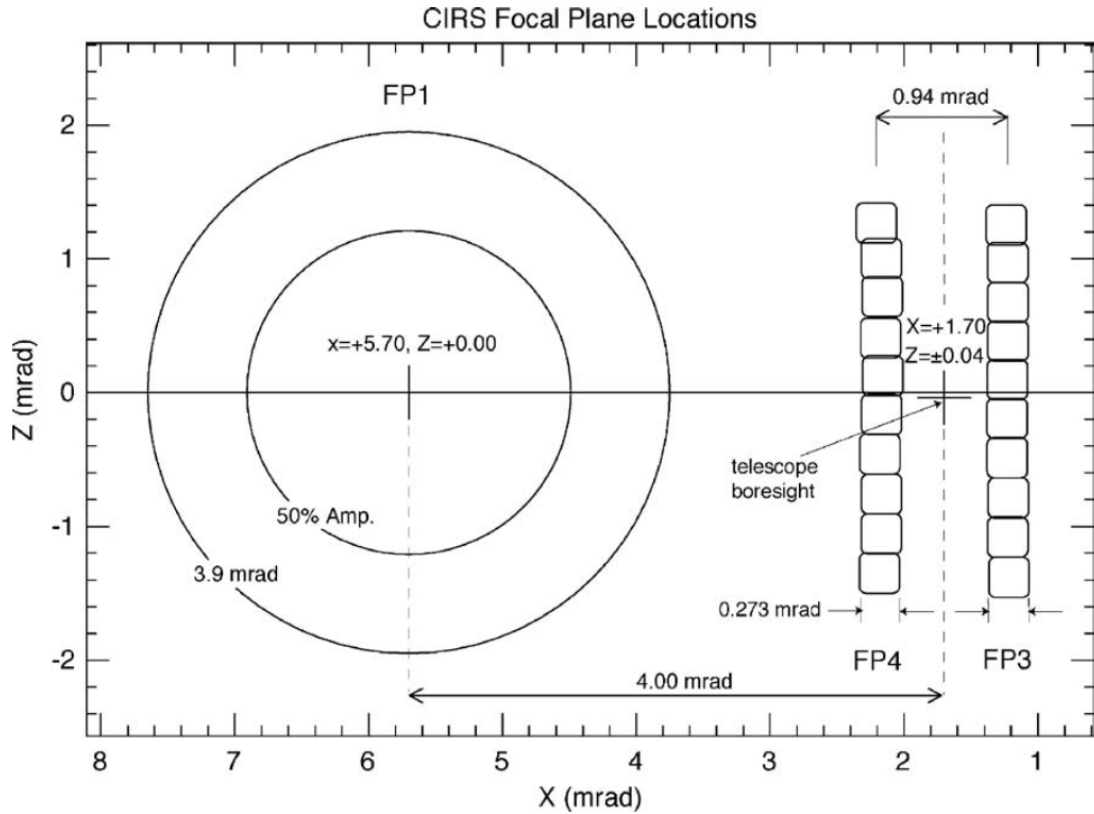


Figure 4.4: Placement of the three focal planes of CIRS and their respective fields of view. FP1 ($10\text{-}600\text{ cm}^{-1}$) was a single circular pixel, optimized for nadir viewing geometries, whereas FP3 and FP4 ($600\text{-}1100$ and $1100\text{-}1490\text{ cm}^{-1}$, respectively) were linear arrays of ten square pixels which could be rotated with respect to the target, allowing latitudinal maps across the disk of a targeted body to be constructed, in addition to limb-viewing geometries, with the linear arrays angled perpendicular to the disk-tangent, permitting altitude-dependent investigations of spectral properties. This figure has been adapted from Figure 1 of Flasar et al. (2004) [21].

FIRLMBINT
±1:15 to ±2:15 hrs

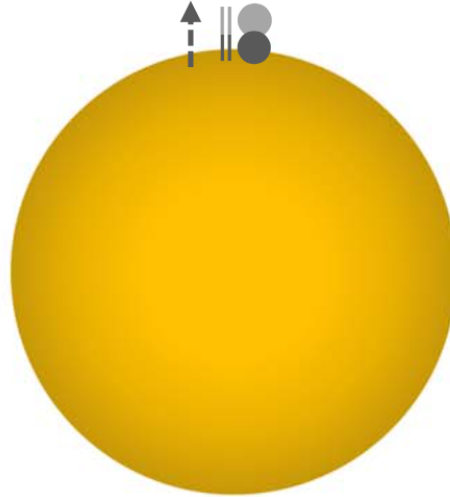


Figure 4.5: Adapted from Figure 7 of Nixon et al. (2019) [128], the disk of Titan is shown along with the footprint of CIRS in the “FIRLMBINT” (i.e. Far-Infrared Limb-Integration) mode, one of multiple viewing modes employed to gather a wide variety of observations of Titan, as well as Cassini’s other Kronian targets. The linear arrays of FP3 and FP4 can be seen on the left at the top of the disk, whereas the circular pixel of FP1 is on the right.

CIRS was actually based on the earlier IRIS (Infrared Interferometer Spectrometer [17]) instrument which flew on the Voyager 1 mission, with several intended improvements incorporated into the new design, such as:

- Extended coverage in the far-infrared: the extremely far infrared wavenumbers $10\text{-}180\text{ cm}^{-1}$ were not available to IRIS. This range was added to CIRS to increase the range of altitudes that CIRS could sound in the atmospheres of Titan and Saturn, and also to increase the capabilities of detecting new organics in both Saturn and Titan’s atmosphere, as organic molecules tend to have rotational or rovibrational features in this region.

- Higher spectral resolution: CIRS was designed to offer almost an order of magnitude higher spectral resolution (0.5 cm^{-1} , compared to IRIS's 4.3 cm^{-1}). This greatly facilitates the problem of identifying distinct spectral contributions due to trace constituents in atmosphere and has been crucial to the explicit detection of many of Titan's trace atmospheric gases.
- Sensitivity: Particularly in the mid infrared regions ($600\text{-}1490 \text{ cm}^{-1}$), CIRS was designed to have greatly improved sensitivity, via the use of cooled HgCdTe detectors, rather than thermopiles. This, in turn, permits the use of the smaller 0.27×0.27 milliradian field of view detectors to be used, which yields higher spatial resolution. This is crucial for the three dimensional mapping of temperature and atmospheric composition.
- Limb-viewing: As previously mentioned, through the use of FP3 and FP4 (see Figures 4.4 and 4.5), CIRS was able to orient the linear FP3 and FP4 arrays to be perpendicular to the tangent of the target body disk, enabling altitude-dependent investigations of atmospheric spectral properties (i.e. limb sounding).

Needless to say, the fact that CIRS was affixed to a Saturn-orbiting platform (i.e. the Cassini spacecraft) represented a tremendous improvement in the ability to do Saturn system science over IRIS, which was forced to just flyby the system on Voyager 1.

4.2.2 The CIRS Observations

The CIRS limb observations of Titan were obtained via Focal Plane 4. Three different sets of these limb observations were modeled and analyzed, these coming

from different Cassini flybys of Titan. The flybys and the important details of the data sets which resulted from them are contained in Table 4.1. Of these three data sets, one was focused on equatorial latitudes, and the other two were focused on Titan’s northern pole, those two having been gathered during Titan’s mid-northern winter (2005-2007). The selections were made this way in order to start a preliminary investigation of the possible dependence of n -C₄H₁₀’s abundance on season and latitude, expecting to see yet another case of hydrocarbon abundances that are enhanced at the poles with respect to the equator, particularly during winter [140]. This enrichment is thought to be caused by meridional overturning circulation in the stratosphere of Titan, which delivers low-latitude air from the upper stratosphere to the middle stratosphere, where it can subsequently be trapped in the stratospheric polar vortex. (Note that CO₂ is the one well-known, and prominent exception to this ‘rule’ [141].)

Table 4.1: Cassini CIRS Observations: The final column shows the average projected detector footprint for the observation set. Note that Titan’s atmospheric scale height is approximately 50 km in the stratosphere. The EQ observations are described more thoroughly in Nixon et al. (2013) [60], whereas details for the T3, T10 and other Cassini-Titan flybys can be found in Nixon et al. (2019) [128].

Obs.	Date	Season	L _S	Start Time	Hours	Lat.	Det. Footprint (km)
T3	2/15/05	N. Winter	305°	19:57:53	4	82° N	50
T35	8/31/07	N. Winter	345°	21:32:34	4	70° N	50
EQ	‘04-‘10	...	277°-9°	30°S - 10°N	40

Each of the three sets of observations contains five spectra, each of which was generated by co-adding multiple spectra from similar altitude ranges along the limb. Those altitude ranges, as well as the actual number of spectra which were co-added are contained in Table 4.2. It is worth noting that, as previously stated,

though the FP4 detector of CIRS actually has 10 individual pixels, each of which will record a spectrum, we made the decision to bin the spectra by altitude range, yielding a total of five co-added spectra for each of the datasets. This decision was made in consideration of both signal to noise but also computation time for the modeling process.

Table 4.2: Altitude ranges and number of co-added spectra.

Obs.	Spec. ID	Alt. (km)	No. of Co-adds	Noise (nW cm ⁻² sr ⁻¹ cm)
T3	1	104-214	38	1.66
	2	162-272	37	2.53
	3	227-337	51	2.35
	4	287-397	48	1.83
	5	352-452	37	1.48
T35	1	113-203	75	0.25
	2	172-262	77	0.60
	3	237-307	68	1.11
	4	293-383	35	1.27
	5	346-456	48	1.21
EQ	1	85-165	356	0.56
	2	110-190	443	0.97
	3	136-216	561	1.23
	4	159-239	570	1.22
	5	177-267	570	0.96

Hereafter, these three data sets in Tables 4.1/4.2 will be referred to by EQ (which of course refers to the composite equatorial data set), or T3/T35, referring

to the polar winter datasets collected from the respectively named flybys. Note that all three sets of observations were obtained at CIRS’s highest spectral resolution (0.5 cm^{-1}). However, each of the original sets of data were in fact *sampled* every 0.25 cm^{-1} . For this reason, every other data point was manually removed before any modeling of the observations took place, so as to ensure the correct computation of the goodness-of-fit metrics (which depend on the number of ‘real’ data points) which will later be used to derive upper limits on the *n*-butane abundance in each dataset.

Note also that even though the FP4 observations do cover the full spectral range of $1100\text{-}1490 \text{ cm}^{-1}$, focus was ultimately placed on just the $1300\text{-}1490 \text{ cm}^{-1}$ region. This decision was made in consideration of computation expense, but more importantly, to focus time on targeting the 1465 cm^{-1} region, which, as discussed in Section 3.4.3, and seen very well in Figures 3.6 and 3.8, contains the extremely strong ν_{14} vibrational band, a promising target for detecting *n*-butane or constraining its abundance.

The CIRS observational data were reduced following the standard data reduction pipeline described in Jennings et al. (2017) [139]. The individual observations themselves were extracted directly from an internal server located at Goddard Space Flight Center using a copy of Planetary Data System Version 4, and then coadded together. The noise levels of these observations were estimated by measuring the RMS (root mean square) residual between the preliminary model fit and the observations, and then fine-tuning the overall noise level to match that RMS in the actual spectral data.

4.2.3 Modeling

As stated earlier, NEMESIS was used to model the Cassini CIRS observations. Importantly, it was necessary to model each of the five coadded spectra belonging to a given data set *individually*, so as to extract information that is specific only to that particular altitude bin of that particular dataset.

Spectral line data from HITRAN [118] were implemented in the modeling of emissions from methane (CH_4), ethane (C_2H_6), ethene (C_2H_4), and ethyne (C_2H_2), and hydrogen cyanide (HCN). Each of these gases is spectrally active in the 1300-1490 cm^{-1} range. Both propane (C_3H_8) and propene (C_3H_6) are also active in the region; JPL’s pseudoline lists were used in the modeling of emissions from those two gases (propane: Sung et al. (2013) [88], propene: Sung et al. (2018) [90]). Naturally, to model the possible *n*-butane emissions, the pseudoline list generated earlier, as described in Section 3.4.4 [112], was used.

The methodology for the CIRS modeling closely follows that of Lombardo et al. (2019) [142]. In that study, the authors modeled the ν_4 , ν_8 , and ν_{12} bands of ethane in FP4 CIRS data. Following their steps, the abundance of methane in the model is first held fixed while NEMESIS is used to retrieve a temperature profile for each dataset, by modeling methane’s ν_4 band at 1305 cm^{-1} . To do this, a methane abundance profile based on measurements from the Cassini Huygens Landing Probe’s GCMS instrument was implemented [24]. This altitude profile assumes a constant methane abundance of approximately 1.48% above 84.6 km, which is consistent with photochemical models [143].

Note that this is a very reliable procedure for measuring temperature profiles for Titan’s atmosphere (see Lellouch et al. (2014) [144]), due to the reliability of the in-situ methane profile data that was gathered years back by the Cassini Huygens

lander during its descent [24]; we essentially treat the *a priori* methane abundance profile as ground truth (to within a tight uncertainty, of course), and allow only the temperature profile to vary in this preliminary NEMESIS calculation, until the ν_4 band of methane is fit to within a reasonable tolerance. The temperature profile that achieves this fit is the ‘retrieved’ temperature profile. Examples of this methodology being successfully implemented can be found, for example, in Nixon et al. (2013) [60] or Lombardo et al. (2019) [27].

In Figure 4.6, the retrieved temperature profiles for each of the three data sets that were modeled are shown, in addition to the *a priori* temperature profiles that were used. The *a priori* temperature profile for the equatorial dataset was derived from the T126 flyby following the methodology of Achterberg et al. (2014) [145]. For the two polar datasets, the *a priori* temperature profiles were derived from retrievals that were selected from Teanby et al. (2019) [140]. For those, the Teanby measurements were selected which were as close as possible in solar elongation angle with respect to the correct flyby (T3 or T10), and as close as possible to the latitude targeted by CIRS during that flyby.

Next, the retrieved temperature profiles were held fixed, preventing them from varying in future modeling calculations, and subsequently, abundances for ethane (C_2H_6), ethene (C_2H_4), ethyne (C_2H_2), propane (C_3H_8), propene (C_3H_6), and hydrogen cyanide (HCN) were retrieved. This was executed by retrieving scaling factors that were applied to the *a priori* abundance profiles of these gases that resulted in the optimum fit of the model to the observations. Allowing the entire profiles of the gases to vary (i.e. how much of each gas at each point on the altitude grid) is an option as well, but this is much more expensive, computationally, and was determined not to be necessary.

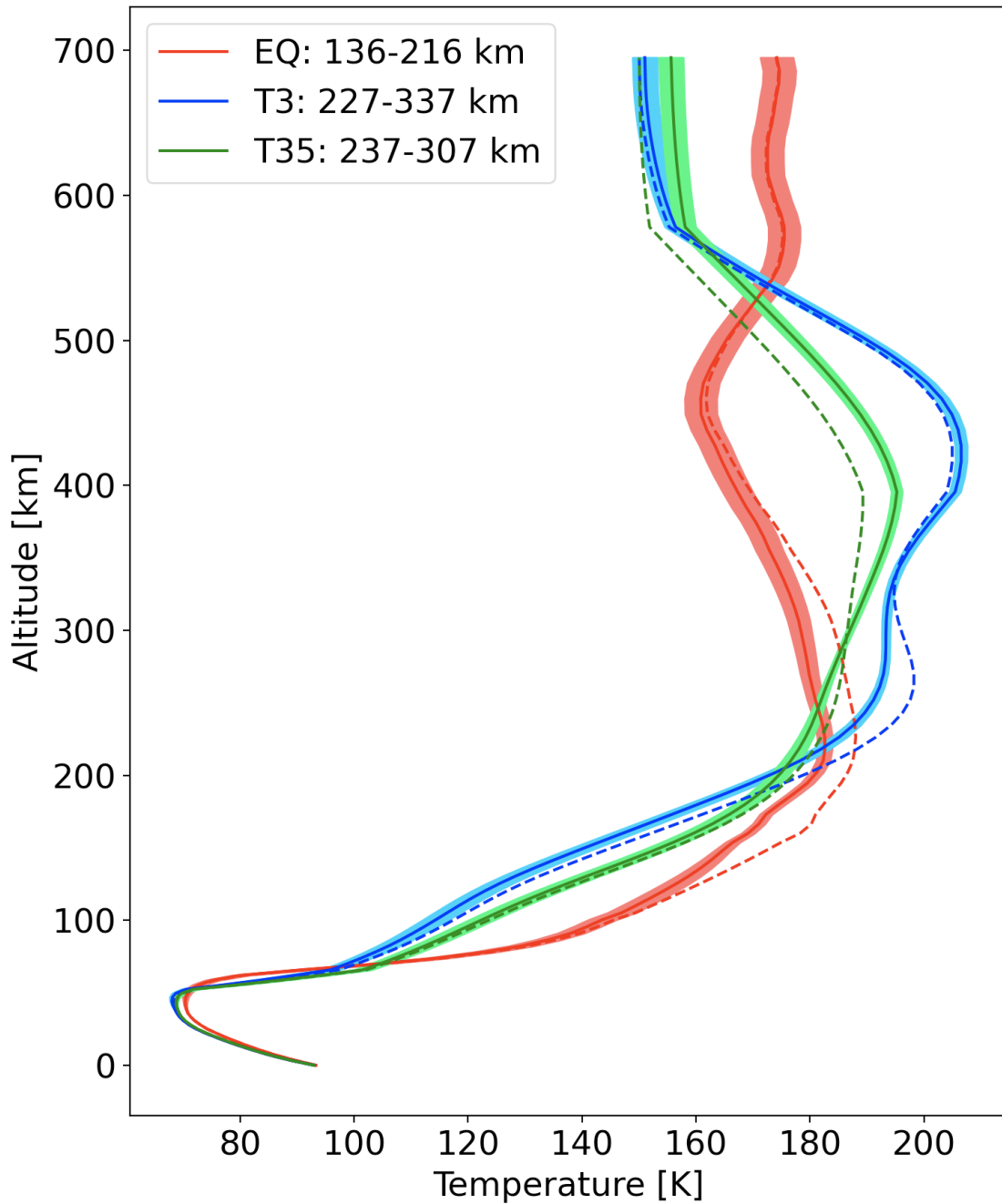


Figure 4.6: Display of the retrieved temperature profiles for all three data sets (solid curves), in addition to the *a priori* profiles (dashed curves) used for each of the three cases [140; 145]. For each of the colored curves, the 1σ uncertainty in the retrieved profile is identified by the corresponding, similarly-colored shading.

From there, sets of forward models were systematically generated which contained various amounts of n -butane. A sample fit of the model both before and after adding n -butane can be seen in Figure 4.7, for the EQ observations, focused on the ν_{14} vibrational band at 1466 cm^{-1} .

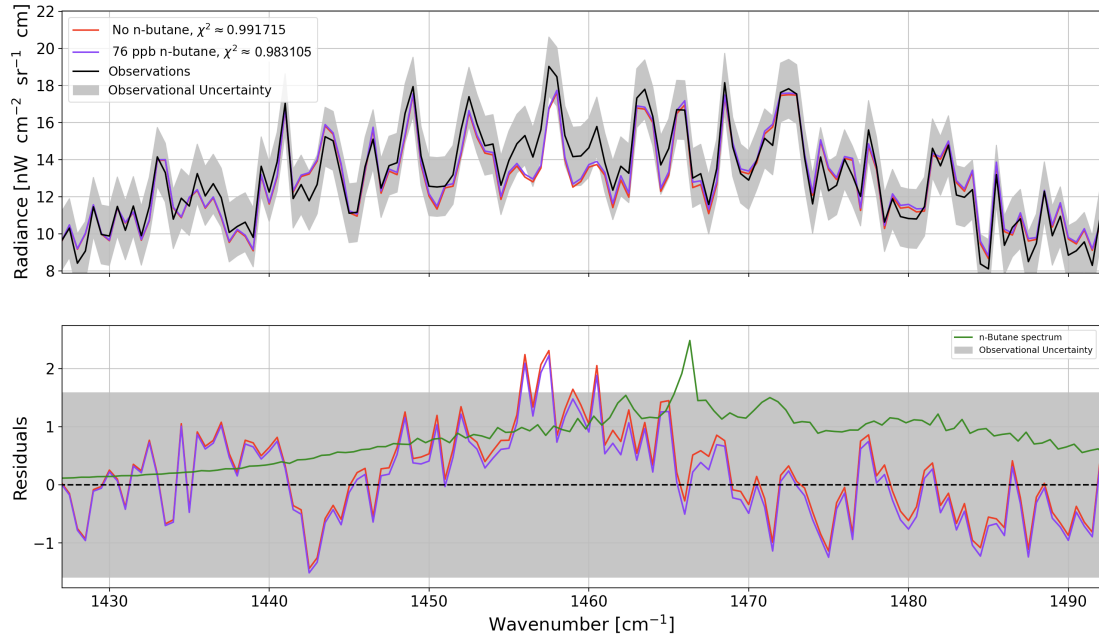


Figure 4.7: One example of the model’s fit to the Cassini CIRS observations. Top panel: the model excluding any n -butane (red curve) and also including approximately 76 ppb n -butane (purple curve), with 1σ noise envelope shown in gray. Bottom panel: residuals (i.e. the data minus the model), which follow the same color scheme, and an additional green curve showing n -butane’s laboratory transmission spectrum at $T = 200\text{K}$ [112], which has been convolved to the 0.5 cm^{-1} CIRS resolution. Note the strong Q-branch of n -butane’s ν_{14} band around 1466 cm^{-1} as we saw in Section 3.4.3, and the fact that even this particularly *strong* vibrational feature has become substantially broadened at CIRS resolution in the green curve for the laboratory n -butane spectrum.

It is easily seen that there are no strong spectral line features that are fitted to below the noise floor when n -butane is added to the model, and instead that *aggregate* improvement is observed upon the addition of n -butane (i.e. the purple

residuals tend to be closer to zero than the red residuals). This description is true of all of the other CIRS results associated with this dissertation as well. Keeping this in mind, no explicit detection of *n*-butane is claimed from this CIRS modeling work; instead, only a comprehensive set of upper limits on Titan's *n*-butane abundance at various ranges of altitudes for each of the three datasets can be provided. Additionally, the statistical significance of the improvement to the model's fit when various amounts of *n*-butane are added to the model is also provided. This process will be described in much more detail in the following Section [4.2.4](#).

Before displaying any more results from this study, it is worth discussing a few more aspects of the modeling process and methodology. Figure [4.8](#) contains an example of the normalized temperature contribution functions of the model, in the region of the ν_4 band of methane. For the unfamiliar reader, the contribution functions of a radiative transfer model retrieval are a measurement as a function of wavenumber and altitude of the sensitivity of the model and the observations it seeks to replicate. These are often used, in particular, to identify the altitude range for which the information retrieved in a NEMESIS calculation is most valid. With that said, it can be seen that particularly strong sensitivity to the 175-350 km altitude range (stratospheric altitudes for Titan) is attained in the sample shown.

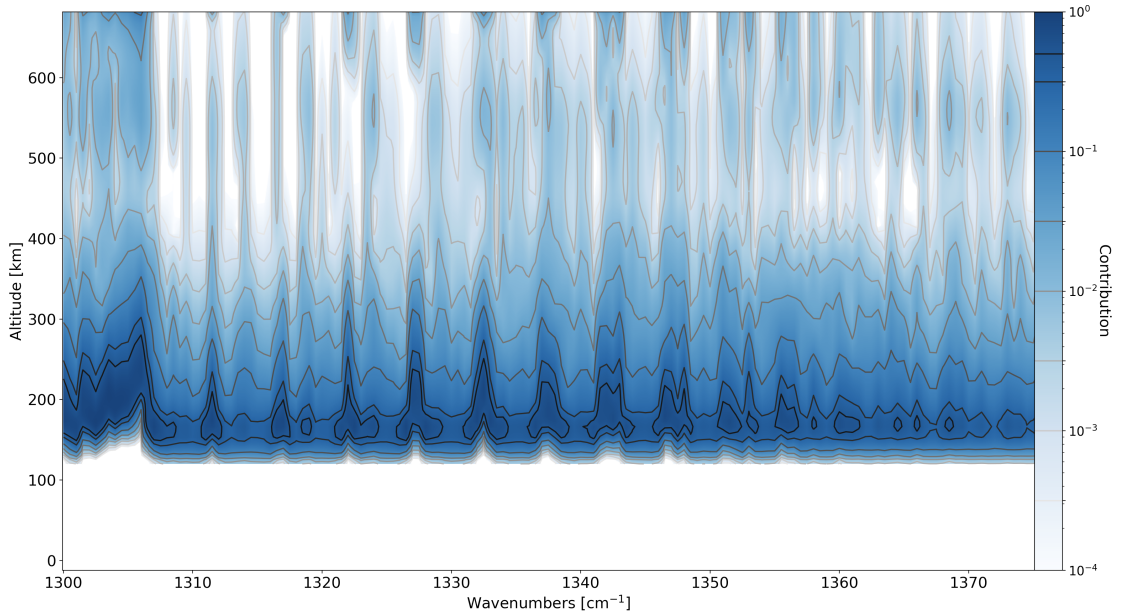


Figure 4.8: Normalized temperature contribution contour plot for the EQ data in the 136-216 km altitude range, showing high sensitivity corresponding to that particular altitude range, as expected. The regions of strong sensitivity to temperature in terms of the wavenumber axis correspond to the individual transitions in methane’s ν_4 band, since it is the methane abundance that we hold constant as the temperature profile is varied during the NEMESIS calculation in order to fit the observations. Hence, this aspect explains why the ‘ghost’ of a methane spectrum can be seen in a figure like this. Spooky...

If we compare the approximately 175-350 km range of altitude sensitivity revealed by Figure 4.8 to the temperature retrievals of Figure 4.6, it can be seen that, depending on the latitude of the data set in question, this altitude range typically corresponds to temperatures ranging from about 160 K to 200 K. This is extremely important to appreciate, with respect to the fact that the n -C₄H₁₀ pseudoline list was derived from spectra gathered at temperatures of at least 180 K; the n -butane pseudoline list is technically only valid for modeling emissions from temperatures of 180 K or larger. Thus, a potential limitation in the analysis is observed here. It may be worth noting, however, that that this limitation is unlikely to be severe,

given that the n-butane transmission spectra and cross sections were observed to change smoothly as a function of decreasing temperature in the work described in the first half of Chapter 3. This limitation could be considered *more* problematic, however, in the retrievals for the T3 and T35 data sets, which, being drawn from northern polar latitudes, correspond to colder temperatures in the lower stratosphere. We will return to this point when summarizing our conclusions for the full dissertation work, in Chapter 5.

With that said, the final step in the process is to actually determine upper limits on the abundance of n-butane in each of the sets of observations, for each of the n-butane abundance profiles that were tested. This is accomplished with the following procedure: from the χ^2 goodness-of-fit metrics which result from the models with an n-butane abundance q , and from the χ^2 of the original n-butane-free model (i.e. $q = 0$), the difference in χ^2 's, $\Delta\chi^2 = \chi_q^2 - \chi_0^2$ is calculated, and then plotted as a function of n-butane abundance q .

It is important to state that for this case, χ^2 is defined as $\sum_{\alpha} [(D_{\alpha} - M_{\alpha}) / \sigma_{\alpha}]^2$, where D_{α} is the data spectrum, and M_{α} is the model spectrum, and σ_{α} is the estimate of the spectral noise, with index α covering each spectral point in the observations. A good fit will occur when $\chi^2 \approx n - m$, with n being the number of spectral points, and m being the number of degrees of freedom in the calculation. In this case, the number of degrees of freedom is the number of parameters to be retrieved by NEMESIS. A scalar retrieval for an abundance profile is a single degree of freedom, but, for example, a retrieval of a spatial *profile* on an altitude grid with a total of η points is η degrees of freedom, since there will be η parameters that will be varied throughout the calculation.

The $\Delta\chi^2$ curve which results from this process marks an improving fit to the

observations as its value decreases below zero. Conversely, as $\Delta\chi^2$ increases above zero, this marks a degrading fit to the data. Additionally, if a negative minimum of the $\Delta\chi^2$ curve exists and has a value β^2 , this will imply an improvement to the model's fit to the data of statistical significance equal to $\beta\sigma$, relative to the *n*-butane-free model. After its minimum, the $\Delta\chi^2$ curve is bound to become positive and increasing. Where it does so and reaches a value ϵ^2 , this will mark an upper limit on the *n*-butane abundance of statistical significance $\epsilon\sigma$.

This procedure was executed for three different abundance profiles for *n*-butane. This is a potentially useful component of the investigation, given that not only do we not know whether any *n*-butane is present in Titan's atmosphere, but if it *is* present, we also do not know what its altitude-abundance profile looks like. We do, however, have several predictions from photochemical models to use as preliminary guesses. The profiles that were tested are the following:

1. A step function profile (i.e. constant profile), which turns on at 70 km above Titan's surface and then remains constant above that point.
2. The photochemically predicted profile for butane from Krasnopolsky et al. (2009) [64].
3. The photochemically predicted profile for butane from Loison et al. (2019). [65].

Each of these profiles is depicted in Figure 4.9.

Figure 4.10 contains the contribution functions from *n*-butane, which display the altitudes at which each of the spectra that were modeled is sensitive specifically to the possible *n*-butane emission, for each of the three *n*-butane profiles that were tested.

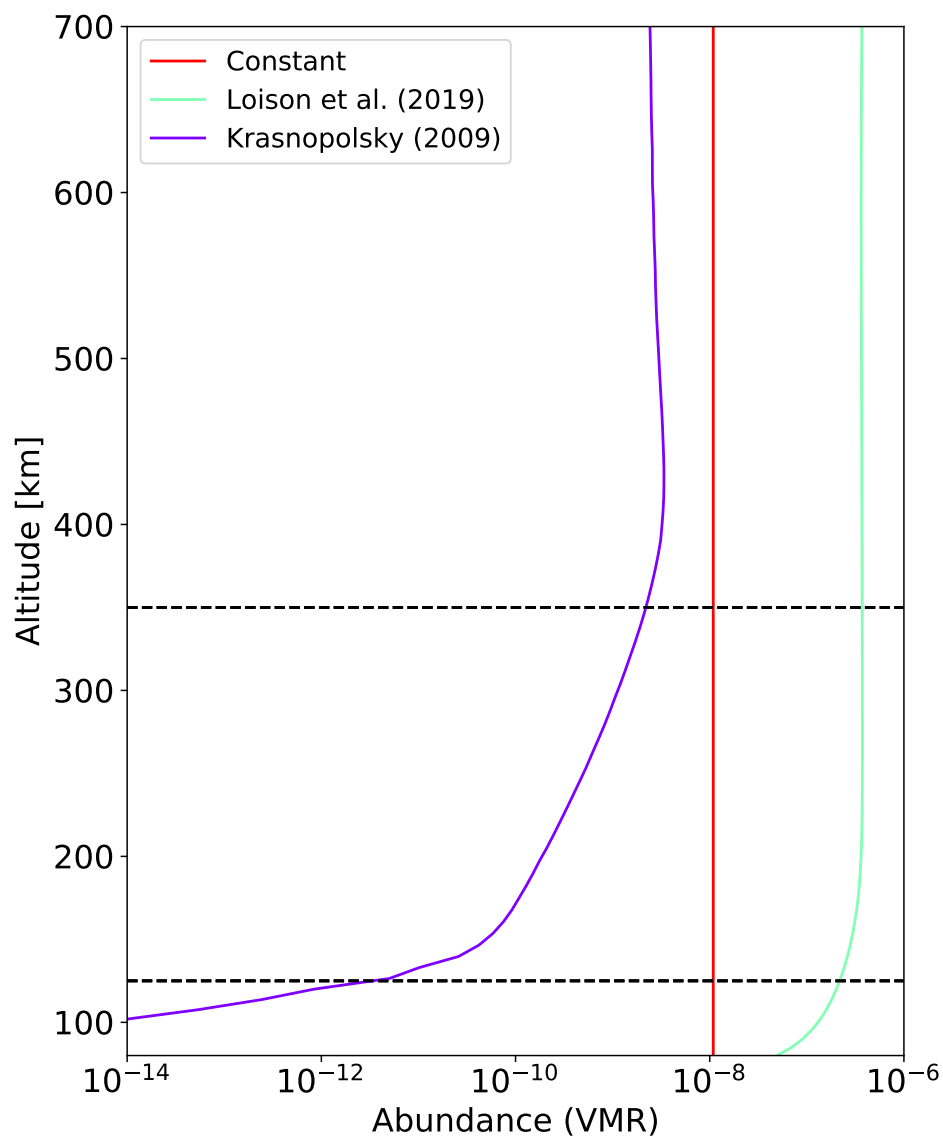


Figure 4.9: The dependence of the *n*-butane upper limit calculations on three different altitude profiles is explored here. The black horizontal dashed lines approximate the range of altitudes in which my models and observations are most sensitive. See Figures 4.8 and 4.10 regarding this sensitivity. Note that ultimately, the placement of the red curve (constant profile) is rather arbitrary in a figure such as this, since my analysis will involve scaling it to achieve a set of differing abundances.

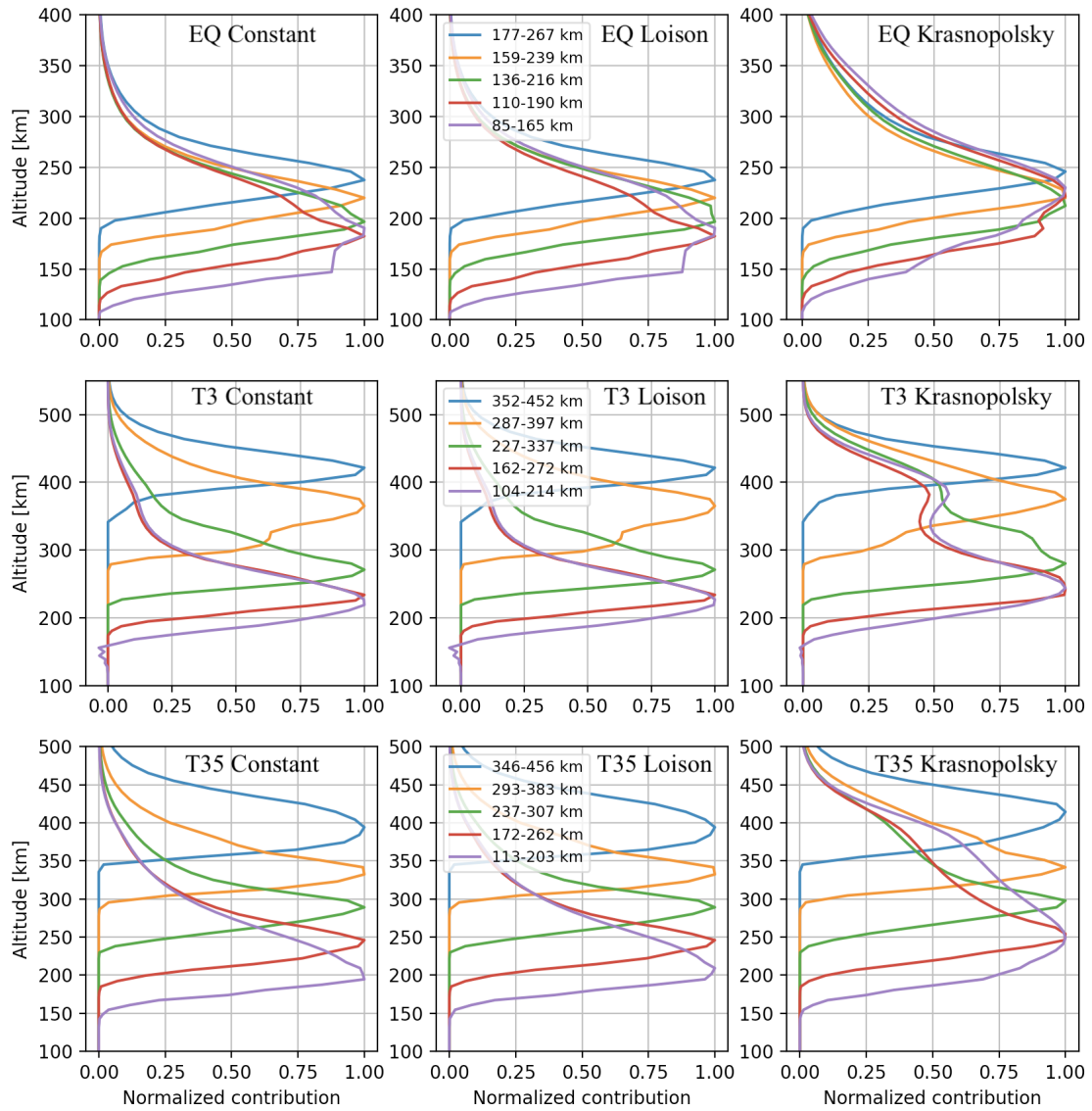


Figure 4.10: The n -butane contribution curves at 1465 cm^{-1} (very close to the Q-branch of the strong ν_{14} band of n -butane) for each of the nine cases that were explored (i.e. three different data sets, three different profiles). All of the n -butane results which follow will be reported at the altitudes corresponding to the peaks shown for these curves. Please note that the legends appearing in the central panels also apply to the other two panels in that row, which belong to the very same data set.

The results are best depicted by the aforementioned $\Delta\chi^2$ curve – concept. Thus, to close this section, a single sample of one of these curves is shown in Figure 4.11. This example was obtained from the EQ data and utilized the constant *n*-butane profile. This example shows that though the addition of *n*-butane to the model (especially with abundance of about 80 ppb) *will* improve the fit to the data, the significance of this improvement is not very substantial, at 1.25σ . $\Delta\chi^2$ curves for all three data sets, their corresponding altitudes, and the other *n*-butane profiles that were tested are contained in Section 4.2.4. Additionally, that section contains a full tabulation of those results, which display the upper limits and their corresponding *n*-butane abundances.

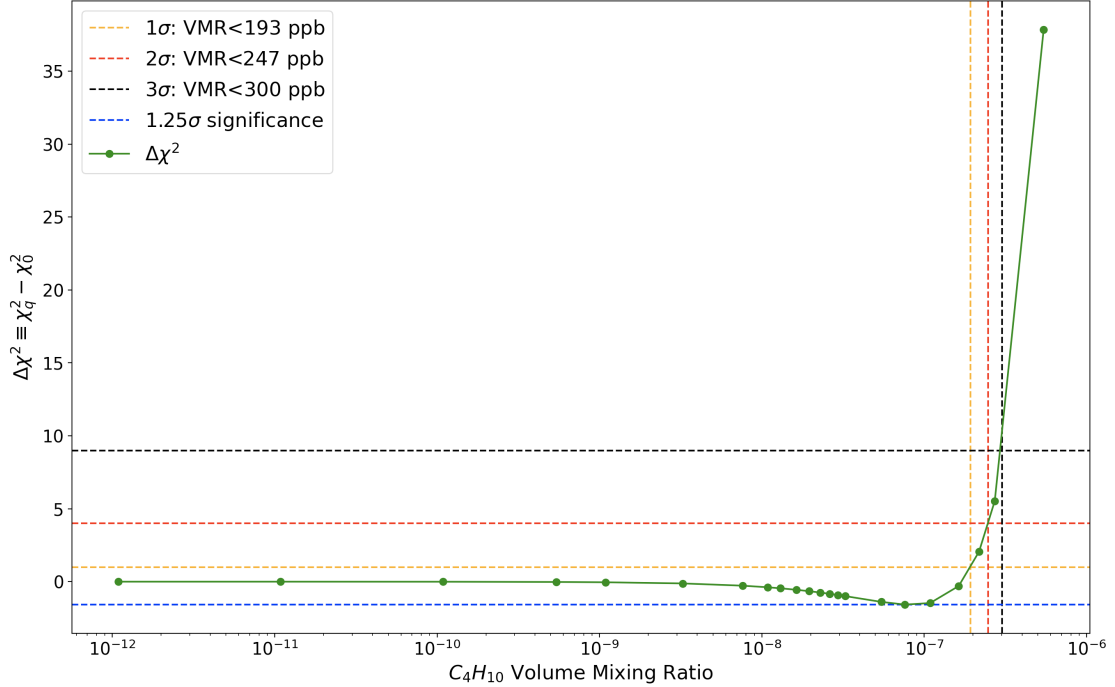


Figure 4.11: Sample $\Delta\chi^2$ curve, this one belonging to the EQ data, 136-216 km altitude range, and using the constant n -butane profile. The fit improvement is seen to be maximized for an n -butane abundance of roughly 80 ppb, although the significance of that improvement, statistically speaking, is fairly small at 1.25σ . All of the $\Delta\chi^2$ curves display 1, 2, and 3σ upper limits, as denoted in the legend. These are marked by colored dashed vertical lines at their corresponding abundances. Additionally, the minimum of the $\Delta\chi^2$ curve (if present) is marked by a blue dashed horizontal line, and quantified in the legend.

4.2.4 CIRS Modeling - N -Butane Upper Limit Results

The full tabulated results of this study are now presented, in the form of 1, 2, and 3σ upper limits on the abundance of n -butane at various altitudes in Titan's atmosphere for the three datasets, assuming one of the three abundance profiles that were tested. Results for the equatorial (EQ) data are contained in Table 4.3. Results for the two polar data sets, T3 and T35, are contained in Tables 4.4 and 4.5 respectively.

In these tables, the column labeled “ID” refers to which of the 5 spectra from that data set the results belong to. Recall that each of these data sets was generated from limb observations gathered during flybys, and they are therefore sensitive to a range of altitudes. The observations were organized into five altitude ‘bins’, differentiated by their “ID” in these tables; these were created by coadding dozens or hundreds of spectra from the same altitude range. The reported altitudes in these tables here are the altitudes at which the associated *n*-butane contribution functions peak (see Figure [4.10](#)).

Table 4.3: Upper Limits for EQ Data, derived from $\Delta\chi^2$ curves, using the constant profile, and the photochemically predicted profiles of Loison et al. (2019) [65] and Krasnopolsky et al. (2014) [146]. These are reported at the peak altitudes of the *n*-butane contribution functions shown in Figure 4.10. Strengths of the resulting minima in the curves (also measured in σ) are shown as well, in addition to the gas abundance (in ppb) corresponding to that minimum.

Profile	ID	Alt. (km)	1σ (ppb)	2σ (ppb)	3σ (ppb)	Min. (σ)	Abundance (ppb)
Const.	1	190	166	214	272	1.23	76
	2	183	162	214	274	1.11	76
	3	197	192	246	299	1.25	76
	4	220	169	230	292	0.98	76
	5	238	143	212	282	0.72	54
Loison	1	185	186	239	304	1.21	40
	2	180	174	229	294	1.12	74
	3	200	199	254	320	1.26	74
	4	220	173	234	303	0.98	92
	5	240	146	214	287	0.72	74
Kras.	1	225	99	131	167	1.15	54
	2	225	77	101	130	1.12	46
	3	215	111	142	179	1.27	31
	4	230	111	152	196	0.99	46
	5	248	102	150	203	0.72	47

Table 4.4: Upper Limits for T3 Data. Note that the ellipses marking empty entries in the table correspond to instances where a minimum in the $\Delta\chi^2$ curve was not observed at all.

Profile	ID	Alt. (km)	1σ (ppb)	2σ (ppb)	3σ (ppb)	Min. (σ)	Abundance (ppb)
Const.	1	220	423	623	864	0.66	163
	2	230	336	527	718	0.55	109
	3	270	177	367	556
	4	375	381	703	1046	0.15	54
	5	420	861	1675	2521	0.73	0.01
Loison	1	220	427	643	874	0.66	149
	2	230	339	530	733	0.55	112
	3	270	178	370	563
	4	375	384	716	1030	0.15	55
	5	420	678	1540	2449
Kras.	1	235	190	289	392	0.61	63
	2	235	149	232	323	0.54	51
	3	285	107	222	337
	4	385	397	739	1069	0.15	50
	5	415	706	1619	2550

Table 4.5: Upper Limits for T35 Data

Profile	ID	Alt. (km)	1 σ (ppb)	2 σ (ppb)	3 σ (ppb)	Min. (σ)	Abundance (ppb)
Const.	1	200	212	330	456	0.57	76
	2	250	87	187	289
	3	290	85	224	369
	4	340	325	585	859	0.19	55
	5	395	552	1102	1653
Loison	1	200	216	337	466	0.57	62
	2	250	88	190	292
	3	290	85	225	373
	4	340	325	595	862	0.19	56
	5	395	551	1080	1619
Kras.	1	250	78	123	169	0.53	75
	2	250	53	113	173
	3	300	64	168	280
	4	345	266	485	709	0.18	56
	5	415	577	1140	1709

In addition to the tabulated results, and the $\Delta\chi^2$ curves to be shown later, another convenient way to display the *n*-butane upper limits that were derived in this work is seen in Figures 4.12-4.14. These figures show the three *n*-butane abundance profiles that I tested, overlaid with the retrieved 1, 2, and 3 σ upper limits. As before, those upper limits are shown at the altitude for which the respective *n*-butane contribution function peaks (Figure 4.10).

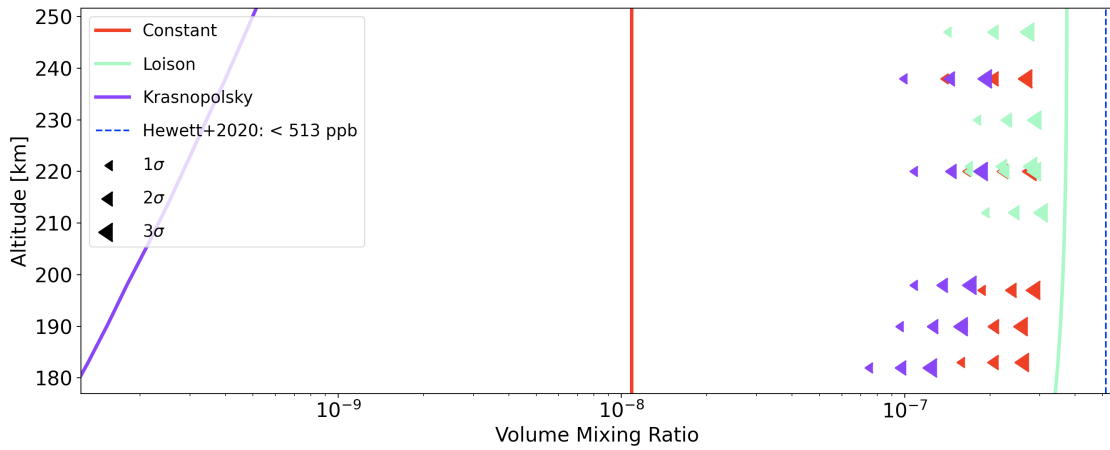


Figure 4.12: 1, 2, and 3σ upper limits for the abundance of n -butane, marked by left-pointing arrows, for the EQ data set. The upper limit point colors correspond to the similarly colored profile curves. The blue, vertical dashed line marks the upper limit of 513 ppb which was derived by Hewett et al. (2020) [92], to be discussed further in Section 4.2.4.

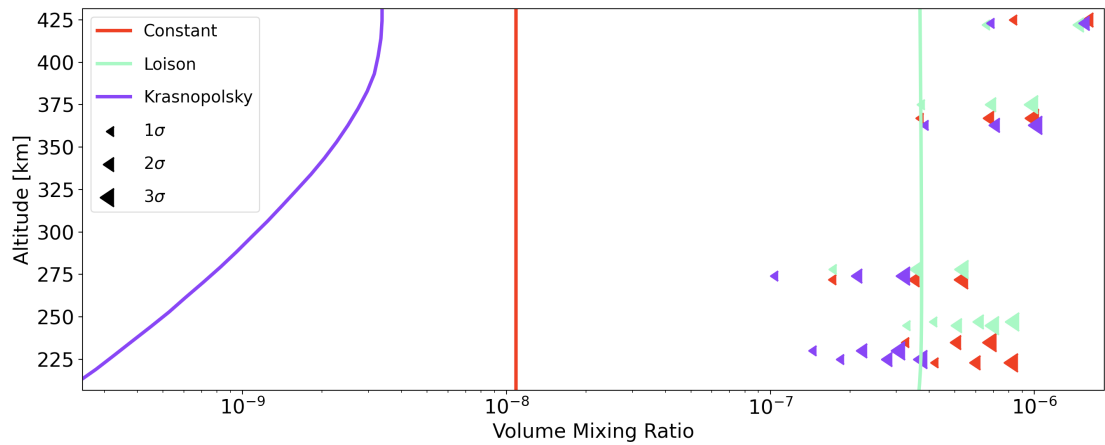


Figure 4.13: 1, 2, and 3σ upper limits for the abundance of n -butane, marked by left-pointing arrows, for the T3 data set. The upper limit point colors correspond to the similarly colored profile curves.

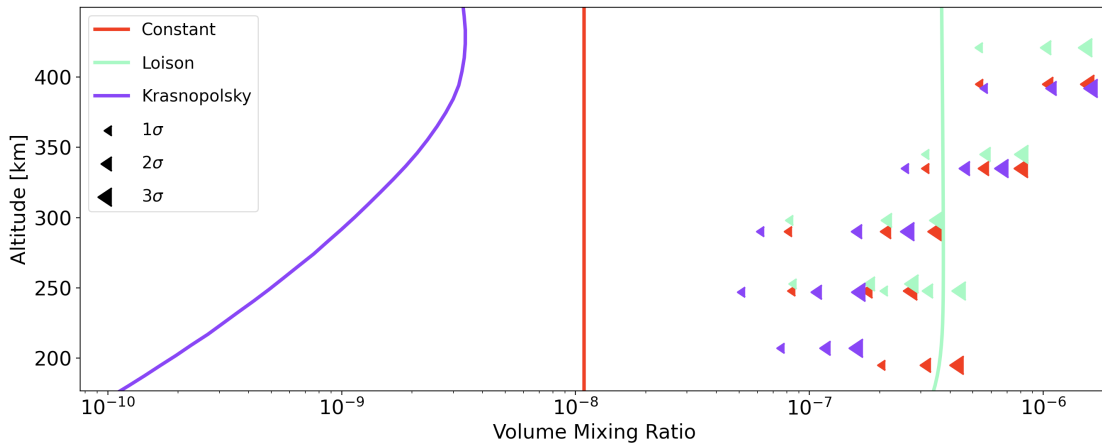


Figure 4.14: 1, 2, and 3σ upper limits for the abundance of n -butane, marked by left-pointing arrows, for the T35 data set. The upper limit point colors correspond to the similarly colored profile curves.

Finally, the full set of $\Delta\chi^2$ curves that were retrieved from the three sets of data are now displayed. These are shown in Figures 4.15-4.23. Each figure corresponds to the upper limits retrieved for a particular dataset, using a particular n -butane abundance profile. Also, each figure contains five individual panels, which, from top to bottom, correspond to lowest to highest altitude bin (i.e. Spectrum ‘ID’, in Tables 4.3-4.5) for the dataset.

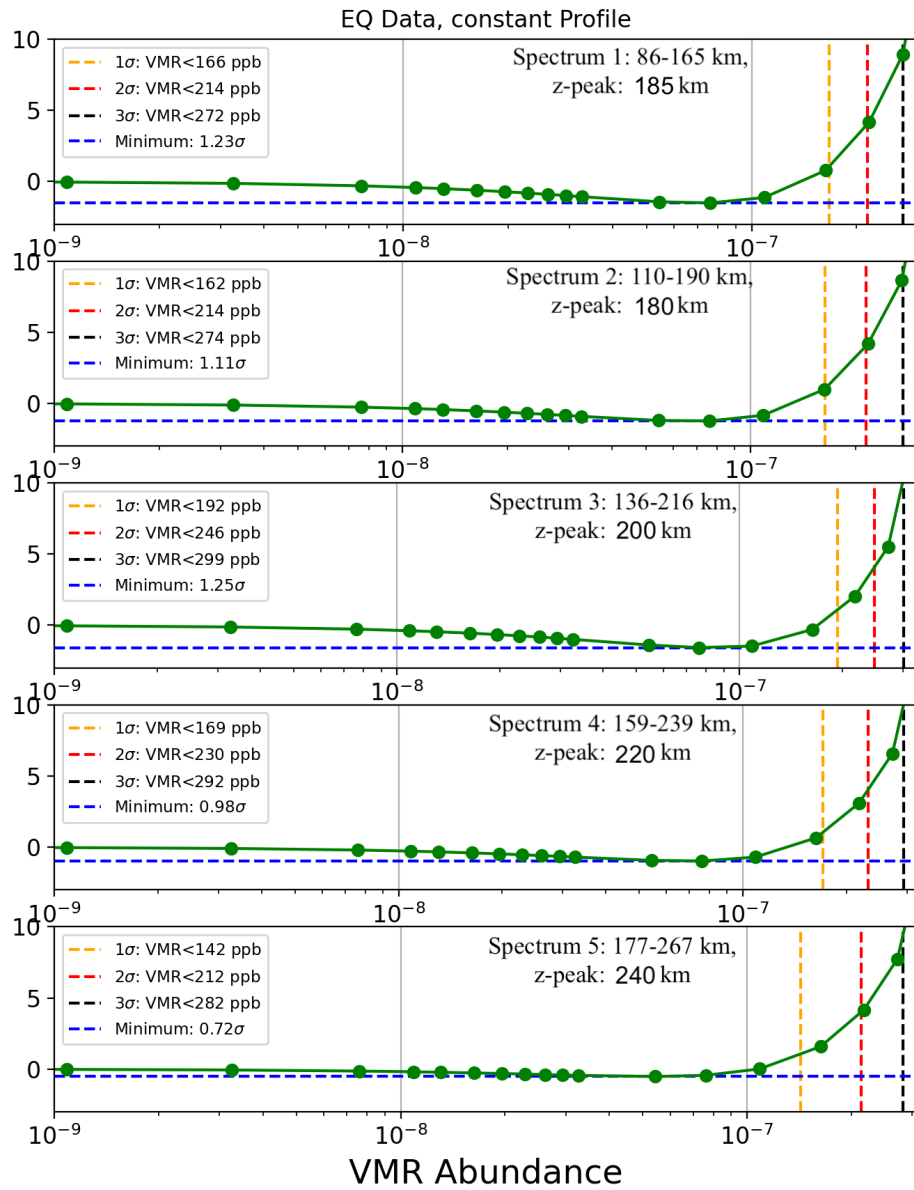


Figure 4.15: $\Delta\chi^2$ curve for EQ data, using the constant n -butane profile.

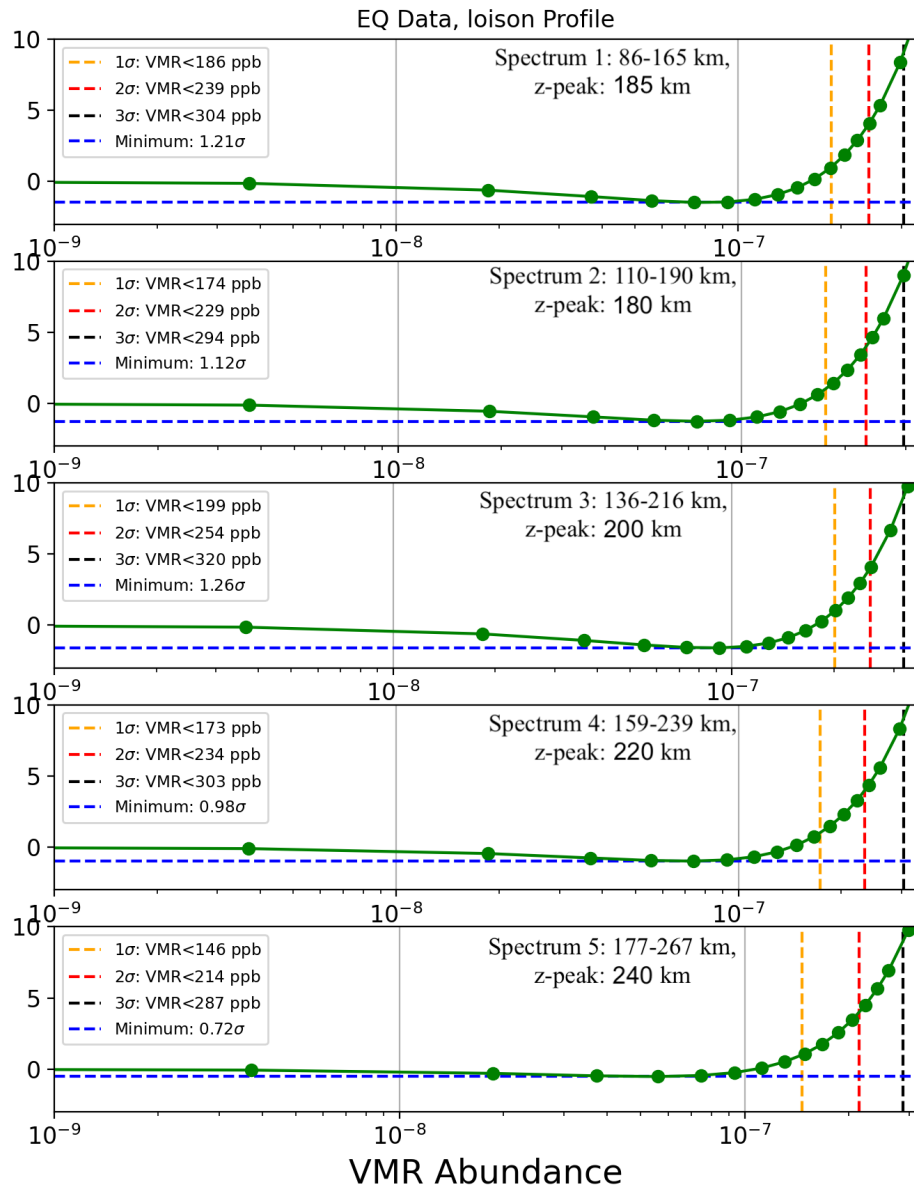


Figure 4.16: $\Delta\chi^2$ curve for EQ data, using the Loison *n*-butane profile.

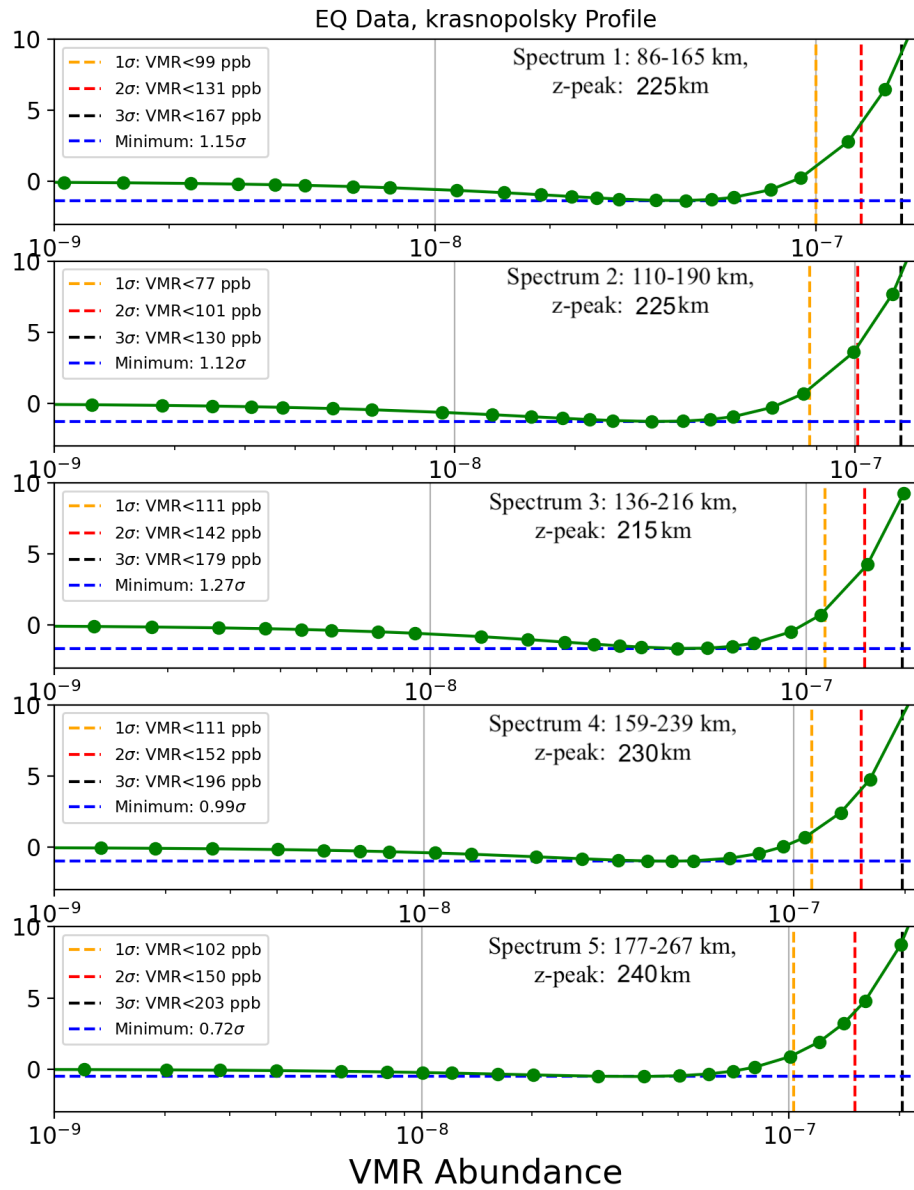


Figure 4.17: $\Delta\chi^2$ curve for EQ data, using the Krasnopolsky *n*-butane profile.

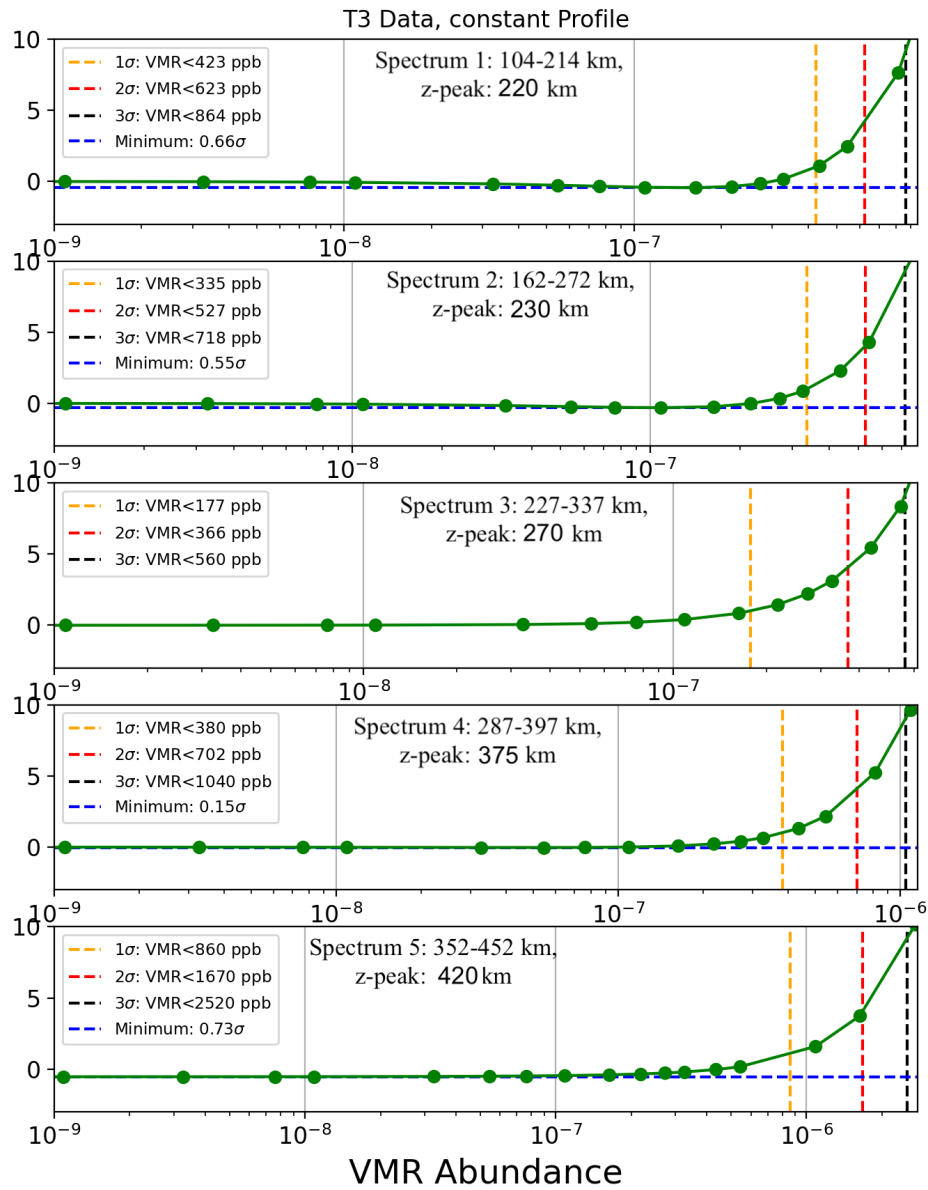


Figure 4.18: $\Delta\chi^2$ curve for T3 data, using the constant *n*-butane profile.

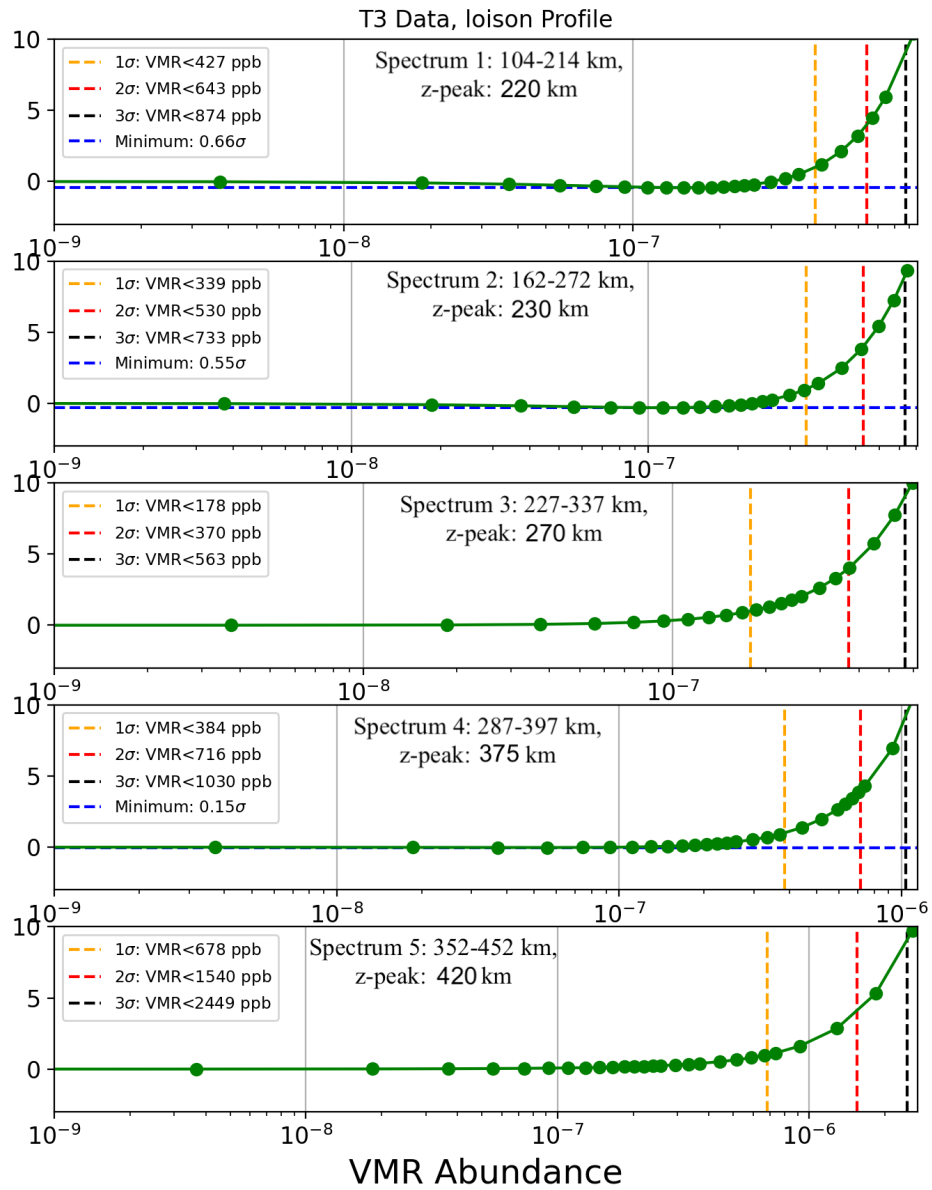


Figure 4.19: $\Delta\chi^2$ curve for T3 data, using the Loison *n*-butane profile.

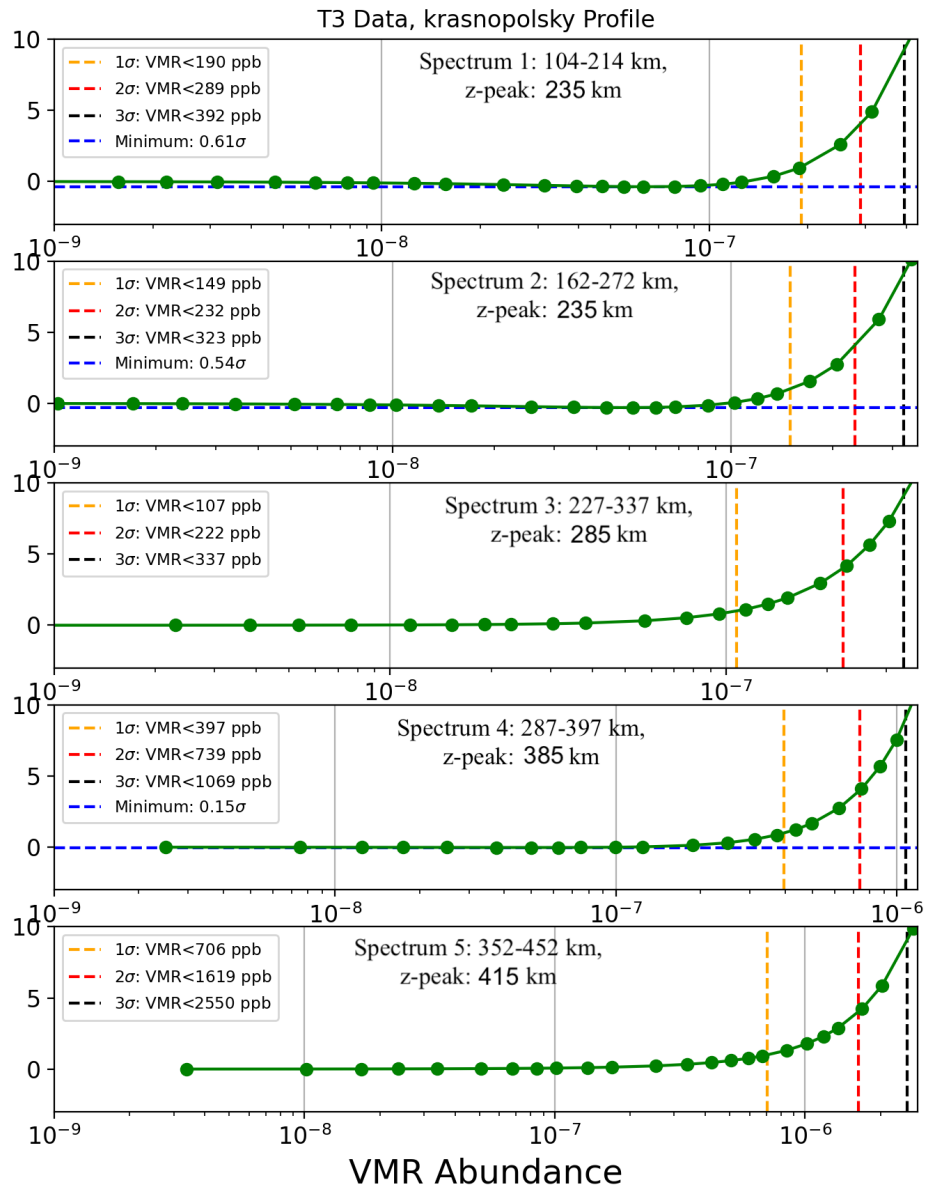


Figure 4.20: $\Delta\chi^2$ curve for T3 data, using the Krasnopolsky *n*-butane profile.

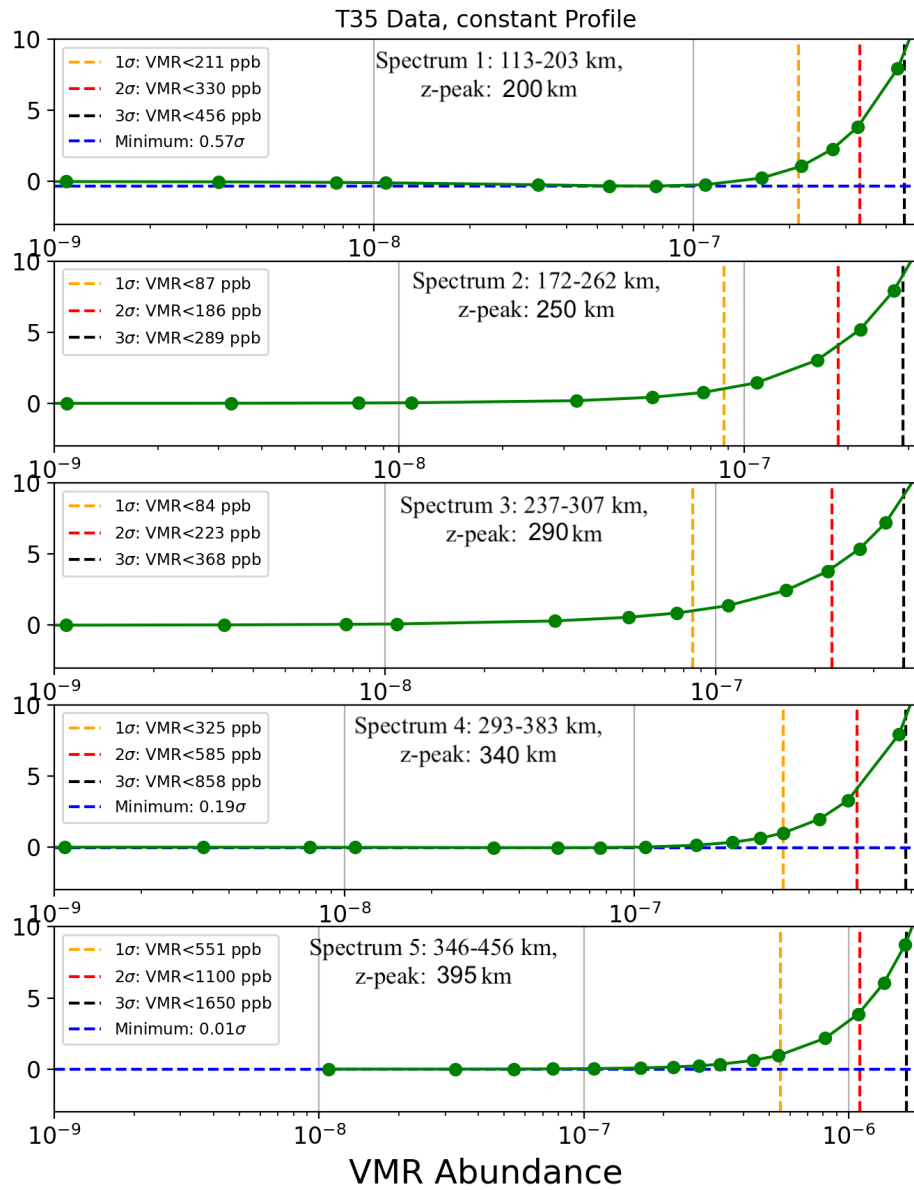


Figure 4.21: $\Delta\chi^2$ curve for T35 data, using the constant *n*-butane profile.

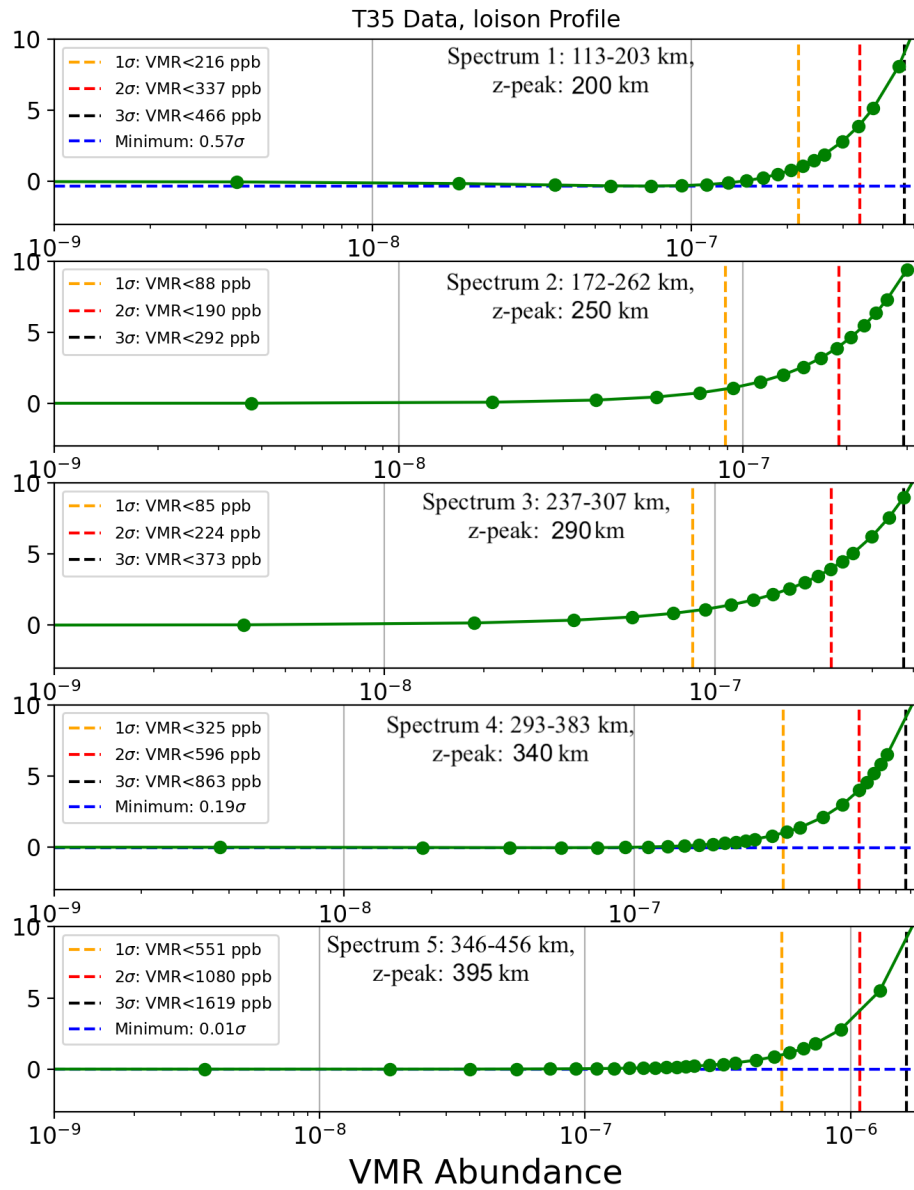


Figure 4.22: $\Delta\chi^2$ curve for T35 data, using the Loison *n*-butane profile.

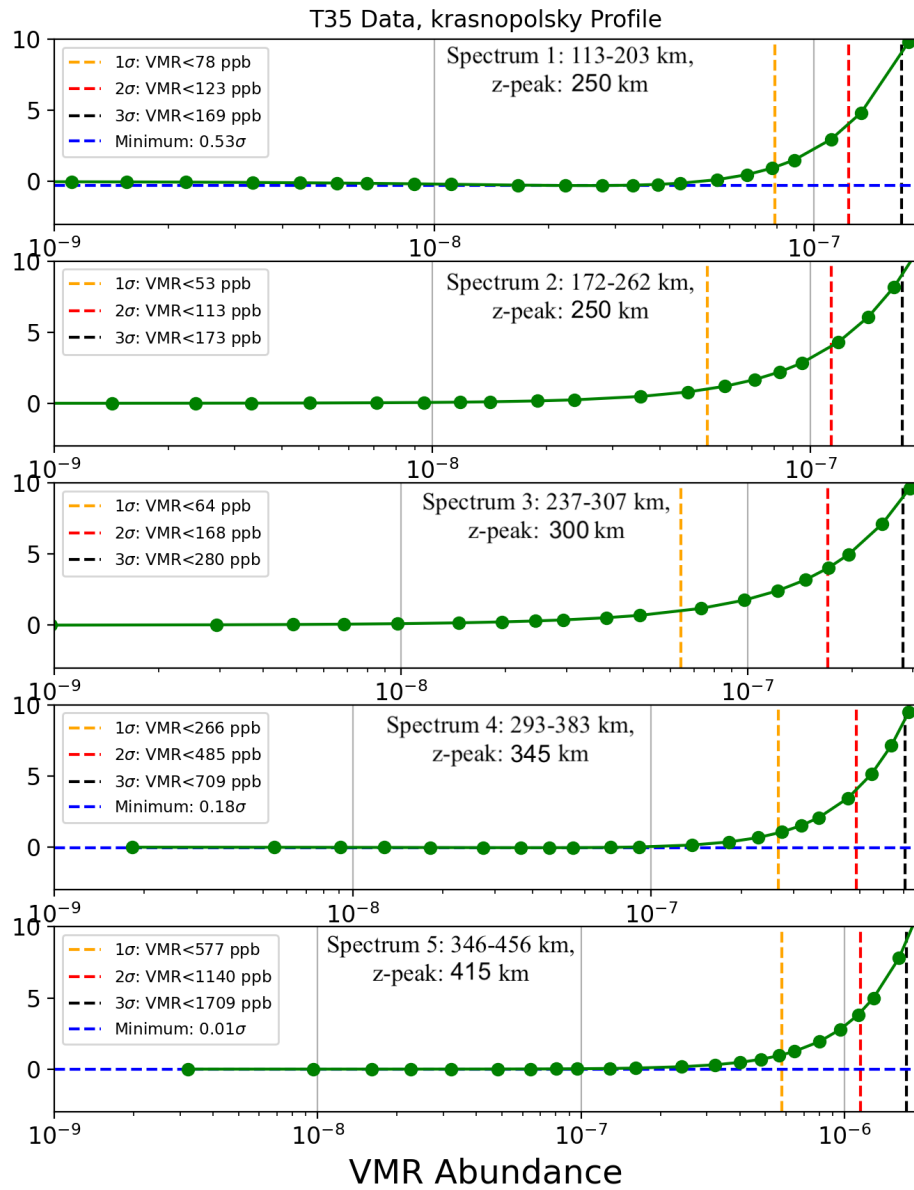


Figure 4.23: $\Delta\chi^2$ curve for T35 data, using the Krasnopolsky *n*-butane profile.

4.2.5 CIRS Modeling - *N*-Butane Discussion

N-butane, predicted to be a resident molecule in Titan’s atmosphere by multiple photochemical models [63; 98; 64; 147; 65; 66], has eluded all detection efforts thus far, including this one, the reader has now seen. In some cases, though, these results *do* provide some tentative evidence for *n*-butane’s presence in Titan’s atmosphere, though looking at these results alone, it is obvious that there is more work to be done. In Section 4.3, the ‘next steps’ taken along those lines, toward *further* constraining *n*-butane’s abundance, will be described. First, however, a closer discussion of a few aspects of this first set of results is warranted.

A few years ago, Hewett et al. (2020) [92] used previously gathered infrared cross-section measurements of *n*-butane to derive a 513 ppb upper limit for *n*-butane’s abundance at Titan. The cross-sections they implemented came from the Pacific Northwest National Laboratory (PNNL) [115], and those measurements were obtained at 278 K. As that particular temperature is closest to (although still quite a bit warmer than) the retrieved stratospheric temperatures for the EQ data of this work, it is perhaps useful to begin by comparing those results. It can be seen in Figure 4.12 and Table 4.3 that each of the 3σ upper limits is in fact consistent with the 513 ppb result of Hewett et al. (2020) [92]. For instance, when using the Loison profile, abundances less than 320 ppb were found in the stratosphere for the equatorial data, with 3σ confidence. And when using the constant *n*-butane profile, similar upper limits in the same altitude ranges were found. Similar upper limits were found using the Krasnopolsky profile as well.

One chief advantage associated with the approach featured in this dissertation with respect to the methodology of Hewett et al. (2020) is the use of the high-resolution *n*-butane pseudoline list (Section 3.4.4) to actually *model* the potential

n-butane emissions. That pseudoline list, as stated before, is the most up-to-date and detailed spectroscopic representation of *n*-butane at cold, Titan-appropriate temperatures and N₂-broadened pressures. It is also worth restating that high resolution, cold-temperature pseudoline lists for both propane [88] and propene [90] were also implemented in the modeling of the CIRS observations.

With that said, while the use of these pseudoline lists does constitute an advantage to the approach, it does bear repeating that they are not perfect! Though collected expressly for the purposes of modeling emissions for specific species in Titan-like conditions, often the extremely lower temperatures of Titan's lower stratosphere ($T \leq 160$ K) cannot be obtained in the laboratory without the risk of causing condensation to occur within the gas cell. As noted earlier, while this should be regarded as a limitation to the analysis described in this chapter, it is unlikely to be a severely limiting one, in terms of the modeling framework's ability to correctly detect *n*-butane's emissions or to confidently constrain its abundance to various upper limits, within the stated confidence intervals.

It is worth noting that *n*-butane is very likely to condense in Titan's upper troposphere, slightly below the 'activation altitude' at which the constant profile used in this work 'turns on'. For instance, according to a recent study by Barth et al. (2017) [148], who modeled the microphysics of cloud formation in the atmosphere of Titan, *n*-butane is likely to condense at an altitude of 65 km above Titan's surface. Thus, the constant profile that was utilized in this dissertation is validated by that study.

Lastly, it is interesting to examine the upper limits shown in Figure 4.12 for the equatorial data and observe that the photochemically predicted altitude profile from Loison et al. (2019) [65] appears to potentially be ruled out in the case of

these equatorial latitudes, across the entire altitude range of sensitivity; each 3σ *upper* limit corresponds to an abundance of about 15% *lower* than the abundance predicted by that profile. It is important to recall, however, that the Loison photochemical model (and all other photochemical models discussed in this dissertation) do not distinguish between the two different C_4H_{10} isomers: *n*-butane, and *iso*-butane, which are spectroscopically distinct. No attempt was made in this work to quantify the contribution of isobutane emissions in these observations, choosing instead to leave that as future work. For this reason, it is not strictly correct to claim that my analysis rules out the Loison profile.

With that noted, this section is brought to a close with a discussion of another vital limitation in the methodology and analysis described in this chapter, all of which is purely statistical in nature. The $\Delta\chi^2$ definition, as discussed in Section 4.2.4, naturally relies on the estimate of the spectral noise level in the observations. The spectral noise was assumed to be Gaussian, or to have white noise properties, which could be estimated well by the RMS across the spectral residuals from preliminary fittings. In certain cases, particularly the EQ data, the residuals do show that this assumption is not perfectly valid (e.g. Figure 4.7), and that, for example, a vibrational band of at least one gas, likely either ethane (C_2H_6) or propane (C_3H_8), may not be fit perfectly well by the model. The results' dependence on this component were tested by first retrieving propane and ethane *altitude profiles*, instead of just scaling factors for the *a priori* altitude profiles. While some improvements could be seen in the fit (i.e. smaller and more white-noise-like residuals) using this alternative methodology, the improvement was not very significant, and mattered very little in the context of the subsequent $\Delta\chi^2$ analysis with *n*-butane. Because of this, it is suspected that a large portion of the

non-Gaussian and continuum-like features that are occasionally observed in the residuals of the results are arising from imperfect fitting of aerosols and hazes in that particular spectral region. This could be improved in the future by implementing more sophisticated models of Titan’s aerosols and hazes. For instance, one approach of merit could be to implement the 4-haze model described in de Kok et al (2007) [149], which features four different types of haze with various absorption cross sectional profiles and altitude abundance profiles.

4.2.6 *N*-Butane Modeling - Conclusion

Using previous results from the JPL Molecular Spectroscopy Laboratory, a comprehensive set of new upper limit constraints on the abundance of *n*-butane in the stratosphere of Titan has been derived, as observed by Cassini CIRS. These upper limits were obtained for three different atmospheric abundance profiles, either photochemically predicted, or otherwise set as constant above an altitude of 70 km [64; 65]. Results for the equatorial dataset are consistent in all cases with the previous upper limit established by Hewett et al. (2020). Though certainly no claim of a firm detection of *n*-butane is made by this work, some tentative evidence for the molecule’s presence in Titan’s stratosphere is instead demonstrated.

In addition to helping to further constrain *n*-butane’s role in photochemical models of Titan’s atmosphere in future work, these results will also inform the continued investigation of Titan’s elusive C₄ hydrocarbons, as will be discussed in this following section.

4.3 NASA Infrared Telescope Facility

Though the *manuscript* for the *n*-butane modeling was still a work in progress come early 2021, the results of that study were essentially in at that time, and it was quite clear that higher resolution observations were required in order to continue the *n*-butane investigation in earnest (rather than, say, investing further time in an investigation of additional CIRS data from other Cassini flybys). Right around that time, NASA IRTF put out a call for 2021 Semester B proposals, and with much help from Conor Nixon, I led the drafting of a proposal designed to target *n*-butane emissions from Titan in the vicinity of the gauche conformer’s ν_{33} band at 955 cm^{-1} and the trans conformer’s ν_{35} band at 964 cm^{-1} . These bands are not quite as strong as the ν_{14} band up at 1466 cm^{-1} , but they could still be detectable by IRTF. Moreover, focusing on this region *also* allowed us to search for what we had preliminarily identified as the strongest *trans*-2-butene vibrational mode (though I had yet to actually measure its cross-sections at JPL). As discussed earlier in Section 3.5, *trans*-2-butene is also predicted to be present in trace abundances in Titan’s atmosphere by photochemical models [63; 146; 147; 65; 66; 67], was observed to be one of many major products formed during the irradiation of ethane ices in simulated Titan conditions in the laboratory [69], and may form up to 1% by volume of Titan’s lakes and seas [71].

We proposed to use the Texas Echelon Cross Echelle Spectrograph (TEXES) [39] instrument with IRTF. We selected the TEXES instrument for our proposal for a number of reasons:

- TEXES covers the desired mid-infrared wavenumber range for the two target gases (the 956 and 964 cm^{-1} region).

- It also covers the ν_4 band of methane (1200-1400 cm^{-1}). This is important for retrieving temperature profile information, which as we saw in Section 4.2.3 is crucial to the modeling process.
- TEXES has a very high resolving power ($R \sim 100,000$), compared to CIRS, which has $R \sim 2,000$ in the same targeted spectral region.
- Co-Investigator Conor Nixon already had previous experience with TEXES, through Nick Lombardo, a former intern of his, who detected propadiene (C_3H_4) at Titan with IRTF/TEXES a few years back [142].
- The TEXES 2021 Semester B observing window (as opposed to that of other instruments) was late September through early October, and Titan was visible for 4-5 hours through during this time frame, which is ideal, as we needed long integration times in order to detect the potentially weak signals of the targeted trace gases (Figure 4.24).

Ultimately, the proposal was successful and was awarded four full nights of telescope time in September 2021 with IRTF/TEXES. Much of the material contained within the proposal has already been covered elsewhere in this dissertation (i.e. motivations for detecting Titan’s new C_4 hydrocarbons, constraining photochemical models, etc.). However, there is one aspect of this proposal that is new and worth discussing in detail though, namely the calculation of the integration times which were proposed in order to achieve our science goals.

In order to detect *n*-butane and *trans*-2-butene, it was determined that a total of 3.75 hours of integration time on Titan was needed at the 956 cm^{-1} setting and 2.25 hours on the 965 cm^{-1} setting. Those integration times would allow us to make 5σ detections if the abundances of *n*-butane and *trans*-2-butene were each even as

low as 40 ppb. To determine this, we made use of the pseudoline list for *n*-butane (Section 3.4.4) as well as PNNL laboratory spectra for 2-butene [115], combined with previous experience of preliminary modeling of legacy TEXES observations of Titan at similar spectral settings (which are not discussed in this dissertation).

To determine these integration times, NEMESIS was once again used to generate a model of short integration (~ 1 minute-long) TEXES observations from 2010 centered on 966 cm^{-1} . Then, *n*-butane was introduced into the model via the pseudoline list, exploring various scalings of the Loison profile [65]. Next, we calculated the differences between the ‘*n*-butane-free’ model and those with the varying amounts of *n*-butane. Signal strengths for the ν_{35} band were then calculated from these differences. For instance, a model with the nominal Loison profile abundance of 370 ppb caused a signal strength of 8.16 Janskys. The outcome of these calculations can be seen in Figure 4.24.

For *trans*-2-butene, as no line list was available, the same method could not really be applied; instead, we scaled the *n*-butane ν_{35} signal strength by the ratio of band strengths between *trans*-2-butene and *n*-butane, that ratio having been estimated using the PNNL laboratory spectra.

Additionally, in order to retrieve a reliable temperature profile on the 1254 cm^{-1} setting, it was found that we needed a total of 30 minutes of integration time on Titan in order to obtain a sufficiently large signal to noise ratio. That decision was based on modeling of previous TEXES observations of Titan from 2009 at similar settings (centered on 1226 cm^{-1} , with an integration time of 4.3 minutes) within the methane ν_4 band for temperature retrieval purposes.

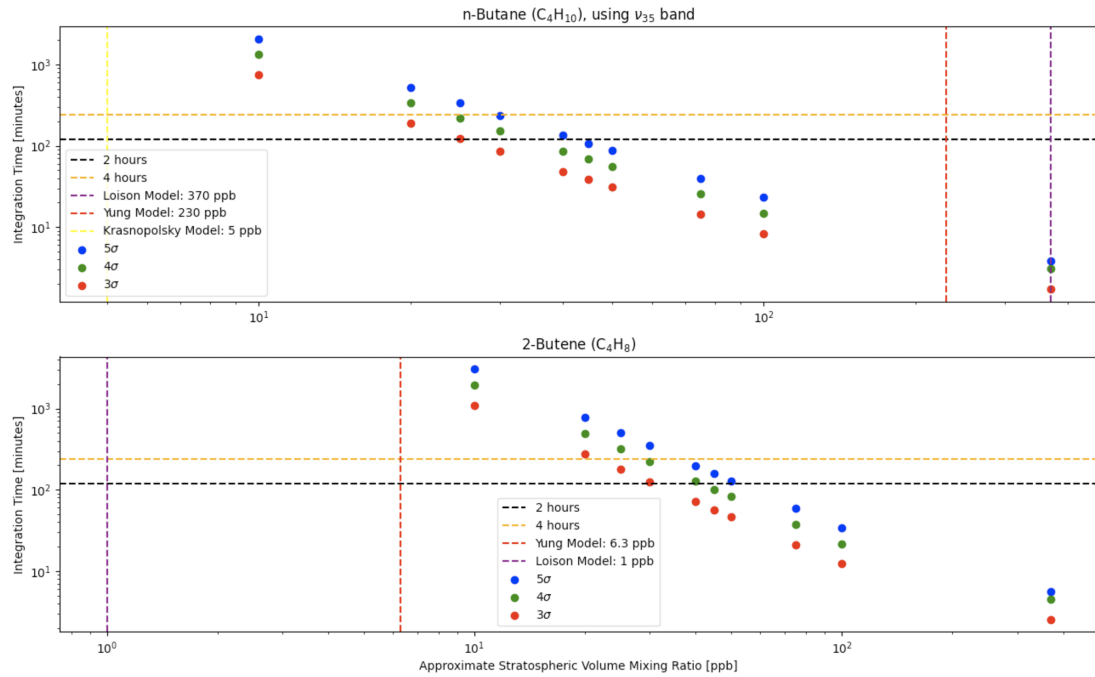


Figure 4.24: Estimated integration times for targeted C_4 hydrocarbons based on profiles from Loison et al. 2019 [65] and scaled to explore a range of possible stratospheric abundances for each molecule. Required integration times for 3, 4, and 5σ detections are shown for a variety of possible abundances. Photochemically predicted abundances for several models are marked by vertical dashed lines.

For nodding a target along the slit, we also requested an additional factor of 2 in overhead to account for time taken in making flats and time lost due to telescope motion. Summarizing, we found that we needed a total telescope time on Titan of 7.5 hours, 4.5 hours at the 956 cm^{-1} and 966 cm^{-1} settings, and one hour on the 1254 cm^{-1} setting. On each night, we also planned to take an observation of a telluric divisor, which would take an additional 30 minutes per night. This brought the total time request to 15 hours.

The determination of integration times, and the determination of overall time requested on the telescope, was by far the most challenging aspect of writing this proposal. It is for that reason that this description was included here in this

dissertation, in the hopes that it may provide guidance to a future Florida Tech student who finds themselves in a similar situation, writing an important observing proposal for the first time with no prior experience.

4.3.1 The Texas Echelon Cross Echelle Spectrograph (TEXES) Instrument

Before discussing the observations that were collected at NASA IRTF and the subsequent modeling work that was completed with them, a more detailed discussion of the instrument itself is first warranted. The Texas Echelon Cross Echelle Spectrograph (TEXES) is a mid-infrared spectrograph with spectral coverage between 400-2000 cm^{-1} (5-25 μm) [39]. It is able to operate in several different modes:

- High resolution, cross-dispersed mode, with resolving power $R = \frac{\lambda}{\delta\lambda} \approx 100,000$ with a $1.5'' \times 8''$ slit
- Medium resolution mode, $R \approx 15,000$, with a long-slit ($1.5'' \times 45''$)
- Low-resolution, $R \approx 2000$, with long slit ($1.5'' \times 45''$)
- Source acquisition imaging mode with $0.33''$ pixels and $25'' \times 25''$ field of view

In addition to being employed at NASA Infrared Telescope Facility (IRTF), TEXES has also been employed at the McDonald Observatory 2.7 m telescope at the University of Texas.

To combat the large thermal background, which makes any mid-infrared observation difficult, TEXES is housed in a 1.5 m long, 0.4 m diameter liquid helium dewar. In order to achieve $R \approx 100,000$ in a grating spectrometer like TEXES, an

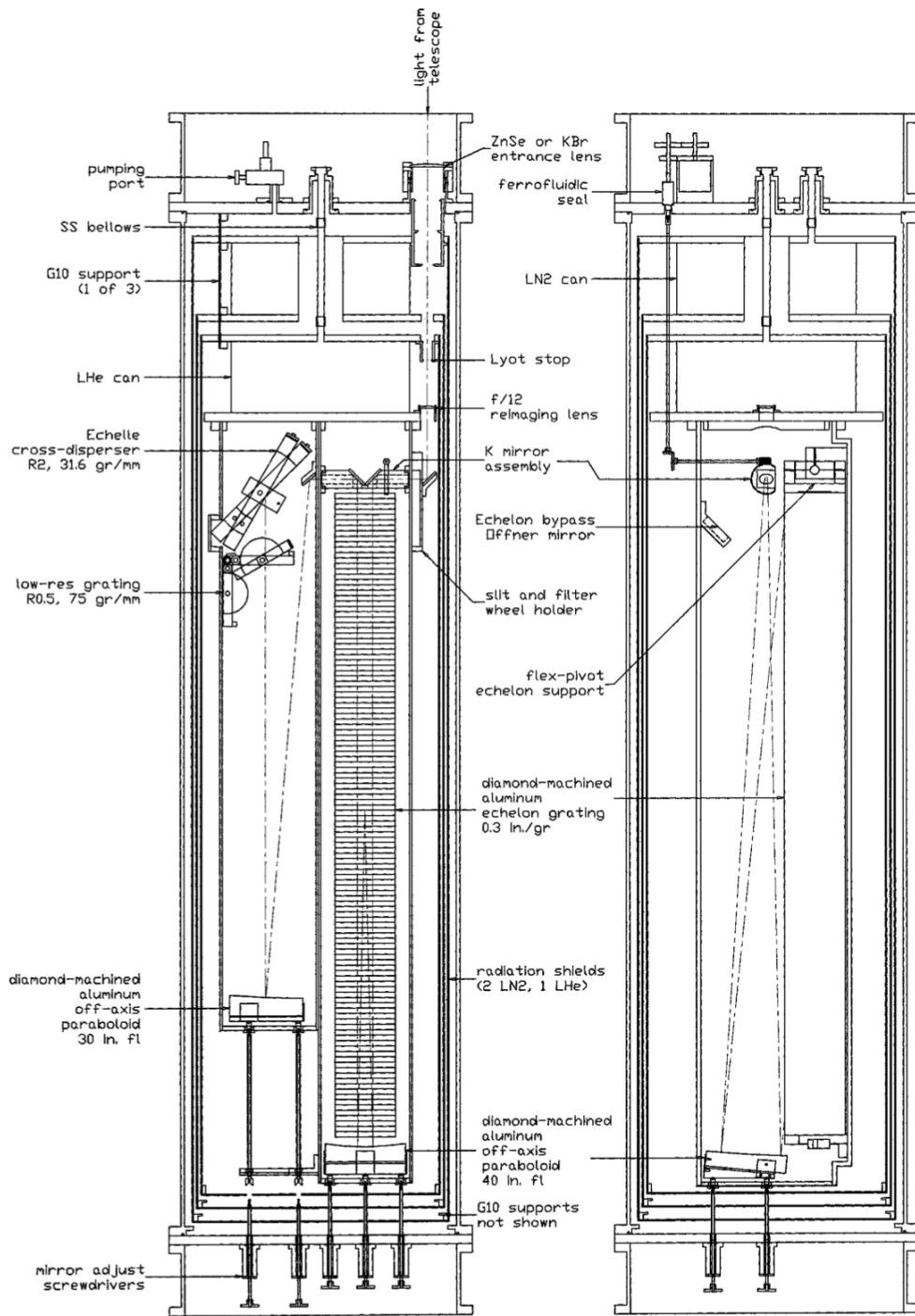


Figure 4.25: Schematic look at the TEXES instrument; the dotted-dashed line shows the path of light through the instrument when operating in high-resolution mode. Figure adapted from Figure 1 of Lacy et al. (2002) [39]

extremely large grating is required. The resolving power at a given wavelength λ is well approximated by

$$R \approx \frac{L}{\lambda}, \quad (4.5)$$

where L is the length of the illuminated grating. Thus, in order to achieve $R \approx 100,000$ in the infrared region, a grating on the order of 1 m in length is required. Ultimately, TEXES was designed with a 36 inch (≈ 0.914 m) long grating which is 3.4 inches wide. The grating is illuminated by a beam of diameter 3.3 inches, formed by a mirror with 40 inch focal length. The path of light through the TEXES instrument while operating in high-resolution is shown as the dotted-dashed line in Figure 4.25.

Operating for almost twenty years now, the TEXES instrument has been very productive within the field of Titan science in particular. It was used to achieve the first detections of the propane (C_3H_8) molecule [96] in Titan's atmosphere, as well as the propadiene (C_3H_4) molecule [27], more recently. It has also helped to constrain the ratio of Titan's atmospheric CH_3D to CH_4 [150], and obtained the first mid-infrared observation of cyanoacetylene (HC_3N) [151].

4.3.2 The data



Figure 4.26: A small subset of the observatories at the summit of Mauna Kea, on Hawaii. From left to right: Subaru Telescope, Keck I and Keck II, and NASA IRTF. Maui, the next closest island to Hawaii, can just be seen on the horizon between Keck II and IRTF.

In September, 2021, I travelled to Hawaii with co-investigator Conor Nixon to conduct our observations with the TEXES team. The observations ended up spanning about five nights. Ultimately, we were successful in obtaining fairly long integrations on both the 956 cm^{-1} and the 966 cm^{-1} settings, although the total integrations for either setting were not as long as we originally proposed, due to bad weather and seeing in some cases, and technical difficulties with the telescope and instrument in other cases.



Figure 4.27: A charming and talented young space scientist enjoys the view from 14,000 feet before commencing his observing run at NASA IRTF.

Additionally, it was unfortunate that circumstances did not allow for us to observe at all on the final (temperature profile retrieval) setting, at 1254 cm^{-1} . Luckily, Titan was observed by TEXES/IRTF on a similar setting just a few months earlier in July, that dataset was still available for use, and Titan's temperature profile is known to be fairly stable on such short timescales [97].

While the modeling and analysis of these observations remains unpublished at this point, and the work is certainly not to be considered complete, few preliminary results are included here to show where the search for *n*-butane and *trans*-2-butene might be headed with these higher resolution observations. The

methodology for the results that follow is largely the same as the CIRS modeling methodology described in Section 4.2.3: Once again, the first step is modeling the region of methane’s ν_4 band in order to retrieve a temperature profile that is (approximately) concurrent with the observations. Next, that retrieved temperature profile is implemented in the modeling of the target gas regions (956 and 965 cm^{-1}). In this case, these regions are dominated by emission from strong ethylene lines. This is evident in Figure 4.28, where a small section of the raw (but reduced) 956 cm^{-1} data is shown, with the HITRAN linelist for ethylene overlaid. However, there is also some weak emission from both propane and propene in the targeted regions, so those two gases (via their pseudoline lists) must be included in the model as well.

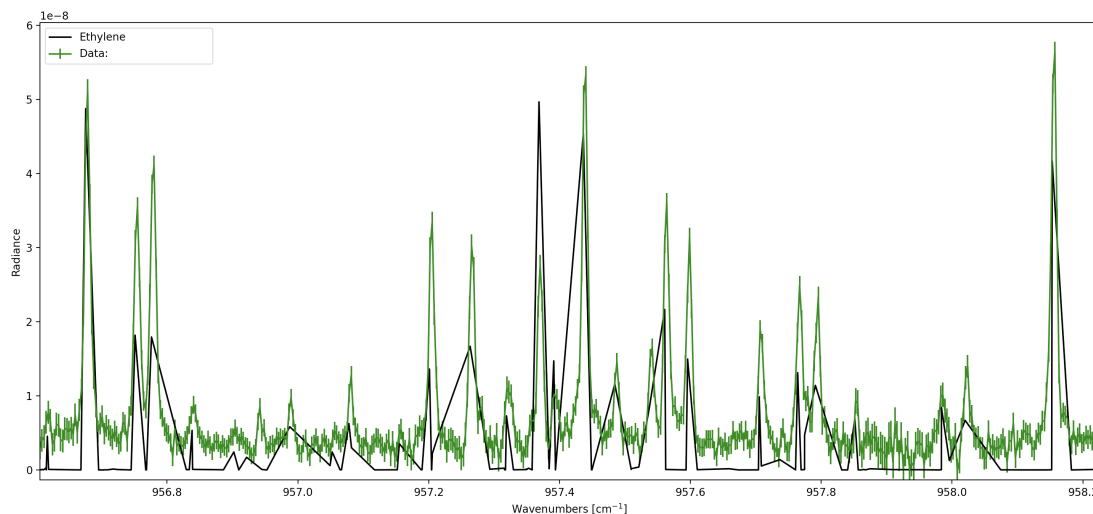


Figure 4.28: Reduced data in the 956 cm^{-1} region (in green), with the HITRAN linelist for ethylene (C_2H_4) overlaid in black, and scaled to be of similar brightness, for the purpose of comparison. It can be seen that the vast majority of large spectral lines in the data are coming from ethylene. This is true of the 965 cm^{-1} region as well.

From this point, as before, varying amounts of *n*-butane are systematically introduced, via the pseudoline list described in Section 3.4.4, and changing qualities

in fits are compared via the $\Delta\chi^2$ parameter, obtaining upper limits of various statistical confidences on the *n*-butane abundance in the data. Unfortunately, it is not possible to go through this full process to rigorously determine upper limits for *trans*-2-butene's abundance, since no line list is currently available. However, now that high resolution, cold temperature cross-sections have been measured (Section 3.5.3), a rough estimate of the upper limits *can* be provided by comparing the band strengths of *n*-butane and *trans*-2-butene. This will be described in more detail after displaying the *n*-butane results.

A disk-averaged profile that was derived with help from Nick Lombardo from the T10 Cassini-Titan flyby was implemented as an *a priori* temperature profile for this retrieval. The T10 flyby occurred in early 2006, which corresponds to approximately half of a Titan year (Saturn orbital period: ~ 29 years) before the July 2021 methane ν_4 band observations. We expect reasonable seasonal symmetry for disk averaged temperature profiles that are generated approximately one half of a Titan year apart from one another. The reason for this is that even though the seasons have flipped, the season that the northern hemisphere was experiencing has gone to the southern hemisphere, and vice versa, after one half of a Titan year, more or less preserving the information that a disk-averaged measurement of temperature would obtain in either case.

To generate the temperature *a priori*, a latitude-weighting scheme is implemented, which averages together zonal temperatures as measured by Achterberg et al. (2008) [152] using CIRS. The temperature average of a given region on the disk is weighted according to the size of the apparent area of that latitude range as viewed from Earth at the time of the observations. This is depicted in Figure 4.29.

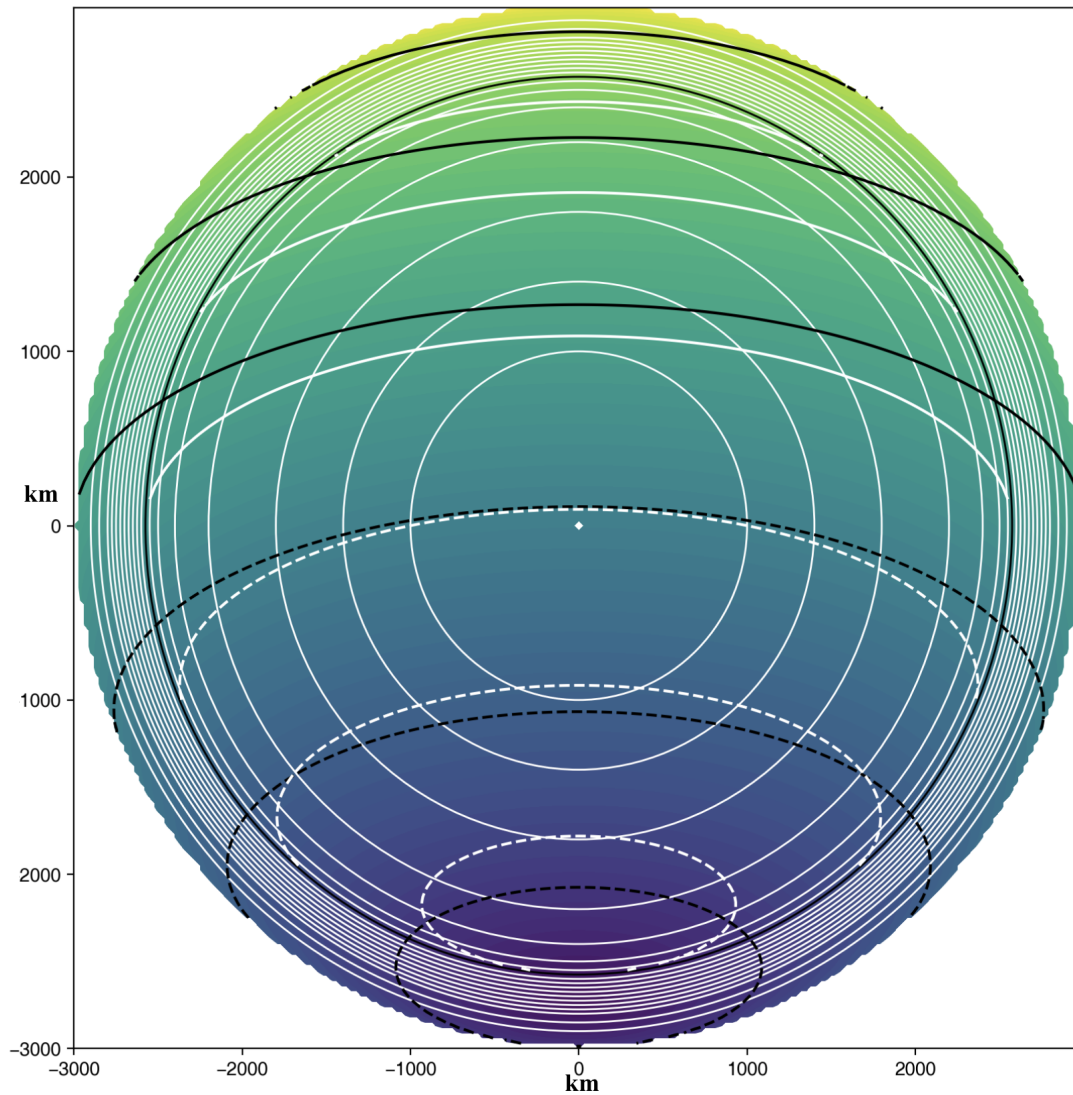


Figure 4.29: Weighted averaging of zonal temperature measurements from CIRS [152]. The disk of Titan is shown, with white concentric circles representing areas of “constant weighting” in the averaging scheme we used to derive the temperature profile. Obviously, stronger weights are given to areas that are closer to the sub-Earth observer point, which is represented by a white dot at the center of all of the circles, as those areas will contribute more flux to the observations. Various latitude bands are shown in black. Credit to Nick Lombardo for helping to generate this figure.

As stated previously, the target regions (956 and 965 cm^{-1}) are dominated

by strong ethylene lines, with minor emission coming from propane and propene. Thus, the NEMESIS model, which takes the retrieved temperature profile as input, only allows the profiles (i.e. the abundance at each altitude point) of those three gases to vary. Very good agreement is observed between my model and the observations, in both the 956 and the 965 cm^{-1} cases. However, some isolated cases do seem to indicate that the lineshape used by the model (dictated by the lineshape for which the k-table/opacity tables are calculated) could still be fine tuned.

Regardless, these preliminary results, displayed in Figures 4.31-4.32, seem to suggest very little emission from either target gas, neither *n*-butane nor *trans*-2-butene. This can be observed in the bottom panel of each of these figures, which displays the residuals (data minus model), compared to the transmission of spectra of both *n-butane* in green and *trans*-2-butene in purple. It can be seen that no distinct spectral lines are missed by the model that clearly belong to either target gas. Moreover, there is clearly no strong correlation between the residuals and transmission spectra of either target gas.

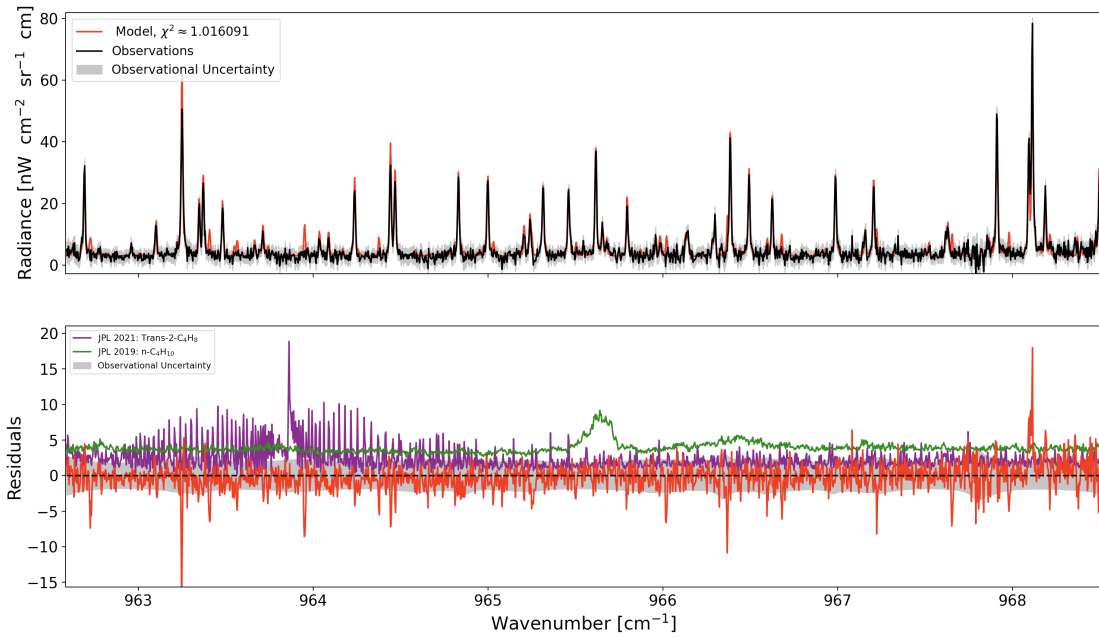


Figure 4.30: Model fit of the full 965 cm^{-1} region. A χ^2 value of 1.016 is achieved in this case.

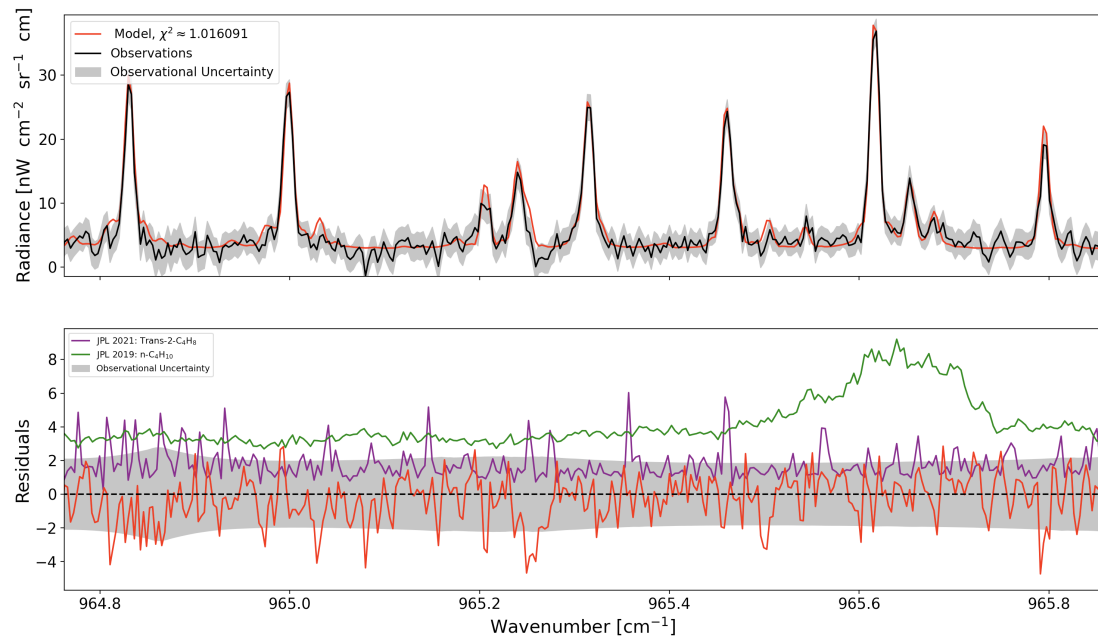


Figure 4.31: A closer look at a spectral line-dense region of the 965 cm^{-1} model fit. A good example of the model lineshape still needing some improvement is observed around $965.20\text{--}965.25\text{ cm}^{-1}$. Improving features such as this in the model's fit of these observations before actually *publishing* these results in a fourth “Titan’s C_4 hydrocarbons”-paper is an obvious next step, though it is extremely unlikely that such minor changes will significantly impact the resulting upper limits determined for *n*-butane and *trans*-2-butene and reported here.

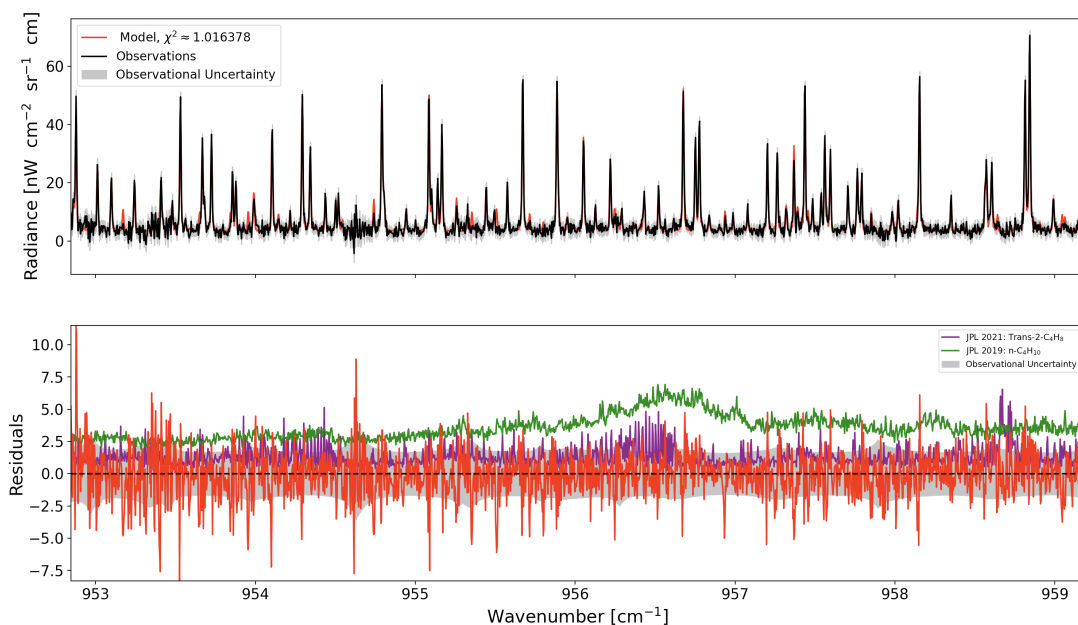


Figure 4.32: Model fit of the full 956 cm^{-1} region. A χ^2 value of 1.016 is achieved in this case as well.

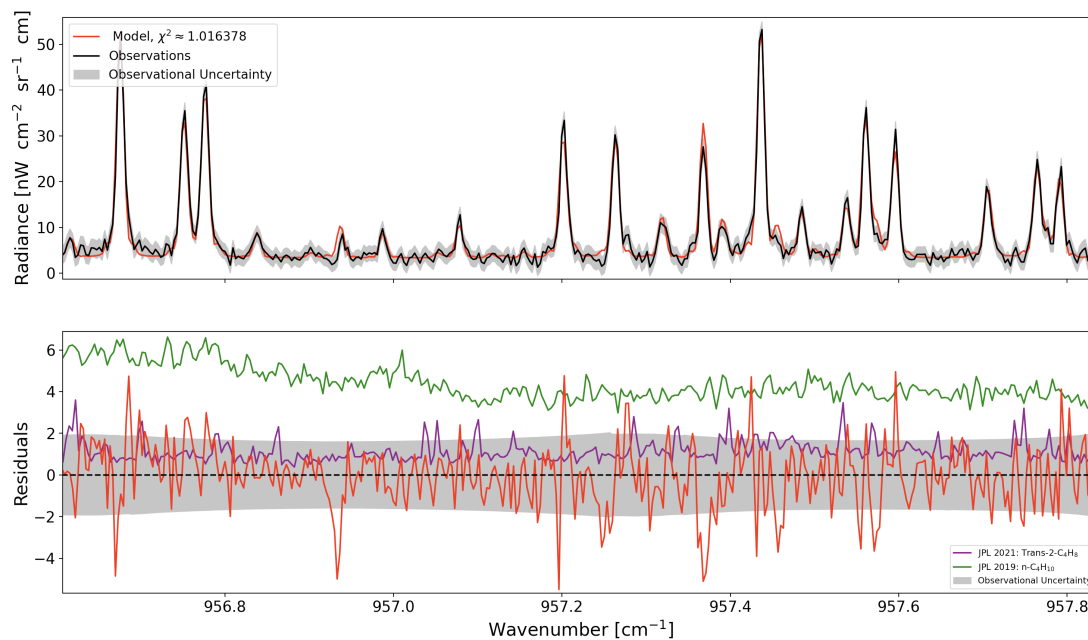


Figure 4.33: A closer look at a spectral line-rich region of the 956 cm^{-1} model fit.

The upper limits that have been derived for *n*-butane's abundance in these new

IRTF/TEXES observations are now presented via the familiar $\Delta\chi^2$ curves, one for each of the two data sets. These are shown in Figures 4.34-4.35. In an effort to keep things as simple as possible in this preliminary work with these new data, only the constant *n*-butane abundance profile has been tested.

As before, these $\Delta\chi^2$ figures show 1, 2, and 3σ upper limits, as denoted in the legend. These are marked by colored dashed vertical lines at their corresponding abundances. However, no minima are found in either cases, indicating that the addition of *n*-butane to the model offers only trivial improvement to the fit to the observations.

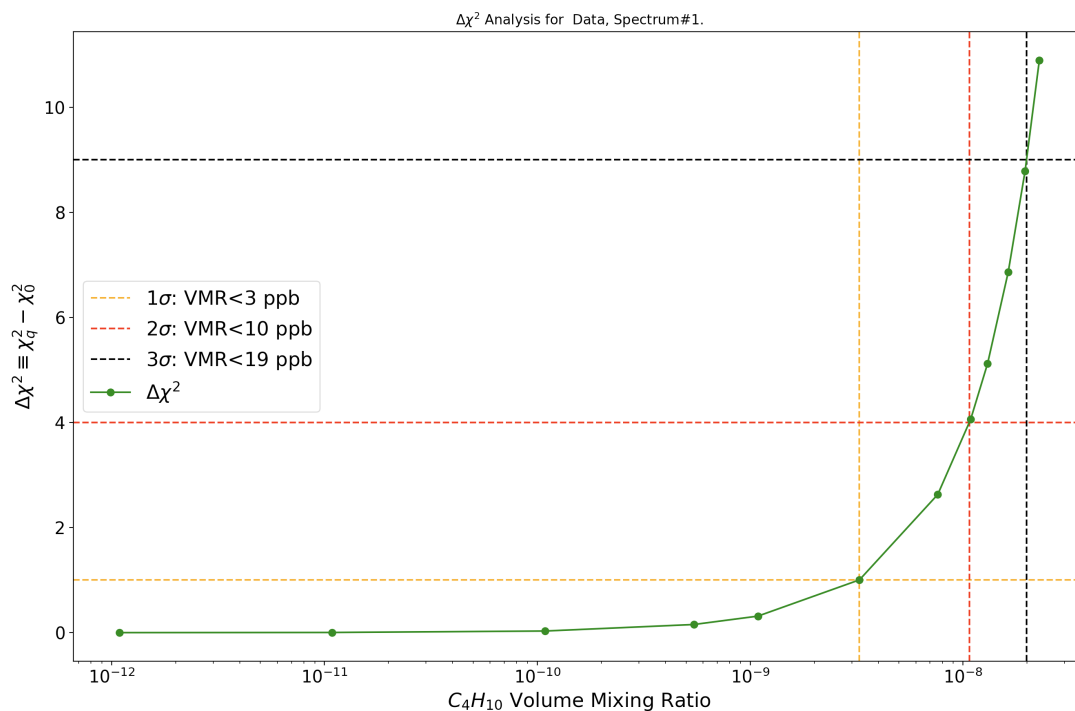


Figure 4.34: Upper limits retrieved for *n*-butane for the 2021 IRTF/TEXES observations centered on 956 cm^{-1} .

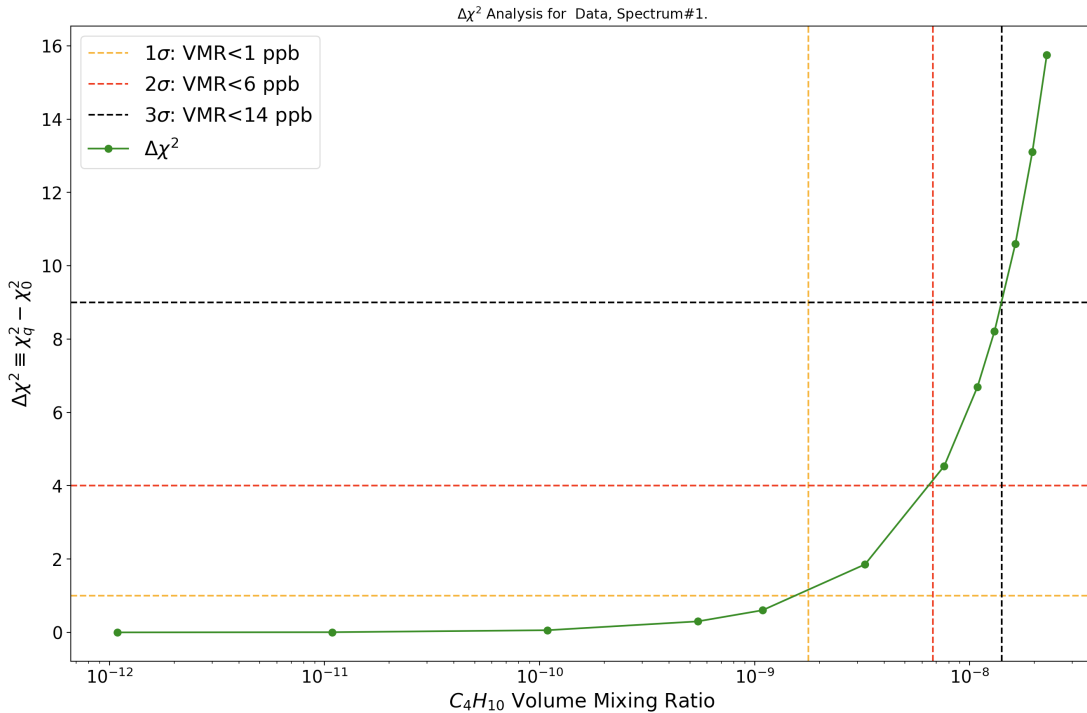


Figure 4.35: Upper limits retrieved for *n*-butane for the 2021 IRTF/TEXES observations centered on 965 cm⁻¹.

It can be seen that the retrieved upper limits are substantially smaller, in both the 956 and the 965 cm⁻¹ cases, than the upper limits retrieved for the constant profile in the Cassini/CIRS observations. In fact, the upper limits retrieved here in these new observations are a full order of magnitude smaller than those retrieved from CIRS.

Regarding *trans*-2-butene, a very rough upper limit from these results is derived by comparing the intensity of the spectral features of *trans*-2-butene to those of *n*-butane. *Trans*-2-butene's spectral lines in the 956 cm⁻¹ region are approximately 4 times stronger than those of *n*-butane, whereas they are approximately 12 times stronger in the 965 cm⁻¹ region. Thus, the *trans*-2-butene upper limits for these results can be estimated to be a factor of $\frac{1}{4}$ and $\frac{1}{12}$ of those of *n*-butane, respectively.

These rough estimates are collected in Table 4.6.

Table 4.6: Rough upper limits (in ppb) for *trans*-2-butene in the new IRTF/-TEXES data, estimated by first calculating *n*-butane’s upper limits using its pseudoline list, and then scaling those results by the ratio of band intensities in the region.

Data Set	1σ	2σ	3σ
956 cm^{-1}	0.75	2.25	4.75
965 cm^{-1}	0.25	1.50	3.50

In the case of the *n*-butane upper limits, interpretation of these substantially different results between CIRS and TEXES is still very much a work in progress. As stated previously, the *purpose* behind securing the TEXES observations was to search for *n*-butane with substantially higher spectral resolution ($R\sim 100,000$) than was available to CIRS ($R\sim 2,000$). Higher spectral resolution should result in the retrieval of upper limits of higher precision. Thus, it may be the case that the larger upper limits seen with CIRS (on the order of 100’s of parts per billion) were being artificially bloated by the comparatively smaller spectral resolution, or perhaps by inaccurate estimation of the spectral noise in those observations.

Before closing this chapter, I reiterate one final time that the *trans*-2-butene upper limits contained in Table 4.6 should be taken as an extremely rough estimate, a first step of many, if you will, toward constraining *trans*-2-butene’s stratospheric abundance at Titan. To advance this investigation further, most likely, a linelist or pseudoline list for *trans*-2-butene needs to be developed. This will be discussed further in the final, concluding chapter to follow.

Chapter 5

Conclusion

5.1 Brief Summary

In this dissertation, I have described the research that I have conducted or contributed to across the previous three years, all of which has been focused upon investigating the possible presence of large, as-of-yet undetected hydrocarbons in Titan's atmosphere, which are of vital importance for understanding this moon's chemistry and astrobiological potential. Enormous progress has been made across recent decades in characterizing the composition of Titan's fascinating atmosphere, but obviously much work remains to be done!

This work has focused in part on the study of Titan's potential C₄ hydrocarbon molecules in the infrared in the laboratory, *n*-butane and *trans*-2-butene, deriving both cross-sections and a pseudoline list for *n*-butane, and just cross-sections in the case of *trans*-2-butene. These laboratory results were obtained at cold temperatures appropriate for Titan's lower atmosphere, and are now available for public use on the HITRAN molecular database, or the JPL Molecular Spectroscopy Lab-

oratory’s website, in the case of the *n*-butane pseudoline list.

These results have then been *implemented* in a search for these molecules, or an attempt to constrain their abundances at Titan, through observations obtained both from spacecraft (Cassini CIRS) and from ground-based observatories (NASA IRTF/TEXES). The observations from IRTF in particular came from a successful proposal that I led myself and designed to target detections of both of the molecules of interest.

These investigations have led to two journal publications, with a third currently about to be submitted, and a fourth in preparation, and a number of conference papers, talks, and posters. Ultimately, the investigations have thus far yielded no firm detections of either of the targeted molecules. However, instead, a fairly comprehensive set of upper limits on the abundance of *n*-butane in Titan’s atmosphere as a function of altitude and latitude is derived from the Cassini CIRS observations and added to the Titan literature. Preliminary results from the 2021 IRTF/TEXES observations suggest that those CIRS upper limits may be in need of even *further* constraining. In the case of *trans*-2-butene, the first rough upper limits on its abundance in the recent observations which were collected at NASA IRTF were also achieved. These can serve as a first step toward a proper and thorough investigation of *trans*-2-butene’s abundance in Titan’s atmosphere, perhaps continuing with the development with a linelist or pseudoline list for that molecule.

The upper limits for these molecules will be useful in the future in constraining the roles that these C₄ hydrocarbons play in Titan’s chemistry, specifically by constraining their roles in photochemical models. Understanding the roles of these larger hydrocarbons is particularly important, given that they may play a role in the nucleation process of haze particles and Titan’s clouds [102]. An additional

point of interest concerning these larger hydrocarbons is that either molecule is separately estimated to contribute up to 1% by volume to Titan’s lakes and seas [71]. Given that life as we understand it currently requires some sort of liquid medium in order to act as a solvent, and that liquid *methane*, *ethane*, as well as larger hydrocarbons may serve as such media [4], the connection between these C₄ hydrocarbons and Titan’s astrobiological potential is clear.

5.2 Conclusions and Future Steps

In this section, we return briefly to each component of the work that was completed for this dissertation, examining the major conclusions, identifying any serious limitations pertinent to the methodology or results, and determining what future steps are necessary or may be recommended to facilitate further progress toward constraining the composition of Titan’s atmosphere.

5.2.1 Laboratory Work: *n*-C₄H₁₀

- *Scope of study:* Both absorption cross-section measurements *and* a pseudoline list were obtained for *n*-butane, derived from spectra gathered across a temperature range of approximately 180 K to 297 K.
- *Uncertainty of collected data:* The transmission spectra themselves were estimated to comprise a combined average uncertainty of $\sim 4\%$ (Figure 3.11), estimated by using the pseudoline list to fit every one of the transmission spectra, each of which was collected under unique experimental conditions (temperature, total pressure, and spectral resolution), individually.

- *Uncertainty of derived results:* The pseudoline list itself, the primary product of this study, is reported to be accurate to within 2% from 700-1200 cm^{-1} , and to within 4% from 1200-1500 cm^{-1} , the region which contains the much stronger vibrational features such as the ν_{14} band of $n\text{-C}_4\text{H}_{10}$. These uncertainties are measured (see Figure 3.10) by using the pseudoline list to fit *all* of the transmission spectra at a given temperature at the same time.
- *Limitations of study:* As the goal of this study was of course to produce a pseudoline list that could be used for modeling $n\text{-C}_4\text{H}_{10}$ emissions in Titan's stratosphere, where temperatures *do* in fact reach colder temperatures than 180 K, this can be considered the primary limitation of this study. The lower temperature bound of 180 K accessible to this study was caused by taking ample caution against the prospect of $n\text{-C}_4\text{H}_{10}$ condensing within the gas cell of the Bruker FT-IR. It is possible that more careful handling of the sample-addition phase of the procedure may allow the reduction of this lower bound by 10-20 K for molecules with similar saturation vapor pressure curves in the future. For instance, extremely careful handling of the needle pressure valves connected to the gas cell could allow for finer amounts of sample to be added more slowly, without risk of adding *too much* sample, which would cause condensation within the cell at the given temperature. For the case of $n\text{-C}_4\text{H}_{10}$, however, it should be noted that it is unlikely that adding spectra obtained at slightly colder temperatures (e.g. T=160 K) would greatly have affected the subsequent $n\text{-C}_4\text{H}_{10}$ search within CIRS data. This will be discussed in more detail in Section 5.2.3 below.

5.2.2 *Trans-2-C₄H₈*

- *Scope of study:* Absorption cross-section measurements were gathered across a temperature range of approximately 160 K to 297 K.
- *Uncertainty of collected data:* Referring back to Table 3.8, the average uncertainty associated with the absorption cross sections derived in this study was calculated to be 4%, across the entire spectral region studied. This is taken to be a combined estimate of all sources of uncertainty, such as baseline corrections to the spectra that were necessary in some cases, and outgassing that could be occurring within the cell and inlet tubes (particularly at low temperature). This outgassing occurs after adding/removing sample gas from the gas cell. Some of the sample gas necessarily ‘sticks’ to the inner walls and corners of the inlet valves and tubes leading to the gas cell, and such gas does not contribute to the measurement of gas pressure within the cell. As sample gas is added or removed to achieve new experimental conditions for the next set of spectra to be collected, it takes time for this situation to reach an actual equilibrium. It is therefore possible to measure the pressure within the gas cell *prematurely*, for a given data set to be collected, as the pressure will actually still be equilibrating slightly during the collection of data. This is a totally negligible problem at higher temperatures, where large amounts of sample gas are typically used. At lower temperatures, however, where one is forced to use extremely small amounts of sample gas (to avoid condensation within the gas cell), this outgassing/equilibrating problem becomes a much larger source of uncertainty.
- *Limitations of study:* As in the case of the *n*-C₄H₁₀ study, the primary

limitation here is once again the inability to measure these hydrocarbons at the extremely cold temperatures of Titan's lower stratosphere. Though we were able to obtain one spectrum at 160 K in this study, whereas the coldest *n*-butane spectra were recorded at 180 K, it can be easily seen in Figure 3.19 that this data point is a major outlier. As stated above, outgassing within the gas cell becomes a relatively larger source of uncertainty at the low pressures necessary to study cross sections at low temperatures. This is very likely the explanation for this outlying data point. An obvious way to mitigate this problem in future work is to simply gather more data at these lower temperatures. Additionally, extending the 'equilibrating' time allowed of the system in between sample addition/removal and collection of the next cold temperature data set may offer a major improvement. It is worth noting that the amount of time allowed for these 'equilibrating' periods was already considered generous in our work, and extending these windows in future studies would therefore likely be considered to be quite costly, from a time-use perspective. This phase of data collection would therefore need to be extremely well-planned in advance and very meticulously executed.

- *Lack of pseudoline list:* A major distinction between the two lab studies conducted for this dissertation is the lack of pseudoline list derived for the *trans*-2-butene species. This was a combined outcome of less available data in the literature on vibrational band centers for this species, and accessible, on-site lab time at JPL during peak COVID closures. In order to actually incorporate this species in future modeling efforts (i.e. retrieve its abundance or atmospheric profile), a pseudoline list is indeed required. The primary hindrance to achieving this is the lack of a reliable measurement for the

lowest lying (i.e. lowest energy) torsional band, which is missing altogether from the most recent work on this topic, Chhiba and Vergoten et al. (1994) [125]. In that work, however, the authors do provide a *calculation* of the location of that band center's location, albeit with a fairly large uncertainty. This calculated value, along with the experimental values (which have smaller uncertainties) for the other 29 vibrational bands, could in principle be applied in the calculation of the *trans*-2-butene partition function approximation (Equation 3.14), which is necessary for the pseudoline intensity calculation (Equation 3.12.) Naturally, there is no guarantee that this will produce a sensible result. The resulting pseudoline list would of course then need to be tested in the same way that is described for *n*-C₄H₁₀ in Figures 3.10 and 3.11, testing their ability to fit the initial transmission spectra collected in this work. If this approach were not to produce satisfactory convergence (i.e. reproducibility to within $\sim 5\%$), correction factors could be applied to the low-energy torsional band center and associated uncertainty in an iterative procedure until satisfactory fitting is achieved.

5.2.3 Cassini CIRS Modeling

- *Scope of study:* This study attempted to detect or constrain the abundance of *n*-butane in Titan's atmosphere by modeling its potential emissions in three different data sets collected by Cassini CIRS, using the *n*-C₄H₁₀ pseudoline list discussed above in Section 5.2.1. The CIRS data spanned a number of Titan flybys, covering Titan's equatorial latitudes, as well as its polar latitudes for its northern winter. Three different altitude-abundance profiles for *n*-butane were tested, two of these coming from photochemical model

predictions [146; 65].

- *Uncertainty of derived results:* Though no detections of $n\text{-C}_4\text{H}_{10}$ were made, a comprehensive set of upper limits of various statistical confidences were achieved, as a function of latitude, altitude, and photochemical profile being tested. The uncertainty of these results is naturally quantified by the statistical uncertainty associated with each upper limit which is reported.
- *Limitations of study:* As discussed in Section 5.2.1, there is some mismatch between the temperatures retrieved in Titan’s lower stratosphere, particularly for the two northern winter pole data sets, and the lower-most temperature at which the $n\text{-C}_4\text{H}_{10}$ pseudoline list was derived (180 K). As can be seen in Figure 4.8, and comparing with the temperature retrievals of Figure 4.6, the NEMESIS retrievals are also sensitive to the mid and higher altitude regions of the stratosphere (e.g. 200-300 km), where retrieved temperatures typically range from 180 - 200 K. As n -butane is expected to be present at these altitudes as well, as can be seen in the Krasnopolsky and Loison profiles, shown in Figure 4.9, the anticipated temperature mismatch in the lower stratosphere is unlikely to have *severely* impacted the results of this study.

The other major limitation of the methodology of this study is the statistical nature of the $\Delta\chi^2$ upper limit determination. Quantification of upper limits (and their statistical confidences) via this method necessarily relies strongly on the estimate of the *noise* in the spectral observations. To estimate those noise levels, we must assume the noise is Gaussian-dominant (i.e. has white-noise properties). However, as discussed in Section 4.2.5, there are some clear

cases in the results where this assumption is not perfectly valid.

- *Future work:* As the presence of *n*-butane in Titan’s atmosphere is typically regarded as a strong prediction of photochemical models, results here seem to indicate that further work is required. Future observations with NASA IRTF (perhaps with longer integrations), or observations using the now-ready JWST observatory and its MIRI (Mid-Infrared Instrument), may help to further constrain the abundance of Titan’s *n*-butane abundance. It could very well be that the true abundances of this gas are simply much lower than those predicted by photochemical models, perhaps due to some previously unincorporated chemical sink for this particular molecule, or perhaps even one of biological nature; as discussed in Chapter 1, recent studies of terrestrial metabolic pathways involving hydrocarbons suggest that *n*-butane may be more important of a molecule in metabolic processes than once thought [74; 73].

A final possible sink for Titan’s atmospheric *n*-butane that is just now beginning to be explored is the possibility of a strong coupling between Titan’s *n*-butane population and its acetylene-butane co-crystal population. In recent years, the acetylene-butane co-crystal has been studied in the laboratory and results seem to indicate that this may be one of the most prevalent molecules to form spontaneously on Titan’s surface [104; 105]. However, it has recently been observed that atmospheric formation of this co-crystal may also be favored, particularly in the upper stratosphere, where temperatures around 180 K are found (Steffens, Cable, 2022 - private communication). If the altitude(s) at which *n*-butane formation is favored also favor the forma-

tion of this co-crystal, that could complicate the search for infrared signals of pure *n*-butane and could contribute toward explaining some of the rather remarkably low upper limits reported in this dissertation, with respect to the predictions of photochemical models. This idea is currently in its infancy, and much future work is needed in order to test this hypothesis. In particular, a more rigorous study of the structure of the acetylene-butane co-crystal is needed. Following that, first-order estimations of the infrared spectrum of the co-crystal could be calculated quantum mechanically, following the method of Remsing and Bates. (2020) [153], for example. These spectra could then be compared against the residuals of the CIRS modeling of Chapter 4, to identify if any promising correlations are present.

5.2.4 2021 IRTF/TEXES Modeling

- *Scope of work:* New observations, optimized for the detection or further constraint of *n*-butane, as well as the first dedicated search for *trans*-2-butene, were designed and collected at NASA IRTF using the TEXES instrument in September of 2021. Observations were collected on two spectral settings, centered on 956 and 965 cm^{-1} , these being areas of peak vibrational activity for both target gases. Preliminary modeling efforts and upper limit determinations are currently underway.
- *Preliminary results:* Currently, results derived from this work seem to suggest even tighter upper limits on the abundance of *n*-butane within Titan's atmosphere. These results may be 'real', in the sense that the higher spectral resolution of TEXES versus CIRS is allowing the retrieval of more precise

upper limits, unmarred by the statistical biases associated with the white noise assumption invoked in the CIRS analysis. However, additional work is needed to more confidently demonstrate this outcome: as discussed in Section 4.3.2, the model’s lineshape needs to be more closely examined. Additionally, the suitability of the data being used for the temperature retrieval needs to be double-checked. That data was collected several months in advance of the observations on the *n*-C₄H₁₀/*trans*-2-C₄H₈ settings. While we expect Titan’s disk-averaged temperature profile to be relatively stable on these timescales [97], this source of uncertainty should be examined.

Lastly, rough upper limits for *trans*-2-butene, consistent with photochemical modeling predictions have been provided based on the relative band strengths of *trans*-2-butene and *n*-butane. However, these necessarily rely on the *n*-butane upper limit determinations, which, as stated previously, deserve more thorough analysis.

5.2.5 Summary

This section has sought to present, in condensed form, the scope of each portion of this dissertation, and further to collect the major conclusions from these components, as well as the limitations associated with their results, and important ideas regarding how to make further progress on these topics in the future. These selective summaries should certainly not be regarded as all-encompassing. In addition to the future work described in this section, some more general comments on this topic are now warranted, concerning the experience gained in working on this dissertation and moving forward with it; these reflections will naturally serve as a good closing of this dissertation.

5.3 Leveraging Experience, and Moving Forward

In Chapter 2, a brief ‘roadmap’ toward detecting a new molecule in any planetary atmosphere was provided. Reiterating the three steps described in that recipe, constraining the abundance of an undetected molecule in an atmosphere involves, at a minimum, the following main steps:

1. Laboratory spectroscopic characterization of the targeted molecule.
2. Observations of the targeted planetary atmosphere.
3. Radiative transfer modeling of observations.

After reading Chapters 3 and 4, you have seen that I myself have been fortunate enough to have gained valuable experience in *all three* of these areas in the last half of my graduate career.

As I progress further into this career and develop more contacts involved in planetary science and learn about their experience in the field, I find that having *some* experience in each of these three areas places me in a rather exclusive group. I am convinced that this can be extremely valuable, moving forward. In the relatively short time that I have been involved with these three endeavors, I have seen that often, all three of these sub-fields could benefit from improved inter-communication, and that could certainly be facilitated by someone who actually has at least *some* experience in each of the three sub-fields.

Were laboratory scientists to know exactly which molecules to measure cross-sections for and develop line lists for next, and if observers could better cater their observing proposals to target molecules that are simultaneously being studied (or will be studied in the near future) by laboratory scientists, and if atmospheric

modelers knew in advance which molecules they can expect to be able to incorporate into their models in the near future, this could make the entire enterprise of characterizing the compositions of planetary atmospheres more efficient and more successful.

In Chapter 2, I depicted this general concept with a triangular figure similar to Figure 5.1 below. Here, I add to the original figure, providing some examples of the sorts of communication channels that can be established or improved upon, to better facilitate the efficiency with which planetary atmospheres are characterized. This efficiency will become more and more crucial in the coming years, with powerful new observatories such as JWST coming online, and with a myriad of exoplanetary atmospheres that are waiting to be characterized.

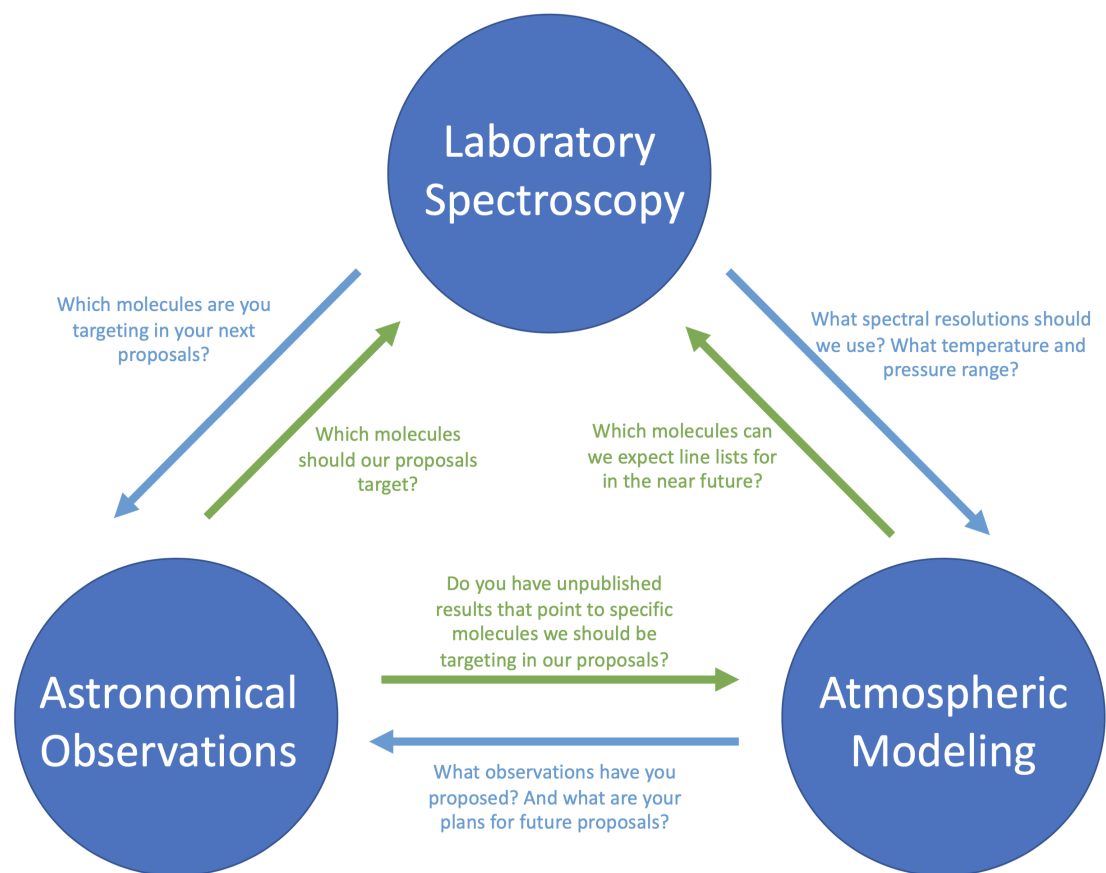


Figure 5.1: Schematic depiction of idealized communication channels between the three main components of characterization of planetary atmospheres.

It is my hope to contribute to this very role. I have a mind to ideally help to establish an annual or perhaps biannual meeting with as many scientists as possible that fit into the three roles described in Figure 5.1. The purpose of these meetings, which could be hybrid meetings to accommodate those who wish to meet in person but also those who are unable to travel, would be to establish a regular, consistent channel of communication between each corner of the triangle. This could allow observing proposals to be planned *based* on future laboratory work that has already been funded, and vice versa. It would also allow an opportunity for more young scientists to network and seek out new opportunities to gain experience in multiple

corners of the triangle.

5.3.1 A Final Word

With all this said, I will close the dissertation with a final thank you to **you**, the reader, for spending the time to make it all the way through this lengthy document. You have now read through my best attempt to communicate the efforts that have taken place across some of the most important years of my life. My hope is that it was an enjoyable read for you, as the work was certainly an enjoyable and rewarding experience for me.

Brendan Steffens

Bibliography

- [1] “Combination Bands, Overtones and Fermi Resonances,” Feb 4 2022. [Online; accessed 2022-04-03].
- [2] E. R. Stofan, C. Elachi, J. I. Lunine, and R. D. Lorenz, “The lakes of Titan,” *Nature*, vol. 445, pp. 61–64, Jan. 2007.
- [3] C. A. Griffith, T. Owen, G. A. Miller, and T. Geballe, “Transient clouds in Titan’s lower atmosphere,” *Nature*, vol. 395, pp. 575–578, Oct. 1998.
- [4] M. Lingam and A. Loeb, *Life in the Cosmos: From Biosignatures to Technosignatures*. Cambridge: Harvard University Press, 2021.
- [5] D. Schulze-Makuch and L. N. Irwin, *Life in the Universe: Expectations and Constraints*. Cham: Springer, 3rd ed., 2018.
- [6] M. Trainer, “Atmospheric Prebiotic Chemistry and Organic Hazes,” *Current Organic Chemistry*, vol. 17, pp. 1710–1723, July 2013.
- [7] C. McKay, “Titan as the Abode of Life,” *Life*, vol. 6, p. 8, Feb. 2016.
- [8] F. Nimmo and R. T. Pappalardo, “Ocean worlds in the outer solar system,” *Journal of Geophysical Research: Planets*, vol. 121, pp. 1378–1399, Aug. 2016.

- [9] A. Crósta, E. Silber, R. Lopes, B. Johnson, E. Bjornnes, M. Malaska, S. Vance, C. Sotin, A. Solomonidou, and J. Soderblom, “Modeling the formation of Menrva impact crater on Titan: Implications for habitability,” *Icarus*, vol. 370, p. 114679, Dec. 2021.
- [10] J. E. Hedgepeth, J. J. Buffo, C. J. Chivers, C. D. Neish, and B. E. Schmidt, “Modeling the Distribution of Organic Carbon and Nitrogen in Impact Crater Melt on Titan,” *The Planetary Science Journal*, vol. 3, p. 51, Feb. 2022.
- [11] G. Kuiper, “Titan: A Satellite with an Atmosphere,” *Astrophysical Journal*, 1944.
- [12] R. Knacke, T. Owen, and R. Joyce, “Infrared observations of the surface and atmosphere of Titan,” *Icarus*, vol. 24, pp. 460–464, Apr. 1975.
- [13] F. C. Gillett, W. Forrest, and K. Merrill, “Further observations of the 8-13 micron spectrum of Titan,” *The Astrophysical Journal*, vol. 201, p. L41, Oct. 1975.
- [14] A. Coustenis and B. Bézard, “Titan’s Atmosphere from Voyager Infrared Observations,” *Icarus*, vol. 89, pp. 152–167, 1991.
- [15] A. Coustenis and E. Lellouch, “Titan’s Surface: Composition and Variability from the Near-Infrared Albedo,” 1995.
- [16] M. Kessler, “The Infrared Space Observatory (ISO) mission,” *Advances in Space Research*, vol. 30, pp. 1957–1965, Nov. 2002.

- [17] A. Coustenis, A. Salama, B. Schulz, S. Ott, E. Lellouch, T. Encrenaz, D. Gautier, and H. Feuchtgruber, “Titan’s atmosphere from ISO mid-infrared spectroscopy,” *Icarus*, vol. 161, pp. 383–403, Feb. 2003.
- [18] O. Mousis, D. Gautier, and A. Coustenis, “The D/H Ratio in Methane in Titan: Origin and History,” *Icarus*, vol. 159, pp. 156–165, Sept. 2002.
- [19] R. Meier, B. Smith, and T. C. Owen, “The Surface of Titan from NICMOS Observations with the Hubble Space Telescope,” *Icarus*, vol. 145, pp. 462–473, June 2000.
- [20] C. C. Porco, R. A. West, and S. Squyres, “Cassini Imaging Science: Instrument Characteristics and Anticipated Scientific Investigations at Saturn,” *Space Science Reviews*, vol. 115, p. 135, 2004.
- [21] F. M. Flasar, V. G. Kunde, and M. M. Abbas, “Exploring the Saturn System in the Thermal Infrared: The Composite Infrared Spectrometer,” *Space Science Reviews*, p. 129, 2004.
- [22] H. B. Niemann, S. K. Atreya, and S. J. Bauer, “The abundances of constituents of Titan’s atmosphere from the GCMS instrument on the Huygens probe,” *Nature*, vol. 438, pp. 779–784, Dec. 2005.
- [23] A. Coustenis and F. Taylor, *Titan: Exploring an Earthlike World*. Series on atmospheric, oceanic and planetary physics, World Scientific, 2008.
- [24] H. B. Niemann, S. K. Atreya, and J. E. Demick, “Composition of Titan’s lower atmosphere and simple surface volatiles as measured by the Cassini-Huygens probe gas chromatograph mass spectrometer experiment,” *Journal of Geophysical Research*, vol. 115, p. E12006, Dec. 2010.

- [25] S. Gibbard, B. Macintosh, D. Gavel, C. Max, I. de Pater, E. Young, and C. McKay, “Very High Resolution IR Imaging of Titan’s Surface and Atmosphere,” vol. 29 of *AAS/Division for Planetary Sciences Meeting Abstracts*, p. 33.01, July 1997.
- [26] M. Ádámkóvics, J. L. Mitchell, and A. G. Hayes, “Meridional variation in tropospheric methane on Titan observed with AO spectroscopy at Keck and VLT,” *Icarus*, vol. 270, pp. 376–388, May 2016.
- [27] N. A. Lombardo, C. A. Nixon, T. K. Greathouse, B. Bézard, A. Jolly, S. Vinatier, N. A. Teanby, M. J. Richter, P. J. G. Irwin, A. Coustenis, and F. M. Flasar, “Detection of Propadiene on Titan,” *The Astrophysical Journal*, vol. 881, p. L33, Aug. 2019.
- [28] C. A. Nixon, A. E. Thelen, M. A. Cordiner, Z. Kisiel, S. B. Charnley, E. M. Molter, J. Serigano, P. G. J. Irwin, N. A. Teanby, and Y.-J. Kuan, “Detection of Cyclopropenylidene on Titan with ALMA,” *The Astronomical Journal*, vol. 160, p. 205, Oct. 2020.
- [29] A. E. Thelen, M. A. Cordiner, C. A. Nixon, V. Vuitton, Z. Kisiel, S. B. Charnley, M. Y. Palmer, N. A. Teanby, and P. G. J. Irwin, “Detection of CH₃C₃N in Titan’s Atmosphere,” *The Astrophysical Journal*, vol. 903, p. L22, Nov. 2020.
- [30] E. P. Turtle, J. E. Perry, and J. M. Barbara, “Titan’s Meteorology Over the Cassini Mission: Evidence for Extensive Subsurface Methane Reservoirs,” *Geophysical Research Letters*, vol. 45, pp. 5320–5328, June 2018.

- [31] T. L. Zebker, H.A., “Size and Shape of Saturn’s Moon Titan,” *Science*, vol. 324, pp. 917–921, May 2009.
- [32] G. Mitri, A. P. Showman, J. I. Lunine, and R. D. Lorenz, “Hydrocarbon lakes on Titan,” *Icarus*, vol. 186, pp. 385–394, Feb. 2007.
- [33] R. Jacobson, P. Antreasian, and J. Bordi, “The Gravity Field of the Saturnian System from Satellite Observations and Spacecraft Tracking Data,” *The Astronomical Journal*, vol. 132, pp. 2520–2526, Jan. 2006.
- [34] L. Iess, N. J. Rappaport, R. A. Jacobson, P. Racioppa, D. J. Stevenson, P. Tortora, J. W. Armstrong, and S. W. Asmar, “Gravity Field, Shape, and Moment of Inertia of Titan,” *Science*, vol. 327, pp. 1367–1369, Mar. 2010.
- [35] S. M. MacKenzie, S. P. D. Birch, and S. Hörst, “Titan: Earth-like on the Outside, Ocean World on the Inside,” *The Planetary Science Journal*, vol. 2, p. 112, June 2021.
- [36] R. Hanel, D. Crosby, L. Herath, D. Vanous, D. Collins, H. Creswick, C. Harris, and M. Rhodes, “Infrared spectrometer for Voyager,” *Applied Optics*, vol. 19, p. 1391, May 1980.
- [37] T. de Graauw, L. N. Haser, and D. A. Beintema, “Observing with the ISO Short-Wavelength Spectrometer?,” p. 6, 1996.
- [38] W. Kasprzak, H. Niemann, D. Harpold, J. Richards, H. L. K. Manning, E. Patrick, and P. Mahaffy, “Cassini orbiter ion and neutral mass spectrometer instrument,” (Denver, CO), pp. 129–140, Oct. 1996.

- [39] J. Lacy, M. Richter, T. Greathouse, D. Jaffe, and Q. Zhu, “TEXES: A Sensitive High-Resolution Grating Spectrograph for the Mid-Infrared,” *Publications of the Astronomical Society of the Pacific*, vol. 114, pp. 153–168, Feb. 2002.
- [40] G. Lindal, G. Wood, H. Hotz, D. Sweetnam, V. Eshleman, and G. Tyler, “The atmosphere of Titan: An analysis of the Voyager 1 radio occultation measurements,” *Icarus*, vol. 53, pp. 348–363, Feb. 1983.
- [41] A. L. Broadfoot, B. R. Sandel, and D. E. Shemansky, “Extreme Ultraviolet Observations from Voyager 1 Encounter with Saturn,” *Science*, vol. 212, pp. 206–211, Apr. 1981.
- [42] L. Trafton, “The Bulk Composition of Titan’s Atmosphere,” *The Astrophysical Journal*, vol. 175, p. 295, July 1972.
- [43] R. Hanel, “Infrared Observations of the Saturnian System from Voyager 1,” *Science*, 1981.
- [44] B. L. Lutz, C. de Bergh, J.-P. Maillard, T. Owen, and J. Brault, “On the possible detection of CH₃D on Titan and Uranus,” *The Astrophysical Journal*, vol. 248, p. L141, Sept. 1981.
- [45] F. C. Gillett, W. J. Forrest, and K. M. Merrill, “8-13 Micron Observations of Titan,” *The Astrophysical Journal*, vol. 184, p. L93, Sept. 1973.
- [46] R. Danielson, J. J. Caldwell, and D. Larach, “An inversion in the atmosphere of Titan,” *Icarus*, vol. 20, pp. 437–443, Dec. 1973.

- [47] J. H. Waite, H. Niemann, and R. V. Yelle, “Ion Neutral Mass Spectrometer Results from the First Flyby of Titan,” *Science*, vol. 308, pp. 982–986, May 2005.
- [48] A. Coustenis, R. K. Achterberg, and B. J. Conrath, “The composition of Titan’s stratosphere from Cassini/CIRS mid-infrared spectra,” *Icarus*, vol. 189, pp. 35–62, July 2007.
- [49] W. Maguire, “C₃H₈ and C₃H₄ in Titan’s Atmosphere,” *Nature*, 1981.
- [50] V. G. Kunde, A. C. Aikin, R. A. Hanel, D. E. Jennings, W. C. Maguire, and R. E. Samuelson, “C₄H₂, HC₃N and C₂N₂ in Titan’s atmosphere,” *Nature*, vol. 292, pp. 686–688, August 1981.
- [51] R. Moreno, “OT1_rmoreno_1: Confirmation of the first detection of HNC on Titan.” Herschel Space Observatory Proposal, id.1046, July 2010.
- [52] R. Samuelson, L. Mayo, M. Knuckles, and R. Khanna, “C₄N₂ ice in Titan’s north polar stratosphere,” *Planetary and Space Science*, vol. 45, pp. 941–948, Aug. 1997.
- [53] B. Bezard, A. Marten, and G. Paubert, “Detection of Acetonitrile on Titan,” 1993.
- [54] B. Lutz, C. de Bergh, and T. Owen, “Carbon monoxide in the atmosphere of Titan: search and discovery.,” *Science*, vol. 95, p. 593, Sept. 1983.
- [55] R. E. Samuelson, W. C. Maguire, R. A. Hanel, V. G. Kunde, D. E. Jennings, Y. L. Yung, and A. C. Aikin, “CO₂ on Titan,” *Journal of Geophysical Research: Space Physics*, vol. 88, pp. 8709–8715, Nov. 1983.

- [56] A. Coustenis, A. Salama, E. Lellouch, T. Encrenaz, G. L. Bjoraker, R. E. Samuelson, T. de Graauw, H. Feuchtgruber, and M. F. Kessler, “Evidence for water vapor in Titan’s atmosphere from ISO/SWS data,” *Astronomy and Astrophysics*, vol. 336, pp. 85–89, 1998.
- [57] V. Vuitton, R. V. Yelle, and V. G. Anicich, “Detection Of Complex Molecules In Titan’s Upper Atmosphere,” vol. 38 of *AAS/Division for Planetary Sciences Meeting Abstracts*, p. 36.03, Sept. 2006.
- [58] M. A. Cordiner, M. Y. Palmer, and C. A. Nixon, “Ethyl Cyanide on Titan: Spectroscopic Detection and Mapping Using ALMA,” *The Astrophysical Journal*, vol. 800, p. L14, Feb. 2015.
- [59] M. Y. Palmer, M. A. Cordiner, C. A. Nixon, S. B. Charnley, N. A. Teanby, Z. Kisiel, P. G. J. Irwin, and M. J. Mumma, “ALMA detection and astrobiological potential of vinyl cyanide on Titan,” *Science Advances*, vol. 3, p. e1700022, July 2017.
- [60] C. A. Nixon, D. E. Jennings, and B. Bézard, “Detection of Propene in Titan’s Stratosphere,” *The Astrophysical Journal*, vol. 776, p. L14, Sept. 2013.
- [61] P. Lavvas, M. Galand, R. Yelle, A. Heays, B. Lewis, G. Lewis, and A. Coates, “Energy deposition and primary chemical products in Titan’s upper atmosphere,” *Icarus*, vol. 213, pp. 233–251, May 2011.
- [62] S. M. Hörst, “Titan’s atmosphere and climate: Titan’s Atmosphere,” *Journal of Geophysical Research: Planets*, vol. 122, pp. 432–482, Mar. 2017.

- [63] Y. L. Yung, M. Allen, and J. P. Pinto, “Photochemistry of the atmosphere of Titan - Comparison between model and observations,” *The Astrophysical Journal Supplement Series*, vol. 55, p. 465, July 1984.
- [64] V. A. Krasnopolsky, “A photochemical model of Titan’s atmosphere and ionosphere,” *Icarus*, vol. 201, pp. 226–256, May 2009.
- [65] J. C. Loison, “The photochemical production of aromatics in the atmosphere of Titan,” p. 17, 2019.
- [66] V. Vuitton, R. Yelle, S. Klippenstein, S. Hörst, and P. Lavvas, “Simulating the density of organic species in the atmosphere of Titan with a coupled ion-neutral photochemical model,” *Icarus*, vol. 324, pp. 120–197, May 2019.
- [67] K. Willacy, S. Chen, D. J. Adams, and Y. L. Yung, “Vertical distribution of cyclopropenylidene and propadiene in the atmosphere of Titan,” *The Astrophysical Journal*, 2021.
- [68] B. N. Tran, J. C. Joseph, M. Force, R. G. Briggs, V. Vuitton, and J. P. Ferris, “Photochemical processes on Titan: Irradiation of mixtures of gases that simulate Titan’s atmosphere,” *Icarus*, vol. 177, pp. 106–115, Sept. 2005.
- [69] Y. S. Kim, C. J. Bennett, L.-H. Chen, K. O’Brien, and R. I. Kaiser, “Laboratory Studies on the Irradiation of Solid Ethane Analog Ices and Implications to Titan’s Chemistry,” *The Astrophysical Journal*, vol. 711, pp. 744–756, Mar. 2010.
- [70] P. M. Chu, F. R. Guenther, G. C. Rhoderick, W. J. Lafferty, and W. Phillips, “Sample and data processing considerations for the NIST quantitative infrared database,” (Boston, MA), pp. 204–211, Feb. 1999.

- [71] D. Cordier, O. Mousis, J. I. Lunine, P. Lavvas, and V. Vuitton, “An Estimate of the Chemical Composition of Titan’s Lakes,” *The Astrophysical Journal*, vol. 707, pp. L128–L131, Dec. 2009.
- [72] R. Laso-Pérez, G. Wegener, K. Knittel, F. Widdel, K. J. Harding, V. Krukenberg, D. V. Meier, M. Richter, H. E. Tegetmeyer, D. Riedel, H.-H. Richnow, L. Adrian, T. Reemtsma, O. J. Lechtenfeld, and F. Musat, “Thermophilic archaea activate butane via alkyl-coenzyme M formation,” *Nature*, vol. 539, pp. 396–401, Nov. 2016.
- [73] R. Laso-Pérez, C. Hahn, D. M. van Vliet, H. E. Tegetmeyer, F. Schubotz, N. T. Smit, T. Pape, H. Sahling, G. Bohrmann, A. Boetius, K. Knittel, and G. Wegener, “Anaerobic Degradation of Non-Methane Alkanes by “*Candidatus Methanoliparia*” in Hydrocarbon Seeps of the Gulf of Mexico,” *mBio*, vol. 10, pp. e01814–19, /mbio/10/4/mBio.01814–19.atom, Aug. 2019.
- [74] S. W. Ragsdale, “Deep-sea secrets of butane metabolism,” *Nature*, vol. 539, pp. 367–368, Nov. 2016.
- [75] A. A. Lukashvskaya and V. I. Perevalov, “Bank of Spectral Line Parameters of the H₂S Molecule,” *Atmospheric and Oceanic Optics*, vol. 33, pp. 449–458, Oct. 2020.
- [76] G. C. Toon, C. B. Farmer, P. W. Schaper, L. L. Lowes, and R. H. Norton, “Composition measurements of the 1989 Arctic winter stratosphere by airborne infrared solar absorption spectroscopy,” *Journal of Geophysical Research: Atmospheres*, vol. 97, no. D8, pp. 7939–7961, 1992.

- [77] A. Berk, L. Bernstein, G. Anderson, P. Acharya, D. Robertson, J. Chetwynd, and S. Adler-Golden, “MODTRAN Cloud and Multiple Scattering Upgrades with Application to AVIRIS,” *Remote Sensing of Environment*, vol. 65, pp. 367–375, Sept. 1998.
- [78] K. Stamnes, S.-C. Tsay, W. Wiscombe, and K. Jayaweera, “Numerically stable algorithm for discrete-ordinate-method radiative transfer in multiple scattering and emitting layered media,” *Applied Optics*, vol. 27, p. 2502, June 1988.
- [79] P. Irwin, N. Teanby, R. de Kok, L. Fletcher, C. Howett, C. Tsang, C. Wilson, S. Calcutt, C. Nixon, and P. Parrish, “The NEMESIS planetary atmosphere radiative transfer and retrieval tool,” *Journal of Quantitative Spectroscopy and Radiative Transfer*, vol. 109, pp. 1136–1150, April 2008.
- [80] A. Anguiano-Arteaga, S. Pérez-Hoyos, A. Sánchez-Lavega, J. F. Sanz-Requena, and P. G. J. Irwin, “Vertical Distribution of Aerosols and Hazes Over Jupiter’s Great Red Spot and Its Surroundings in 2016 From HST/WFC3 Imaging,” *Journal of Geophysical Research: Planets*, vol. 126, Nov. 2021.
- [81] N. Rowe-Gurney, L. N. Fletcher, G. S. Orton, M. T. Roman, A. Mainzer, J. I. Moses, I. de Pater, and P. G. Irwin, “Longitudinal variations in the stratosphere of Uranus from the Spitzer infrared spectrometer,” *Icarus*, vol. 365, p. 114506, Sept. 2021.

- [82] D. Toledo, P. G. Irwin, P. Rannou, L. N. Fletcher, N. A. Teanby, M. H. Wong, and G. S. Orton, “Constraints on Neptune’s haze structure and formation from VLT observations in the H-band,” *Icarus*, vol. 350, p. 113808, Nov. 2020.
- [83] C. D. Rodgers, *Inverse Methods for Atmospheric Sounding*. WORLD SCIENTIFIC, 2000.
- [84] C. Nixon, D. Jennings, J.-M. Flaud, B. Bézard, N. Teanby, P. Irwin, T. Ansty, A. Coustenis, S. Vinatier, and F. Flasar, “Titan’s prolific propane: The Cassini CIRS perspective,” *Planetary and Space Science*, vol. 57, pp. 1573–1585, Nov. 2009.
- [85] W. Herres and J. Gronholz, “Understanding FTIR data processing part 1 : Data acquisition and fourier transformation 1,” 2007.
- [86] K. Smith, D. Newnham, M. Page, J. Ballard, and G. Duxbury, “Infrared band strengths and absorption cross-sections of HFC-32 vapour,” *Journal of Quantitative Spectroscopy and Radiative Transfer*, vol. 56, pp. 73–82, July 1996.
- [87] E.-t. Es-sebbar, Y. Benilan, and A. Farooq, “Temperature-dependent absorption cross-section measurements of 1-butene (1-C₄H₈) in VUV and IR,” *Journal of Quantitative Spectroscopy and Radiative Transfer*, vol. 115, pp. 1–12, Jan. 2013.
- [88] K. Sung, G. C. Toon, A. W. Mantz, and M. A. H. Smith, “FT-IR measurements of cold C₃H₈ cross sections at 7–15 μ m for Titan atmosphere,” *Icarus*, vol. 226, pp. 1499–1513, Nov. 2013.

- [89] K. Sung, G. C. Toon, and T. J. Crawford, “N₂- and (H₂+He)-broadened cross sections of benzene (C₆H₆) in the 7–15 μm region for the Titan and jovian atmospheres,” *Icarus*, vol. 271, pp. 438–452, June 2016.
- [90] K. Sung, G. C. Toon, B. J. Drouin, A. W. Mantz, and M. A. H. Smith, “FT-IR measurements of cold propene (C₃H₆) cross-sections at temperatures between 150 and 299 K,” *Journal of Quantitative Spectroscopy and Radiative Transfer*, vol. 213, pp. 119–132, July 2018.
- [91] D. Hewett, P. Bernath, and B. Billingham, “Infrared absorption cross sections of isobutane with hydrogen and nitrogen as broadening gases,” *Journal of Quantitative Spectroscopy and Radiative Transfer*, vol. 227, pp. 226–229, Apr. 2019.
- [92] D. Hewett, P. F. Bernath, A. Wong, B. E. Billingham, J. Zhao, N. A. Lombardo, C. A. Nixon, and D. E. Jennings, “N₂ and H₂ broadened isobutane infrared absorption cross sections and butane upper limits on Titan,” *Icarus*, vol. 344, p. 113460, July 2020.
- [93] Y. Ding, W.-W. Su, S. E. Johnson, C. L. Strand, and R. K. Hanson, “Temperature-dependent absorption cross section measurements for propene, 1-butene, cis-/trans-2-butene, isobutene and 1,3-butadiene in the spectral region 8.4–11.7 μm,” *Journal of Quantitative Spectroscopy and Radiative Transfer*, vol. 255, p. 107240, Nov. 2020.

- [94] T. J. Johnson, K. D. Hughey, T. A. Blake, S. W. Sharpe, T. L. Myers, and R. L. Sams, “Confirmation of PNNL Quantitative Infrared Cross-Sections for Isobutane,” *The Journal of Physical Chemistry A*, vol. 125, pp. 3793–3801, May 2021.
- [95] P. F. Bernath, *Spectra of Atoms and Molecules*. 2020.
- [96] Roe, “Propane on Titan,” *The Astrophysical Journal*, vol. 597, pp. L65–L68, 2003.
- [97] A. Coustenis, G. Bampasidis, and R. K. Achterberg, “Evolution of the Stratospheric Temperature and Chemical Composition Over One Titanian Year,” *The Astrophysical Journal*, vol. 779, p. 177, Dec. 2013.
- [98] L. M. Lara, E. Lellouch, J. J. López-Moreno, and R. Rodrigo, “Vertical distribution of Titan’s atmospheric neutral constituents,” *Journal of Geophysical Research: Planets*, vol. 101, pp. 23261–23283, Oct. 1996.
- [99] C. A. Nixon, R. K. Achterberg, and M. Ádámkóvics, “Titan Science with the James Webb Space Telescope,” *Publications of the Astronomical Society of the Pacific*, vol. 128, p. 018007, Jan. 2016.
- [100] M. Ádámkóvics, “Photochemical formation rates of organic aerosols through time-resolved in situ laboratory measurements,” *Journal of Geophysical Research*, vol. 108, no. E8, p. 5092, 2003.
- [101] J. Moses, “Photochemistry of Saturn’s Atmosphere I. Hydrocarbon Chemistry and Comparisons with ISO Observations,” *Icarus*, vol. 143, pp. 244–298, Feb. 2000.

- [102] D. B. Curtis, D. L. Glandorf, O. B. Toon, M. A. Tolbert, C. P. McKay, and B. N. Khare, "Laboratory Studies of Butane Nucleation on Organic Haze Particles: Application to Titan's Clouds," *The Journal of Physical Chemistry A*, vol. 109, pp. 1382–1390, Feb. 2005.
- [103] D. Cordier, T. Cornet, J. Barnes, S. MacKenzie, T. Le Bahers, D. Nnamvondo, P. Rannou, and A. Ferreira, "Structure of Titan's evaporites," *Icarus*, vol. 270, pp. 41–56, May 2016.
- [104] M. L. Cable, T. H. Vu, M. J. Malaska, H. E. Maynard-Casely, M. Choukroun, and R. Hodyss, "A Co-Crystal between Acetylene and Butane: A Potentially Ubiquitous Molecular Mineral on Titan," *ACS Earth and Space Chemistry*, vol. 3, pp. 2808–2815, Dec. 2019.
- [105] M. L. Cable, T. H. Vu, H. E. Maynard-Casely, M. J. Malaska, and M. Chouk, "The New Field of Titan Cryomineralogy: Six Confirmed Co-Crystals And Counting," no. 2548, p. 2, 2021.
- [106] R. M. Lopes, R. S. Peckyno, and A. A. Le Gall, "Titan's methane cycle and its effect on surface geology," in *AGU Fall Meeting Abstracts*, vol. 2010, pp. P31C–1548, Dec. 2010.
- [107] P. F. Bernath, D. M. Bittner, and E. L. Sibert III, "Isobutane Infrared Bands: Partial Rotational Assignments, ab Initio Calculations, and Local Mode Analysis," *The Journal of Physical Chemistry A*, vol. 123, pp. 6185–6193, July 2019.

- [108] H. M. Pickett, “The fitting and prediction of vibration-rotation spectra with spin interactions,” *Journal of Molecular Spectroscopy*, vol. 148, no. 2, pp. 371–377, 1991.
- [109] H. M. Pickett, “Reprint of: Submillimeter, millimeter, and microwave spectral line catalog,” *Journal of Quantitative Spectroscopy and Radiative Transfer*, vol. 111, pp. 1617–1624, July 2010.
- [110] T. Shimanouchi, U. S. N. B. o. Standards, and U. S. D. o. Commerce, *Tables of Molecular Vibrational Frequencies*. No. pt. 1 in NSRDS-NBS, National Bureau of Standards, 1972.
- [111] W. F. Murphy, J. M. Fernandez-Sanchez, and K. Raghavachari, “Harmonic force field and raman scattering intensity parameters of n-butane,” *The Journal of Physical Chemistry*, vol. 95, no. 3, pp. 1124–1139, 1991.
- [112] K. Sung, B. Steffens, G. Toon, D. Nemchick, and M. A. Smith, “Pseudoline parameters to represent n-butane (n-C₄H₁₀) cross-sections measured in the 7-15 μ m region for the Titan atmosphere,” *Journal of Quantitative Spectroscopy and Radiative Transfer*, p. 107011, May 2020.
- [113] A. E. Thelen, C. Nixon, N. Chanover, M. Cordiner, E. Molter, N. Teanby, P. Irwin, J. Serigano, and S. Charnley, “Abundance measurements of Titan’s stratospheric HCN, HC₃N, C₃H₄, and CH₃CN from ALMA observations,” *Icarus*, vol. 319, pp. 417–432, Feb. 2019.

- [114] K. Sung, A. Mantz, M. Smith, L. Brown, T. Crawford, V. Devi, and D. Benner, “Cryogenic absorption cells operating inside a Bruker IFS-125HR: First results for $^{13}\text{CH}_4$ at 7m,” *Journal of Molecular Spectroscopy*, vol. 262, pp. 122–134, Aug. 2010.
- [115] S. W. Sharpe, T. J. Johnson, R. L. Sams, P. M. Chu, G. C. Rhoderick, and P. A. Johnson, “Gas-Phase Databases for Quantitative Infrared Spectroscopy,” *Applied Spectroscopy*, vol. 58, pp. 1452–1461, Dec. 2004.
- [116] G. C. Toon, J.-F. Blavier, and B. Sen, “Comparison of MkIV balloon and ER-2 aircraft measurements of atmospheric trace gases,” *Journal of Geophysical Research: Atmospheres*, vol. 104, pp. 26779–26790, Nov. 1999.
- [117] P. Virtanen, R. Gommers, and T. E. Oliphant, “SciPy 1.0: Fundamental Algorithms for Scientific Computing in Python,” *Nature Methods*, vol. 17, pp. 261–272, 2020.
- [118] I. E. Gordon, L. S. Rothman, R. J. Hargreaves, R. Hashemi, E. V. Karlovets, F. M. Skinner, E. K. Conway, C. Hill, R. V. Kochanov, and Y. Tan, “The HITRAN2020 Molecular Spectroscopic Database,” *Journal of Quantitative Spectroscopy and Radiative Transfer*, vol. 277, p. 107949, 2022.
- [119] E. V. Anslyn, D. A. Dougherty, and E. V. Dougherty, *Modern Physical Organic Chemistry*. University Science Books, 2006.
- [120] B. Crawford, “Vibrational intensities. x. integration theorems,” *The Journal of Chemical Physics*, vol. 29, no. 5, pp. 1042–1045, 1958.

- [121] J. C. Breeze, C. C. Ferriso, C. B. Ludwig, and W. Malkmus, "Temperature Dependence of the Total Integrated Intensity of Vibrational—Rotational Band Systems," *Journal of Chemical Physics*, vol. 42, pp. 402–406, Jan. 1965.
- [122] J. Sams, R.L., Sharpe, S.W., "Do integrated infrared band strengths change with temperature in the gas-phase?." 60th International Symposium on Molecular Spectroscopy at Columbus, Ohio., 2005.
- [123] A. G. Hayes, "The Lakes and Seas of Titan," *Annual Review of Earth and Planetary Sciences*, vol. 44, pp. 57–83, June 2016.
- [124] D. McKean, M. Mackenzie, A. Morrisson, J. Lavelley, A. Janin, V. Fawcett, and G. Edwards, "Vibrational spectra of cis and trans but-2-enes: assignments, isolated CH stretching frequencies and CH bond lengths," *Spectrochimica Acta*, vol. 41A, no. 3, pp. 435–450, 1985.
- [125] M. Chhiba and G. Vergoten, "The structures and vibrational frequencies of a series of linear alkenes obtained using the spectroscopic potential SPASIBA," *Journal of Molecular Structure*, vol. 326, pp. 35–38, 1994.
- [126] P. Derreumaux and G. Vergoten, "A new spectroscopic molecular mechanics force field. Parameters for proteins," *Journal of Chemical Physics*, vol. 102, pp. 8586–8605, June 1995.
- [127] S. Bell, B. Drew, G. Guirgis, and J. Durig, "The far infrared spectrum, ab initio calculations and conformational energy differences of 1-butene," *Journal of Molecular Structure*, vol. 553, pp. 199–219, Oct. 2000.

- [128] C. A. Nixon, T. M. Ansty, and N. A. Lombardo, “Cassini Composite Infrared Spectrometer (CIRS) Observations of Titan 2004–2017,” *The Astrophysical Journal Supplement Series*, vol. 244, p. 14, Sept. 2019.
- [129] CRC Handbook, *CRC Handbook of Chemistry and Physics, 88th Edition*. CRC Press, 88 ed., 2007.
- [130] P. Varanasi, “Intensities of the fundamental bands of the nu sub 3 system in CO₂ and N₂O spectra,” in *Heat and mass transfer - V, Volume 8*, vol. 8, pp. 191–195, Jan. 1977.
- [131] P. Varanasi and S. Chudamani, “Self- and N₂-broadened spectra of water vapor between 7.5 and 14.5 μm.,” *Journal of Quantitative Spectroscopy and Radiative Transfer*, vol. 38, pp. 407–412, Dec. 1987.
- [132] A. Hayes, O. Aharonson, P. Callahan, C. Elachi, Y. Gim, R. Kirk, K. Lewis, R. Lopes, R. Lorenz, J. Lunine, K. Mitchell, G. Mitri, E. Stofan, and S. Wall, “Hydrocarbon lakes on Titan: Distribution and interaction with a porous regolith,” *Geophysical Research Letters*, vol. 35, p. L09204, May 2008.
- [133] R. M. Lopes, R. S. Peckyno, A. A. Le Gall, L. Wye, E. R. Stofan, J. Radebaugh, A. G. Hayes, O. Aharonson, S. D. Wall, M. A. Janssen, and Cassini RADAR Team, “Titan’s methane cycle and its effect on surface geology,” in *AGU Fall Meeting Abstracts*, vol. 2010, pp. P31C–1548, Dec. 2010.
- [134] R. F. W. Bader and J. I. Generosa, “The Chemistry of Singlet and Triplet Methylene,” *Canadian Journal of Chemistry*, vol. 43, pp. 1631–1644, June 1965.

- [135] R. C. Woodworth and P. S. Skell, “Methylene, ch_2 . stereospecific reaction with cis- and trans-2-butene,” *Journal of the American Chemical Society*, vol. 81, no. 13, pp. 3383–3386, 1959.
- [136] P. Pérez, J. Andrés, V. S. Safont, R. Contreras, and O. Tapia, “Exploring Two-State Reactivity Pathways in the Cycloaddition Reactions of Triplet Methylene,” *The Journal of Physical Chemistry A*, vol. 109, pp. 4178–4184, May 2005.
- [137] T. Gilchrist and C. Rees, “Carbynes, nitrenes, and arynes.,” *Appleton Century Croft, New York*, 1969.
- [138] M. Trainer, W. B. Brinckerhoff, A. Grubisic, R. Danell, and D. Kaplan, “Development of the Dragonfly Mass Spectrometer (DraMS) for Titan,” in *LPI Contrib. No. 2548*, 2021.
- [139] D. E. Jennings, F. M. Flasar, V. G. Kunde, and C. A. Nixon, “The Composite Infrared Spectrometer (CIRS) on Cassini,” *Applied Optics*, vol. 56, no. 18, pp. 5274–5294, 2017.
- [140] N. A. Teanby, M. Sylvestre, J. Sharkey, C. A. Nixon, S. Vinatier, and P. G. J. Irwin, “Seasonal Evolution of Titan’s Stratosphere During the Cassini Mission,” *Geophysical Research Letters*, vol. 46, pp. 3079–3089, Mar. 2019.
- [141] J. Sharkey, “Potential vorticity structure of Titan’s polar vortices from Cassini CIRS observations,” *Icarus*, p. 16, 2021.

- [142] N. A. Lombardo, C. A. Nixon, M. Sylvestre, D. E. Jennings, N. Teanby, P. J. G. Irwin, and F. M. Flasar, “Ethane in Titan’s Stratosphere from Cassini CIRS Far- and Mid-infrared Spectra,” *The Astronomical Journal*, vol. 157, p. 160, Apr. 2019.
- [143] E. H. Wilson, “Current state of modeling the photochemistry of Titan’s mutually dependent atmosphere and ionosphere,” *Journal of Geophysical Research*, vol. 109, no. E6, p. E06002, 2004.
- [144] E. Lellouch, B. Bézard, F. Flasar, S. Vinatier, R. Achterberg, C. Nixon, G. Bjoraker, and N. Gorius, “The distribution of methane in Titan’s stratosphere from Cassini/CIRS observations,” *Icarus*, vol. 231, pp. 323–337, Mar. 2014.
- [145] R. K. Achterberg, P. J. Gierasch, B. J. Conrath, F. M. Flasar, D. E. Jennings, and C. A. Nixon, “Post-equinox Variations of Titan’s Mid-stratospheric Temperatures from Cassini/CIRS Observations,” vol. 46 of *AAS/Division for Planetary Sciences Meeting Abstracts*, p. 102.07, Nov. 2014.
- [146] V. A. Krasnopolsky, “Chemical composition of Titan’s atmosphere and ionosphere: Observations and the photochemical model,” *Icarus*, vol. 236, pp. 83–91, July 2014.
- [147] M. Dobrijevic, J. Loison, K. Hickson, and G. Gronoff, “1D-coupled photochemical model of neutrals, cations and anions in the atmosphere of Titan,” *Icarus*, vol. 268, pp. 313–339, Apr. 2016.
- [148] E. L. Barth, “Modeling survey of ices in Titan’s stratosphere,” *Planetary and Space Science*, vol. 137, pp. 20–31, Mar. 2017.

- [149] R. de Kok, P. Irwin, N. Teanby, C. Nixon, D. Jennings, L. Fletcher, C. Howett, S. Calcutt, N. Bowles, and F. Flasar, “Characteristics of Titan’s stratospheric aerosols and condensate clouds from Cassini CIRS far-infrared spectra,” *Icarus*, vol. 191, pp. 223–235, Nov. 2007.
- [150] P. F. Pentead, C. A. Griffith, T. K. Greathouse, and C. de Bergh, “Measurements of CH₃D and CH₄ in Titan from Infrared Spectroscopy,” *The Astrophysical Journal*, vol. 629, pp. L53–L56, Aug. 2005.
- [151] L. M. Trafton, J. H. Lacy, H. Roe, and M. Richter, “Detection of Cyanoacetylene on Titan During Southern Summer Near the Epoch of the Huygens Probe Descent,” vol. 37 of *AAS/Division for Planetary Sciences Meeting Abstracts*, p. 45.29, Aug. 2005.
- [152] R. K. Achterberg, B. J. Conrath, P. J. Gierasch, F. M. Flasar, and C. A. Nixon, “Titan’s middle-atmospheric temperatures and dynamics observed by the Cassini Composite Infrared Spectrometer,” *Icarus*, vol. 194, pp. 263–277, Mar. 2008.
- [153] R. C. Remsing and J. E. Bates, “Effective mass path integral simulations of quasiparticles in condensed phases,” *The Journal of Chemical Physics*, vol. 153, p. 121104, Sept. 2020.

Appendix A

TEXES User Guide

by Brendan Steffens

A.1 Introduction

The following is intended to be a useful guide for new users of TEXES data. Proper use of these data require several processing steps and a variety of corrections before any modeling work can be done. All of these steps, as well as information about the tools available for executing them, are documented here for the user. Other helpful documentation and resources are also tabulated here for convenience.

It is assumed that the reader is using MacOS, as I did. It is also assumed that the reader is using C Shell, since the documentation for installation/compilation of NEMESIS is catered to use of C Shell. I realize these conditions may not apply to your system, but I assume that changes to the following procedure for other operating systems / other shells are minor and straightforward.

A.1.1 Contact

If you have questions concerning the use of this guide, feel free to contact me (Brendan Steffens) by email: BrendanSteffens@gmail.com

If you have questions concerning TEXES or your TEXES data, please contact Tommy Greathouse, the lead for that instrument, at: Thomas.Greathouse@swri.org

A.1.2 Acknowledgements

The construction of this guide benefitted tremendously from input from Tommy Greathouse, John Lacy, and Nicholas Lombardo. I also wish to acknowledge the helpful contributions from my mentor, Conor Nixon.

A.2 Acquiring/Installing IDL:

First things first! You need IDL (Interactive Data Language) on your system. IDL is a programming language owned and operated by Harris Corporation.

You will need either an active IDL license, or a working installation of GDL in order to use several of the scripts which perform the initial processing of the raw, unformatted TEXES data. If you are new to IDL/GDL, as I was, here are a few tips to get you started:

- Make sure you have XQuartz installed and working properly. You can find this easily online with a Google search, and installation is a breeze. If you already have it installed but don't use it often, check to make sure that it is updated.
- Purchase IDL license, or acquire license by some other means (through your

university, or other institution, perhaps). I was able to get a 12 month student license for 89 USD. Alternatively, you can use GDL, which is free software for running IDL scripts. I tried this route initially, but eventually gave up during the complicated installation process. For the remainder of this guide, I will assume you have gone with IDL.

- Download and install IDL from the Harris website. If you purchased a license, they will email you the link for your download. Installation of the software is straightforward.
- After installing, you will be prompted to activate your license, which will also have been sent to you in the same email.

A.3 Getting Started

Locate the directory of your IDL installation, i.e. the one that contains the `/bin` directory. I will refer to this directory as `/IDL_install`, regardless of what you named it.

Before you can run IDL from your machine via the command line, you need to add a few lines to your `.cshrc` file in your home directory. If you don't already have a `.cshrc` file in your home directory, you will have to create one. This can be done with any text editor, but I use *vi* myself. So, to create that new file, change directories to the terminal to your home directory, and then do

```
vi .cshrc
```

If you *do* have a `.cshrc` file already, this command will automatically open it up for you. Either way, to add the necessary line, you can type `'i'` to enter 'interactive'

mode, and then type

```
source /IDL_install/bin/idl_setup
```

To exit interactive mode, hit 'Escape'. Then, to save the new file, type ':', followed by 'w', followed by 'q', and then enter. (The colon tells the *vi* text editor that you are going to be inserting a command. The w and q stand for 'write and then quit', i.e. quit, and actually save the changes that you made to the file, rather than discarding them.) The next step is to return to the terminal and do

```
source .cshrc
```

Return to the .cshrc file and now add the following line, exactly as you see it below, regardless of where your IDL installation is located,

```
Setenv LM_LICENSE_FILE /usr/local/idl/license/license.dat
```

Then, once again, exit the file, and do

```
source .cshrc
```

You should now be able to access IDL from the command line, from anywhere on your machine, by simply doing

```
idl
```

After doing so, you should then see something along the lines of the following, where of course you will see your name, institution, and license number, rather than my own:

```
[Brendan-2020-Macbook-Pro:~] brendan% idl
IDL 8.8.0 (darwin x86_64 m64).
(c) 2020, Harris Geospatial Solutions, Inc.

Licensed for use by: Florida Institute of Technology - Steffens
License: MNT-5522494
License expires 31-Oct-2021.
IDL> █
```

A.4 Using `rdpipe.pro` and `lacetoms_ver2.pro`

You're now ready to use the above two scripts to process your raw, unformatted TEXES data for later use in your modeling work. In your terminal, change directories to wherever you have stored these scripts. Your data files need to be located there as well. The TEXES team has a convention of naming files using the first three letters of the name of whatever the target body of the observations was. Thus, for me, the data files were named 'tit.962.all', 'tit.962.all.hd', and 'tit.962.all.inp', where 962 refers to the center of the wavenumber (cm^{-1}) band being observed, and "tit" refers to Titan. The main data file is the one with just the '.all' extension. The other two contain information (that the IDL scripts will need) about when and how the observation was conducted with TEXES at IRTF. For the instructions that follow, I will use `file_name.all` to represent your main ".all" data file.

Start by running your main data file through **`rdpipe.pro`**. To do so, activate IDL, and then do the following. Note that in the following IDL script calling commands, you do need to explicitly type the commas, and the apostrophes around your file name. First, do

```
rdpipe, 'file_name.all', tit
```

The output of this process is stored in an array structure called `tit`, or whatever

you named it in your case. I suggest you follow the convention and use the first three letters of the target of your observations for the name of that structure. In what follows, I will keep referring to the Titan-specific labels that I used, though yours may of course be different.

So, as I said, the above command stores its output in a variable/array called `tit`. If you now type `tit` and hit enter, you will see that array printed out. This `tit` structure will serve as the input for the next step, which is to use **`lacetoms_ver2.pro`**, by doing

```
lacetoms_ver2, tit, titl
```

This will take everything in the `tit` structure and reformat it into the structure labeled `titl`. Again, the naming convention for this second output is to simply add an `l` (that's a lower-case 'L' for 'laced') to your original array. Essentially what these scripts are doing is lacing together the various orders in your raw data, via some interpolation method, since there is bound to be some overlap between the different spectral orders. For more information on the spectral orders, the main paper for TEXES is cited below:

Lacy, J. H., M. J. Richter, T. K. Greathouse, D. T. Jaffe, and Q. Zhu. "TEXES: A Sensitive High-Resolution Grating Spectrograph for the Mid-Infrared." *Publications of the Astronomical Society of the Pacific* 114, no. 792 (February 2002): 153–68. [DOI](#)

Note that **`lacetoms_ver2.pro`** will automatically sample the data at resolution 0.5 km/s. This may or may not be appropriate for your work. You can sample at a different rate by adding the `'kms=#'` parameter in the above command, e.g.

```
lacetoms_ver2, tit, titl, kms=1
```

which will sample at resolution 1 km/s rather than the default 0.5 km/s.

The output of doing this last step are several one-dimensional arrays, labeled by an extension after titl, or whatever you called it for your work. The two most important are titl.wn and titl.sp. You can type those names individually and hit enter to print them, if you like. The .wn one contains the wavenumber grid for your data, i.e. the x-axis of your newly processed spectrum. The .sp one contains the y-axis, measured in units of Janskys (more information on that unit to come, if you're not familiar). You can save these arrays to standard comma-separated-value (CSV) text files by doing

```
WRITE_CSV, 'whatever_file_name_you_like', titl.wn
```

and similarly for the titl.sp array as well. You can also obtain the uncertainties in your spectrum via titl.noi, so you should probably write that one to file as well. You're then free to use that spectral data however you wish. It's straight forward to plot things like this with **python3**, via something like the following short script that I wrote, which you should just be able to copy and paste into whatever editor you use for python, if you like. Feel free to make modifications as you see fit. Note that my script below does not include errorbars via titl.noi, but you may want to do so in order to see the uncertainties in the spectrum.

```
'''  
  
This script reads 'titl.wn' and 'titl.sp', which you must generate  
using rdpipe.pro and lacetoms_ver2.pro within IDL, and must be  
stored in the 'input_files' directory. The script then plots the  
resulting spectrum.  
  
'''  
  
import matplotlib.pyplot as plt
```

```

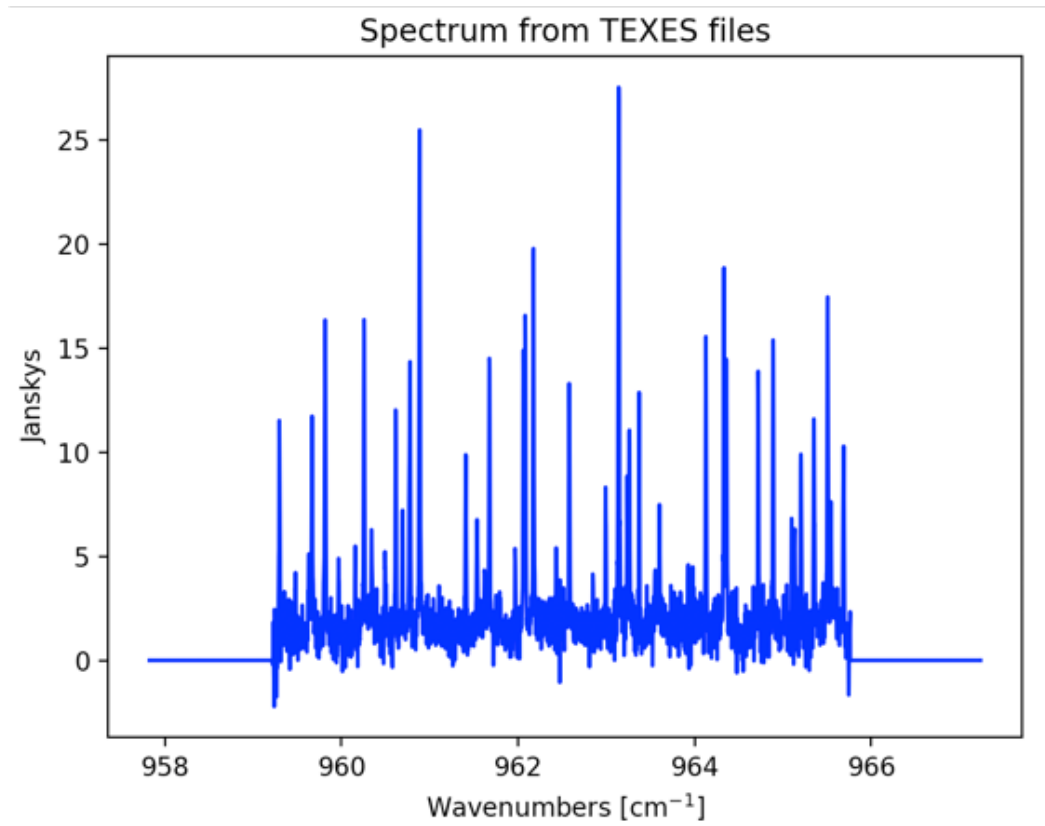
wavenumbers_file='input_files/titl.wn'
wavenumbers=[]
with open(wavenumbers_file) as file:
    for row in file:
        wavenumbers.append(float(row))

spectrum_file='input_files/titl.sp'
spectrum=[]
with open(spectrum_file) as file:
    for row in file:
        spectrum.append(float(row))

plt.plot(wavenumbers,spectrum,color='blue',label='Some spectrum lol')
plt.xlabel(r'Wavenumbers [cm$^{-1}$]')
plt.ylabel('Janskys')
plt.title('Spectrum from TEXES files. Congrats on surviving 2020 by the
        way!')
plt.legend()
plt.show()

```

For the data I was using, this is the output I see when I execute the above script:



A.5 Corrections to your data

You now need to perform a set of three corrections to the processed data that you just created. These are as follows:

1. Divide data by normalized blackbody spectrum that was used to calibrate your observations.
2. Apply doppler correction to wavenumber grid to account for Titan/Earth relative velocity.
3. Convert spectrum's y-axis from Jansky's to NEMESIS-friendly radiance units.

We'll now go through each of these steps in turn.

A.5.1 Blackbody correction

At the time that your data was collected, an approximately blackbody target was also observed, for calibration purposes. This is likely an asteroid (e.g. Hygeia or Juno) or a minor planet (e.g. Vesta). So, in your set of data files, you should also see some files labeled by ‘Hyg’ or ‘Jun’ or ‘Ves’ or something similar. For me, I had files like ‘ves.8002’ and ‘ves.8002.hd’, with the number 8002 indexing the order in which observations were taken that night.

You need to run the data file for this blackbody observation through the same gauntlet that you just did for your actual observations, i.e. run it through `rd-pipe.pro` and `lacetoms_ver2.pro`. Make sure to use the same sampling (i.e. the `kms` parameter in the `lacetomsver2.pro` command). The output, once again, will be two one-dimensional arrays which constitute the black body spectrum. Use python or something similar to first normalize the blackbody spectrum, such that its maximum value is unity (i.e. divide the entirety of the spectrum by the maximum value obtained by the y-axis). Then, re-scale your data by that normalized blackbody spectrum.

A.5.2 Doppler correction

We need to account for the Doppler effect, caused by your target body’s relative velocity with respect to Earth at the time of the observation. You can check any of your `.hd` files to determine the time of the observation, if need be; look for the following two parameters: The above indicates that for me, observations were taken on June 6th, 2010, at 8:52AM, beginning 55.983 seconds after that minute. The format is YEAR-MONTH-DAY. Note that times and dates in your `.hd` files

```
date-obs= 10-06-06
time      = 08:52:55.983
```

are always in UTC.

Now, use JPL Horizons (a web-based tool for this sort of thing, linked below) to determine your target body's velocity at that time. For convenience, you will need the official observatory code for IRTF, which being on Mauna Kea, is 568. JPL Horizons will give you the x, y, and z components of your target body's velocity with respect to Earth in units of AU per day at the time(s) you input into the software. Calculate the magnitude of the velocity vector, convert to appropriate units, and then finally, scale the wavenumber grid of your data by a factor of $(1 + \frac{v}{c})$, where v is Titan's speed, and c is the speed of light in vacuum.

JPL Horizons: <https://ssd.jpl.nasa.gov/horizons.cgi>

A.5.3 Jansky conversion

The last 'correction' is to convert the y-axis units of your spectrum from Janskys to the NEMESIS radiance units of $[\text{nW cm}^{-2} \text{sr}^{-1} \text{cm}]$. Of course, this step may not apply to you if you're not intending to do modeling work via NEMESIS with your results.

The main complication in this conversion is the $[\text{sr}^{-1}]$ dependence of NEMESIS radiance units, which basically implies a dependence on the distance between the Earth and the target of your observations. You can see the full derivation of the conversion factor in the following paper:

Teanby, N.A., P.G.J. Irwin, C.A. Nixon, R. Courtin, B.M. Swinyard,

R. Moreno, E. Lellouch, M. Rengel, and P. Hartogh. “Constraints on Titan’s Middle Atmosphere Ammonia Abundance from Herschel SPIRE Sub-Millimetre Spectra.” *Planetary and Space Science* 75 (January 2013): 136–47. <https://doi.org/10.1016/j.pss.2012.11.008>.

The conversion factor turns out to be as follows:

$$1 \text{ Jansky} = \left[10^{-21} \cdot \left(\frac{cd^2}{\pi R^2} \right) \right] nW \text{ cm}^{-2} \text{ sr}^{-1} \text{ cm}$$

where c is the speed of light in vacuum, d is the distance between the telescope and Titan (you should already have this from your ephemeris), and R is the radius of your target. Note that you need to include the atmosphere itself in this radius, since the atmosphere does emit radiation, and therefore contributes to the observed solid angle of the target.

Convert your corrected data into the normal Nemesis radiance units using the factor above and your ephemeris. After that, it’s just a matter of generating a (NEMESIS-friendly) .spx file from your data.

A.6 Closing remarks

That’s it! Have fun! Remember, while you’re modeling your atmosphere, you **need** to keep track of the exact vectorial positions and momenta of each of the $\sim 10^{40}$ particles in your atmosphere. Make sure you’re accurately solving the Schrödinger equation for each of these particles at each time step in your simulation. Note that you may need roughly $\sim 10^{28}$ laptops to do this correctly. If you need funding for all of that extra hardware, you can always check [here](#) for starters. Best of luck, and happy modeling!